RF Filtering Using Nanomechanical Resonators



Kairan Huang

Wolfson College

University of Oxford

Supervisor: Professor Harish Bhaskaran FREng

A thesis submitted for the degree of

Doctor of Philosophy

Trinity 2025

This thesis is dedicated to my parents,
Yong Huang and Li Zhang
for their everlasting support and love.

Acknowledgements

I wish to express my deepest thanks to my supervisor, Professor Harish Bhaskaran FREng. He is not only my supervisor, mentor, but also a dear friend who provides support and joy. Academically, he knows what I need the most to achieve a successful DPhil, to write a convincing paper, and to graduate smoothly.

I owe great thanks to Dr. Utku Emre Ali, Dr. June Sang (Jason) Lee, and Dr. Mingde Du for their valuable advice, insights, and encouragement. I really enjoyed talking to them. Utku is professional not only in electronics but also in photonics and in every topic he was working on. He is always warm and cheerful as a friend. Jason is also a professional researcher and always offers to help others in the humblest way. The advice he provides is critical, pertinent, and beneficial. He is also a fun guy with a cold sense of humour and knows how to enjoy his life. I especially enjoyed drinking and chatting with him. Mingde has the loudest and happiest laughter in the group. On the other hand, he speaks very wisely from his life experiences and truly wants others to live better. He shares his opinions, words he heard, and valuable information selflessly, which can help everyone in the group. I also thank the rest of the research group with which I have worked: Luci Bywater, Dr. Bowei Dong, Dr. Wen Zhou, Dr. Mengyun Wang, Dr. Guoce Yang, Dr. Mingde Du, Dr. Yu Shu, Dr. Yuhan He, Dr. Samarth Aggarwal, Dr. Nick Farmakidis, Dr. Angel Ortega, Dr. Ying Tan, Yi Zhang, Håvard Hem Toftevaag, Maxine Ong, Ruveyda Taskin, Jock Dearlove, Serena Sabnani, Sharon Morgan, Sijing Zhong, Sergei Zotkin, Tara Milne, Sirui Liu, Zhiyun Xu, Zhongyu Tang, Yuhang Lee, Yu Hao, Toby Edison, Andy Moskalenko.

I would like to thank Professor Harri Lipsanen and Vladislav Khayrudinov from Aalto University for their support in characterising, growing, and sending the high-quality indium phosphide nanowires.

I would like to thank Paul Pattinson and Radka Chakalova, the cleanroom managers, who helped me enormously with everything in the cleanroom in DWB and Begbroke. They are always nice, friendly, and chatty. I believe everyone likes working with them.

I would like to thank my best friends, Liwei Dai, Jiaqi Tang, Liang Yu, Zhuoqi Li, and Xingrui Cheng, for their companionship and support.

My infinite gratitude and love for my parents, Li Zhang and Yong Huang, go without saying. They have raised me and provided for me selflessly. They encouraged

me to pursue a DPhil and always believed in me unconditionally. They taught me critical thinking and self-discipline, yet left me enough space to live independently and make my own decisions. I will always look up to them. I would not be anywhere near the person I am today if I did not have such outstanding parents.

I also wish to express my most sincere love and thanks to my perfect wife (Dr. to be soon) Yutong Cheng. You are the other half of my life and you have made me a complete person. You brought me laughter and joy every day and taught me so much about everything. My life would not be complete without you.

Declaration

I, Kairan Huang, hereby declare that this thesis is my own work and has not been submitted to another institution for any other degree or qualification. All contributions from collaborators have been appropriately referenced throughout the work.

Abstract

Chapter 1 surveys resonator-based RF filters from lumped LC to SAW/BAW, noting strong selectivity and power handling but limited scalability and on-chip integration in dense front ends. It assesses micro-/nano-electromechanical resonators, noting the attractions of high Q, low power and tunability alongside practical concerns such as thermal drift, nonlinearity and array-level parasitics. The discussion turns to photonic integrated circuits, evanescent coupling, and cavity optomechanics in the context of microwave photonics, highlighting opportunities for high-bandwidth analogue processing while stressing the persistent difficulty of compact, low-loss, multi-channel RF filtering on chip. The chapter motivates two contributions: a CMOS-compatible nanomechanical resonator array as a compact RF filter bank, and a scalable optoelectronic multi-channel RF filter bank that maps RF passbands to distinct optical wavelengths via a multi-wavelength encoder.

Chapter 2 outlines experimental and numerical methods. on-chip structures were defined by electron-beam lithography and reactive-ion etching, with thin films by thermal/e-beam evaporation and magnetron sputtering. An optimised PDMS pick-and-place workflow enabled InP nanowire transfer. Vacuum measurements with fibre-to-grating coupling and polarisation control used a digital lock-in (HF2LI) in thermal-noise, driven-sweep and time-domain modes. Optical coupling was modelled by 3D FDTD; mechanical eigenmodes by finite elements, with meshes and boundaries calibrated to test structures.

Chapter 3 establishes and verifies a Si_3N_4 PIC architecture for multi-channel RF filtering with multi-wavelength optical encoding. Each channel couples a high-Q micro-ring to a suspended InP nanowire; piezo-driven out-of-plane motion modulates the rings effective index via evanescent coupling, imprinting the RF signal on a CW carrier. Channelisation of the device is from distinct $\{\lambda_i, f_i\}$ set by ring radius and NW length. COMSOL confirms nanowire modes; FDTD reveals resonance red-shift/broadening. A Lorentzian model considers dispersive and dissipative effects, and identifies the optimal detuning for readout.

Chapter 4 experimentally presents the simulated optomechanical multi-channel filter bank on a Si_3N_4 PIC. Design and fabrication are detailed (high-Q micro-rings, Au supports, pick-and-place InP nanowires), followed by characterisation of ring spectra before/after transfer, thermomechanical noise in air and vacuum,

and piezo-driven responses. A phase-lock stabilises detuning. Two-channel RF filtering with multi-wavelength optical encoding is demonstrated by recovering AM audio and triangular envelopes; responses scale linearly with drive and reach ≈30 dB SNR with bandwidth-limited distortion.

Chapter 5 develops a lithographically defined Si_3N_4 nanomechanical resonator array for multi-channel RF filtering, with each RF frequencies precisely defined by resonator dimensions. Euler-Bernoulli scaling and a thermal-admittance model link geometry and drive to displacement and piezoresistive readout. The refined fabrication process improved alignment tolerance and yield. High-aspect-ratio beams were fabricated and measured, but no unambiguous high-Q resonance was observed under thermoelastic or indirect piezoelectric drive. Evidence points to tensile stress shifting eigenfrequencies beyond the search window and weak transduction from interfacial thermal resistance and low gold gauge factor.

Contents

List of Figures **xii**

List of Abbreviations **xxii**

1 Literature Review **1**

1.1 Introduction 1
1.2 Conventional Radio Frequency Signal Filtering 3
1.2.1 LC Filters 4
1.2.2 Acoustic Filters 6
1.3 Nanomechanical Resonators 9
1.3.1 Actuation and Readout Methods 10
1.4 Photonic Integrated Circuits 15
1.4.1 Evanescent Field Coupling and Optomechanics 17
1.4.2 RF in Photonics 19
1.4.3 Optomechanics for RF Photonics Applications 23

2 Methodology **27**

2.1 Introduction 27
2.2 Nanofabrication Techniques 28
2.2.1 Electron-Beam Lithography 28
2.2.2 Reactive-Ion Etching 28
2.2.3 Physical Vapour Evaporation of Metals 29
2.2.4 Sputtering Deposition 30
2.3 Nanowire Pick-and-Place Technique 37
2.4 Integrated Photonics Measurements in Vacuum 41
2.5 Lock-In Detection 42
2.5.1 Thermal Noise Sweep Mode 46
2.5.2 Frequency Response Sweep Mode 46
2.5.3 Plotter Mode 46
2.6 Simulation Methods 47
2.6.1 Lumerical 47
2.6.2 COMSOL Multiphysics 48

3 Simulations on Nanowire and Mirco-Ring Resonator Coupling 49
3.1 Introduction . . . 49
3.2 COMSOL Simulations . . . 54
3.3 Lumerical FDTD Simulations . . . 55
3.4 Numerical Simulation . . . 58
3.5 Discussion . . . 60

4 RF Signal Processing with Mechanical and Optical Resonances 63
4.1 Introduction . . . 63
4.2 Device Design and Fabrication . . . 64
4.2.1 Choice of Nanowire Material . . . 65
4.2.2 Choice of Nanowire Support Material . . . 66
4.2.3 Choice of Waveguide and Micro-Ring Resonator Material . . . 67
4.2.4 Device Design . . . 68
4.2.5 Fabrication Flow . . . 69
4.3 Device Characterisation . . . 71
4.3.1 Micro-Ring Resonator Spectra . . . 72
4.3.2 Thermal Noise Measurements . . . 75
4.3.3 Wavelength Dependence of Response . . . 82
4.3.4 Driven Response . . . 90
4.4 Filtering and Encoding Capabilities . . . 98
4.5 Conclusion . . . 107

5 RF Filter Bank Based on a Nanomechanical Resonator Array 110
5.1 Introduction . . . 110
5.2 Analytical Model . . . 113
5.3 Design and Fabrication . . . 119
5.3.1 Dimensions of the Beams . . . 120
5.3.2 Design Iterations . . . 121
5.3.3 Fabrication Methods . . . 124
5.3.4 Etching of Silicon Nitride . . . 126
5.3.5 Buffered Oxide Etch . . . 129
5.3.6 Failed Fabrications . . . 132
5.4 Actuation and Readout . . . 135
5.4.1 Measurement Results . . . 135
5.5 Reasons of Failure . . . 140
5.5.1 Tensile Stress in the Silicon Nitride Film . . . 140
5.5.2 Inadequate Transduction Efficiency . . . 141
5.6 Conclusion . . . 143

6 Conclusion and Outlook **145**
6.1 Summary of Research 145
6.2 Principal Findings 146
6.2.1 Optoelectronic Filter Bank 146
6.2.2 Electrical Nanomechanical Filter Bank 147
6.3 Implications and Integration 148
6.4 Future Work 149
6.4.1 Optoelectronic RF Filter Bank 149
6.4.2 Electrical RF Filter Bank 150
6.5 Concluding Remarks 152

References **153**

List of Figures

1.1 Global submarine fibre-optic cable systems and landing stations (2025). Reproduced from [14]. 3
1.2 Schematic of basic low-pass and high-pass LC filters. 5
1.3 Schematics of a Q-enhanced LC bandpass filter design. M_{Qa} and M_{Qb} are the cross-coupled transistor pair providing negative transconductance to offset tank loss. Reproduced from [27], © 2007 IEEE, with permission. 5
1.4 (a) Basic SAW device. (b) SAW device based on the $LiNbO_3/SiO_2/SiC$ multilayered substrate. Reproduced from [6, 33], © 2007 Elsevier, © 2021 IEEE, with permission. 8
1.5 Schematics of BAW resonator designs: FBAR and SMR. Reproduced from [38]. 9
1.6 (a) A doubly clamped beam that is actuated in x direction (out-of-plane) by electrostatic actuation. (b) A contour-mode resonator that is actuated in out-of-plane direction by piezoelectric actuation. (c) A schematic showing how grating-based optical interferometry can readout displacement of a MEMS resonator. (d) A scheme to capacitively readout displacement of a resonator by applying a static gate voltage V_g. Reproduced from [43, 45–47], © 2000, 2006, 2022 IEEE, © 2007 American Chemical Society, with permission. 11
1.7 (a) Scanning electron micrograph of one of the devices used in the experiments. The insets show top-view close-up images of the detection (left) and drive (right) metal loops. (b) Schematic of the experimental setup: DC denotes directional coupler, FD: frequency doubler; HPF: high-pass filter. Reproduced from [54], © 2007 AIP Publishing, with permission. 13
1.8 (a) The whole integrated system board. SOM: system on module, connecting the SiP and the host computer through Ethernet IO. SiP: system in package. (b) Diagram of the advanced packaged SiP with 2.5D flip-chip bonding. Inset, packaged SiP with fibre attach and wire bonds to the substrate. EIC: electronic integrated circuit. FA: fibre array. (c) PIC chips with signal flow diagram. Adapted from [56], under the CC BY-NC-ND 4.0 licence. 16

1.9 Schematic illustration of the Taichi photonic chiplet system [57]. (Top) High-resolution input data are processed in parallel by multiple Taichi chiplets (1, 2, 3,) through chiplet multiplexing, enabling sliding-window input perception and yielding high-throughput outputs. (Bottom) Optical micrograph of a single Taichi chiplet, where incident light enters the diffractive encoder (DE), propagates through the interference embedding (IE) region, and exits via the diffractive decoder (DD). Reproduced from [57, 58], © 2024 AAAS, with permission. 17

1.10 High-quality nanomechanical oscillators coupled to an ultra-high-finess optical microtoroid resonator. (a) Schematic of the experiment, showing a tapered-fibre-interfaced optical resonator dispersively coupled to an array of nanomechanical oscillators. (b) Scanning electron micrograph (false colour) of an array of doubly clamped Si_3N_4 nanostring oscillators. (c) Scanning electron micrograph (false colour) of a toroid silica microcavity acting as an optomechanical near-field sensor. Reproduced from [67], with permission from Springer Nature. 19

1.11 (a) SEM image of the nanomechanical directional coupler used as a transducer. (b) Schematic illustration of the displacement sensor, showing light passing through the directional coupler before (up) and after (down) actuation. Reproduced from [18], under the CC BY 4.0 licence. 20

1.12 Schematics showing components of a typical RF photonic system with the RF filter and encoder highlighted. 21

1.13 Schematic diagram of LN-based MWP processing engine by Feng *et al.*, consisting of a high-speed electro-optic modulation block and a low-loss, multipurpose photonic processing section. Reproduced from [72], with permission from Springer Nature. 21

1.14 Schematic of the photonic processor by Zhang *et al.* Mod: modulator. BPD: balanced photodetector. TIA: transimpedance amplifier. Signal pathway starts at MRR Mod and ends at BPD, composing an on-chip waveguide with a length of 1.6 mm, which has an index of refraction near 2.44. The latency is, accordingly, the light propagation time, which is about 15 ps. Reproduced from [73], under the CC BY 4.0 licence. 22

1.15 (a) Schematics diagram of the cavity-waveguide device (a and b represent the optical and mechanical cavity modes). The mechanical cavity mode couples to the phonon waveguide at rate γ_e and has an intrinsic decay rate γ_i and an optically induced decay rate γ_{OM}. (b) SEM image of a SOI optomechanical cavity-waveguide device. The zoomed-in views show the nanobeam cavity and optical coupler, the phonon waveguide section and the waveguide termination, respectively. Reproduced from [19], with permission from Springer Nature. 23

1.16 Multiresonance RF-to-optical conversion. (a) Schematic diagram of the setup to characterize the TE_0-to-TE_1 intermodal conversion through the optical S_{21} measurement. EDFA: erbium-doped fibre amplifier; VNA: vector network analyser. (b) The optical S_{21} spectrum of TE_0-to-TE_1 conversion at 4 K around the central RF frequency of 2.22 GHz. The green translucent background indicates the TE_1 mode resonance. The inset illustrates that multiple phononic resonances can phase- match the TE_0- to- TE_1 conversion within the bandwidth of one photonic resonance. The red circles indicate the phononic resonances. The blue (green) translucent area indicates the TE_0 (TE_1) spread on the dispersion diagram. Reproduced from [20], under the CC BY-NC 4.0 licence. 25

2.1 AJA International Orion Sputtering System. (a) Overall appearance, showing the vacuum chambers and the control hardware. (b) The load-lock and main chambers with key components. 31

2.2 A damaged Sb (antimony) target. (a) The Sb target with the indium bonding melted. The copper mesh is stuck on the target by overflown indium. (b) The backside of the Sb target with melted indium bonding. Overflown and re-solidified indium can be seen. 35

2.3 Cracked sputtering targets: (a) GST; (b) ITO. (c) A severely damaged Sb_2Se_3 sputtering target, with most of the damage around the annulus at approximately half the target radius, showing the 'race-track' erosion pattern. (d) A heavily used Ge target also showing the 'race-track' erosion pattern which the majority of material removal occurs around this annulus. 36

2.4 NW transfer process. a) A single NW is picked up by the tapered polymer tip from a forest of NWs on the growth substrate. The NW adheres to the tip due to the enhanced van der Waals forces overcoming the weaker interactions between smooth, crystalline NW surfaces. b) The NW on the tip is placed onto a dome-shaped PDMS stamp cured over a glass slide. Note that the adhesion of the PDMS stamp to the NW is greater than that of the tip. c) The stamp with the NW is turned upside down and its alignment with the device chip is done under a light microscope. Following alignment, the stamp is imprinted over electrodes on the device substrate. d) NW deposition is completed with the removal of the stamp. Reproduced from [97]. 38

2.5 Photos showing the setup for the first step (picking up the NW). (a) The XYZ stage which controls moves the glass tip, the microscope stage which moves the substrate and the glass slide where the PDMS stamp is on. (b) The glass tip is above the NW substrate, ready to pick up NWs and leave the NWs on the PDMS stamp. 39

2.6 Optical microscopy images of: (a) The InP NW forest on substrate and the glass tip picking up the NWs. NW seeds which did not successfully grow NWs are also visible, and they might be picked up. (b) Some NWs picked up by the glass tip. (c) Some NWs placed on the PDMS stamp by the glass tip. (d) One NW successfully transferred onto the metal supports using the pick-and-place process. 40

2.7 Working principle of a lock-in amplifier. The input signal $V_t(t)$ is split into two identical parts, and they are multiplied by the reference signal $V_r(t)$ and its 90°phase-shifted version. The outputs from both mixers, X and Y, are low-pass filtered to retain the DC component and reject the noise and the 2ωcomponent. Then the signals were converted into polar coordinates R and θ. Reproduced from [98]. . . 43

2.8 Temporal data and frequency spectra of: (a) $V_s(t)$, where $R = 1$, $\omega_s = 100$ Hz, $N = 2$, $\omega_n = 320$ Hz; (b) $V_s(t) \times V_r(t)$, where $\omega_r = 100$ Hz; (c) $Z(t)_{filtered}$, cutoff of the low-pass filter is 10 Hz. 45

3.1 Schematic showing how CW light can be encoded with information at resonant frequency of the NW in the MRR. 51

3.2 Schematic of the filter bank device with 2 MRRs and 2 NWs with NW 1 resonating at f_1 coupled to Ring 1 and NW 2 resonating at f_2 coupled to Ring 2. The optical inputs are CW light at λ_1 and λ_2 which are resonant wavelengths of Ring 1 and Ring 2 sent to the bus waveguide. The electrical input is the sum of two different AM signals at f_1 and f_2. λ_1 would be coupled into Ring 1 and encoded with the AM signal at f_1, and λ_2 would be coupled into Ring 2 and encoded with the AM signal at f_2. The through optical outputs are then collected and measured from the bus waveguide. 53
3.3 COMSOL simulated shapes of trough and peak positions of the doubly-clamped beam above the waveguide with colour scale on its normalised displacement. 55
3.4 (a) The FDTD simulated MRR spectra when the NW is at peak and trough positions of its vibration. (b) The absolute difference between the two spectra, showing a trough at the centre where two spectra intersect, and two asymmetrical maxima with the one on the left (lower wavelength) taller. 57
3.5 Purely numerical simulation of two MRR spectra (Lorentzian distributions), where Spectrum A is the original MRR spectrum, and Spectrum B is the modified MRR spectrum: (a) Red-shifted; (c) Broadened; (e) Red-shifted + Broadened. (b), (d) and (f): Calculated absolute differences between the two spectra in (a), (c) and (e) respectively. 59
3.6 FDTD simulated electric field profile around a Si_3N_4 MRR with and without the suspended NW. Schematics showing the 3D simulated model (a) with, (b) without the suspended NW. (c) Tangential cross-sectional electric field profile of a bare a Si_3N_4 MRR as in (a), showing the nodes of optical resonances and most of the electric field confined within the waveguide. (d) Tangential cross-sectional electric field profile of a Si_3N_4 MRR with a InP NW suspended above the waveguide as in (b), showing that the nodes of optical resonance are disturbed, and electric field is not only confined in the waveguide, but also distributed in the NW and above the waveguide. This is the evidence that the suspended NW acts as a scatter above the waveguide, introducing optical loss to the MRR. 62

4.1 Design for the first EBL process, including the photonic components and two pairs of the supports. 68
4.2 Fabrication process flow of the optoelectronic filter bank device with two MRRs and NWs. 69

4.3 (a) Optical image of a successfully fabricated device. Insets show the NWs on supports. (b) Tilted SEM image of a NW positioned above the MRR. 71
4.4 MRR spectra before and after the NW transfer. (a) Comparison between the MRR spectra with and without the suspended NW on a 2-ring device. The resonances from the two rings can be distinguished by the different FSRs. The smaller FSR (1.49 nm) corresponds to resonances of Ring 1 ($R = 120$ µm), and the larger FSR (1.58 m) corresponds to resonances of Ring 2 ($R = 113$ µm). (b) Zoom-in view of (a) showing the red-shifts of the resonant wavelengths, increase of resonance linewidth and decrease of ER (decrease of quality factor) after the NW is transferred above the MRR. The MRR spectra with fitted Lorentzian curves and quality factors for resonances at: (c) 1503.98 nm; (d) 1504.47 nm; (e) 1504.32 nm; (f) 1504.85 nm. 73
4.5 MRR spectra with smaller quality factors before and after the NW transfer. (a) Comparison between the MRR spectra with and without the suspended NW on a 2-ring device with lower quality factors. (b) Zoom-in view of (a) showing the decreased quality factors and ERs. 75
4.6 Schematics showing the experimental set-up that is used to measure thermal noise spectrum of the device under ambient pressure with the PLL. 77
4.7 Thermal noise spectra under ambient pressure. (a) Thermal noise spectrum of a 2-ring device measured under ambient pressure. (b) Thermal noise from (a) with baseline subtracted, centre frequency and quality factors from Lorentzian fitting. 78
4.8 Schematics showing the experimental set-up that is used to measure thermal noise spectrum of the device under vacuum with the PLL. . 79
4.9 Thermal noise spectra under vacuum. (a) Thermal noise spectra of a 2-ring device measured under vacuum. (b) Thermal noise from (a) with baseline subtracted. The thermal noise spectra and Lorentzian fittings of resonances from (c) Ring 1 and NW 1 and (d) Ring 2 and NW 2. 80
4.10 Thermal noise spectra of a device with MRR but without suspended NW. There is no resonance peak, but only the baseline from the noise floor of the PD. 82
4.11 Wavelength (detuning) dependence of the response amplitude and the MRR spectrum. 83
4.12 Drift of transmission when the wavelength of the optical input is set to the highest sensitivity position, which has a small negative detuning and is very close to the resonant wavelength, under vacuum environment. 86

4.13 The user interface for the PLL LabVIEW VI. The loop maintains a fixed transmission (hence detuning) by adjusting the laser wavelength, locking to the left-slope maximum sensitivity point. 87
4.14 Wavelength dependence of the response amplitude and the MRR spectrum in absolute transmission. 88
4.15 Schematics showing the experimental set-up that is used to measure PZT-driven frequency response of the device under vacuum with the PLL. 91
4.16 Driven responses of the device. (a) Driven responses of the two MRRs with two NWs over a large range with a driving voltage of 0.889 V. The peaks from 5 to 13 MHz are noise from the vibration of the assembly and spurious modes of the PZT chip. The peaks around 15.6 and 30.0 MHz are the driven responses of the NWs. Driven responses of: (b) Ring 1 & NW 1; (c) Ring 2 & NW 2, with larger driving amplitudes, higher resolution, and Lorentzian fitting. 92
4.17 Driven responses of a device with driving voltage up to 53.3 V. The readout amplitude stays linear with the driving voltage until the assembly breaks when the driving voltage increases beyond 53.3 V. 95
4.18 Filtering and encoding capability experiment. (a) Schematics showing the experimental set-up that is used to show the filtering and encoding capabilities of the device. AWG: arbitrary wavefront generator; LO: local oscillator. (b) Prepared Audio 1 signal with an amplitude of 100 mV (output from the AWG) that would be mixed with the sine wave at f_1, 15.67 MHz, with an amplitude of 100 mV (output from the LIA) by one of the frequency mixers. (c) Prepared Audio 2 signal with an amplitude of 100 mV that would be mixed with the sine wave at f_2, 29.95 MHz, with an amplitude of 100 mV by the other frequency mixer. 99
4.19 Time-domain demodulated outputs. (a,b) Optical input at Ring 1's resonant wavelength: demod at f_1 recovers Audio 1; demod at f_2 shows slight leakage. (c,d) Optical input at Ring 2's resonant wavelength: demod at f_1 shows only noise; demod at f_2 recovers Audio 2. 101
4.20 Original audio envelopes (black) and retrieved signals (red) for both channels: (a,c) full 200 ms; (b,d) zoom-ins. High-amplitude features are recovered; low-level details are limited by the background noise floor. 103

4.21 AM triangular-wave test at f_1 with 4.2 kHz envelope. (a) Output amplitude plotted against driving voltage, showing linear scaling. (b) SNR plotted against driving voltage, showing that SNR rises then saturates at ∼30 dB. (c) Normalised recovered envelopes at different driving voltages. 105

4.22 (a) Recovered outputs at several drive levels with the input triangular wave in the background. (b) Bandwidth study at fixed drive, increasing LPF bandwidth sharpens waveform but raises noise level. (c) SNR plotted against LPF bandwidth, showing improvement that plateaus as noise increases. 106

5.1 A doubly clamped beam resonator with length L, width b and thickness t. 111

5.2 Schematics showing the working principle of the electromechanical filter bank system with 4 suspended beams with different length resulting in 4 bandpass filters with different frequencies. All beams are actuated via thermoelastic method, and readout via piezoresistive method. 112

5.3 Simulated eigenfrequency mapping and mode shape. (a) Beam length that would result in upper and lower frequency limits for different thicknesses calculated using Equation 3.2. Any combinations within the two curves result in frequency between 5 and 50 MHz. An example was chosen to have 200 nm thickness and 12 µm length. (b) Simulated (by COMSOL Multiphysics) mode shape of fundamental z-plane mode of the 200 nm thick, 12 µm long and 600 nm wide beam. Simulated eigenfrequency is 12.88 MHz which lies in the target range. 121

5.4 Design of the first iteration. (a) Overall chip layout including in total 49 devices. (b) Design of a single device showing the NW array, source pads and the shared ground pads. (c) Details of the NW array and electrodes. (d) Dimensions of the electrode and the nanobeam. 122

5.5 Design of the second iteration addressing the problems of the first iteration. (a) Overall chip layout including in total 6 devices. (b) Design of a single device showing the NW array, electrical routings and contact pads. (c) Details of the NW array, electrodes and electrical routings to contact pads. (d) Dimensions of the electrode and the nanobeam. 124

5.6 Nanofabrication process flow of the nanobeam array (not to scale). . 125

5.7 (a) Optical microscope image showing the wires connecting the on-chip electrodes and the electrical contacts on the PCB. (b) Image showing the whole PCB with the device chip glued on it, and with SMA cables connected. The chip was broken accidentally during dicing, but the filter bank device was undamaged. Note that there is a piezoelectric chip underneath the device chip, and it is for the alternative piezoelectric actuation method which would be explained in Section 5.4.1. 126

5.8 Nanobeams fabricated with different thicknesses of Si_3N_4. (a) Original thickness (330 nm). Scale bar: 2.5 µm. (b) 165 nm. Scale bar: 5 µm. (c) 100 nm. Distortions and abnormal bright spots due to local charging effect. Scale bar: 2.5 µm. (d) 80 nm, the beams collapsed. Scale bar: 5 µm. 127

5.9 (a) Developed mask of the lithographically defined beams of different widths and lengths. The Si_3N_4 in the exposed areas would first be etched via RIE to expose oxide, and the oxide would then be etched via BOE. Scale bar: 20 µm. (b) and (c) SEM image showing BOE etched beams with 3 minutes of etching. (b) A beam with 0.6 µm width and 4 µm length showing a suspension (gap between the beam and the substrate). Scale bar: 5 µm. (c) A beam with 0.6 µm width and 24 µm length also showing suspension, but also the large amount of residues around the etched areas. Scale bar: 10 µm. 130

5.10 (a) SEM image of the sample after the second BOE run (3 minutes of BOE) where lengths of the beams are increased, and another DI water rinsing step was added. The crystalline residues are not present. Scale bar: 5 µm. (b) Close up image of the sample after the second BOE run. Scale bar: 2 µm. (c) SEM image of a sample with gold electrodes after 4 minutes of BOE. The suspension is visible, but very small. Scale bar: 5 µm. (d) SEM image of a sample with gold electrodes after 8 minutes of BOE. The suspension is large, showing complete release of the Si_3N_4 beam. Note that the thickness of nitride is also thinner, since the first RIE step is added for this sample. Scale bar: 2.5 µm. 131

5.11 Images of failed fabrications. (a) SEM image of a device with improperly patterned electrode with an unopened loop. Scale bar: 2 µm. (b) Image of a device where the mask for electrodes and routings misaligned with the nanobeams. Scale bar: 10 µm. (c) Image of a device where the deposited gold layer is patterned with vertical and horizontal lines. Scale bar: 20 µm. (d) SEM image of the same sample in (c), showing the gaps between the segments of gold. Scale bar: 5 µm. (e) Image of a device where the deposited gold layer disappeared after the lift-off process. Scale bar: 50 µm. (f) Image of a device where a small portion of the deposited gold layer remains. Scale bar: 100 µm. 133
5.12 An image of the setup used to characterise the filter bank device. . 136
5.13 (a) The schematics used for thermoelastic actuation and piezoresistive readout the device. LIA: lock-in amplifier; LNA: low-noise amplifier. (b) Readout signal of a single beam using the setup. The DC voltage on readout electrode is 100 mV. The expected resonant frequency of the measured beam is 12.88 MHz. 137
5.14 (a) The schematics used for indirect piezoelectric actuation and piezoresistive readout the device. HPA: high-power amplifier. (b) Readout signal of a single beam with indirect piezoelectric actuation and piezoresistive readout methods. The expected resonant frequency of the measured beam is 12.88 MHz. 139

List of Abbreviations

5G . . . . . Fifth generation of cellular network technology

6G . . . . . Sixth generation of cellular network technology

AC . . . . . Alternating current

ADC . . . . . Analogue-to-digital converter

AWG . . . . . Arbitrary waveform generator

AlN . . . . . Aluminium nitride

BAW . . . . . Bulk acoustic wave

CMOS . . . . . Complementary metal-oxide-semiconductor

CW . . . . . Continuous wave

DAC . . . . . Digital-to-analogue converter

DC . . . . . Direct current

DI . . . . . Deionised water

EBL . . . . . Electron-beam lithography

EM . . . . . Electromagnetic

EMI . . . . . Electromagnetic interference

EOM . . . . . Electro-optic modulator

ER . . . . . Extinction Ratio

FDTD . . . . . Finite-difference time-domain

FBAR . . . . . Thin film bulk acoustic resonator

FPGA . . . . . Field-programmable gate array

FSR . . . . . Free spectral range

FWHM . . . . Full Width at Half Maximum

GPU . . . . . Graphics processing unit

GPS . . . . . Global Positioning System

HPF . . . . . High-pass filter

HPA . . . . . High-power amplifier

IDT . . . . . Interdigital transducer

InP . . . . . Indium phosphide

IPA . . . . . Isopropanol

ITR . . . . . Interfacial thermal resistance

LIA . . . . . Lock-in amplifier

LN . . . . . Lithium niobate

LO . . . . . Local oscillator

LPCVD . . . . Low-pressure chemical vapour deposition

LPF . . . . . Low-pass filter

MAC . . . . . Multiply-accumulate

MIBK . . . . . Methyl isobutyl ketone

MRR . . . . . Micro-ring resonator

MWP . . . . . Microwave photonics

MZI . . . . . Mach-Zehnder interferometer

NEMS . . . . . Nanoelectromechanical systems

NW . . . . . Nanowire

OMR . . . . . Optomechanical ring resonator

PCB . . . . . Printed circuit board

PD . . . . . Photodetector

PDMS . . . . . Polydimethylsiloxane

PEC . . . . . Proximity effect correction

PIC . . . . . Photonic integrated circuit

PLL . . . . . Phase-locked loop

PSD . . . . . Power spectral density

PVD . . . . . Physical vapour deposition

PZT . . . . . Lead zirconate titanate, $\mathrm{Pb[Zr}x\mathrm{Ti1} - x\mathrm{]O_3}$

Q . . . . . Quality factor

QCM . . . . . Quartz crystal microbalance

RIE . . . . . Reactive-ion etching

RF . . . . . Radio frequency

SAW . . . . . Surface acoustic wave

SEM . . . . . Scanning electron microscope

SMR . . . . . Solidly mounted resonator

SNR . . . . . Signal-to-noise ratio

SOI . . . . . Silicon on insulator

SOS . . . . . Silicon on sapphire

SQL . . . . . Standard quantum limit

TOPS . . . . . Tera operations per second

TPA . . . . . Two-photon absorption

ZnO . . . . . Zinc oxide

1 Literature Review

Contents

1.1 Introduction 1
1.2 Conventional Radio Frequency Signal Filtering 3
1.2.1 LC Filters 4
1.2.2 Acoustic Filters 6
1.3 Nanomechanical Resonators 9
1.3.1 Actuation and Readout Methods 10
1.4 Photonic Integrated Circuits 15
1.4.1 Evanescent Field Coupling and Optomechanics 17
1.4.2 RF in Photonics 19
1.4.3 Optomechanics for RF Photonics Applications 23

1.1 Introduction

Radio-frequency (RF) filtering is crucial to modern communication and sensing systems [1–4]. Industrial practice has long relied on resonator-based approaches, from lumped-element electrical filters to surface and bulk acoustic wave (SAW/BAW) devices. Their advantages, including efficient transduction, compact footprints and manufacturing maturity, have enabled multi-band front ends in mobile devices [5–7]. In parallel, advances in micro- and nano-electromechanical systems (M/NEMS) have demonstrated exceptional quality factors (Q), low power consumption, and wide

tunability, attracting interest in RF filtering [8–10]. Building on these developments, this work introduces a lithographically defined *nanomechanical resonator array that realises a compact, CMOS-compatible RF filter bank, capable of precise frequency selection* through thermoelastic actuation and piezoresistive readout.

RF front ends are not only indispensable in wireless communication networks; they are also implemented at the electro-optic boundary of fibre systems, including radio-over-fibre links, cable landing stations, and data centre interconnects, where RF-band information is imposed on and recovered from optical carriers [11–13]. The global optical network, dominated by submarine cable systems that interconnect the continents, forms the backbone of the global Internet, as shown in Figure 1.1 [14, 15]. Although the optical carriers are at hundreds of terahertz, the information is structured as RF envelopes from kilohertz to tens of gigahertz. Therefore, RF operations such as filtering, channelisation and frequency translation remain essential at these interfaces. Integrating these functions on PICs cuts down on electrical-optical conversions and improves scalability [11, 13]. PICs have emerged as strong candidates for high-bandwidth analogue and neuromorphic processing, with demonstrations of low-latency microwave-photonic systems and large-scale optical accelerators [16, 17]. Exploiting evanescent coupling and optomechanics, recent work has also realised ultra-sensitive displacement sensing, low-loss RF photonic front ends, and RF-to-optical conversion on chip [18–20]. Yet compact, scalable multi-channel RF filters remain difficult to implement, due to accumulated insertion loss, tight passband alignment and thermal-crosstalk constraints. This thesis proposes a scalable, integrated *optoelectronic multi-channel RF filter bank with a multi-wavelength optical encoder* by coupling nanomechanical resonators with optical cavities.

This chapter first reviews the foundations of conventional RF filters, including inductor-capacitor (LC) networks, SAW and BAW devices, in order to situate their strengths and limitations in the context of modern communication systems. It then examines the emergence of M/NEMS resonators, with emphasis on their actuation and readout mechanisms, compactness, and CMOS compatibility, highlighting their

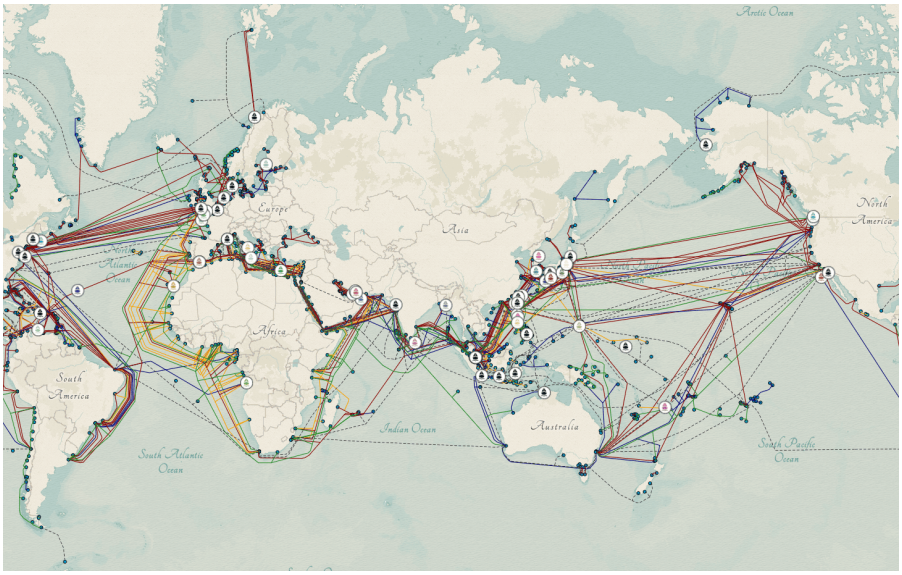


Figure 1.1: Global submarine fibre-optic cable systems and landing stations (2025). Reproduced from [14].

potential for integrated RF filtering. Building on this, the discussion turns to PICs, tracing their evolution from discrete optical components to large-scale computing platforms, and surveying recent advances in evanescent coupling, optomechanics, and RF photonics. Finally, these strands are brought together to motivate the proposed devices developed in this thesis: a scalable, integrated optoelectronic multi-channel RF filter bank with a multi-wavelength optical encoder and a lithographically defined nanomechanical resonator array for electrical RF filtering.

1.2 Conventional Radio Frequency Signal Filtering

All wireless communication systems that are used today, including analogue radio, the Global Positioning System (GPS), mobile networks, and television broadcasting, are based on electromagnetic (EM) waves in the RF range [21]. Increasing data-rate demands have driven RF systems towards greater architectural complexity and functional density. Given spectrum congestion, RF filters provide low-loss selection of desired bands while suppressing interference, thereby preserving link integrity and spectral efficiency [3, 4]. By optimising the performance of RF systems,

filters help achieve precise frequency selection, improved bandwidth utilisation, and better overall system performance, which makes them crucial in modern RF technologies such as 5G and 6G.

Most filtering technologies are based on one or more coupled resonators, including EM and mechanical resonators [1, 2, 22]. The working range of the filters depends on the resonant frequencies. A resonator is any system or device designed to oscillate naturally with greater amplitude at specific frequencies, called its resonant frequencies. When energy (such as sound waves, EM waves, or mechanical vibrations) is introduced at or near a resonant frequency of the system, the resonator can store and amplify that energy.

The following subsections outline resonator-based RF filters, including electrical LC and acoustic (SAW/BAW), and contrast their properties.

1.2.1 LC Filters

During the early 20th century, when radio communication was emerging, the need for RF filters started developing. The LC filter was amongst the earliest RF filter technologies. The inductor in an LC filter opposes changes in current, and its reactance increases with frequency. The capacitor opposes changes in voltage and its reactance decreases with frequency [23]. The complementary reactances of L and C form resonant networks that enable LC filtering [1]. The resonant frequency of a passive LC tank can be calculated:

$$f_0 = \frac{1}{2\pi\sqrt{LC}} \tag{1.1}$$

Different connections between inductors and capacitors exhibit various functionalities, leading to different filters. Adjusting the inductances and capacitances of the components shifts the frequency range of the filter.

LC filters can be easily designed and simulated with lumped-element models, and their performance can be effectively predicted and tuned [24]. Figure 1.2 shows the basic designs of low-pass and high-pass LC filters. Passive LC filters can exhibit low insertion loss, but performance depends on component Q and layout at RF [1].

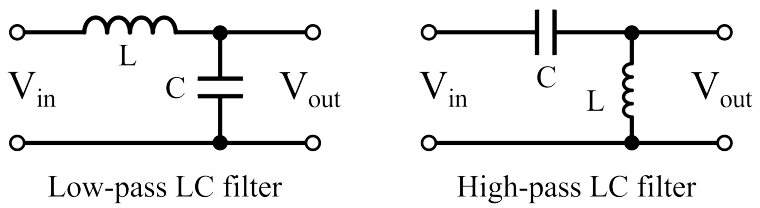


Figure 1.2: Schematic of basic low-pass and high-pass LC filters.

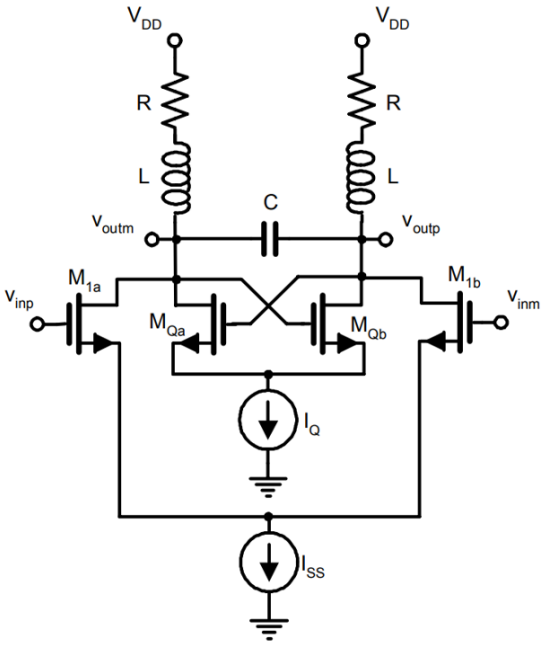


Figure 1.3: Schematics of a Q-enhanced LC bandpass filter design. M_{Qa} and M_{Qb} are the cross-coupled transistor pair providing negative transconductance to offset tank loss. Reproduced from [27], © 2007 IEEE, with permission.

This characteristic makes LC filters well-suited for applications that require efficient power usage and low signal attenuation. The passive nature also means that LC filters do not need external power to operate, which could be beneficial for power-sensitive applications [25]. LC filters operate linearly over a broad dynamic range and can handle higher power levels. They do not introduce significant nonlinearities or distortions under normal operating conditions, making them ideal for applications that demand signal integrity, such as RF front ends and audio filtering [26].

Efforts are made to improve the performance of LC filters. For example, as shown in Figure 1.3, the authors introduced a cross-coupled transistor pair in the middle of the schematic, which provides negative transconductance (or negative

resistance) that compensates for losses [27]. With reduced energy losses, the Q factor of this resonator can be enhanced, leading to a narrower resonance and more accurate bandpass filtering, but at the cost of noise and potential stability concerns.

However, LC filters are less prevalent in RF communication applications nowadays due to several weaknesses compared to other filter technologies. On-chip LC filters become less effective and unpredictable above a few GHz due to the growing influence of parasitic effects. At these high frequencies, components no longer behave as ideal elements [28]. According to Equation 1.1, to achieve higher frequencies, the product of LC needs to be smaller, but there are physical limitations that prevent it from decreasing infinitely.

1.2.2 Acoustic Filters

For modern mobile devices such as smartphones, smart watches, and tablets, acoustic filters are the filter technology that meets the stringent size, performance, and cost requirements necessary to support high-frequency multi-band wireless connectivity (4G/5G/Wi-Fi/Bluetooth), while maintaining reliable signal integrity [5]. The core component of an acoustic filter is a piezoelectric material (e.g., quartz, lithium tantalate, or aluminium nitride) [29]. When an electrical signal is applied to this material, it creates mechanical vibrations; conversely, mechanical vibrations induce electrical signals.

When the filter is working, an alternating current (AC) signal is applied to the piezoelectric material through specialised electrodes (often arranged in an interdigitated pattern), exciting mechanical (acoustic) vibrations at specific frequencies [29]. These vibrations then propagate along the surface or through the bulk, creating a resonant filter effect that selectively allows certain frequencies to pass while attenuating others [6]. The different propagation paths of the acoustic wave give rise to two distinct types of acoustic filters, which are described here.

Surface Acoustic Wave Filters

The existence of an SAW was shown in 1885 by Lord Rayleigh [30]. An SAW propagates along the plane surface of an isotropic solid half-space, with an amplitude that decays exponentially away from the surface [30]. Its propagation speed is much lower than that of an EM wave, which is convenient for processing acoustic signals [31]. Later, researchers working with piezoelectric materials discovered that the interdigital transducer (IDT, metal electrodes patterned on piezoelectric materials) could generate and detect SAWs by matching the electrode periodicity [6, 32]. A basic SAW device is shown in Figure 1.4 (a). Applying a voltage to the input IDT creates a periodic electric field. Due to the piezoelectric effect, this field induces elastic stress in the material. When the frequency is such that the acoustic wavelength aligns with the spacing of the transducer electrodes, surface waves are generated efficiently. At the output end, the output IDT operates in reverse, converting these incoming waves into an electrical output signal. In this way, the device effectively transforms an electrical input into another electrical output [6].

Figure 1.4 (b) shows an SAW device based on the $LiNbO_3/SiO_2/SiC$ multilayered substrate [33]. It is used to design high-performance passband filters with a centre frequency of 1.28 GHz and a fractional 3-dB bandwidth of 16.65%.

SAW filters often exhibit high quality factors (Q) in narrowband applications, though the overall insertion loss can be affected by substrate properties and fabrication imperfections. However, the operating frequency is determined primarily by the spatial periodicity of the IDTs and the intrinsic velocity of the SAW in the substrate. This typically confines SAW devices to the sub 3 GHz range [34]. Due to the surface-bound nature of the acoustic wave, SAW devices can be susceptible to temperature-induced drift, often requiring compensation in precision applications [35].

Despite limitations, SAW filters are widely used in television receivers, mobile communications, and radars due to their simple structure, mature miniaturisation, and low cost [36].

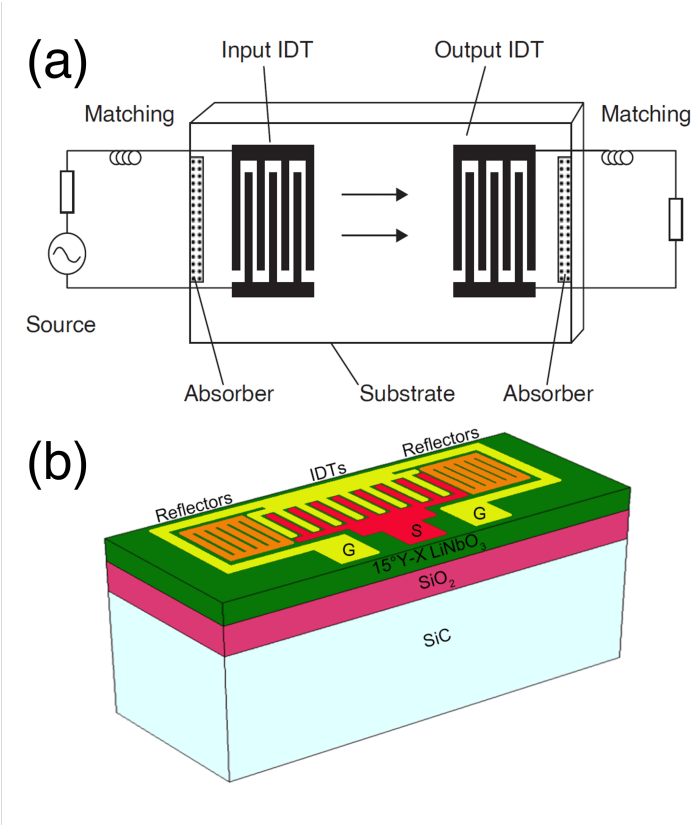


Figure 1.4: (a) Basic SAW device. (b) SAW device based on the $LiNbO_3/SiO_2/SiC$ multilayered substrate. Reproduced from [6, 33], © 2007 Elsevier, © 2021 IEEE, with permission.

Bulk Acoustic Wave Filters

In BAW devices, the acoustic energy propagates through the thickness of a substrate rather than along its surface [37]. BAW resonators are usually composed of a piezoelectric thin film (commonly aluminium nitride (AlN) or zinc oxide (ZnO)) deposited between two metal electrodes. Thin-film stacks are commonly deposited by sputtering, which affords tight thickness control critical to setting the acoustic resonance [7, 37]. When an AC RF voltage is applied across the electrodes, the piezoelectric film undergoes mechanical deformation due to the piezoelectric effect. This deformation generates an acoustic wave that propagates through the thickness of the film. In BAW devices, the resonant frequency is predominantly determined by the thickness of the film and the acoustic velocity in the piezoelectric material [7].

Two popular configurations of BAW resonators are the thin film bulk acoustic

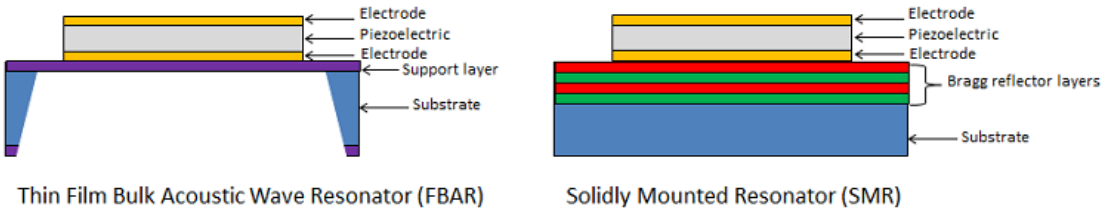


Figure 1.5: Schematics of BAW resonator designs: FBAR and SMR. Reproduced from [38].

wave resonator (FBAR) and the solidly mounted resonator (SMR), with their structures shown in Figure 1.5. In the FBAR configuration, the resonator is free-standing, and an air cavity beneath the resonator is used to isolate and confine the acoustic energy from the substrate or surroundings, so that a standing wave between the electrodes can form. In contrast, an SMR achieves acoustic isolation using a multilayer Bragg reflection (acoustic mirror) deposited directly on a solid substrate [7]. SMRs avoid cavities by using Bragg reflectors but require tight layer thickness control to maintain acoustic stop-bands.

1.3 Nanomechanical Resonators

As discussed above, the resonator is a perfect candidate for filtering applications. LC filters are based on electrical resonators, while acoustic filters are based on mechanical resonators. In this thesis, the applications of microelectromechanical system (MEMS) and nanoelectromechanical system (NEMS) resonators in RF filtering technology are discussed. Compared to traditional resonators, they have many advantages.

- **Miniaturisation:** M/NEMS resonators can be fabricated on a much smaller scale than traditional RF filters. The reduction in size allows for more compact designs and larger possibilities for on-chip integration, which are crucial in modern electronics where space is at a premium [39, 40].

- **Low power consumption:** Due to their small size and efficient design, M/NEMS resonators consume less power than conventional RF filters. This

advantage is particularly beneficial for battery-operated devices and applications where energy efficiency is critical [39, 41].

- **Broad frequency tuning range:** M/NEMS resonators offer a wide frequency tuning range, allowing them to adapt to various RF applications and environmental conditions. They can be dynamically tuned through electrostatic or magnetic forces, providing flexibility that traditional filters lack [10, 39].

- **High quality factor:** M/NEMS resonators can achieve exceptionally high quality factors, often exceeding those of traditional filters. For example, by controlling the tensile stress in a doubly clamped silicon nanomechanical resonator, the quality factor can be increased to up to 390,000 at room temperature [8, 10, 42].

1.3.1 Actuation and Readout Methods

The performance of the nanomechanical resonators critically depends on effective actuation and readout mechanisms, which have evolved to meet the demands for higher sensitivity, lower power consumption, and greater integration with photonic or electronic systems. Several widely used actuation and readout methods are discussed here with examples [9].

Electrostatic actuation is often used in M/NEMS due to its simplicity and compatibility with complementary metal-oxide-semiconductor (CMOS) processes. Bannon *et al.* constructed free-standing nanomechanical beams made of conductive polysilicon, as shown in Figure 1.6 (a) [43]. A DC bias voltage is applied to the beam, and an AC voltage is applied to the electrode below. The AC signal creates a time-varying electrostatic force, driving the beam into an out-of-plane flexural resonance (x direction in Figure 1.6 (a)). It has advantages, including lower power requirements and a simple operating principle, but it requires a large bias, small gaps, and conductive resonators, and it introduces nonlinearities at high driving amplitudes [44].

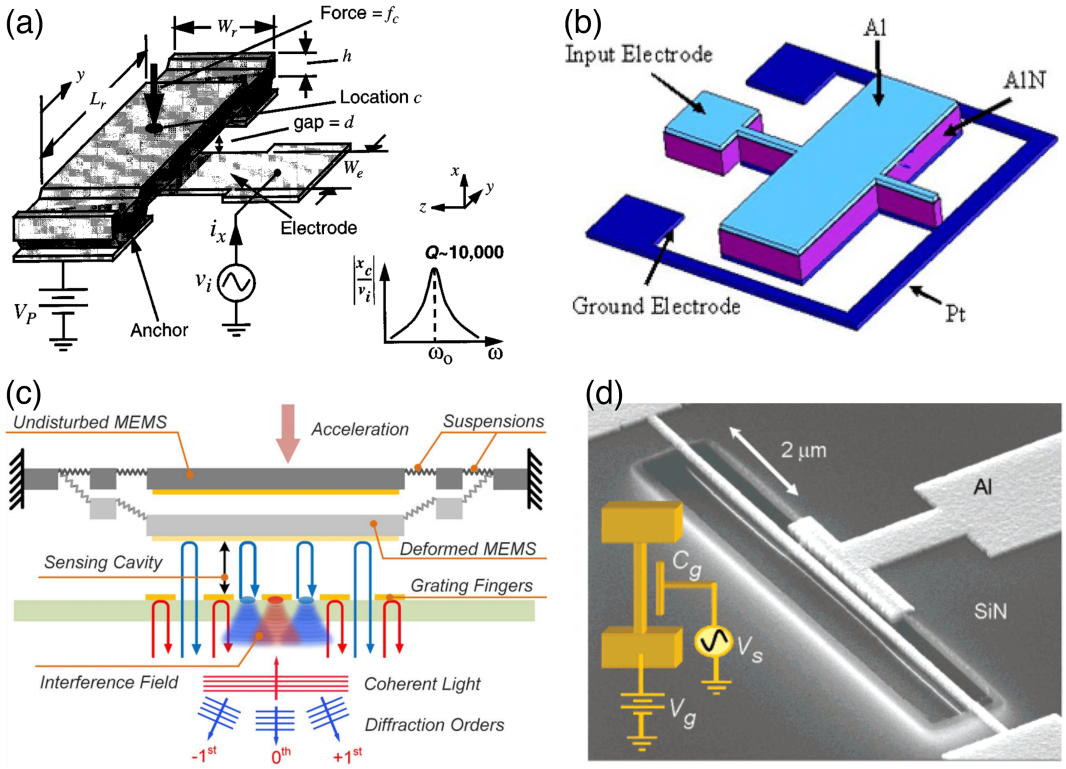


Figure 1.6: (a) A doubly clamped beam that is actuated in x direction (out-of-plane) by electrostatic actuation. (b) A contour-mode resonator that is actuated in out-of-plane direction by piezoelectric actuation. (c) A schematic showing how grating-based optical interferometry can readout displacement of a MEMS resonator. (d) A scheme to capacitively readout displacement of a resonator by applying a static gate voltage V_g. Reproduced from [43, 45–47], © 2000, 2006, 2022 IEEE, © 2007 American Chemical Society, with permission.

Piezoelectric actuation relies on piezoelectric materials (e.g., AlN, PZT) to convert electrical signals into mechanical strain, thereby enabling direct actuation of resonators. Piazza *et al.* demonstrated contour-mode MEMS resonators made of AlN, where the fundamental resonant frequency is defined by in-plane dimensions rather than the thickness, as shown in Figure 1.6 (b) [45]. The piezoelectric material is sandwiched between the input and ground electrodes, and by sending AC voltage at resonant frequencies to the input electrode, the resonator can be actuated. The advantages include high actuation strength, linear response, and high frequency capability, but challenges remain in integration with the CMOS process and the fact that material losses and acoustic leakage can limit Q [48].

Piezoelectric actuation can also be indirect, where the piezoelectric element

is not part of the resonator structure itself but is instead mechanically coupled to it. The strain generated by the piezoelectric material under the applied electric field is transferred to the resonator through a supporting substrate or mechanical link. The indirect method avoids the need for piezoelectric material for the resonator, which is very useful for driving materials such as silicon, silicon nitride, or graphene [49]. This method is widely used in cryogenic or vacuum experiments, where the integration of electrical contacts to nanoscale devices is challenging. It enables clean mechanical driving of high-Q resonators without adding lossy or stress-inducing piezoelectric films [50, 51]. However, it has disadvantages such as broadband excitation, limited control over spatial driving forces, and large mechanical coupling losses [52].

On readout methods, optical interferometry is a traditional and highly sensitive method that involves detecting the displacement of a resonator by the interference of reflected or scattered light. Li *et al.* employ optical interferometry for displacement readout on a MEMS accelerometer as shown in Figure 1.6 (c) [46]. The device uses a grating-based interferometer, where a reference grating is fixed and another grating is attached to a deformable proof mass that moves out-of-plane under acceleration. A laser source is directed onto the two gratings, and the interference between the two reflected lights changes due to the minute vertical movement, modulating the light intensity, which is tracked by an integrated photodetector (PD). The advantages of optical interferometry include ultra-high resolution (sub-picometre has been reported), and the disadvantages include bulky setups and high requirements for alignment sensitivity [53].

The capacitive (or electrostatic) readout method relies on the variation in capacitance between the resonator and an electrode to infer displacement. Truitt *et al.* used the capacitive readout method to perform a multiplexed readout of an array of individually addressable resonators with a side gate over a wide temperature range, as shown in Figure 1.6 (d) [47]. It is one of the most widely used methods because it is CMOS-compatible and requires very low power. However, it suffers from limited sensitivity at nanoscale gaps and parasitic capacitance.

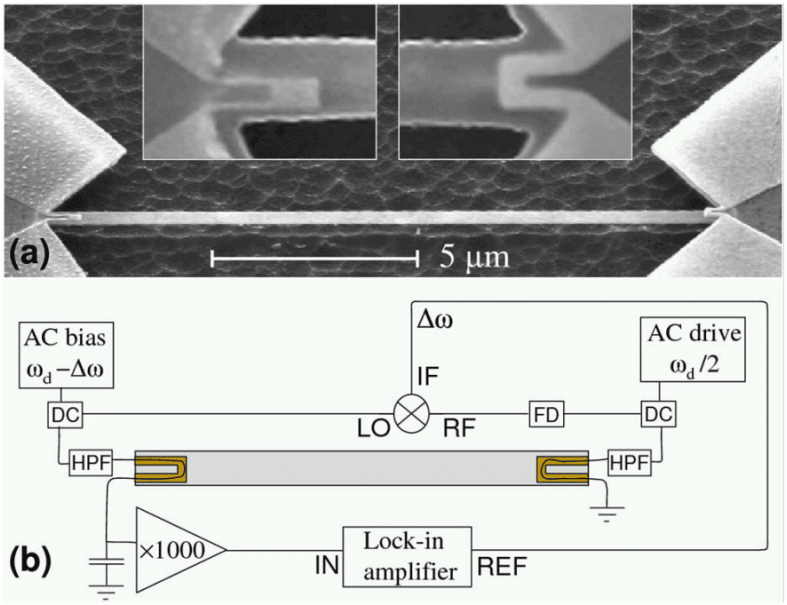


Figure 1.7: (a) Scanning electron micrograph of one of the devices used in the experiments. The insets show top-view close-up images of the detection (left) and drive (right) metal loops. (b) Schematic of the experimental setup: DC denotes directional coupler, FD: frequency doubler; HPF: high-pass filter. Reproduced from [54], © 2007 AIP Publishing, with permission.

Bargatin *et al.* introduced an electrothermal actuation method to drive the vibration of high-frequency NEMS resonators [54]. As shown in Figure 1.7 (a), the right electrode, which consists of gold, is the actuator. The actuation is achieved through the thermoelastic behaviour of the bilayer structure (the gold electrode and the silicon carbide beam). It relies on the difference between the thermal expansions of the two materials. When an AC voltage is sent to the gold electrode, local joule heating of the gold actuation loop causes stress between it and the carbide beam, which flexes the beam vertically. If the AC frequency is adjusted so that the thermal fluctuations match the resonant frequency of the beam, the amplitude of deflection would be greatly enhanced due to the high quality factor of the nanomechanical resonator beam. To drive the vibration of the beam at ω_d, the setup as shown in Figure 1.7 (b) is used. A sinusoidal AC voltage at $\omega_d/2$ is sent to the actuation electrode, causing a current $I(t)$, where:

$$I(t) = I_0 \cos(\frac{\omega_d}{2}t) \tag{1.2}$$

Note that the vibration frequency (ω_d) would be two times the AC frequency ($\omega_d/2$) since the Joule heating power would be:

$$\begin{aligned} P(t) &= I^2(t)R \\ &= I_0^2 \cos^2(\frac{\omega_d}{2}t)R \\ &= \frac{I_0^2 R}{2}[1 + \cos(\omega_d t)] \end{aligned} \tag{1.3}$$

The resulting temperature modulation contains a DC term and a component at ω_d, which drives the bilayer thermoelastically [54]. The readout electrode, the electrode on the left in Figure 1.7 (a), is made of a gold-palladium alloy, and its shape changes periodically when the beam resonates, inducing a periodic change in resistance [55]. By applying a DC voltage across the electrode, the resistance change can be measured and analysed to obtain the frequency response of the beam, and this is the piezoresistive detection method.

In summary, while lumped LC networks remain power-robust, parasitics, size, and Q constraints above a few GHz limit their suitability for dense, multi-band front ends [1, 26]. SAW and BAW technologies deliver excellent selectivity and are the industrial mainstay in handsets, yet their centre frequencies are fundamentally tied to acoustic velocity and feature pitch, complicating co-design across many closely spaced channels; packaging demands and heterogeneous integration with CMOS further constrain scalability [5, 6]. These limitations motivate the approach proposed in this thesis: a lithographically defined array of nanomechanical resonators that realises a compact, CMOS-compatible, multi-channel RF filter bank with precisely set passbands through geometry, enabling wafer-level reproducibility and tight channel spacing. Thermoelastic actuation provides strong on-chip drive without piezoelectric films, and piezoresistive readout affords compact electrical readout and straightforward multiplexing, allowing a mixed-frequency input to be decomposed into parallel, frequency-selective output channels [54, 55]. Critically, this architecture is CMOS-compatible and inherently scalable in channel count and footprint, though attention must be paid to thermal cross-talk, self-heating-induced drift, and readout noise floors.

1.4 Photonic Integrated Circuits

Light has emerged as a powerful medium for carrying information, offering advantages such as wide bandwidth, low propagation loss, and resistance to electromagnetic interference. In communication and sensing systems, optical carriers are frequently modulated by RF signals, enabling the transmission and processing of RF information in the optical domain. To further exploit these advantages within a compact and scalable platform, photonic integrated circuits (PICs) have become increasingly important. By integrating optical components such as waveguides, resonators, and modulators on a single chip, PICs combine the high-speed, low-loss nature of light with the miniaturisation, stability, and complexity of semiconductor fabrication, providing an enabling platform for RF-photonic filtering and processing.

PICs have evolved from discrete optical components in the 1980s to today's sophisticated platforms capable of integrating thousands of optical elements on a single chip [17]. PICs use the manipulation of light to perform the generation, modulation, memory, routing, and detection of optical signals within a single microchip. By using photons rather than electrons, PICs offer high bandwidth, low latency, low power consumption, support for in-memory computing, and dense functional integration [16].

As shown in Figure 1.8, Hua *et al.* report the implementation of a large-scale silicon photonic accelerator, integrating over 16,000 photonic components to perform matrix multiply-accumulate (MAC) operations with ultra-low latency and high throughput [56]. Utilising a hybrid 2.5D packaging approach to co-integrate electronic and photonic chips, the system achieves sub-5 ns MAC latency and over 8 tera operations per second (TOPS) computing performance, demonstrating superior efficiency in solving combinatorial optimisation problems like Ising models [56]. Compared to a commercial graphics processing unit (GPU), the accelerator system shows order-of-magnitude speed-ups in computation time under the reported workload, establishing a major milestone in scalable photonic computing [56].

Xu *et al.* introduced Taichi, a large-scale photonic chiplet platform designed to address the energy and scalability limitations of PIC, as shown in Figure 1.9

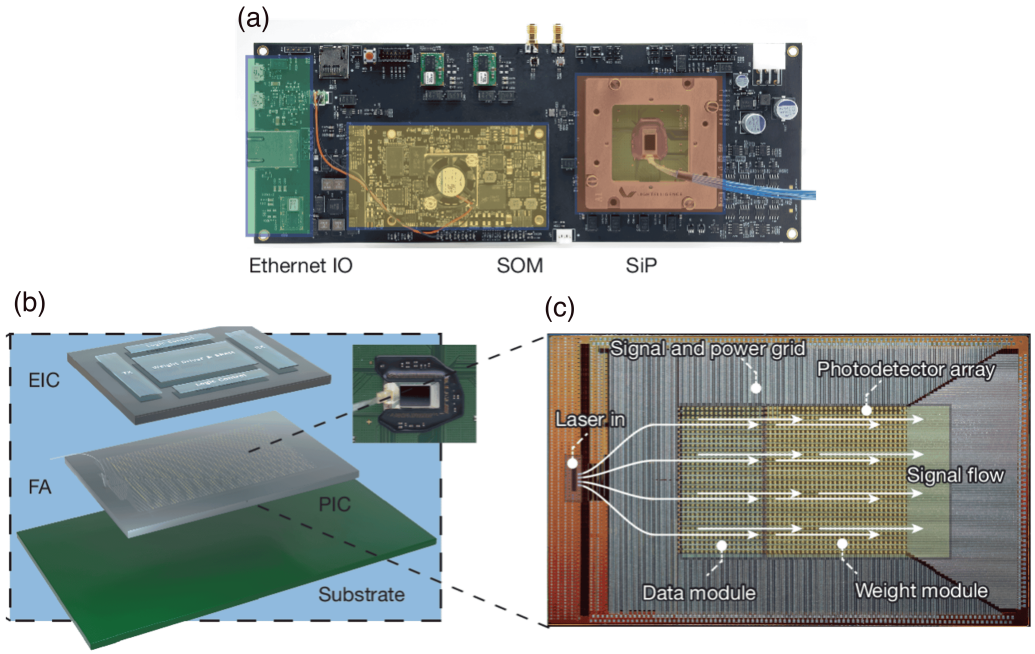


Figure 1.8: (a) The whole integrated system board. SOM: system on module, connecting the SiP and the host computer through Ethernet IO. SiP: system in package. (b) Diagram of the advanced packaged SiP with 2.5D flip-chip bonding. Inset, packaged SiP with fibre attach and wire bonds to the substrate. EIC: electronic integrated circuit. FA: fibre array. (c) PIC chips with signal flow diagram. Adapted from [56], under the CC BY-NC-ND 4.0 licence.

[57]. By employing a distributed computing architecture that combines diffractive and interferometric photonic elements, Taichi achieves a neuron capacity on the order of millions with an energy efficiency of approximately 160 TOPS/W. The system demonstrated experimentally robust performance in demanding tasks such as 1000-category image classification (91.89% accuracy on the Omniglot dataset) and versatile artificial intelligence-generated content, including both music and image synthesis. Crucially, the distributed design mitigates noise accumulation across layers, enabling wide but shallow optical networks that maintain robustness while scaling to real-world AI workloads. This achievement establishes a new benchmark in photonic artificial intelligence hardware and reports energy-efficiency advantages relative to electronic baselines under the tested tasks.

Recent advances in PICs, ranging from high-speed optical interconnects to large-scale photonic accelerators, demonstrate the remarkable potential of light-based

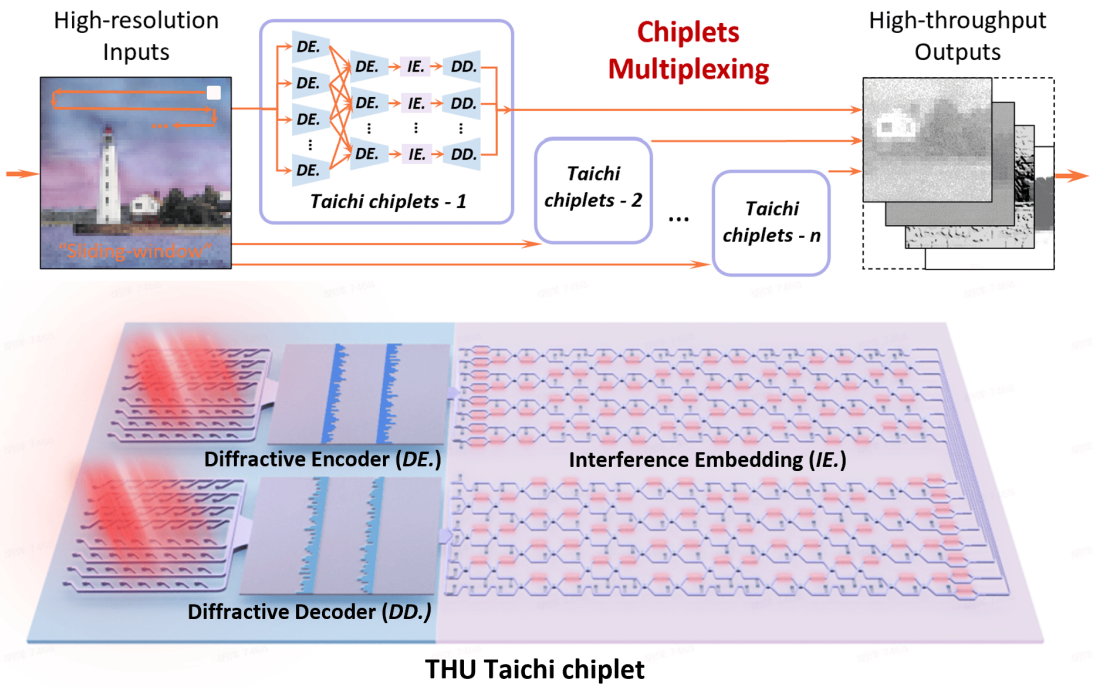


Figure 1.9: Schematic illustration of the Taichi photonic chiplet system [57]. (Top) High-resolution input data are processed in parallel by multiple Taichi chiplets (1, 2, 3,) through chiplet multiplexing, enabling sliding-window input perception and yielding high-throughput outputs. (Bottom) Optical micrograph of a single Taichi chiplet, where incident light enters the diffractive encoder (DE), propagates through the interference embedding (IE) region, and exits via the diffractive decoder (DD). Reproduced from [57, 58], © 2024 AAAS, with permission.

computation. Devices such as Hua's silicon photonic accelerator and Xu's Taichi chiplet system illustrate how integration strategies and architectural innovations are converging towards scalable, low-power, and high-performance photonic computing. These developments not only reinforce the role of PICs in next-generation information processing but also highlight their promise as an enabling technology for artificial intelligence and beyond.

1.4.1 Evanescent Field Coupling and Optomechanics

The evanescent field coupling is a fundamental mechanism for energy transfer between photonic components without direct physical contact [59]. This near-field interaction occurs when optical modes from different waveguides or resonators overlap through their exponentially decaying evanescent tails. The coupling strength

depends critically on the gap between components, with typical separations ranging from tens to hundreds of nanometres [60].

Phase-change materials (PCMs) such as $Ge_2Sb_2Te_5$ (GST) are introduced into the evanescent field of integrated photonic waveguides, which enable compact, non-volatile in-memory photonic computing [16, 61, 62]. When a PCM patch overlaps the evanescent tail of the guided mode, rapid optical or electrical pulses can switch the PCM between amorphous and crystalline phases, producing a large and persistent refractive index change that encodes multilevel weights on the chip [61, 63, 64]. Such non-volatile in-memory photonic architectures deliver neural network inference at nanosecond-scale speeds without external electronic memory, transforming passive PICs into energy-efficient high-throughput computing platforms [62, 63].

Apart from placing PCM near evanescent field for in-memory computing, nanomechanical resonators can also be placed within the evanescent field for ultra-sensitive displacement and force sensing [65]. When a nanomechanical resonator is positioned within the evanescent field of a high-Q optical cavity, its motion perturbs the local refractive index or scattering environment, modulating the cavity's resonance frequency or optical transmission [18, 66]. The strength of this optomechanical coupling depends critically on the spatial overlap between the mechanical resonator and the exponentially decaying evanescent tail [67].

Anetsberger *et al.* demonstrate near-field cavity optomechanics by dispersively coupling high-quality nanomechanical oscillators to an ultra-high-finesse optical microtoroid resonator using its evanescent field as shown in Figure 1.10 [67]. The authors achieve sub-femtometre Hz^{-1} displacement sensitivity, with measurement imprecision reaching the standard quantum limit (SQL) at room temperature, which makes it a milestone in nanomechanical motion detection. Furthermore, the study observes dynamical backaction mediated by radiation pressure, resulting in coherent oscillations of the nanomechanical oscillator. The flexible near-field coupling platform is compatible with a variety of nanomechanical devices and paves the way for quantum-limited measurements, ponderomotive squeezing, and quantum non-demolition experiments in cavity optomechanics.

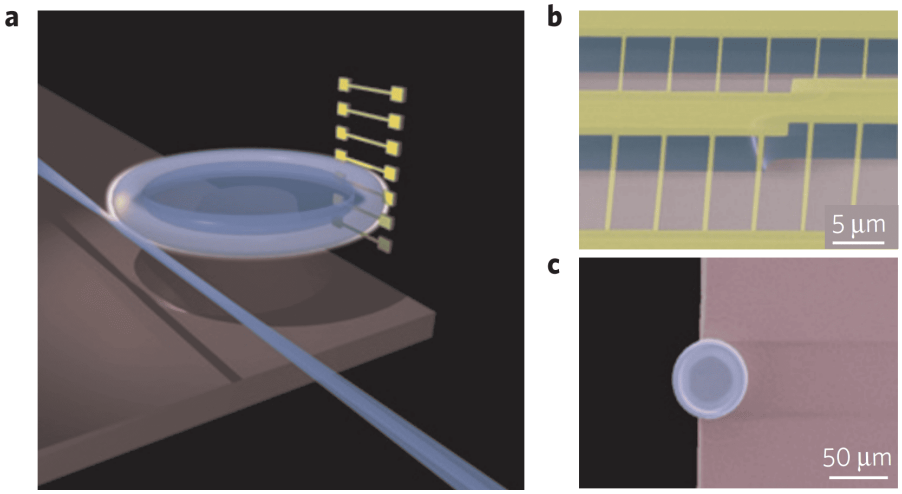


Figure 1.10: High-quality nanomechanical oscillators coupled to an ultra-high-finess optical microtoroid resonator. (a) Schematic of the experiment, showing a tapered-fibre-interfaced optical resonator dispersively coupled to an array of nanomechanical oscillators. (b) Scanning electron micrograph (false colour) of an array of doubly clamped Si_3N_4 nanostring oscillators. (c) Scanning electron micrograph (false colour) of a toroid silica microcavity acting as an optomechanical near-field sensor. Reproduced from [67], with permission from Springer Nature.

Liu *et al.* present an integrated nano-optomechanical displacement sensor, as shown in Figure 1.11, featuring an ultra-wide optical bandwidth (approximately 80 nm) and high sensitivity (45 fm/$\sqrt{\text{Hz}}$), realised on an InP membrane-on-silicon platform [18]. The sensor utilises a nanomechanical three-dimensional directional coupler, where the vertical displacement of suspended waveguides modulates the evanescent field coupling between them, enabling sensitive optical readout via integrated dual-channel waveguide photodiodes. By combining a large dynamic range (>30 nm), cavity-free broadband operation, and on-chip actuation and detection, this work advances the development of fully integrated nanomechanical sensors suitable for precision metrology and scanning probe applications.

1.4.2 RF in Photonics

RF photonics, also known as microwave photonics (MWP), is an interdisciplinary field that combines RF networks and engineering with photonics to harness the unique advantages of optical systems for RF signal processing [11, 68]. The complete RF photonic system can be described as in Figure 1.12. Broadband RF signals

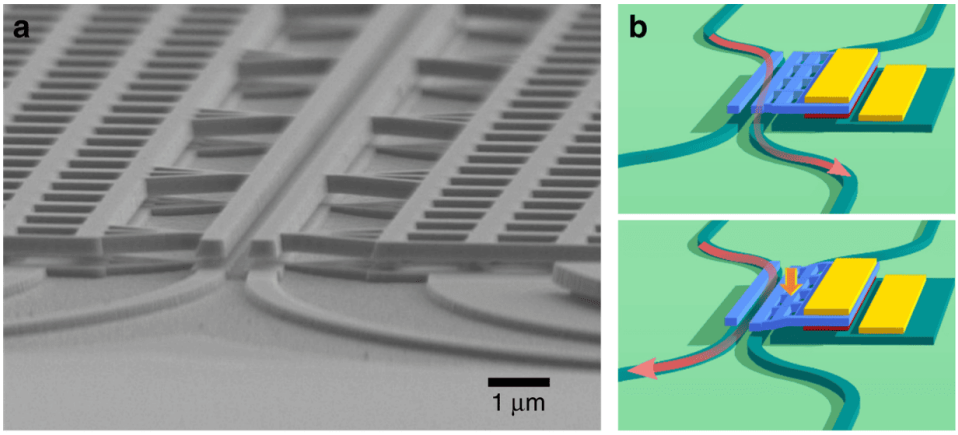


Figure 1.11: (a) SEM image of the nanomechanical directional coupler used as a transducer. (b) Schematic illustration of the displacement sensor, showing light passing through the directional coupler before (up) and after (down) actuation. Reproduced from [18], under the CC BY 4.0 licence.

are received by an RF antenna and the signal of interest at certain frequencies is extracted with an electronic RF filter as the electrical input to the system. Optical input is generated by a continuous-wave (CW) laser and sent to the encoder. The encoder, which is often an electro-optic modulator (EOM), is responsible for encoding the CW light with filtered RF signals and outputting the encoded light. The encoded light is then sent to the RF photonic processor for signal processing in the optical domain, and the output of the processor is received by the PD. The PD then turns the optical signal into the electrical RF output.

RF photonics involves the up-conversion of time-varying electronic signals into the optical domain for high-speed signal processing. This approach enables the manipulation of RF signals using photonic components such as lasers, optical modulators, PDs, and optical fibres [69].

RF photonic systems offer numerous advantages over traditional electronic approaches. The most significant advantage of RF photonics is the massive bandwidth capability. Photonic systems can process RF signals with bandwidths exceeding 100 GHz, with demonstrations reaching the low-THz frequency range [70]. This vast bandwidth comes from the inherent broadband nature of photonics, where optical carriers operate at frequencies several orders of magnitude higher than typical RF signals [71].

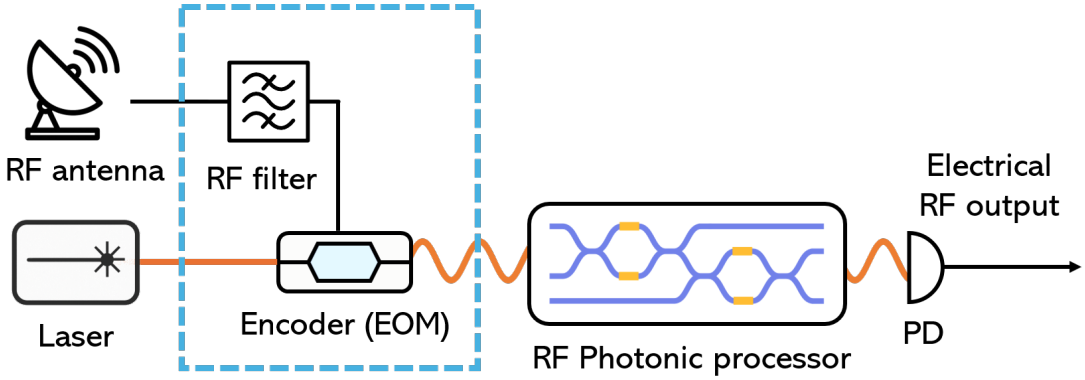


Figure 1.12: Schematics showing components of a typical RF photonic system with the RF filter and encoder highlighted.

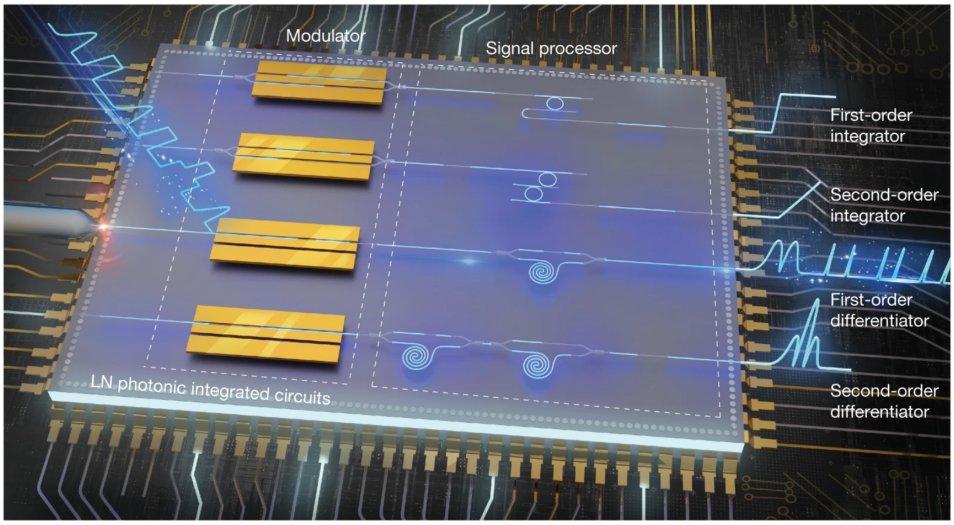


Figure 1.13: Schematic diagram of LN-based MWP processing engine by Feng *et al.*, consisting of a high-speed electro-optic modulation block and a low-loss, multipurpose photonic processing section. Reproduced from [72], with permission from Springer Nature.

Feng *et al.* present an integrated lithium niobate (LN) MWP processing engine on a wafer-scale thin-film LN platform, combining high-speed modulators (up to 67 GHz) with ultra-high-Q ($> 6 \times 10^6$) micro-ring resonators (MRRs) to implement programmable Mach-Zehnder interferometer (MZI) networks for the temporal integration and differentiation of first and second order, as shown in Figure 1.13 [72]. The engine processes arbitrary RF waveforms at up to 256 GSa s^{-1} with impulse responses under 2 ps and ripple below 0.1 dB, enabling the solution of ordinary sub-nanosecond differential equations, the generation of ultra-wideband pulses and the extraction of 244 ns image edges in 250×250 pixel images. Integrated

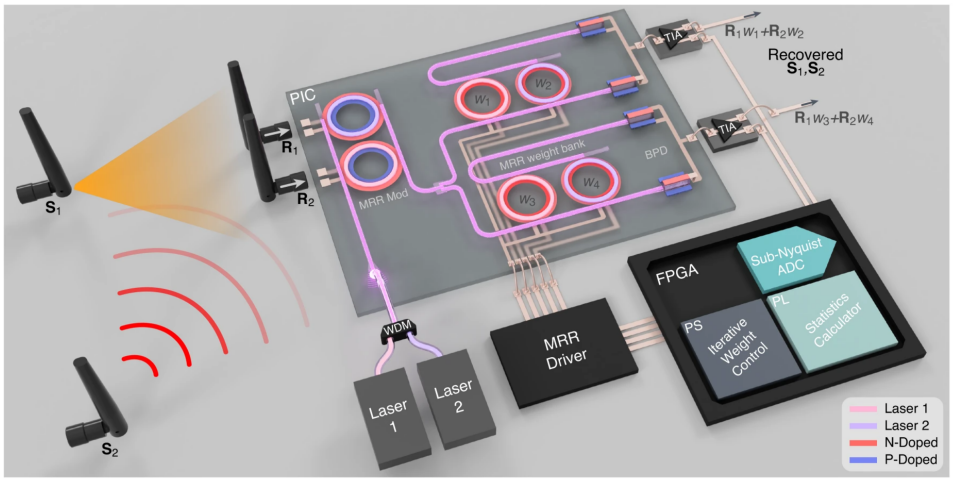


Figure 1.14: Schematic of the photonic processor by Zhang *et al.* Mod: modulator. BPD: balanced photodetector. TIA: transimpedance amplifier. Signal pathway starts at MRR Mod and ends at BPD, composing an on-chip waveguide with a length of 1.6 mm, which has an index of refraction near 2.44. The latency is, accordingly, the light propagation time, which is about 15 ps. Reproduced from [73], under the CC BY 4.0 licence.

into a photonic-assisted deep learning model, it achieves more than 97% precision in melanoma lesion segmentation, demonstrating a scalable, low power MWP computing architecture in sub-nanoseconds.

Zhang *et al.* present a compact silicon photonic system-on-chip for real-time RF interference cancellation, as shown in Figure 1.14 [73]. The photonic system exploits a fully integrated optical pathway comprising PN-type MRR modulators (>5.4 GHz bandwidth), thermally tuned MRR weight banks and balanced PDs to achieve sub-15 ps analogue processing latency, over three orders of magnitude faster than digital methods. By upconverting RF to optical frequencies, the chip delivers multi GHz bandwidth without ADC / DAC (analogue-to-digital converter/digital-to-analogue converter) delays or beam width limitations, offers inherent electromagnetic interference (EMI) immunity, and achieves 9-bit weighting precision with just 4.5 mW per weight (versus 172 mW electrically). A copackaged field-programmable gate array (FPGA) updates the weights at 305 Hz, enabling adaptive, ultra-low-power RF photonic processing for next generation mobile and radar systems that electronic approaches may not match under comparable latency constraints [74].

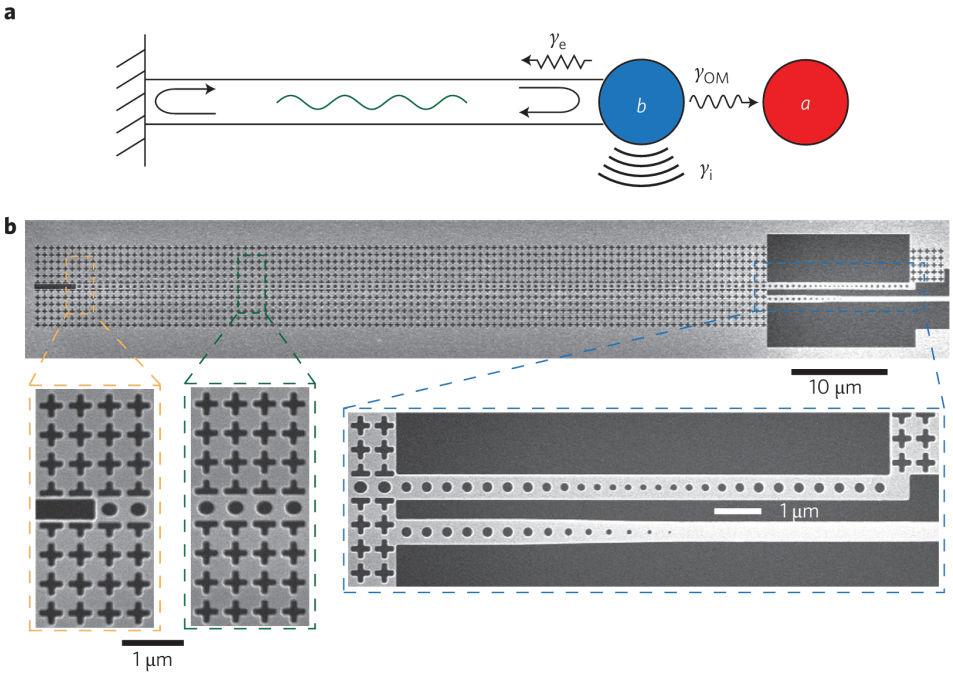


Figure 1.15: (a) Schematics diagram of the cavity-waveguide device (a and b represent the optical and mechanical cavity modes). The mechanical cavity mode couples to the phonon waveguide at rate γ_e and has an intrinsic decay rate γ_i and an optically induced decay rate γ_{OM}. (b) SEM image of a SOI optomechanical cavity-waveguide device. The zoomed-in views show the nanobeam cavity and optical coupler, the phonon waveguide section and the waveguide termination, respectively. Reproduced from [19], with permission from Springer Nature.

1.4.3 Optomechanics for RF Photonics Applications

M/NEMS resonators combine a compact form factor, low power consumption, and co-integration potential, making them suitable for RF front ends in MWP systems; in particular, they are compatible with established photonic platforms, support dense on-chip integration, and allow flexible frequency-response design via dimensional scaling and multi-resonator architectures for multi-channel filtering. [75, 76]. Unlike bulky off-chip RF filters that dominate current MWP front-ends such as SAW and BAW filters, nanomechanical filters can be monolithically integrated alongside optical modulators, waveguides, and PDs, enabling truly compact and power-efficient MWP systems. While fully monolithic PIC implementations of nanomechanical RF filters are still limited, the number of studies exploring optomechanics with PICs for RF applications is growing.

Fang *et al.* demonstrate a monolithic silicon-on-insulator (SOI) cavity-optomechanical circuit that co-localises 1550 nm optical modes and ∼6 GHz mechanical breathing modes in optomechanical crystal cavities linked by engineered phononic waveguides as shown in Figure 1.15 [19]. With vacuum photon-phonon coupling rates of about 1 MHz and optical Q $> 10^5$, the device imprints RF sidebands into light to launch phonons that travel to a second cavity and reconvert into optical signals, realising tunable microwave delay lines and narrowband RF filters (17 kHz linewidth, >70 dB rejection) on chip. By slowing the phonon group velocity to 150 m/s, delays of up to 13.3 µs fit within micron-scale footprints. The platform also supports both real-phonon routing and virtual-phonon coupling for coherent Rabi oscillations, in which energy periodically exchanges between two coupled states, achieving over 89% signal-conversion efficiency and parametric gain with sub-mW pump power, thereby establishing reconfigurable and low-loss RF photonic front ends.

Chen *et al.* report an unsuspended silicon-on-sapphire (SOS) optomechanical ring resonator (OMR) that realises intermodal RF-to-optical transduction via triply resonant Brillouin interactions between two co-propagating optical modes (TE_0, TE_1) and a guided Love-mode phonon near 2.2 GHz, with piezoelectric ZnO IDTs launching the acoustic wave on chip, as shown in Figure 1.16 [20]. The device attains intrinsic photonic quality factors up to 1.0×10^5 for TE_0 and phononic $Q \approx 3 \times 10^3$ at 4 K, a pump-enhanced coupling rate $G_b = 3.6\,\mathrm{GHz\,mW^{-1/2}}$, intermodal optical conversion from TE_0 to TE_1 of $\sim$ 1.2% at a 3.6 mW RF drive, and a measured RF-to-optical transduction efficiency of 1.5×10^{-5} with a 10 mW optical pump. The architecture supports wavelength-division multiplexing by exploiting multiple MRR resonances, and the unsuspended SOS platform improves heat dissipation and compatibility with cryogenic and superconducting environments, which is advantageous for compact, narrowband, and mode-selective RF photonic filtering and frequency translation. Notwithstanding these benefits, the single-phonon coupling $g_0 \approx 350$ Hz and the overall conversion are lower than those of state-of-the-art optomechanical crystals, indicating scope for the optimisation of phase matching, loss, and coupling geometry [20].

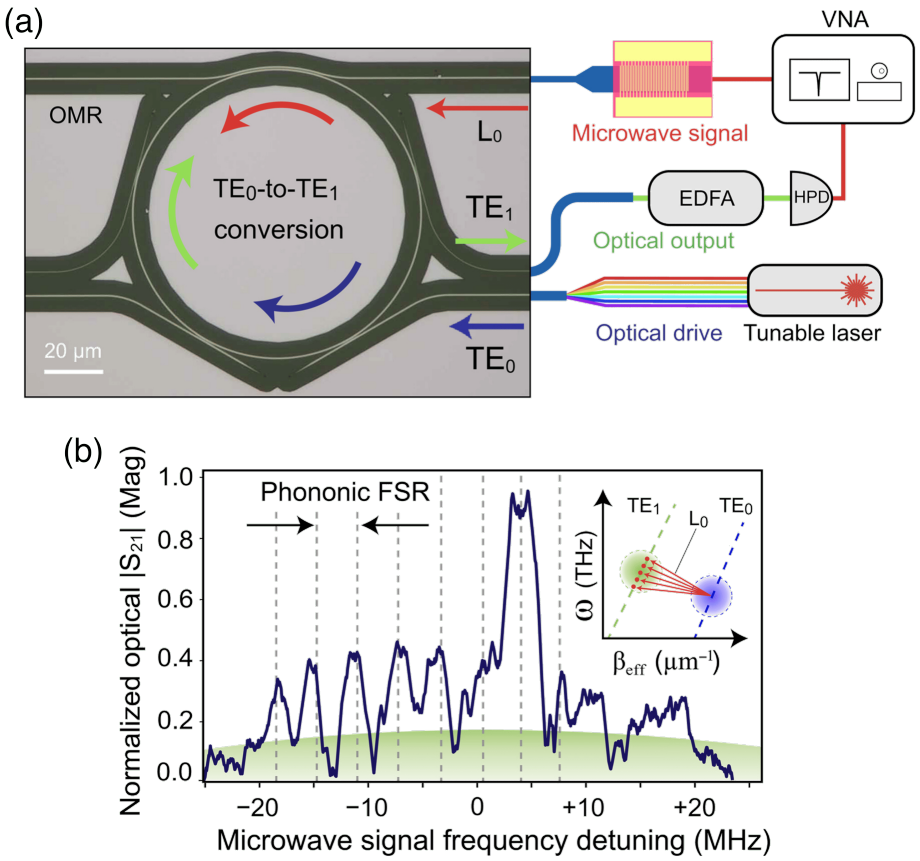


Figure 1.16: Multiresonance RF-to-optical conversion. (a) Schematic diagram of the setup to characterize the TE_0-to-TE_1 intermodal conversion through the optical S_{21} measurement. EDFA: erbium-doped fibre amplifier; VNA: vector network analyser. (b) The optical S_{21} spectrum of TE_0-to-TE_1 conversion at 4 K around the central RF frequency of 2.22 GHz. The green translucent background indicates the TE_1 mode resonance. The inset illustrates that multiple phononic resonances can phase- match the TE_0- to- TE_1 conversion within the bandwidth of one photonic resonance. The red circles indicate the phononic resonances. The blue (green) translucent area indicates the TE_0 (TE_1) spread on the dispersion diagram. Reproduced from [20], under the CC BY-NC 4.0 licence.

Despite the promise of RF photonics, realising compact multi-channel RF filters directly on a photonic integrated circuit remains a major challenge. Conventional electronic solutions, such as SAW and BAW filters, provide excellent RF performance but are inherently difficult to integrate with photonic components due to their size, material incompatibility, and packaging complexity. Photonic approaches to multi-channel filtering typically rely on cascaded or coupled resonators, which accumulate insertion loss and increase design complexity, thereby limiting scalability. Furthermore, on-chip architectures that can simultaneously implement RF filtering

and multi-wavelength optical encoding are rare, with most demonstrations relying on bulk or hybrid systems that compromise footprint and efficiency.

Even though extensive research has been devoted to using RF-encoded light for efficient signal processing, comparatively little attention has been paid to the interface between the RF antenna and the RF-encoded optical domain. This interface is of critical importance, as EM waves in the RF range are predominantly transmitted through free-space wireless channels. To achieve full integration between RF signals and photonic processors, the received RF signals must first be captured by an antenna, then filtered to extract useful information before being encoded into light. Preferably, this encoding process should support wavelength-division multiplexing, where each optical wavelength corresponds to a distinct RF channel, thereby enabling parallel and efficient signal handling within photonic systems.

To address these limitations, this thesis proposes a scalable, integrated *opto-electronic multi-channel RF filter bank with a multi-wavelength optical encoder*. The device combines arrays of MRRs with nanomechanical resonators and couples mechanical and optical resonances to realise multiple narrowband RF filtering while mapping each passband to a distinct optical wavelength channel. Owing to its compact architecture and efficient evanescent coupling, the proposed filter bank can scale to many channels with minimal insertion loss, providing a practical route towards dense and reconfigurable MWP systems.

2 Methodology

Contents

2.1 Introduction 27
2.2 Nanofabrication Techniques 28
2.2.1 Electron-Beam Lithography 28
2.2.2 Reactive-Ion Etching 28
2.2.3 Physical Vapour Evaporation of Metals 29
2.2.4 Sputtering Deposition 30
2.3 Nanowire Pick-and-Place Technique 37
2.4 Integrated Photonics Measurements in Vacuum 41
2.5 Lock-In Detection 42
2.5.1 Thermal Noise Sweep Mode 46
2.5.2 Frequency Response Sweep Mode 46
2.5.3 Plotter Mode 46
2.6 Simulation Methods 47
2.6.1 Lumerical 47
2.6.2 COMSOL Multiphysics 48

2.1 Introduction

This chapter outlines the experimental and numerical methods used in this work. Device fabrication relied on standard nanofabrication techniques. Device performance was characterised primarily using electrical measurements, integrated photonics measurements and lock-in detection. Numerical simulations were employed both

to guide design and to validate measured device behaviour.

2.2 Nanofabrication Techniques

2.2.1 Electron-Beam Lithography

Electron-beam lithography (EBL) is a high-resolution patterning method for defining nanometre-scale features on a resist-coated substrate. All lithographic patterns in this work were written using a JEOL 5500FS (50 kV) system.

In EBL, a focused electron beam is scanned across an electron-sensitive resist. Electromagnetic lenses and discrete apertures shape and focus the beam; the beam current (electron flux) is determined by the choice of aperture. Higher current increases throughput at the expense of resolution due to a larger effective spot size. With the smallest aperture (AP1) and a 100 pA beam current, feature sizes down to ∼20 nm are achievable. In this work, sub-micron features (e.g., grating couplers, waveguides, fine electrodes) were written with AP1, whereas larger features (markers, nanowire supports, bond pads) used AP3 at 3 nA.

Resist tone determines the pattern polarity. Negative-tone resists (e.g., maN-2403) crosslink upon exposure and remain after development; positive-tone resists (e.g., CSAR 62, PMMA) become more soluble and are removed in the developed areas. Both tones were used to define photonic structures for subsequent etching, while positive resists were used to open windows for buffered oxide etching (BOE), phase-change materials (PCMs) and metal deposition.

2.2.2 Reactive-Ion Etching

Reactive ion etching (RIE) is a dry etching technique that utilises chemically reactive plasma to remove materials from a substrate with high anisotropy and selectivity [77]. In a typical RIE process, the substrate is placed in a low-pressure chamber where an RF electric field sustains a plasma composed of ions and reactive neutral species. The reactive species chemically etch the surface material, while the energetic ions bombard the substrate vertically, improving the directionality of the etching process and allowing high-resolution pattern transfer [77].

RIE is particularly useful for silicon, silicon nitride, and silicon oxide etching due to its capability to deliver precise control over etch depth, sidewall profile, and material selectivity. Silicon nitride (Si_3N_4), a chemically inert and robust dielectric, typically requires fluorocarbon-based plasmas (such as CF_4, CHF_3, or SF_6) and elevated ion energies to achieve high etch rates [78]. Silicon oxide etching, on the other hand, benefits from fluorine-rich plasma environments (e.g., CF_4/O_2 mixtures), which promote selective and isotropic or anisotropic etching depending on the application [79]. For crystalline silicon, chlorine- or fluorine-based plasmas (e.g., SF_6, Cl_2) are commonly employed, offering high etch rates with good anisotropy when combined with physical ion bombardment [80]. The versatility of RIE in etching these materials with nanometre precision, coupled with its compatibility with CMOS fabrication flows, makes it a critical technique in the development of MEMS/NEMS structures and silicon/silicon nitride PICs [81].

All RIE processes were performed on an Oxford Instruments PlasmaPro 80.

2.2.3 Physical Vapour Evaporation of Metals

Physical vapour deposition by thermal and electron-beam evaporation was used to form metallic layers for electrical contacts, heaters, and clamps. Gold was selected for contacts owing to its high conductivity and chemical inertness [82]. Because Au adheres poorly to oxides and nitrides, a thin adhesion layer (typically 1-10 nm of Cr or Ti) is required [83]. A 5 nm Cr adhesion layer was used throughout this work.

Thermal Evaporation

Thermal evaporation forms thin films by resistively heating a source in high vacuum until its vapour pressure is sufficient for line-of-sight condensation on the substrate.

The chamber is pumped to $\sim 1 \times 10^{-6}$ Torr (with liquid-nitrogen cryo-trapping) to minimise scattering and contamination, and thickness is monitored in real time using a quartz crystal microbalance (QCM). For chromium, a Cr-coated tungsten filament is used rather than Cr pellets in a boat because Cr has a high melting point (∼1,907°C) and low vapour pressure; it often sublimes at ∼1,400°C, and the

localised heating of a filament couples heat more efficiently than a boat with a limited contact area [83, 84]. After depositing a 5 nm Cr adhesion layer, gold is evaporated from a refractory-metal boat (typically tungsten). The boat is resistively heated while the QCM controls the rate until Au reaches a sufficient vapour pressure for uniform deposition onto the substrate [83, 84].

Electron-Beam Evaporation

Electron-beam (e-beam) evaporation was employed for the deposition of chromium and gold. Compared with the manual thermal evaporator, the Plassys MEB600S system used in this work is automated and equipped with a load-lock, allowing sample exchange without breaking the main chamber vacuum. This reduces pump-down times and shortens the overall deposition process to about 1 hour, compared with over 3 hours for thermal evaporation.

In operation, crucibles are filled with appropriate source materials. For high-melting-point metals such as Cr, ingots or high-density pressed pellets shaped to the crucible are used to ensure stable heating and avoid scattering during initial beam exposure [83]. For noble metals like Au or Ag, pellets or tablets of high purity are sufficient [83]. During deposition, a focused high-energy electron beam, generated by thermionic emission from a tungsten filament and accelerated at $\sim$9.7 kV, is directed onto the source. Localised heating causes the material to melt or sublimate, and controlled beam current enables precise regulation of the deposition rate as monitored by a QCM.

2.2.4 Sputtering Deposition

All sputtering processes were performed in the AJA International Orion Sputtering System as shown in Figure 2.1 with 5 2-inch magnetron sources compatible with RF and DC sputtering. The sputtering system has a load-lock chamber and a main sputtering chamber, so that the high-vacuum environment (around 3×10^{-8} Torr) of the main chamber is not compromised every time the substrate is loaded for deposition. It also speeds up the deposition process, as pumping down the

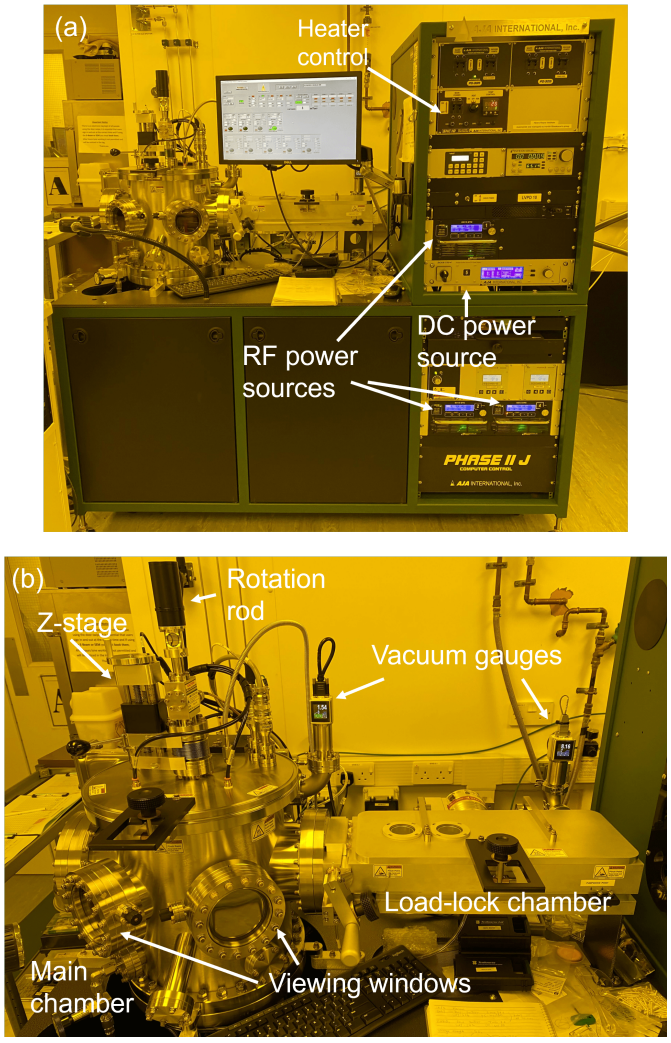


Figure 2.1: AJA International Orion Sputtering System. (a) Overall appearance, showing the vacuum chambers and the control hardware. (b) The load-lock and main chambers with key components.

load-lock chamber to an intermediate vacuum (around 1×10^{-5} Torr) is very fast (in 20 minutes) compared to pumping down the main chamber to high vacuum (which takes more than 8 hours).

Before the sputter deposition, the sample needs to be transferred to the main deposition chamber, and the Z-stage needs to be adjusted to the 33 mm mark, which is the height for the uniform film thickness calibrated by the manufacturer of the sputtering tool (AJA International). The automatic rotation of the sample plate also needs to be turned on for uniform film thickness. Then the sputtering can begin.

Plasma Ignition

At the beginning of the sputter deposition, the Ar gas valve is opened with a set flow (usually 30 sccm), and the pressure of the chamber is controlled by regulating the throttle valve between the chamber and the main turbo pump. The pressure is usually set to 30 mTorr for a plasma to ignite at the beginning, which is a critical step, as it creates the ionised gas (typically Ar^+) necessary to initiate sputtering of the target material. Empirically, ignition is generally more difficult in RF than in DC sputtering because plasmas are sustained differently and charge accumulates differently on the electrodes.

In DC sputtering, a continuous negative voltage is applied to the target (cathode), which accelerates free electrons into the chamber. These electrons ionise neutral argon atoms through collisions, generating Ar^+ ions and sustaining the plasma. The constant potential provides a steady energy input to maintain ionisation, and because the target is typically conductive, the charge is easily dissipated, facilitating stable plasma formation at relatively low voltages and pressures [85, 86].

In RF sputtering, an AC voltage (usually at 13.56 MHz) is applied, causing the electric field to oscillate rapidly. This oscillation makes it more challenging for electrons to gain sufficient energy to sustain ionisation, especially during the initial breakdown phase [85]. Moreover, when sputtering insulating materials (e.g., Si_3N_4 or SiO_2), charge can build up on the target surface due to its inability to conduct away the accumulated electrons. This charging effect distorts the local electric field, further hindering the initial ionisation required to ignite the plasma [87].

Additionally, the RF sheath dynamics are more complex: electrons are much more mobile than ions and respond rapidly to the oscillating field, while ions are too massive to follow the RF frequency. This causes an asymmetry that must stabilise before a self-sustaining discharge is established, which makes the breakdown threshold for plasma formation higher than in DC sputtering [86].

Hence, to successfully ignite the plasma for RF sputtering, three methods can be employed to lower the breakdown threshold and ensure a reliable plasma ignition process in RF sputtering configurations [85]:

- Temporarily increase the chamber pressure, which increases the argon gas density, thereby increasing the probability of electron-neutral collisions and promoting ionisation.
- Briefly open the shutter of the target, allowing a larger contact area between the argon atoms and the target surface to enhance local ionisation near the cathode.
- In a multi-target system, using a neighbouring target to first ignite and stabilise a plasma can aid in igniting another RF plasma through spatial plasma spreading or cross-talk within the chamber.

Once the plasma is successfully ignited and remained stable, the chamber pressure can be lowered to the pressure for sputter deposition (e.g., 3 or 5 mTorr).

Sputtering Targets

During sputtering, the target can be heated to a very high temperature primarily as a result of energetic ion bombardment and associated plasma processes [88]. During sputter deposition, positively charged gas ions (Ar^+) are accelerated across the sheath and strike the target with energies ranging from hundreds to a few thousand electron volts. Each ion impact transfers its kinetic energy to the lattice via inelastic collisions, raising the local temperature [85]. Every ion impact also liberates secondary electrons. When those electrons are recaptured at the negatively biased target or nearby surfaces, they deposit additional energy as heat. Furthermore, for RF sputtering, RF magnetrons couple through a matching network and blocking capacitance, and some RF current flows through the target mount, causing resistive heating (I^2R) in the backing plate, which then conducts heat into the target [85].

For these reasons, the temperature of the sputtering target can reach as high as 700 °C if there is no adequate cooling system, which is above the melting temperatures of some sputtered materials [89]. There is a water cooling system in the sputtering system used in this work; hence, most targets remain at temperatures below their melting temperatures. It is also worth noting that the sputtering target

would be brought to this temperature in a very short period. If a high power is used for plasma ignition, the surface of the target can be heated to a very high temperature the moment the plasma is ignited, while the bulk and backing plate remain cold, creating steep temperature gradients. Materials with inherently poor thermal conductivity, such as some PCMs (e.g., $Ge_2Sb_2Te_5$, Sb_2Se_3), ceramics (e.g., Si_3N_4, SiC), or certain oxide-based compounds (e.g., SiO_2, $ZnS{\cdot}SiO_2$), cannot effectively dissipate the intense heat through their bulk in such a short time [90].

In these cases, the target must be metallurgically bonded to a high-conductivity backing plate (commonly copper or molybdenum) using solders such as indium or reactive multilayer foils to efficiently conduct the excessive heat away [91]. Otherwise, localised hotspots develop under high-power operation, causing cracking or flaking failures. Indium bonds tolerate the coefficient of thermal expansion (CTE) mismatch and provide both mechanical compliance and thermal conductance up to ∼156.6 °C (melting temperature of indium) [91]. The bonding can efficiently conduct heat away from the target to the backing plate, which is more thermally conductive. The heat would eventually be removed by the active water cooling system, but the surface of the permanent magnet array beneath the target is not flat, which causes resistance to thermal contact, blocking thermal conduction. Therefore, a copper mesh is placed between the target and the magnet to reduce thermal contact resistance, enhancing both thermal and electrical conduction. All non-metal targets in this work are bonded using indium solder to copper backing plates to prevent target damage due to thermal shock, and copper meshes are used for all targets.

One of the disadvantages of using indium as the bonding material is that the melting temperature of indium (156.6 °C) is relatively low. Different materials heat up differently even with the same sputtering power due to their varying thermal, electrical, and physical properties, as well as differences in the sputtering dynamics [85]. For materials that heat up more easily to a temperature higher than 150 °C, indium bonding is not a good choice as it would melt during sputtering. Figures 2.2 (a) and (b) show images of a damaged Sb (antimony) target. Temperature of the target was likely higher than 150 °C, causing the indium bonding to melt and

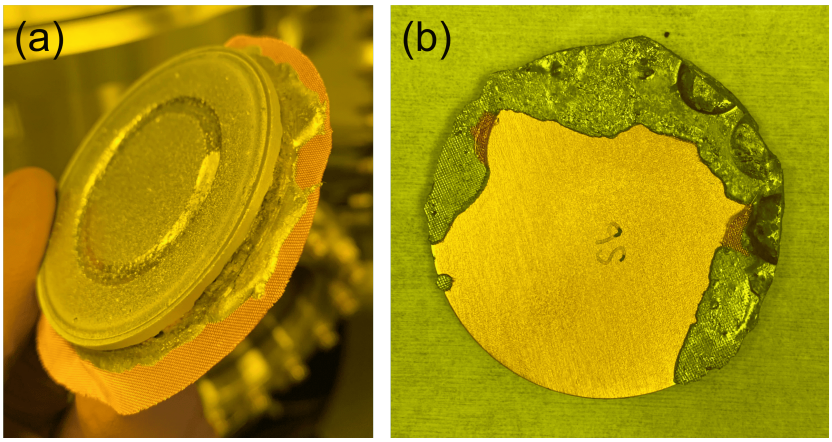


Figure 2.2: A damaged Sb (antimony) target. (a) The Sb target with the indium bonding melted. The copper mesh is stuck on the target by overflown indium. (b) The backside of the Sb target with melted indium bonding. Overflown and re-solidified indium can be seen.

overflow. The overflown indium solidified after the sputter deposition and stuck the copper mesh to the target. There were also overflown indium left on the permanent magnets which could cause damage to the magnets.

Even with the indium bonding layers, the copper mesh, and the active cooling system under the permanent magnet, targets could still be damaged due to thermal shock or local heat accumulation caused by very low thermal conductivity. As shown in Figures 2.3 (a) and (b), GST and ITO targets are cracked due to thermal shock and stress concentration on the target caused by mechanical components inside the chamber.

As shown in Figure 2.3 (c), the Sb_2Se_3 target is severely damaged around the annulus at approximately half the target radius. This is the well-known 'race-track' erosion pattern in magnetron sputtering targets, and it is due to the magnetic confinement of plasma electrons [88]. The closed magnetic field created by the permanent magnet underneath the target traps electrons above the target surface, increasing the density of Ar^+ and the sputter yield where the field is parallel to the surface, which lies approximately half the target radius [92]. As a result, in most targets, the majority of material removal occurs around this annulus, creating a 'race-track' region, as shown in Figure 2.3 (d). This is also the region where the most intense localised heat occurs [88, 93]. The intense localised heat and

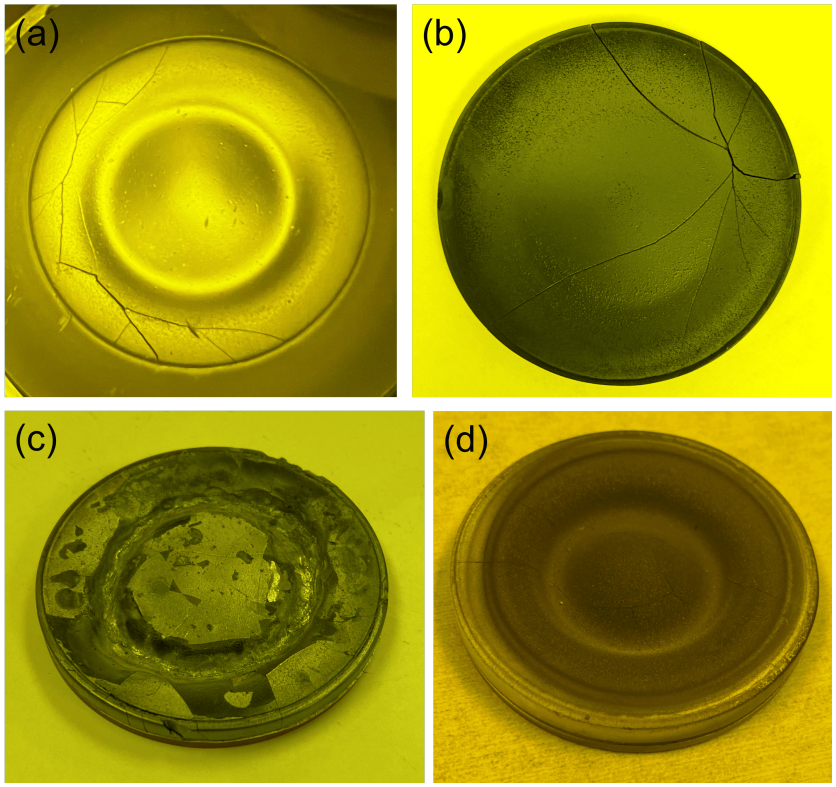


Figure 2.3: Cracked sputtering targets: (a) GST; (b) ITO. (c) A severely damaged Sb_2Se_3 sputtering target, with most of the damage around the annulus at approximately half the target radius, showing the 'race-track' erosion pattern. (d) A heavily used Ge target also showing the 'race-track' erosion pattern which the majority of material removal occurs around this annulus.

the poor thermal conductivity of Sb_2Se_3 (0.2 - 0.4 $Wm^{-1}k^{-1}$) together lead to severe damage to the target during sputtering [94].

To better protect the targets and prevent damage, some protocols are in place.

- A low power, usually 10 to 15 W, is used to ignite the plasma regardless of the sputtering power. This lowers the maximum temperature reached at the moment the plasma is ignited. However, if the plasma is too difficult to ignite at this low power (for some targets), the power can be gradually increased.

- After the plasma is successfully ignited, the power is ramped to the desired sputtering power, and the ramping rate depends on the thermal conductivity of the target. If the target is based on materials with high thermal conductivity (e.g., metals and alloys), the ramping rate is 1 W/s. If the target is based on

materials with low thermal conductivity (e.g., PCMs, oxides, and ceramics), the ramping rate is 4 W/s.

- After sputtering is finished, the power is ramped down from the sputtering power to zero at the same rates specified. The ramping allows the target to heat uniformly and the heat to conduct through the material and into the backing plate without generating excessive local stress. It prevents the steep thermal gradient that causes thermal shock and cracking [95, 96].

2.3 Nanowire Pick-and-Place Technique

The nanowire (NW) pick-and-place technique was developed and published by a previous group member, Utku E. Ali [97]. The main steps of the technique are shown in Figure 2.4. The method involves picking up a single NW from the substrate with a pulled glass tip under an optical microscope. The picked-up NW is placed on a curved polydimethylsiloxane (PDMS) stamp. Then, the PDMS stamp is flipped with its curved face facing downward to place the NW precisely at the desired location of the target substrate. Because of the transparency of the PDMS stamp, the orientation and length of the picked NW can be seen clearly during the placing stage. In addition, the patterns on the target substrate are clearly visible, ensuring that the NW is placed with the desired orientation and location [97].

In this work, this technique is further optimised for a faster and easier process. Firstly, similar to the original technique, the glass tip is fixed to an XYZ stage to help focus and locate the tip under an optical microscope, as shown in Figure 2.5 (a) and (b). Then the heights of the tip and microscope objective are adjusted so that both the glass tip and the NW substrate are in focus, as shown in Figure 2.6 (a). Then, instead of tapping the substrate surface with the glass tip to accurately pick up one NW, the tip is pressed against the substrate, and the stage holding the substrate is moved around, making the tip sweep across the substrate surface, thereby largely increasing the probability of picking up NWs. Using this method, multiple NWs could be picked up simultaneously, as shown in Figure 2.6 (b). Inevitably, unwanted

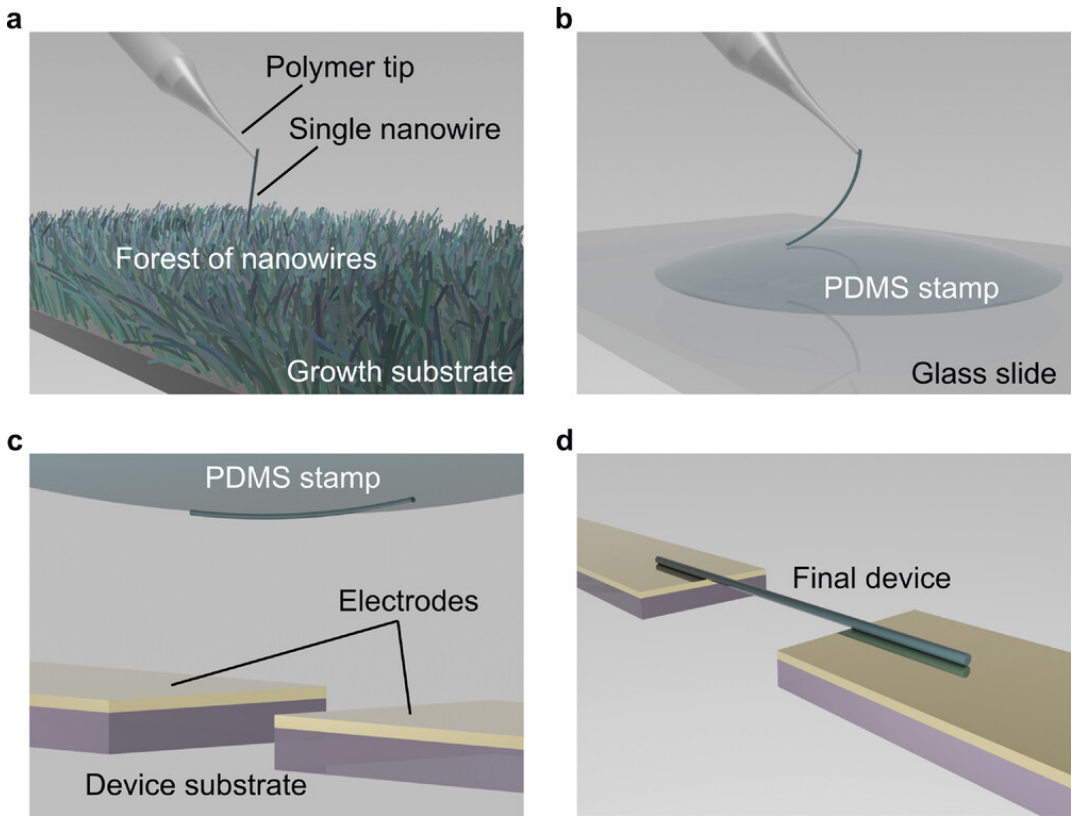


Figure 2.4: NW transfer process. a) A single NW is picked up by the tapered polymer tip from a forest of NWs on the growth substrate. The NW adheres to the tip due to the enhanced van der Waals forces overcoming the weaker interactions between smooth, crystalline NW surfaces. b) The NW on the tip is placed onto a dome-shaped PDMS stamp cured over a glass slide. Note that the adhesion of the PDMS stamp to the NW is greater than that of the tip. c) The stamp with the NW is turned upside down and its alignment with the device chip is done under a light microscope. Following alignment, the stamp is imprinted over electrodes on the device substrate. d) NW deposition is completed with the removal of the stamp. Reproduced from [97].

particles such as dust and seeds for growing NWs are picked up as well; the next steps ensure that only NWs are transferred to the final target substrate. The tip is then pressed against a PDMS stamp to place all picked-up NWs and particles roughly onto the centre of the stamp, as shown in Figure 2.6 (c).

For the next step, the stamp is taped to another XYZ stage with the sticky side facing down. The positions are adjusted so that the surface of the stamp is in focus of the optical microscope. The NWs placed on the stamp in the last stage should be visible under the microscope. An intermediate chip is then fixed (with double-sided tape) on the microscope stage. The stage height of the microscope

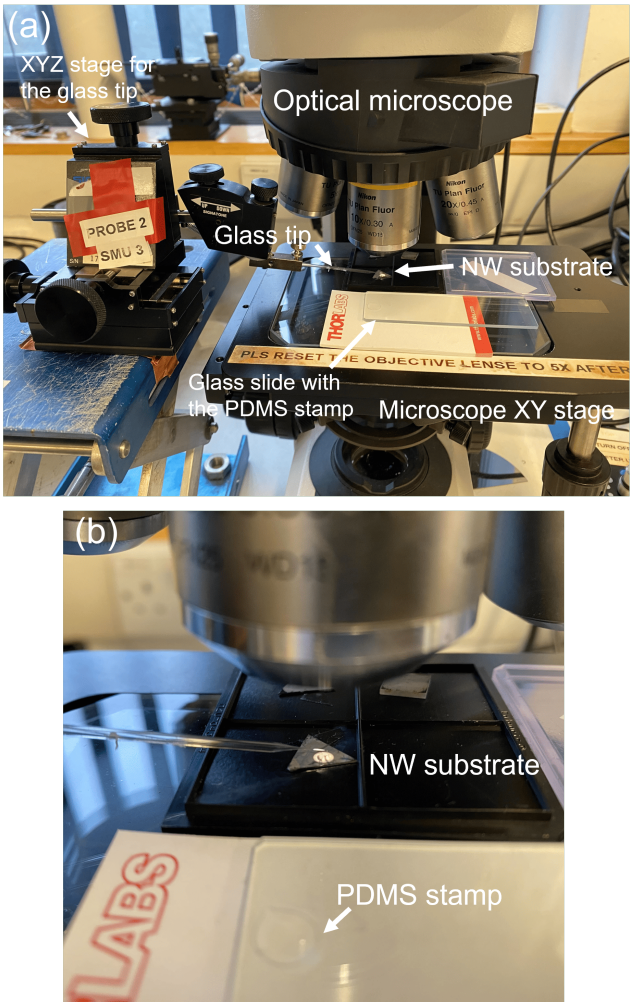


Figure 2.5: Photos showing the setup for the first step (picking up the NW). (a) The XYZ stage which controls moves the glass tip, the microscope stage which moves the substrate and the glass slide where the PDMS stamp is on. (b) The glass tip is above the NW substrate, ready to pick up NWs and leave the NWs on the PDMS stamp.

is increased until the chip meets the surface of the stamp, which can be indicated by the appearance of the circle of contact. Once the chip is in contact with the stamp over a large area, the stage is lowered to break the contact. During this process, NWs might have already been transferred to the chip, and they are easily identified. If the NWs are transferred to the chip, they would become out of focus if the stage is lowered. If some NWs cannot be easily placed on the chip, shear force can be applied in the NW's long direction to help release the NW from the stamp. The process can be repeated several times until all or most of the good-quality NWs are transferred to the chip.

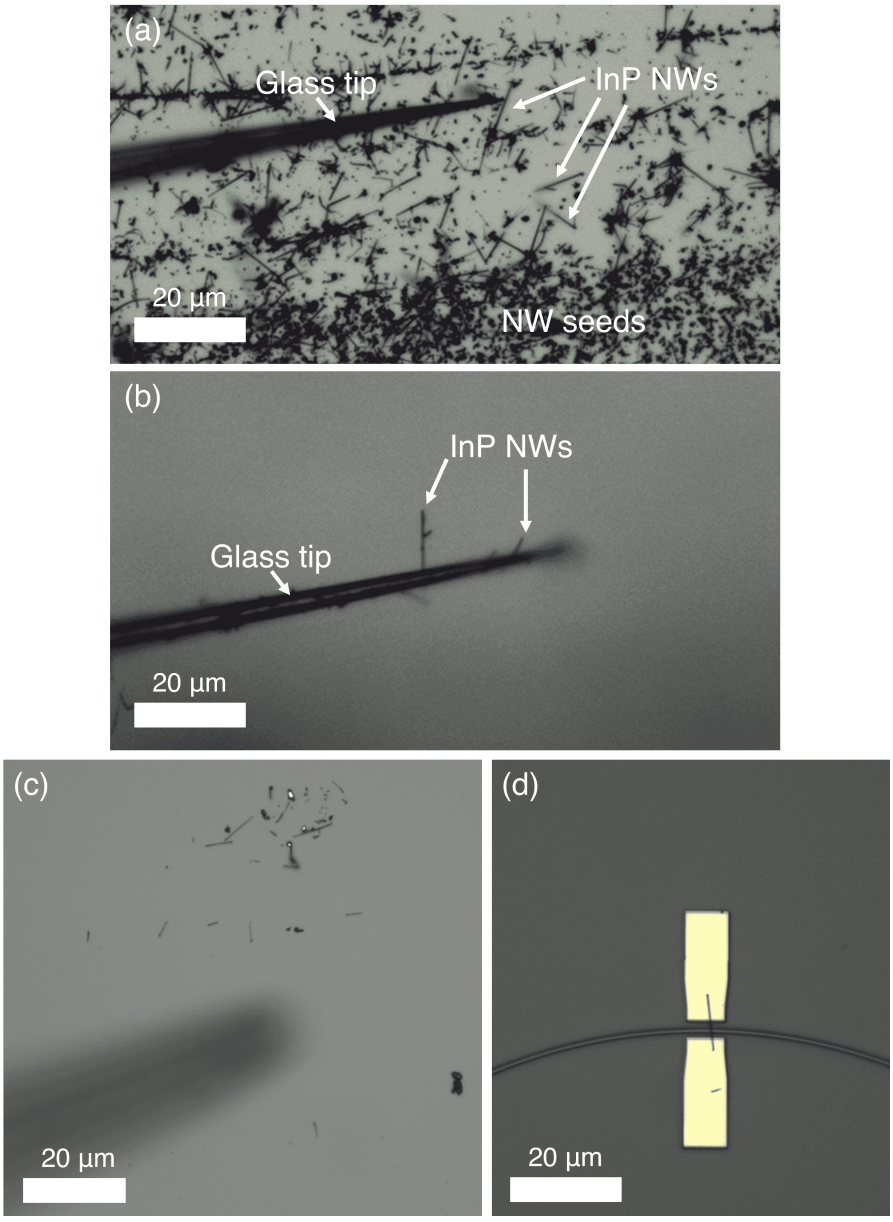


Figure 2.6: Optical microscopy images of: (a) The InP NW forest on substrate and the glass tip picking up the NWs. NW seeds which did not successfully grow NWs are also visible, and they might be picked up. (b) Some NWs picked up by the glass tip. (c) Some NWs placed on the PDMS stamp by the glass tip. (d) One NW successfully transferred onto the metal supports using the pick-and-place process.

In the next step, another stamp with lower 'stickiness' is used to pick up the NWs from the intermediate chip and place them on the final chip with photonic devices. During this stage, the contact area between the stamp and the intermediate chip is controlled by the Z-height of the microscope stage, ensuring that only the desired NW is picked up, leaving the useless particles on the intermediate chip. However, some dust particles or the seeds for NW growth can still be picked up by the stamp. A less 'sticky' PDMS stamp is used to make the placing step easier with fewer contacts with the chip. Therefore, dust particles are less likely to be transferred to the final chip, keeping the devices clear of dust particles. An NW successfully placed without too many particles deposited is shown in Figure 2.6 (d). Sometimes, a 'dirty and old' stamp is used for its very low stickiness. Although there are numerous dust particles on the surface of the stamp, the stamp is able to transfer the NW in less than 5 repetitions, leaving a clean surface on the photonic chip. For comparison, a 'clean and new' stamp with high stickiness may not release the NW in more than 20 repetitions, leaving more particles and possibly residues of the stamp on the chip, which can largely degrade the performance of the photonic devices.

To assist in the placing process, a shear force along the long direction of the NW could be applied by slightly pushing or pulling the microscope stage. This method helps to release the NW from the stamp gradually, increasing the chances of a successful transfer.

2.4 Integrated Photonics Measurements in Vacuum

To access the integrated photonic devices on the chip, light from the laser needs to be directed to the input grating coupler (which couples light into the waveguide) through optical fibres, and light from the output grating coupler needs to be collected and directed to the photodetector (PD) for measurements. Since the grating coupler is sensitive to the polarisation state, a polarisation controller needs to be inserted between the input grating coupler and the laser. A fibre array is usually used to help align the fibre with the on-chip grating coupler.

These measurements are usually performed on a vibration isolation table, and all components are reconfigurable and mobile. However, in experiments involving mechanical vibrations, optical measurements need to be performed under vacuum conditions, which makes the process different. Since the photonic chip must be inside the vacuum chamber, the fibre array also needs to be inside the chamber.

The ideal case would be to insert two motorised stages that can move the chip or fibre array in the XY directions so that multiple devices on one chip could be probed. However, for most of the time during this work, the vacuum chamber available was compact and did not have enough space for stages inside the chamber. As a result, the fibre array needs to be glued at a position where the device provides the best quality signal before placing the device under vacuum. Since the fibre array is glued, only one device can be probed at a time, which largely limits the efficiency of measurements and throughput.

2.5 Lock-In Detection

Lock-in detection was used extensively to measure the frequency responses of filter devices. Measurements employed a Zurich Instruments HF2LI digital lock-in amplifier spanning DC-50 MHz; operation up to 100 MHz is supported with reduced performance [98].

Lock-in detection is a technique used to measure and extract very weak signals from a noisy environment when the signal of interest has a specific frequency with the aid of a reference signal. The basic working principle of a LIA is summarised in Figure 2.7 [98]. The lock-in detection demodulation process can be demonstrated using complex numbers. The input signal $V_s(t)$ can be simulated as a cosine signal with a frequency and amplitude of ω_s and $\sqrt{2}R$, respectively. Another signal with a frequency and amplitude of ω_n and N is added to simulate the noise in the input signal:

$$\begin{aligned} V_s(t) &= \sqrt{2}R\cos(\omega_s t+\theta) + N\cos(\omega_n t+\phi) \\ &= \frac{R}{\sqrt{2}}(e^{+i(\omega_s t+\theta)} + e^{-i(\omega_s t+\theta)}) + N(e^{+i(\omega_n t+\phi)} + e^{-i(\omega_n t+\phi)}) \end{aligned} \tag{2.1}$$

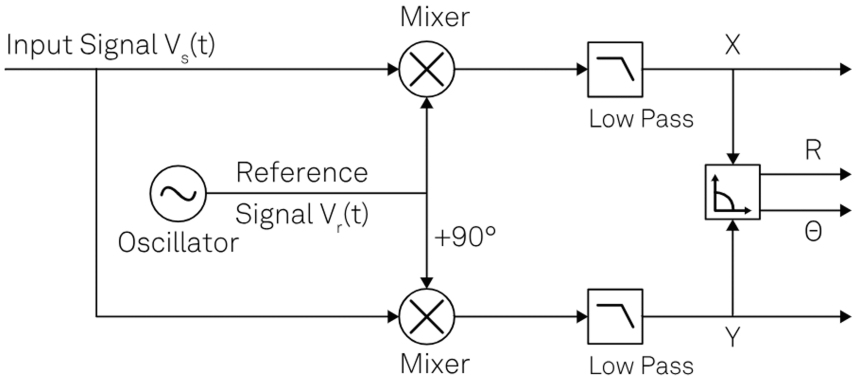


Figure 2.7: Working principle of a lock-in amplifier. The input signal $V_t(t)$ is split into two identical parts, and they are multiplied by the reference signal $V_r(t)$ and its 90°phase-shifted version. The outputs from both mixers, X and Y, are low-pass filtered to retain the DC component and reject the noise and the 2ωcomponent. Then the signals were converted into polar coordinates R and θ. Reproduced from [98].

where θ and ϕ represent the arbitrary phase offsets in the signal and noise components. The reference signal is simulated as a cosine wave with a frequency and amplitude of ω_r and $2\sqrt{2}$ without a phase offset. For convenience, we can take one of the complex exponents of the reference signal for the demodulation analysis:

$$V_r(t) = \sqrt{2}(e^{-i\omega_r t}) \tag{2.2}$$

Then the complex signal after mixing is given by:

$$\begin{aligned} Z(t) &= V_s(t) \times V_r(t) \\ &= \frac{R}{\sqrt{2}}\sqrt{2}(e^{+i(\omega_s t+\theta)} + e^{-i(\omega_s t+\theta)})(e^{-i\omega_r t}) + \sqrt{2}N(e^{+i(\omega_n t+\phi)} + e^{-i(\omega_n t+\phi)})(e^{-i\omega_r t}) \\ &= R[e^{+i[(\omega_s-\omega_r)t+\theta]} + e^{-i[(\omega_s+\omega_r)t+\phi]}] + \sqrt{2}N[e^{+i[(\omega_n-\omega_r)t+\theta]} + e^{-i[(\omega_n+\omega_r)t+\phi]}] \end{aligned} \tag{2.3}$$

with signal components at the sum and difference of the signal and the reference frequencies. The first addend with R as the coefficient is the signal of interest, while the second addend is the noise that needs to be filtered. Filtering is done by applying a low-pass filter to the mixed signal that keeps only slowly varying components (near DC). The summed frequencies $\omega_s + \omega_r$ and $\omega_n + \omega_r$ are typically high frequencies that are well above the cutoff frequency of the low-pass filter. Therefore, signals at these high frequencies would be filtered off, leaving:

$$Z(t)_{\text{filtered}} = Re^{i[(\omega_s-\omega_r)t+\theta]} + \sqrt{2}Ne^{i[(\omega_n-\omega_r)t+\phi]} \tag{2.4}$$

Now, there are still two addends, and the noise is not yet separated from the signal. If ω_r is tuned to ω_s, then $\omega_s - \omega_r = 0$. Meanwhile, since the noise is at a different frequency from the signal, so $\omega_s - \omega_r \neq 0$. The noise term oscillating at $\omega_s - \omega_r$ can be filtered if the frequency is large compared to the cutoff frequency of the low-pass filter. Hence, when $\omega_s = \omega_r$, after sufficient low-pass filtering, the filtered signal becomes:

$$Z(t)_{\text{filtered}} = Re^{i\theta} = R(\cos\theta + i\sin\theta) \tag{2.5}$$

Equation 2.5 is the demodulated signal without noise and the main output of the LIA. From Figure 2.7, there are four outputs: X, Y, R, and θ. X and Y are termed the in-phase and quadrature components, calculated by [98]:

$$\begin{aligned} X &= \text{Re}(Z) = R\cos\theta \\ Y &= \text{Im}(Z) = R\sin\theta \end{aligned} \tag{2.6}$$

The amplitude output R and the phase output ϕ are easily derived from X and Y by a transformation from Cartesian coordinates into polar coordinates [98]:

$$\begin{aligned} R &= \sqrt{X^2 + Y^2} \\ \phi &= \text{Im}(Z) = R\sin\theta \end{aligned} \tag{2.7}$$

A sinusoidal signal with higher tone noise is simulated as the input signal $V_s(t)$. It contains a signal of interest at 100 Hz with an amplitude of $\sqrt{2}$ and noise at 320 Hz with an amplitude of 2. Its temporal data and frequency spectra are shown in Figure 2.8 (a). It is then mixed with the reference signal (a sinusoidal signal with a frequency and amplitude of 100 Hz and $\sqrt{2}$, the results are plotted in Figure 2.8 (b). The four peaks are $100 - 100 = 0$ Hz, $100 + 100 = 200$ Hz, $320 - 100 = 220$ Hz, and $320 + 100 = 420$ Hz. Finally, a virtual low-pass filter is applied to the multiplied signal, leaving only the 0 Hz component, as shown in Figure 2.8 (c). The time domain signal becomes a horizontal line with amplitude $\sqrt{2} \times \sqrt{2} \div 2 = 1$, which is the in-phase amplitude X of V_s. The amplitude of the signal of interest is successfully recovered despite the noise having a higher amplitude. If the signal of interest is amplitude-modulated, the message signal can also be retrieved by adjusting the cutoff frequency of the low-pass filter.

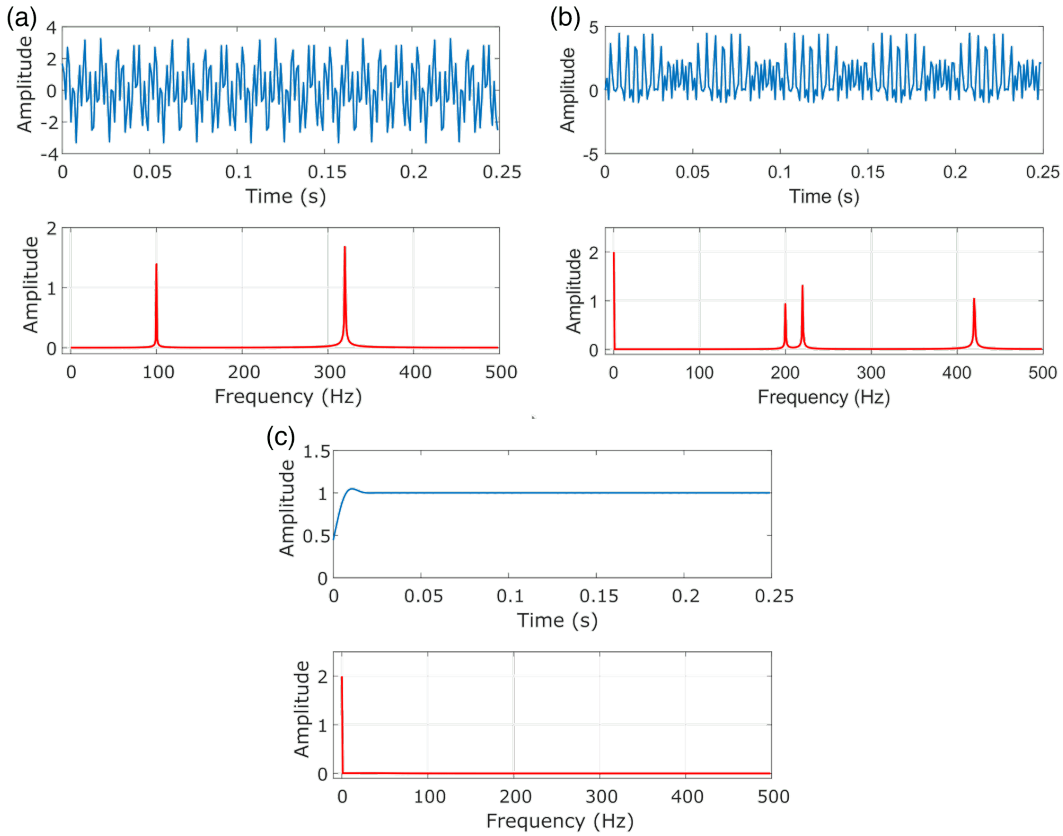


Figure 2.8: Temporal data and frequency spectra of: (a) $V_s(t)$, where $R = 1$, $\omega_s = 100$ Hz, $N = 2$, $\omega_n = 320$ Hz; (b) $V_s(t) \times V_r(t)$, where $\omega_r = 100$ Hz; (c) $Z(t)_{filtered}$, cutoff of the low-pass filter is 10 Hz.

The HF2LI provides a sweeper function that sweeps the frequency of the reference signal, so that the frequency response of the input signal could be plotted. When the frequency matches the frequency of a component of the input signal, it shows a peak in the frequency domain. The central frequency and the Q factor of the peak could help identify the origin of the peak (i.e., whether it is from the resonance of a nanomechanical resonator or from the background, such as the piezoelectric stack).

It is worth mentioning that HF2LI has two voltage inputs and outputs (with DC offsets available). Since the device works by monitoring the voltage across the internal impedance (50 Ω or 1 MΩ), it can also indirectly measure variations in current by measuring the voltage developed across the internal impedance due to the current. For example, if the 50 Ω impedance is used and the readout voltage is V_{in}, then the input current I_{in} can be calculated using Ohm's law:

$$I_{\text{in}} = \frac{V_{\text{in}}}{50\ \Omega} \tag{2.8}$$

2.5.1 Thermal Noise Sweep Mode

The HF2LI thermal-noise mode passively characterises nanomechanical resonators by recording the standard deviation of the demodulated amplitude R and dividing it by the square root of the demodulator bandwidth to estimate the displacement-proportional spectral density. No external drive is applied; thermally driven resonances observed in air and in vacuum reveal the quality factor and confirm effective readout. Comparison with driven sweeps further validates the evanescent coupling between the NW and the micro-ring resonator (MRR) and helps discriminate genuine mechanical modes from spurious signals.

2.5.2 Frequency Response Sweep Mode

The frequency response sweep mode actively drives the NW by sweeping a sinusoidal reference signal through the lock-ins internal oscillator while demodulating the resulting motion. At each drive frequency, the HF2LI computes the complex output components (X and Y) via synchronous detection and low-pass filtering, from which the amplitude R and phase ϕ are obtained as illustrated above. By plotting R and ϕ against frequency, one constructs the resonators transfer function under controlled excitation, enabling the precise determination of the resonance frequency, linewidth, and coupling strength.

2.5.3 Plotter Mode

The plotter function of the HF2LI is primarily utilised to retrieve and reconstruct the time domain signal by acting as a high-precision digitiser for the demodulated outputs. When a specific demodulator frequency is set, the plotter continuously samples the in-phase (X) and quadrature (Y) components of the input signal at a high rate. This process effectively captures the slowly varying envelope of the signal at the reference frequency. By recording these X and Y data streams, the full amplitude and

phase evolution of the signal's envelope can be accurately reconstructed, enabling a detailed analysis of the quality and signal-to-noise ratio (SNR).

2.6 Simulation Methods

Optical and mechanical simulations were performed using Ansys Lumerical and COMSOL Multiphysics, respectively.

2.6.1 Lumerical

Lumerical provides full-wave electromagnetic solvers for modelling photonic structures by numerically solving Maxwells equations. In this work, we used the finite-difference time-domain (FDTD) solver for device-level analysis [99]. Simulations employed perfectly matched layers on the outer boundaries to suppress artificial reflections, and symmetry planes were used where appropriate to reduce computational costs. Material dispersion for silicon nitride, silicon oxide, and indium phosphide was included via refractive-index models provided in the material database. Mesh refinement was applied adaptively, with manual overrides in regions around the NW within the MRR's evanescent field for higher resolution and a more realistic simulation.

FDTD solver The FDTD method (Yee scheme) discretises fields on staggered grids and propagates them in time, enabling broadband characterisation via Fourier transforms of the time response. Here, 3D FDTD was used to model evanescent coupling between a Si_3N_4 MRR and a suspended NW positioned above it, quantifying resonance wavelength shifts and linewidth changes versus the NW-MRR separation. Excitation was provided either by an eigenmode source launched in the bus waveguide; frequency-domain monitors recorded transmission spectra and local field distributions [99].

2.6.2 COMSOL Multiphysics

COMSOL employs the finite-element method for coupled physics problems [100]. We used the Solid Mechanics modules eigenfrequency solver to compute the natural frequencies and mode shapes of nanomechanical structures under appropriate boundary conditions (clamped supports at anchor points; free elsewhere) [101].

Eigenfrequency solver The eigenfrequency solver within COMSOL's solid mechanics module computes the natural frequencies and corresponding mode shapes of mechanical structures by solving the generalised eigenvalue problem derived from the discretised equations of motion. The solver's capability extends to complex three-dimensional geometries where analytical solutions are unavailable, making it particularly valuable for nanomechanical resonator analysis. By applying appropriate boundary conditions such as fixed constraints to represent clamped ends or support points, the solver accurately predicts the resonant behaviour of suspended structures [101].

For nanomechanical resonator characterisation, the eigenfrequency analysis provides critical design parameters including fundamental resonance frequencies, higher-order modal patterns, and quality factor estimation through damping considerations [101]. The solver's ability to handle sub-wavelength features and capture the effects of geometric nonlinearities makes it indispensable for optimising nanomechanical resonator designs.

3

Simulations on Nanowire and Mirco-Ring Resonator Coupling

Contents

3.1 Introduction 49
3.2 COMSOL Simulations 54
3.3 Lumerical FDTD Simulations 55
3.4 Numerical Simulation 58
3.5 Discussion 60

3.1 Introduction

As described in Chapter 1, both the radio-frequency (RF) communication network and the photonic computing platform are very useful for data transmission and processing, and thus bridging them via the RF photonics system is necessary. In the RF photonics system, the electronic RF filter after the antenna, which extracts the signal of interest, and the optical encoder, which encodes the electric signal to light from the laser, are two crucial components. However, the integration of multi-channel RF filters and multi-wavelength optical encoders on the same chip is very difficult and has not yet been realised due to the challenges of integrating bulky conventional RF filters with photonic components. Very few research interests focus

on this interface between the RF antenna and RF-encoded light, even though it is crucial for the integration of RF networks and RF photonic processors.

Here, a scalable optoelectronic multi-channel RF filter bank integrated with a multi-wavelength optical encoder based on the nanomechanical resonator on a silicon nitride (Si_3N_4) photonic integrated circuit (PIC) platform is proposed. The filter bank is composed of individual filters with different frequencies and wavelengths. In each filter, the main component is a micro-ring resonator (MRR. and a pair of gold supports that are 50 nm taller than the waveguide surrounding a section of the MRR. There is a suspended indium phosphide (InP) nanowire (NW) on a pair of gold supports, and the vertical (out-of-plane) mechanical vibration of the NW can be driven by a PZT piezoelectric stack glued to the photonic chip. Since the gap between the NW and the MRR is only 50 nm, the NW is within the evanescent field of the light transmitting inside the MRR waveguide, and thus the light will be encoded with the amplitude of the mechanical vibration of the NW. The working principle of an individual filter can be shown in Figure 3.1.

The vibration amplitude of the NW is largely increased when the frequency of the driving force from the PZT matches the NW's resonant frequency f_1. When this happens, the effective index of the ring will fluctuate at f_1, and if the input wavelength is fixed, the intensity of light propagating inside the ring will also fluctuate at f_1. As a result, part of the continuous wave (CW) optical input becomes fluctuating after it passes through the resonating NW and is encoded with f_1. The through port optical output becomes encoded with the mechanical resonance of the NW, and the resonance of the NW can be readout by monitoring the optical output. If an amplitude-modulated (AM) signal is sent to the PZT, the optical output can also be encoded with the AM signal. Since the NW only responds to f_1 with a large vibration amplitude, it can be used as a bandpass filter at f_1. AM signals with different frequencies or noise containing a signal of interest at f_1 can be sent to the piezoelectric chip (PZT), inducing vibrations at different frequencies. The NW will only resonate at f_1, encoding the optical output with

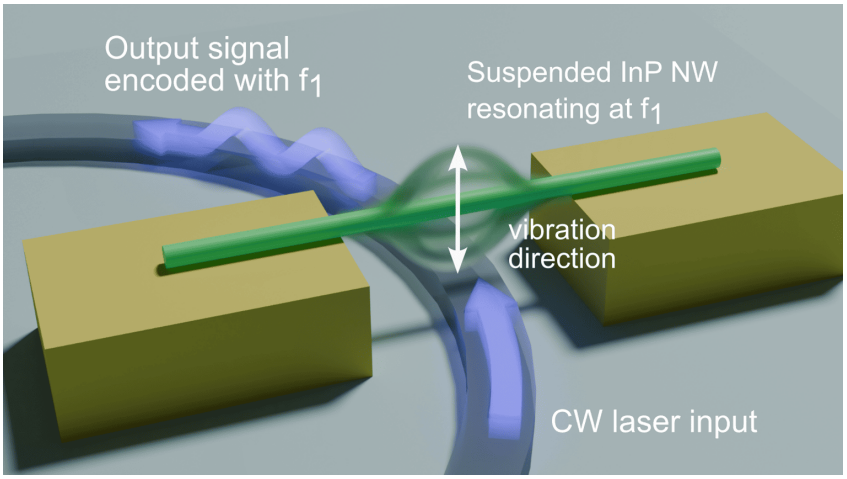


Figure 3.1: Schematic showing how CW light can be encoded with information at resonant frequency of the NW in the MRR.

only the signal of interest at f_1. Therefore, with one MRR coupled with one NW, RF filtering at one frequency and electro-optical encoding can be achieved.

To construct a filter bank with multiple channels and a multi-wavelength electro-optical encoder, multiple individual devices with different radii and spacings between metal supports are integrated. MRRs with different radii provide the multi-wavelength capability, since the resonant wavelength is dependent on the MRR radius, given by:

$$\lambda_{\text{res}} = \frac{n_{\text{eff}} L}{m} = \frac{2\pi \cdot n_{\text{eff}} R}{m} \tag{3.1}$$

where $L = 2\pi R$ is the round-trip length of the MRR (for an MRR of radius R), and $m \in \mathbb{Z}$ is the resonance order (mode number), a positive integer. With different radii and a choice of non-overlapping wavelengths, optical inputs with different wavelengths can be coupled into different MRRs for encodings of various frequencies. The multi-channel capability is provided by the different spacings between the metal supports. The different spacings lead to the varying suspended lengths of the NWs. By modelling the NW as a cylinder, the fundamental resonant frequency of the NW can be estimated. First, the fundamental frequency of the doubly clamped beam can be calculated using the analytical approximation derived from the Euler-Bernoulli beam theory [102]:

$$\omega_0 = \frac{\beta_1^2}{L^2}\sqrt{\frac{EI}{\rho A}} \tag{3.2}$$

where β_1 is a mode-dependent constant, $\beta_1 \approx 4.730$ for the fundamental flexural mode of a doubly clamped beam, L is the suspended length of the beam, E is Young's modulus of the material, I is the second moment of area of the beam cross section ($I = \frac{\pi r^4}{4}$ for a rectangular cross section), ρ is the mass density of the beam, and A is the cross sectional area of the beam ($A = \pi r^2$ for a cylinder). For practical design, Equation 3.2 can be simplified for the NW modelled as a cylinder:

$$\omega_0 = 2\pi(1.78)\sqrt{\frac{E}{\rho}}\frac{r}{L^2} \tag{3.3}$$

where r is the radius of the NW. By changing the suspended length and the radius of the NW, filters with different centre frequencies can be constructed, achieving the multi-channel RF filtering capability.

In this study, a filter bank device with two channels is demonstrated. It consists of two MRRs with different radii and two NWs with different suspended lengths coupled to the MRRs, as shown in Figure 3.2. The two MRRs are labelled Ring 1 and Ring 2, with Ring 1's radius larger than that of Ring 2's. Ring 1 and Ring 2 are optically coupled with NW 1 and NW 2, and NW 1 has a larger suspended length than NW 2. Due to their different suspended lengths, the NWs have different resonant frequencies f_1, f_2, and $f_1 < f_2$. There are two inputs to the device: optical and electrical. The optical inputs are CW infrared lights around 1500-1510 nm, λ_1, and λ_2, which are resonant wavelengths of Ring 1 and Ring 2. The electrical input is the addition of two signals at f_1 and f_2, and is sent to the PZT to drive the vibrations of the NWs.

The optical input with λ_1 will be coupled into Ring 1 and interact with NW 1, which responds only to the signal at f_1. As in the working principle described above, the CW optical input at λ_1 will be encoded with the amplitude of vibration of NW 1 at f_1. Similarly, the other optical input at λ_2 will also be encoded with the amplitude of vibration of NW 2 at f_2. Hence, the multi-channel RF filtering and multi-wavelength optical encoding have been achieved by this single device.

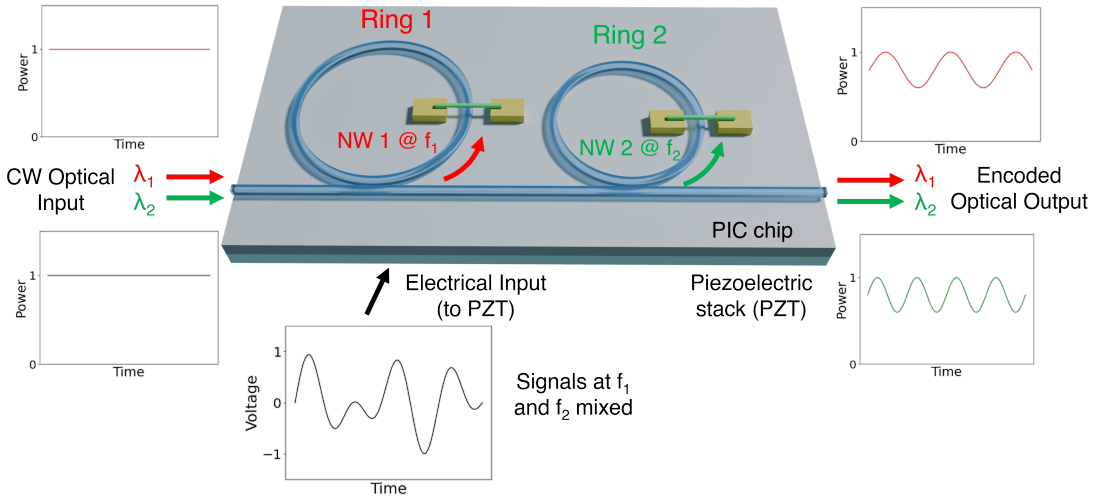


Figure 3.2: Schematic of the filter bank device with 2 MRRs and 2 NWs with NW 1 resonating at f_1 coupled to Ring 1 and NW 2 resonating at f_2 coupled to Ring 2. The optical inputs are CW light at λ_1 and λ_2 which are resonant wavelengths of Ring 1 and Ring 2 sent to the bus waveguide. The electrical input is the sum of two different AM signals at f_1 and f_2. λ_1 would be coupled into Ring 1 and encoded with the AM signal at f_1, and λ_2 would be coupled into Ring 2 and encoded with the AM signal at f_2. The through optical outputs are then collected and measured from the bus waveguide.

In summary, the signal flow of the proposed device can be described as follows: PZT actuation at f_1 and f_2 $\rightarrow$ substrate acceleration $\rightarrow$ NWs out-of-plane vibration at f_1 and f_2 $\rightarrow$ perturbation of the effective index in Ring 1 and Ring 2 $\rightarrow$ MRR transmission modulation of λ_1 and λ_2 at f_1 and f_2 $\rightarrow$ high speed photodetection $\rightarrow$ demodulation at f_1 and f_2.

In real application scenarios, the electrical input from the RF antenna may not only contain signals at two frequencies but may also contain noise and signals at many other frequencies. They would not affect the performance of the filter bank, since the two NWs are naturally mechanical filters with high quality factors (Qs), they can retrieve the signals of interest at specific frequencies regardless of the noise at all other frequencies.

Although only two MRRs with two NWs are demonstrated in this study, the architecture can be readily extended to larger arrays by integrating more MRR-NW pairs, thereby expanding its multi-channel capability for advanced RF photonics applications. This chapter focuses on elucidating the devices working principle and validating its operation through COMSOL and FDTD simulations, laying

the groundwork for the design and experimental implementation discussed in the following chapter.

To verify the proposed operating principle and to understand how the NW-MRR interaction modulates the optical resonance, a series of simulations were performed using COMSOL Multiphysics, Lumerical FDTD, and numerical modelling. COMSOL was employed to determine the eigenfrequencies and mode shapes of the suspended InP NW, while FDTD simulations revealed how the NWs out-of-plane vibration perturbs the effective refractive index of the MRR and alters its transmission spectrum. In addition, a numerical model based on the Lorentzian form of the MRR resonance was used to interpret the FDTD results and to distinguish the effects of refractive index shift and optical loss on the spectral response. Together, these approaches provide a comprehensive understanding of the coupled mechanical-optical behaviour underpinning the operation of the proposed device.

3.2 COMSOL Simulations

The resonant frequency of the suspended NW can be simulated using the Eigenfrequency solver in COMSOL, and it is simulated to compare with the result calculated from Equation 3.3. The Eigenfrequency solver also computes the mode shape of the suspended NW as a reference for the subsequent optical simulations.

The suspended InP NW on the MRR on two supports can be modelled as a doubly-clamped beam. When the doubly-clamped beam is resonating at its fundamental mode, there should be peak and trough positions where the NW is furthest away from the waveguide and closest to the waveguide, respectively. The shapes of the NW when it is at peak and trough positions (of its fundamental mode) and the configuration of the NW with the supports and the underlying waveguide are obtained by a COMSOL simulation using the eigenfrequency solver, as shown in Figure 3.3. Only the suspended part of the NW is able to vibrate freely, so both ends of the NW are fixed with fixed constraints. The InP NW is set to have a radius of 200 nm and a suspended length of 8 µm. Using the Young's modulus of InP NWs reported by Dunaevskiy *et al.*, approximately 65 GPa, the eigenfrequency

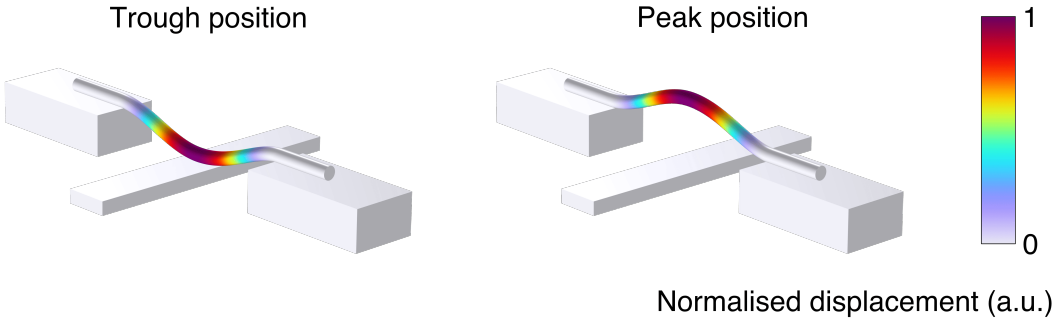


Figure 3.3: COMSOL simulated shapes of trough and peak positions of the doubly-clamped beam above the waveguide with colour scale on its normalised displacement.

of the fundamental mode of this NW is simulated to be 20.36 MHz, which is the same as the result calculated using Equation 3.3 [103].

It should be noted here that the displacement amplitudes shown in Figure 3.3 are not accurate. This is because the eigenfrequency solver does not provide loads or damping and only solves for shapes and natural frequencies. The displacement shown is scaled arbitrarily by a normalisation convention, and its magnitude is not a physical quantity [104].

3.3 Lumerical FDTD Simulations

The experimental results can be approximated by simulations using the Lumerical FDTD solver. Since the principle behind the filter is to probe the out-of-plane mode mechanical resonance of the NW with the integrated MRR by monitoring the through port output (transmission), there should be a large fluctuation in the transmission when the NW is resonating.

Firstly, a simple Si_3N_4 MRR is constructed. Then a cylinder representing the InP NW is constructed above the MRR. The radius and height of the cylinder are 0.2 and 10 µm, respectively. The gap between the cylinder and the MRR can be adjusted to represent different phases of mechanical vibration of the NW. The trough of the vibration is modelled as when the gap between the waveguide and the cylinder is the smallest, and the NW is closest to the MRR, set at 10 nm. The

peak of the vibration is modelled as when the gap is the largest, and the NW is the furthest away from the MRR, set at 160 nm. Therefore, the amplitude of the vibration is set at 75 nm. In the real experiment, the amplitude of vibration is much smaller than this, but the simulation is made more extreme to more clearly show the difference in the optical resonance between the trough and peak positions of the NW. Furthermore, the shape of the NW changes and will not be cylindrical in the actual experiment, but this simulation provides an approximation of the expected results from the measurements.

The simulation results are shown in Figure 3.4 (a), and the results indicate that there is a difference in the MRR spectrum when the NW is in different positions during its vibration. When the NW is at the peak of the vibration, the MRR resonance shows a small blue shift, and when the NW is at the bottom of the vibration, the MRR resonance shows a small red-shift. When the NW is resonating, it oscillates between the peak and trough positions, hence the spectrum of the ring would also oscillate between the two spectra at the NW's resonant frequency. If the wavelength of the optical input is fixed at one of the slopes of the MRR spectrum, the mechanical vibration of the NW should give rise to a fluctuating component at the NW's mechanical resonant frequency in the optical output, and the magnitude of the fluctuating component should be related to the difference between the two spectra at a fixed wavelength.

The absolute difference between the two spectra is plotted against the wavelength as shown in Figure 3.4 (b). There are two maxima and a low point (to be distinguished from trough and peak in Figure 3.4 (a)) between them. The dip in the graph corresponds to the wavelength when the peak and trough MRR spectra intersect with each other. At the dip, which is the optical resonant wavelength (1540 nm), the through port transmissions at peak and trough positions are the same; hence it indicates that there would be no or very little fluctuation in the transmission if the optical input was set at this wavelength. The maximum on the left (at a lower wavelength) is taller than the other maximum, which indicates that the fluctuation of the transmission is expected to be largest at this wavelength,

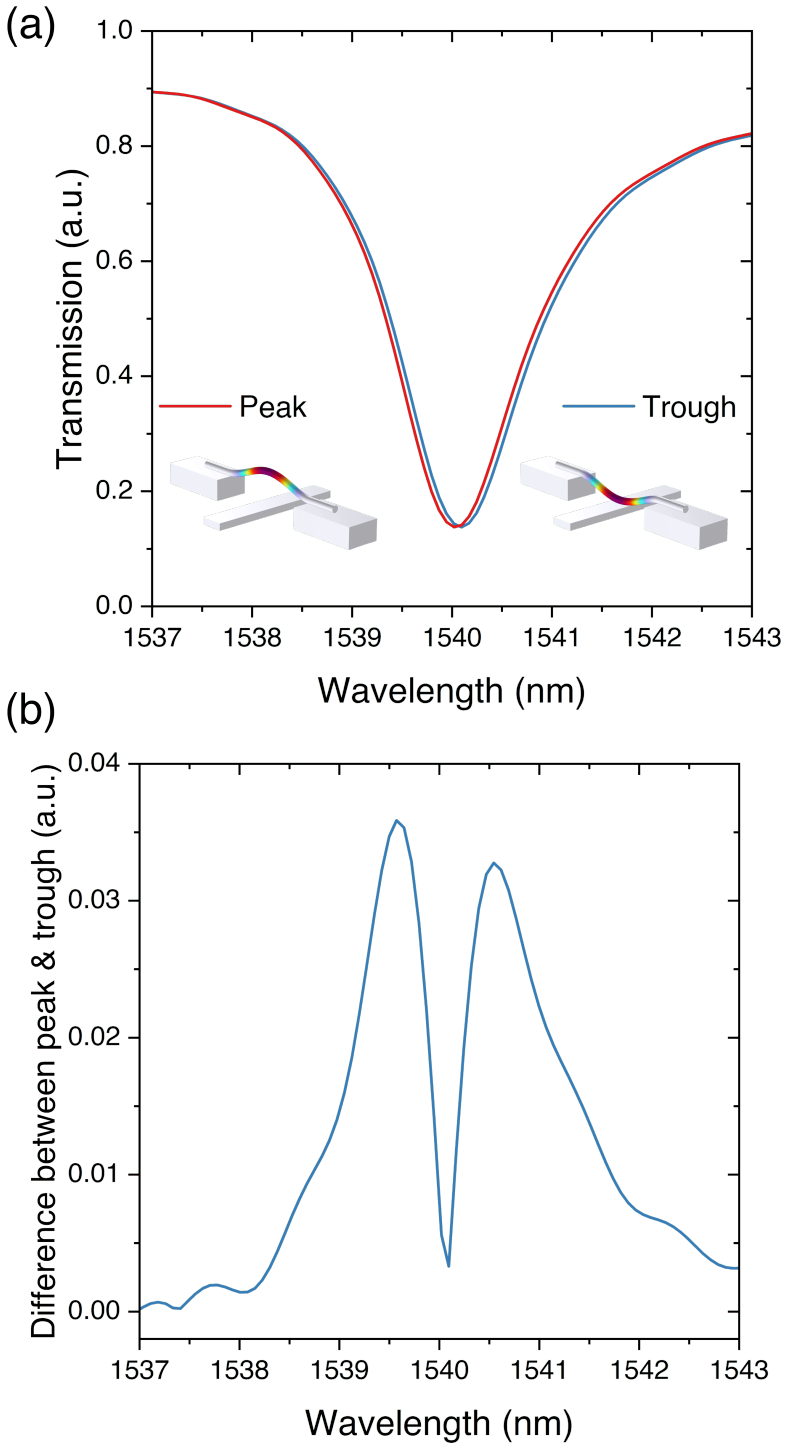


Figure 3.4: (a) The FDTD simulated MRR spectra when the NW is at peak and trough positions of its vibration. (b) The absolute difference between the two spectra, showing a trough at the centre where two spectra intersect, and two asymmetrical maxima with the one on the left (lower wavelength) taller.

which is around 1539.5 nm and on the left slope of the MRR resonance. The other maximum on the right slope (around 1540.5 nm) of the MRR resonance is slightly lower, indicating a smaller expected fluctuation if the input is set at this wavelength.

3.4 Numerical Simulation

To study the reasons behind this pattern, some numerical simulations are performed. It is well known that MRR spectrum can be modelled with a Lorentzian (Cauchy) distribution, which is described by the equation [105]:

$$T(\omega) = T_0 \cdot \left[1 - \frac{A}{1 + \left(\frac{2(\omega - \omega_0)}{\Gamma} \right)^2} \right] \tag{3.4}$$

where ω_0 is the resonant frequency (i.e., the mean of the Lorentzian), Γ is the full width at half maximum (FWHM, which is associated with the Q of the MRR), A is related to the extinction ratio (ER) of the MRR, and T_0 is the off-resonant transmission level (typically 1). Therefore, Lorentzian distributions with different parameters are plotted to represent MRR spectra, and the absolute difference between the spectra is calculated in each case to match the pattern in the FDTD simulation, as shown in Figure 3.4. In these graphs, Spectrum A is considered the original MRR spectrum, and Spectrum B is the MRR spectrum with some modifications. Spectrum B is both red-shifted and broadened compared to Spectrum A, then the difference between them is calculated to determine whether there are similar effects on the MRR as observed in the FDTD simulated results.

In Figures 3.5 (a) and (b), Spectrum B has the identical shape as Spectrum A, but with its centre wavelength shifted to the red (increased ω_0 in Equation 3.4), and the absolute difference between the two spectra shows two identical maxima symmetrical about the dip between them. This represents an increase in the real part of the effective index (n_{eff}) of the MRR, leading only to a red-shift but not to a broadening of the optical resonance [105].

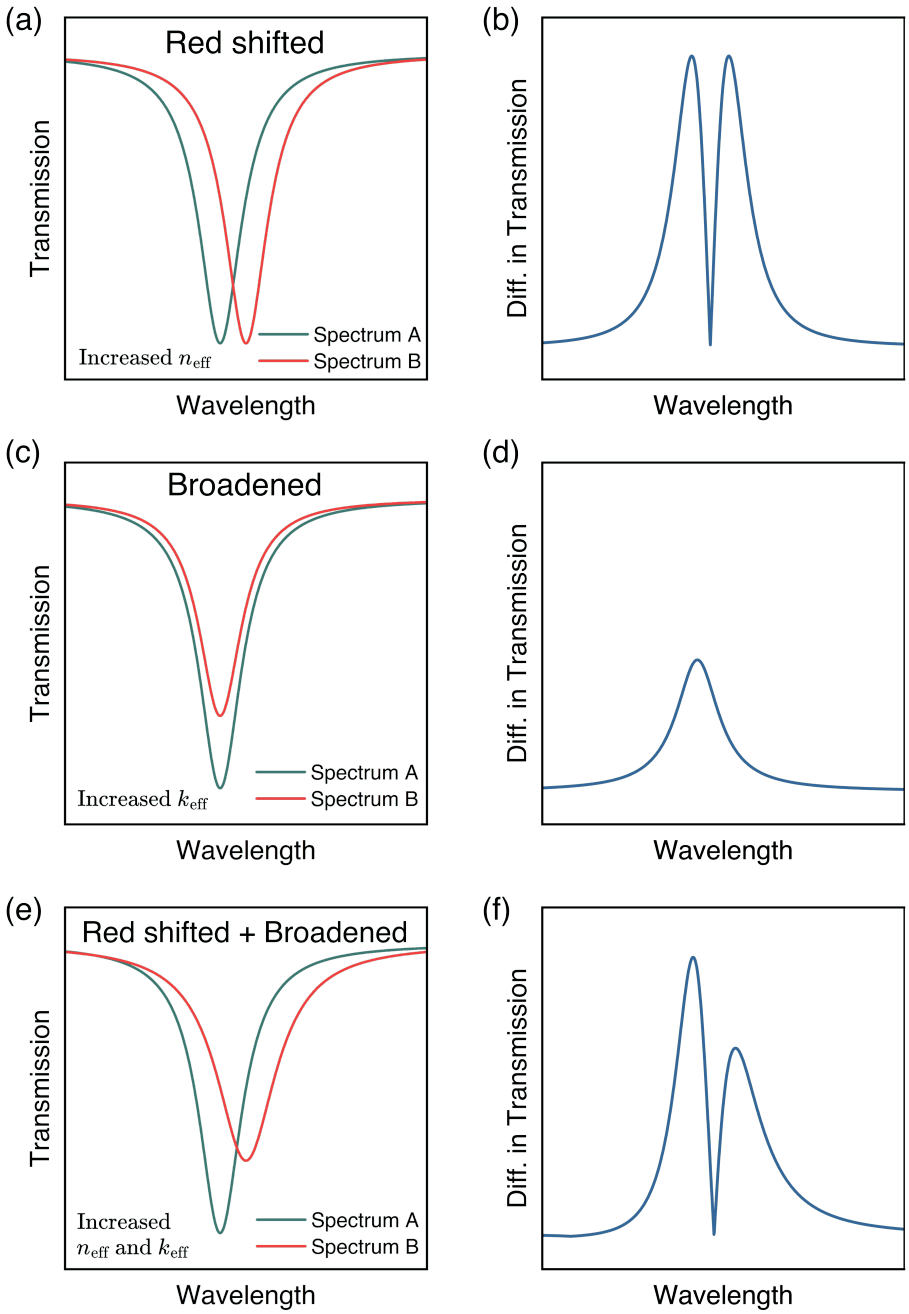


Figure 3.5: Purely numerical simulation of two MRR spectra (Lorentzian distributions), where Spectrum A is the original MRR spectrum, and Spectrum B is the modified MRR spectrum: (a) Red-shifted; (c) Broadened; (e) Red-shifted + Broadened. (b), (d) and (f): Calculated absolute differences between the two spectra in (a), (c) and (e) respectively.

In Figures 3.5 (c) and (d), Spectrum B has the identical centre wavelength as Spectrum A, but Spectrum B has a shallower and broadened linewidth (decreased Γ and A in Equation 3.4), representing an increase in the imaginary part of the effective index (k_{eff}) of the MRR. An increase in k_{eff} not only decreases the Q but also decreases the ER of the MRR [105, 106]. The absolute difference between these two spectra shows only one maximum without a dip.

In Figures 3.5 (e) and (f), Spectrum B is red-shifted and broadened from Spectrum A (increased ω_0 and decreased Γ and A in Equation 3.4), mimicking the scenario when both n_{eff} and k_{eff} increase. In this case, the absolute difference shows two maxima and a dip between them, with the maximum on the left being slightly taller than the other maximum, which is very similar to the FDTD simulated results shown in Figure 3.4 (b). Through these purely numerical simulations, based solely on the Lorentzian equation, it is observed that the trough spectrum is not only shifted from the peak spectrum in Figure 3.4 (a) but is also broadened with decreased Q and ER.

3.5 Discussion

The red-shift caused by the trough position of the NW could be due to the larger overlap between the high-index InP NW and the evanescent field of light propagating in the MRR. The evanescent field of a waveguide mode decays exponentially with distance from the waveguide core [106]:

$$E_{evan}(x) \propto e^{-\kappa x}, \quad \text{for } x > 0 \tag{3.5}$$

Where x is the distance from the waveguide edge, and κ is the decay constant that depends on the mode and the waveguide geometry. When the NW is located closer to the waveguide (at trough position), a larger portion of the evanescent tail interacts with the high-index InP. Consequently, more of the optical energy density is concentrated in the InP region. The effective refractive index is a weighted average over the mode field distribution [106]:

$$n_{\text{eff}} = \frac{\int n(x)|E(x)|^2\,dx}{\int |E(x)|^2\,dx} \tag{3.6}$$

Therefore, a greater weighting from the InP's high refractive index ($n \approx 3.17$) increases n_{eff} more when the NW is closer, i.e., at the trough position. The resonant wavelength of an MRR is given by Equation 3.1. When n_{eff} increases, the resonant wavelength also increases, leading to a red-shift of the spectrum.

The reason why the trough position of the NW broadens the spectrum and decreases its ER could be similar. The broadening and decreased ER are clearly related to an increase in optical loss (k_{eff}) in the MRR. Firstly, InP has a small but non-zero imaginary part of the refractive index. Similarly to how the trough position increases n_{eff} of the MRR, the trough position also increases k_{eff} due to the greater overlap between the NW and the evanescent field of the MRR. Secondly, the NW acts as a scatterer over the MRR and introduces scattering loss to the cavity. The models shown in Figure 3.6 (a) and (b) are constructed to simulate and verify the scattering effect of the NW. Figure 3.6 (c) shows the cross-sectional mode profile (spatial distribution of the electric field) of a normal Si_3N_4 MRR without the NW. From the mode profile, the nodes of the optical resonance can be clearly seen, and the majority of the electric field is contained within the waveguide. Figure 3.6 (d) shows the mode profile of the same Si_3N_4 MRR, but with an InP NW that is suspended above the waveguide with a very small gap between them. The nodes in the waveguide in this case are disturbed by the presence of the high-index InP NW, and the nodes inside the waveguide are disrupted. There is an electric field with a relative strength of around 0.4 in the NW, and the field is less well confined in the waveguide, with a higher intensity above the waveguide. These simulation results have shown that the InP NW introduces scattering loss to the MRR, apart from the loss from material absorption. Therefore, bringing it closer to the waveguide, where the evanescent field is stronger, increases the scattering effect and introduces a larger loss to the MRR, also increasing k_{eff}. As a result, the MRR spectrum is broadened, and its ER is decreased when the NW is at the trough position of its vibration.

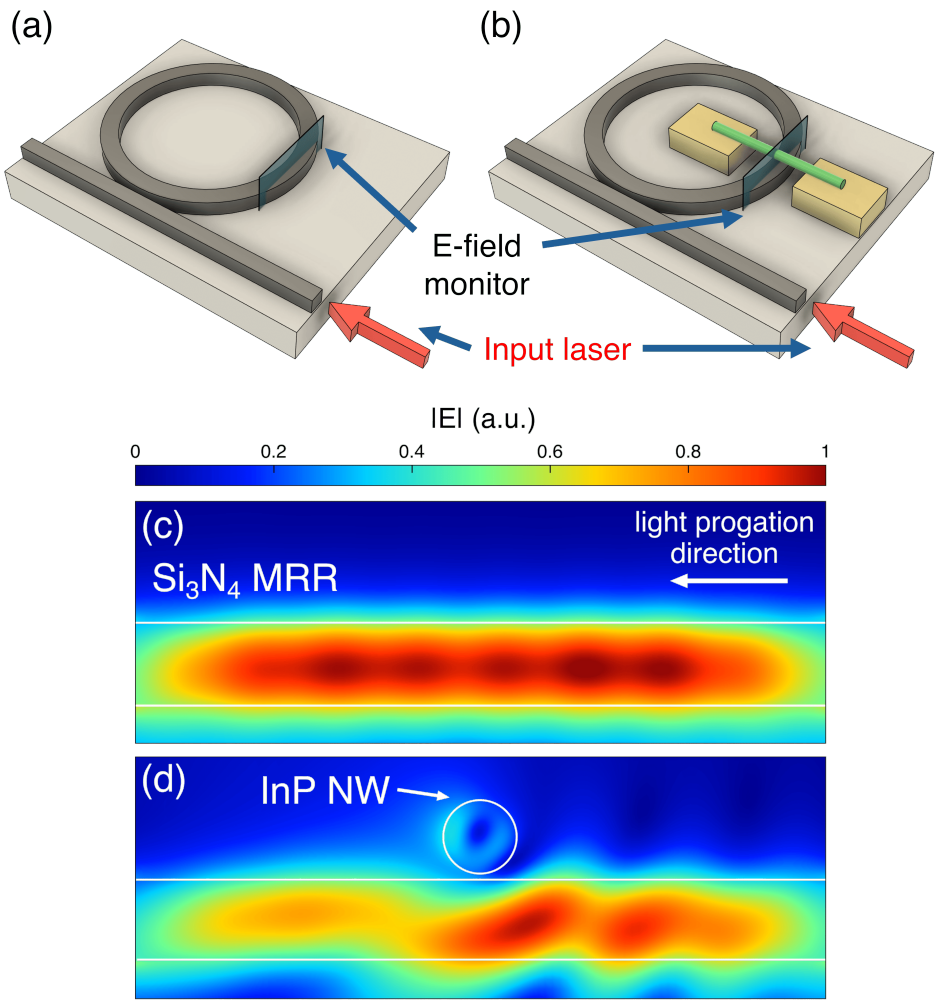


Figure 3.6: FDTD simulated electric field profile around a Si_3N_4 MRR with and without the suspended NW. Schematics showing the 3D simulated model (a) with, (b) without the suspended NW. (c) Tangential cross-sectional electric field profile of a bare a Si_3N_4 MRR as in (a), showing the nodes of optical resonances and most of the electric field confined within the waveguide. (d) Tangential cross-sectional electric field profile of a Si_3N_4 MRR with a InP NW suspended above the waveguide as in (b), showing that the nodes of optical resonance are disturbed, and electric field is not only confined in the waveguide, but also distributed in the NW and above the waveguide. This is the evidence that the suspended NW acts as a scatter above the waveguide, introducing optical loss to the MRR.

4

RF Signal Processing with Mechanical and Optical Resonances

Contents

4.1 Introduction 63
4.2 Device Design and Fabrication 64
4.2.1 Choice of Nanowire Material 65
4.2.2 Choice of Nanowire Support Material 66
4.2.3 Choice of Waveguide and Micro-Ring Resonator Material 67
4.2.4 Device Design 68
4.2.5 Fabrication Flow 69
4.3 Device Characterisation 71
4.3.1 Micro-Ring Resonator Spectra 72
4.3.2 Thermal Noise Measurements 75
4.3.3 Wavelength Dependence of Response 82
4.3.4 Driven Response 90
4.4 Filtering and Encoding Capabilities 98
4.5 Conclusion 107

4.1 Introduction

Building on the simulation-led validation of the working principle in the preceding chapter, this chapter turns to the practical realisation of the optoelectronic multi-channel filter bank on a silicon nitride photonic integrated circuit (PIC). The aim

is to translate the evanescent-field transduction between a micro-ring resonator (MRR) and a suspended nanowire (NW) into a device that is robust, reproducible, and scalable. Doing so requires concurrent attention to optical cavity performance, mechanical resonance control, and process integration, since the figures of merit in one domain are strongly coupled to design choices in the other.

The device architecture follows a modular pattern. Each channel comprises a high-Q Si_3N_4 MRR and a single indium phosphide (InP) NW positioned above the ring within the evanescent field. Out-of-plane NW motion perturbs the complex effective index of the ring, which converts a radio-frequency (RF) drive applied to the substrate into a corresponding intensity modulation on an optical carrier at a chosen ring resonance. In a multi-channel assembly, ring radii set distinct optical carrier wavelengths, while the suspended lengths of the NWs set distinct mechanical centre frequencies. The resulting mapping from $\{f_i\}$ to $\{\lambda_i\}$ enables simultaneous RF filtering and multi-wavelength optical encoding on one chip.

This chapter is organised into three parts. First, the design rationale and fabrication procedures are presented, including the selection of InP NWs, Au supports, and Si_3N_4 waveguides and rings, the device layout, and a two-step lithography process with local metallisation and controlled pick-and-place transfer to set the suspension gap. Second, the fabricated devices are characterised: MRR spectra before and after NW transfer, thermal noise-driven resonances under ambient pressure and vacuum, and piezoelectrically driven frequency responses. Third, multi-channel RF filtering and multi-wavelength optical encoding are demonstrated by applying two amplitude-modulated audio signals and an amplitude-modulated triangular waveform, with selective recovery at (λ_1, f_1) and (λ_2, f_2) used to assess bandwidth, distortion, and signal-to-noise (SNR) performance. Finally, the conclusion section summarises the results and limitations of the proposed device.

4.2 Device Design and Fabrication

The design and fabrication of the proposed optoelectronic filter bank device integrate considerations from both the photonic and nanomechanical domains to achieve

strong optomechanical coupling and stable multi-channel operation. The device combines Si_3N_4 MRRs with InP NWs suspended above the resonators, allowing the mechanical vibrations of the NWs to modulate the optical resonance of the MRRs through evanescent-field interactions. The overall performance of the system depends critically on the material selection, geometric design, and fabrication precision of each component. This section details the rationale behind the choice of materials for the NWs, supports, and photonic structures, followed by the description of the device layout and fabrication process flow. The design strategy aims to optimise optical quality factors, mechanical resonance characteristics, and fabrication reproducibility, thereby ensuring reliable transduction between the mechanical and optical domains.

4.2.1 Choice of Nanowire Material

InP NWs are selected as the material platform for the nanomechanical resonators in this work. The choice is motivated by a combination of optical, mechanical, and practical considerations that make InP particularly well suited for integration with Si_3N_4 PICs.

- **Optical properties:** InP exhibits a relatively high real part of the refractive index ($n \approx 3.17$) with only a small imaginary component ($\kappa \simeq 0.009$-0.017) in the near-infrared regime [107, 108]. This combination allows efficient perturbation of the evanescent field of Si_3N_4 waveguides while minimising optical absorption. Consequently, an InP NW suspended above a Si_3N_4 MRR can induce a significant modulation of the effective index without degrading the cavity quality factor, which is crucial for high-fidelity optical readout.

- **Mechanical robustness and transferability:** InP NWs have been reported to exhibit high mechanical flexibility [97, 103]. This flexibility is advantageous for the pick-and-place transfer process employed in this work, which relies on a polydimethylsiloxane (PDMS) stamp with a curved surface. During the transfer, the NW must endure deformation and shear forces without fracture. The mechanical resilience of InP ensures that the NWs can be

reliably positioned onto the PIC, thereby improving fabrication yield and device reproducibility.

- **Resonant frequency range:** The Youngs modulus of InP is approximately 65 GPa, and the material density is around 4810 kg/m^3. For NWs with typical suspended lengths between 4 and 8 µm and radii of 150-300 nm, the expected fundamental flexural resonance frequencies fall within 15-123 MHz, as estimated using Equation 3.3. This frequency range is experimentally convenient, as it is readily accessible with commercially available lock-in amplifiers (LIAs), spectrum analysers, and function generators. Furthermore, MHz-range mechanical resonances are widely employed in sensing applications, as shifts in resonance frequency due to added mass, applied force, or pressure can be accurately tracked [39, 109].

In summary, the combination of favourable optical constants, mechanical flexibility suitable for transfer, and resonance frequencies in the experimentally accessible MHz regime makes InP NWs an excellent choice for the nanomechanical resonators in this work. The InP NWs were grown on Si (111) substrates using a horizontal flow atmospheric pressure metalorganic vapour phase epitaxy (MOVPE) system. They were grown by collaborators, and the process of NW growth is not within the scope of this work.

4.2.2 Choice of Nanowire Support Material

In addition to the NW itself, the material used for the supporting pads plays a crucial role in determining the quality of the mechanical resonance and the efficiency of the optical transduction. In the present work, three metals were experimentally tested as support materials: chromium (Cr), aluminium (Al), and gold (Au). Among these, only Au consistently yielded strong and reproducible mechanical signals, whereas Cr and Al resulted in weak or unstable responses.

Although the underlying mechanism is not fully understood, it is likely associated with variations in the clamping characteristics at the NW-substrate interface. The

support material influences the adhesion strength, surface roughness, and stress distribution at the point of contact. These factors can significantly alter the effective boundary conditions of the suspended NW, which in turn affect both the resonant frequency and the quality factor of the vibration mode. Gold may provide a more favourable combination of adhesion and compliance, leading to reduced mechanical energy leakage into the substrate and thus a stronger detectable resonance.

Furthermore, Au offers good chemical stability and compatibility with PIC processing, which is advantageous for long-term device reliability. Although a systematic investigation of clamping losses across different support materials is beyond the scope of this work, these experimental findings highlight the crucial role of the NW-support interface. Optimising both the material of the support layer will therefore be an important direction for future device development.

4.2.3 Choice of Waveguide and Micro-Ring Resonator Material

Si_3N_4 is adopted for the MRRs rather than silicon (Si), mainly because Si_3N_4 devices can achieve much higher intrinsic quality factors at 1550 nm due to the absence of two-photon absorption (TPA) and free-carrier absorption, which severely limit Q in Si at telecom wavelengths [110, 111]. In high-Q Si MRRs under typical waveguide dimensions, Qs are around 10^5 to 10^6, and up to 2×10^7 with optimised processing [112–114]. Nonlinear absorption can dominate when the power exceeds a few mW, degrading Q in the Si MRR [110]. In contrast, Si_3N_4 resonators have been demonstrated with intrinsic Qs in the 10^7 regime using subtractive processing methods [115, 116]. More remarkably, integrated Si_3N_4 MRRs with intrinsic Qs over 4×10^8 have been achieved under optimised processing [117]. These values exceed those typically achieved in Si photonics at comparable optical power densities, making Si_3N_4 an ideal choice for maximising sensitivity to nanomechanical perturbations.

In addition, the smaller index contrast of the Si_3N_4/SiO_2 system (compared with Si/SiO_2 in SOI platforms) results in larger mode sizes and reduced sensitivity

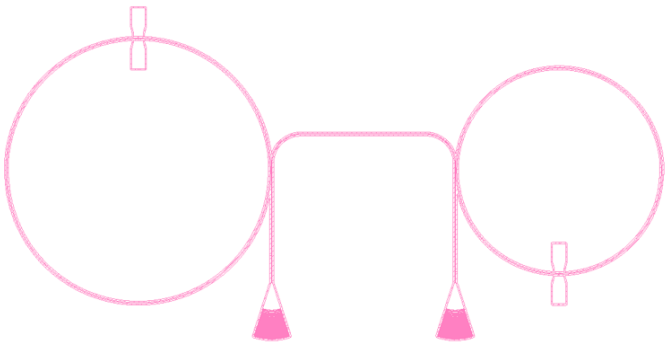


Figure 4.1: Design for the first EBL process, including the photonic components and two pairs of the supports.

to fabrication imperfections, such as sidewall roughness and dimensional deviations [118, 119]. This tolerance improves fabrication yield and consistency across devices, which is beneficial in a system that requires precise control of the height of the suspended NW in the evanescent field of the MRR.

In summary, the use of Si_3N_4 provides two key advantages for the present study: the ability to sustain high quality factors without nonlinear absorption losses and greater robustness to fabrication variations due to the moderate index contrast with the cladding material.

4.2.4 Device Design

The photonic component of the device consists of two MRRs with different radii, a bus waveguide that couples light in and out of the MRRs, and two grating couplers guiding light from the fibre array into the bus waveguide and back. There are also two pairs of supports around the MRRs with different spacings. A typical design for the first electron-beam lithography (EBL) process is shown in Figure 4.1. The radii of the MRRs are designed to be very large, specifically 180 and 140 µm as shown in Figure 4.1, to minimise optical bending losses and enhance the Qs of the MRRs. The large radii primarily determine the overall footprint of the device. However, the footprint could be significantly reduced by employing advanced fabrication techniques such as sidewall smoothing, chemical-mechanical polishing, and optimised annealing to suppress scattering losses [116, 117]. The

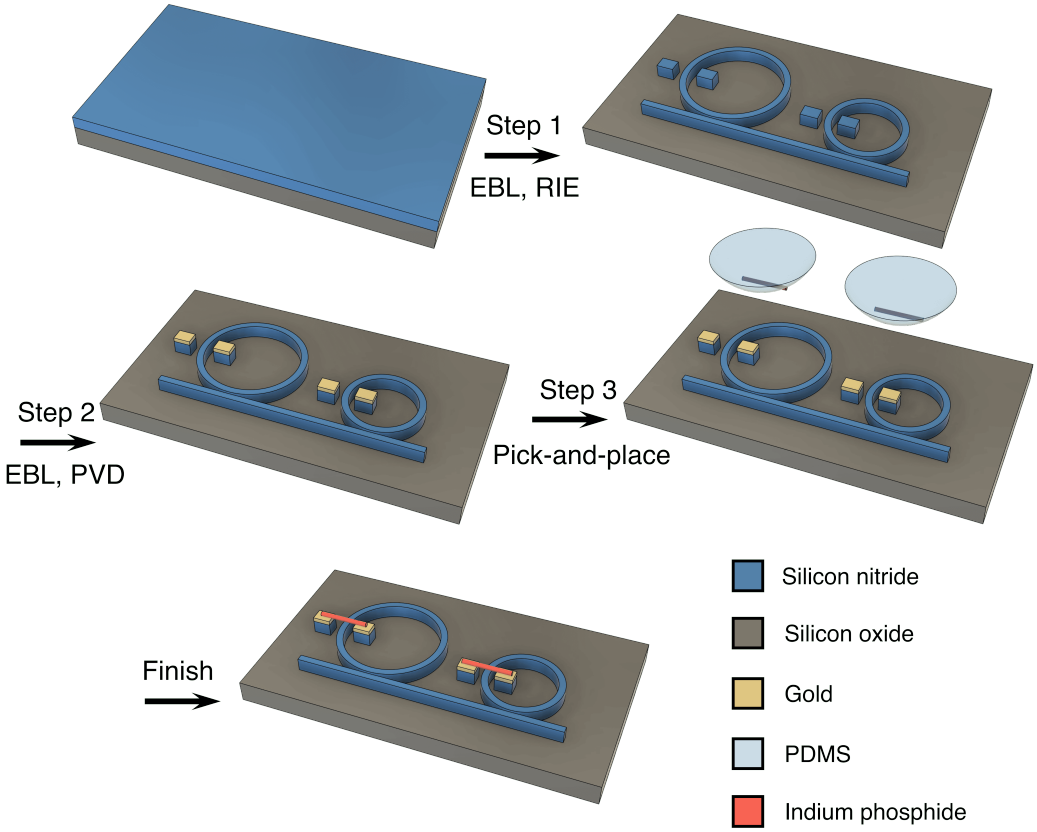


Figure 4.2: Fabrication process flow of the optoelectronic filter bank device with two MRRs and NWs.

spacings between the supports are 5.8 and 5.2 µm, so the NWs have different suspended lengths and different resonant frequencies.

The first EBL process writes the photonic components, and then the second EBL process writes the window for metallisation of the supports.

4.2.5 Fabrication Flow

The fabrication process flow is shown in Figure 4.2. The fabrication starts with a 1×1 cm chip diced from the silicon wafer with 330 nm of Si_3N_4 on 3 µm of SiO_2.

In the first step, the device design shown in Figure 4.1 is input to the electron-beam lithography (EBL) system, and through a Si_3N_4 full etch in reactive-ion etching (RIE), the patterns are transferred to the Si_3N_4. In the second step, the patterns of the supports are written by the EBL system to open windows for deposition, and a thin adhesion layer of Cr, followed by Au, is deposited via physical vapour

deposition (PVD). As a result, the supports are taller than the MRR, enabling the suspension of the NWs above the MRRs, and the height is precisely controlled, as specified in the following paragraph. In the third step, InP NWs are transferred onto the two pairs of supports using the optimised pick-and-place method.

Height of the supports: The suspension height of the NW is primarily determined by the height of the supports, which directly dictates the gap between the NW and the MRR. As the NWs are positioned using a manual pick-and-place process, the actual suspension height inevitably exhibits variations from the designed support height, introducing a certain degree of deviation. If the supports are too low, the NW may come into physical contact with the underlying waveguide, leading to strong mechanical damping and suppression of its vibration amplitude. Conversely, if the supports are excessively high, the NW will be positioned beyond the effective range of the optical evanescent field, whose intensity decays exponentially with distance, thereby significantly reducing the optomechanical coupling strength and readout sensitivity. Through iterative fabrication and characterisation, a support height of approximately 50 nm was identified as optimal, providing a balance between stable suspension and strong optical transduction sensitivity.

A successfully fabricated device is shown in Figure 4.3 (a), with two NWs successfully transferred onto the supports and a generally clean substrate. A false coloured tilted scanning electron microscope (SEM) image is shown in Figure 4.3 (b). From the SEM image, there are darker regions beneath the NW and bright edge features around the suspended region, which may indicate that the NW is suspended above the MRR. However, the darker region here should not be interpreted in the same way as a shadow in an optical image. In secondary-electron SEM imaging, contrast is governed by electron-sample interactions, detector geometry, surface topography, material-dependent secondary electron yield, local charging, and edge enhancement [120]. The darker region beneath the NW may therefore arise from geometric blocking of secondary electrons, reduced collection efficiency from the underlying surface, or local topographic contrast, rather than from the absence of

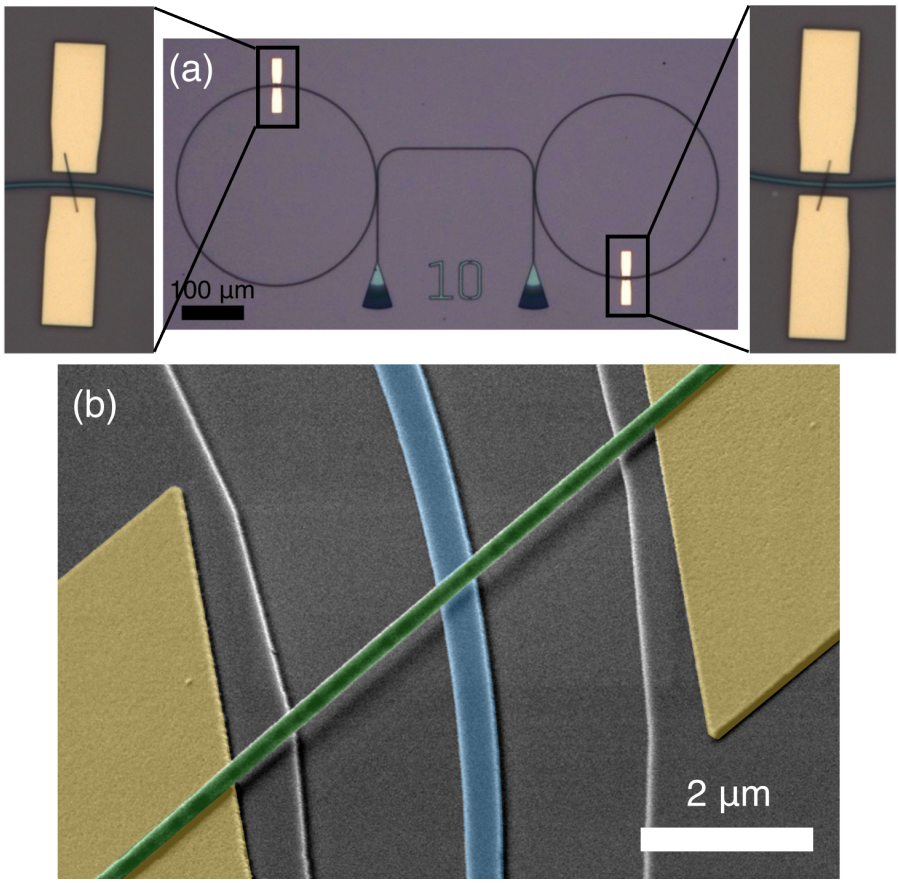


Figure 4.3: (a) Optical image of a successfully fabricated device. Insets show the NWs on supports. (b) Tilted SEM image of a NW positioned above the MRR.

light as in optical shadowing. Similarly, the bright edges commonly observed in SEM images originate from enhanced secondary-electron emission at sharp edges and exposed surfaces, where electrons can escape more efficiently. Therefore, the SEM image provides qualitative evidence that the NW is suspended above the MRR. It is consistent with the designed support height and the subsequent optical and mechanical measurements, but it should not be treated as a direct quantitative measurement of the exact nanowire-substrate gap.

4.3 Device Characterisation

Once a device has been successfully manufactured, the basic characteristics of the device including resonant wavelengths, thermal noise of the NW under ambient pressure and vacuum conditions, driven frequency responses of the NWs, and

sensitivity dependence on wavelength are first measured. These characteristics are crucial for understanding the working principles and expected performance of the device. This section reveals the characterisation techniques and experimental set-ups used for measuring these basic characteristics, along with the results of the measurements.

4.3.1 Micro-Ring Resonator Spectra

The spectra of the two MRR with different radii can be measured using the wavelength sweep function of the laser (Santec TSL-550 or TSL-570) from 1500 to 1630 nm, with the trigger output controlling a photodetector (PD). Since placing the NW in the evanescent field of an MRR causes a change in the effective index of the ring, it is expected that the spectrum of the MRR would change after a NW is placed above it. The MRR spectra before and after the transfer of NWs of a specific device are shown in Figure 4.4 (a). In this device, the radii of the rings are 120 and 113 µm, and they are named Ring 1 and Ring 2, respectively, for the following illustrations. Different radii can lead to different spacings between two successive resonant wavelengths, which are defined as the free spectral range (FSR) $\Delta\lambda_{\mathrm{FSR}}$ [105]. The FSR of an MRR can be calculated using the equation:

$$\Delta\lambda_{\mathrm{FSR}} = \frac{\lambda^2}{n_{\mathrm{eff}}L} = \frac{\lambda^2}{2\pi n_{\mathrm{eff}}R} \tag{4.1}$$

Where λ is the operating wavelength, L is the physical path length around the ring, and R is the radius of the ring. Therefore, Ring 1 ($R = 120$ µm) has a smaller FSR than Ring 2 ($R = 113$ µm) because $\Delta\lambda_{\mathrm{FSR}} \propto 1/R$. From the spectrum of the bare MRR in Figure 4.4 (a), two sets of resonant dips with different FSRs are identified. The FSR of the first set of resonance dips is 1.49 nm, and the FSR of the second set is 1.58 nm, corresponding to the resonances of Ring 1 and Ring 2, respectively. Similar patterns can also be observed in the spectra with NW. The zoom-in spectra of two resonances before and after the transfer of NW are shown in Figure 4.4 (b). The resonance of Ring 1 at 1503.98 nm is shifted to 1504.32 nm after the NW is transferred, resulting in a red-shift of 0.34 nm. The resonance of Ring 2

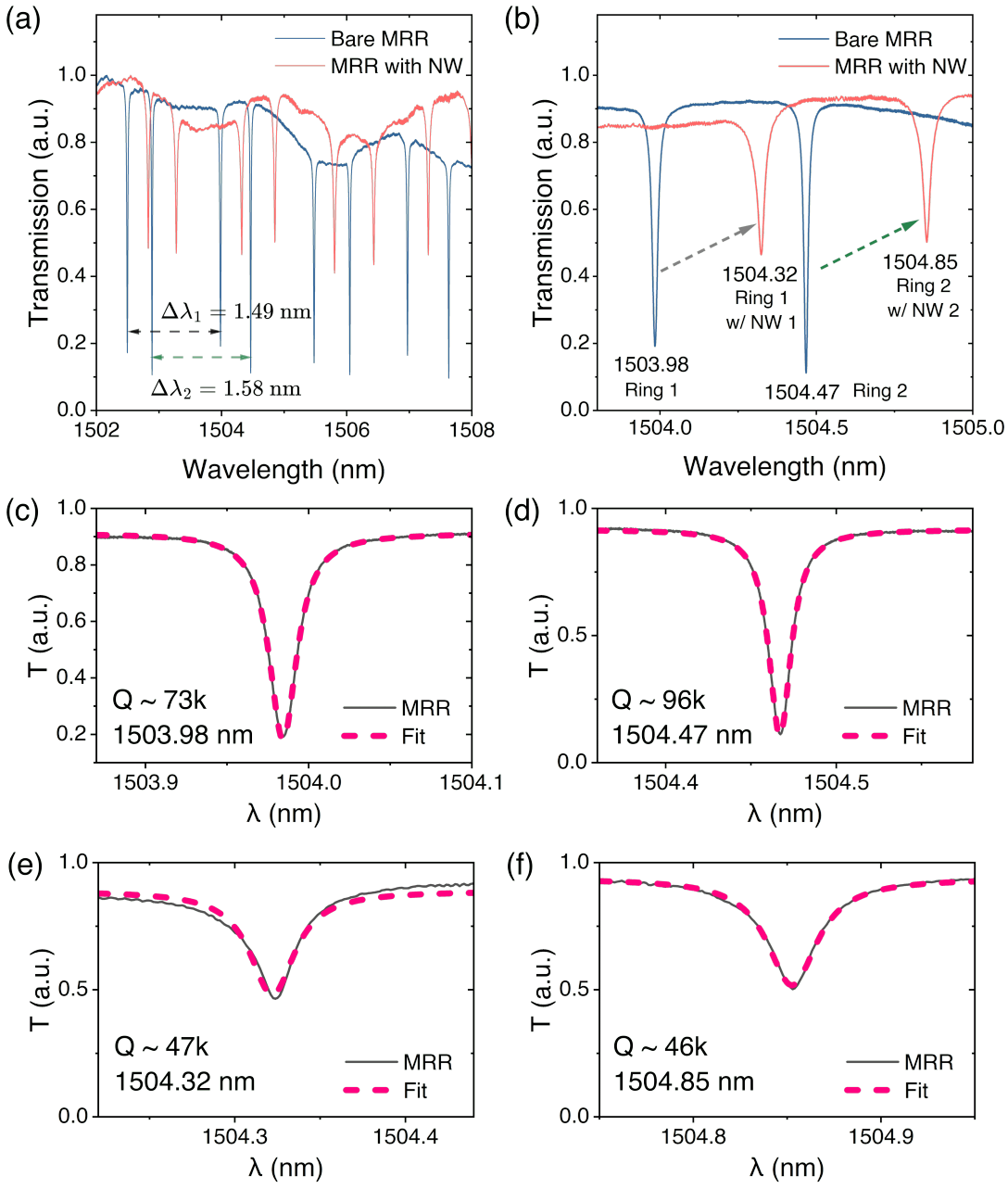


Figure 4.4: MRR spectra before and after the NW transfer. (a) Comparison between the MRR spectra with and without the suspended NW on a 2-ring device. The resonances from the two rings can be distinguished by the different FSRs. The smaller FSR (1.49 nm) corresponds to resonances of Ring 1 ($R = 120$ µm), and the larger FSR (1.58 m) corresponds to resonances of Ring 2 ($R = 113$ µm). (b) Zoom-in view of (a) showing the red-shifts of the resonant wavelengths, increase of resonance linewidth and decrease of ER (decrease of quality factor) after the NW is transferred above the MRR. The MRR spectra with fitted Lorentzian curves and quality factors for resonances at: (c) 1503.98 nm; (d) 1504.47 nm; (e) 1504.32 nm; (f) 1504.85 nm.

at 1504.47 nm is shifted to 1504.85 nm after the NW is transferred, resulting in an effective red-shift of 0.38 nm. The linewidth of the resonance increases, and the ER of the resonance decreases, as expected from the simulation, due to the increase in k_{eff} and n_{eff} caused by the NW in the evanescent field. These measurement results are well-aligned with the simulation results presented in Chapter 3.

These four peaks are fitted with the Lorentzian function to estimate their quality factors, and the fitted curves are shown in Figure 4.4 (c), (d), (e), and (f). The quality factors of the resonances of bare MRRs are approximately 73,000 and 96,000, which are high. Transfer of the NWs caused a decrease in quality factor to approximately 47,000 and 46,000 due to their scattering effects and non-zero optical loss index. The dust and residues of the PDMS stamp may also be deposited onto the MRR during the pick-and-place process, and they could contribute to the reduction of the quality factor via scattering effects and optical losses. The quality factor of the MRR after the NW has been transferred is an important parameter determining the performance of the device. For the same magnitude of driving force, the displacement of the NW is always the same, and the wavelength shift caused by the displacement is also consistent. However, if the quality factor is different, the fluctuations in transmission would be different. A higher quality factor leads to a larger change in the transmission due to the higher sensitivity to shifts in the resonant wavelength, and the amplitude of the readout signal would also be larger. Hence, maintaining a high quality factor after NW transfer is desired. In this case, even though the quality factor is decreased by $1/3 \sim 1/2$, 47,000 and 46,000 are still considered to be quality factors that are high enough, thus, the amplitudes of the readout signals are expected to be sufficiently high.

In some cases, the quality factor of the MRR can drop significantly due to the deposition of dust and residues or the collapse of the NW making the scattering effect too large. For example, the spectra of another 2-ring device before and after the placement of NWs are shown in Figure 4.5 (a), and Figure 4.5 (b) shows more detailed spectra with quality factors. The quality factors of the MRRs decrease from 38k and 30k to 20k and 15k. The quality factors of these two rings are

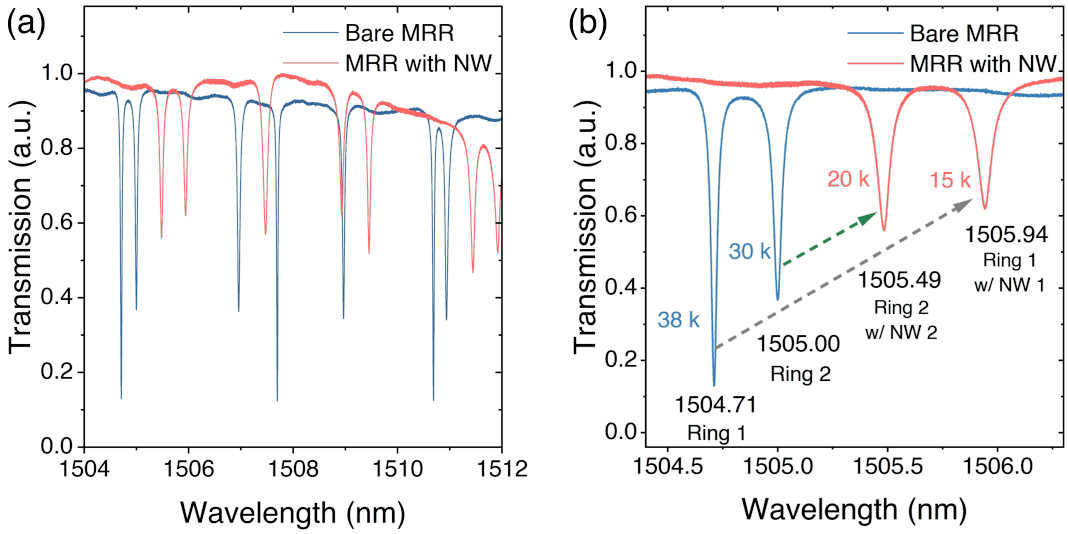


Figure 4.5: MRR spectra with smaller quality factors before and after the NW transfer. (a) Comparison between the MRR spectra with and without the suspended NW on a 2-ring device with lower quality factors. (b) Zoom-in view of (a) showing the decreased quality factors and ERs.

considered to be too low, and they are unlikely to provide responses with good SNRs. Usually, only MRRs with quality factors higher than 30k after the NW transfer could be used and will provide good-quality signals.

4.3.2 Thermal Noise Measurements

After the InP NW is successfully transferred onto supports that are 50 nm taller than the waveguide, it forms a suspended nanomechanical resonator suitable for actuation and optical readout. In the absence of external driving, a nanomechanical resonator in thermal equilibrium is subject to random fluctuations arising from intrinsic dissipation processes, as described by the fluctuation-dissipation theorem [121, 122]. These stochastic forces excite their mechanical modes, producing measurable motion referred to as thermal noise-driven resonance [121].

Thermal Noise Measurement Under Ambient Pressure

The moment a non-defective NW is placed on the supports with proper suspension, the resonant frequency of the NW can already be probed even under ambient

pressure, by measuring the thermal noise spectrum of the NWs.

In experimental measurements of thermal noise-drive resonance using the thermal noise sweep mode of the LIA, the standard deviation of the X and Y quadratures of the amplified input divided by the square root of the low-pass filter (LPF) bandwidth is used as a readout of the vibration spectral density of the resonator. This approach relies on the fact that thermal noise produces zero-mean, stationary fluctuations, whose root-mean-square (RMS) value is equal to the standard deviation. When an LIA with a defined LPF bandwidth is used, the output signal reflects thermal fluctuations integrated over that frequency range. Measuring the standard deviation, therefore, provides a straightforward and accurate estimate of the RMS displacement amplitude within the detection bandwidth, without requiring spectral analysis or curve fitting.

The frequency responses of the device driven by thermal noise are measured using a set-up as shown in Figure 4.6. Continuous-wave (CW) light is generated by the laser and coupled to a single-mode fibre. A polarisation controller (Thorlabs FPC031) is used to adjust the polarisation of the light to maximise the efficiency of the grating couplers. The light is then guided to the grating coupler through a multi-channel fibre array and sent to the device as the optical input. The light would be coupled to one of the MRRs if its wavelength resonates with the MRR. The optical output signal from the device is split into two signals with a ratio of 9:1 by an optical splitter. The signal with higher power (90%) is sent to a high-speed PD, and the electrical output is sent to the LIA for amplification and analysis. The other signal (10%) is sent to a normal PD, and the electrical output is received by a data acquisition (DAQ) board (National Instruments) connected to the PC controlling the laser. This weaker signal is for the phase-locked loop (PLL) to maintain the most sensitive probe wavelength, which will be described in Section 4.3.3.

Once the PLL is active and the optical input is always at the wavelength of highest sensitivity, a frequency sweep in thermal noise mode can be initiated in the LIA. In a particular device, there are two MRRs, each coupled with an InP NW. The two rings in the device are labelled Ring 1 and Ring 2, with radii of

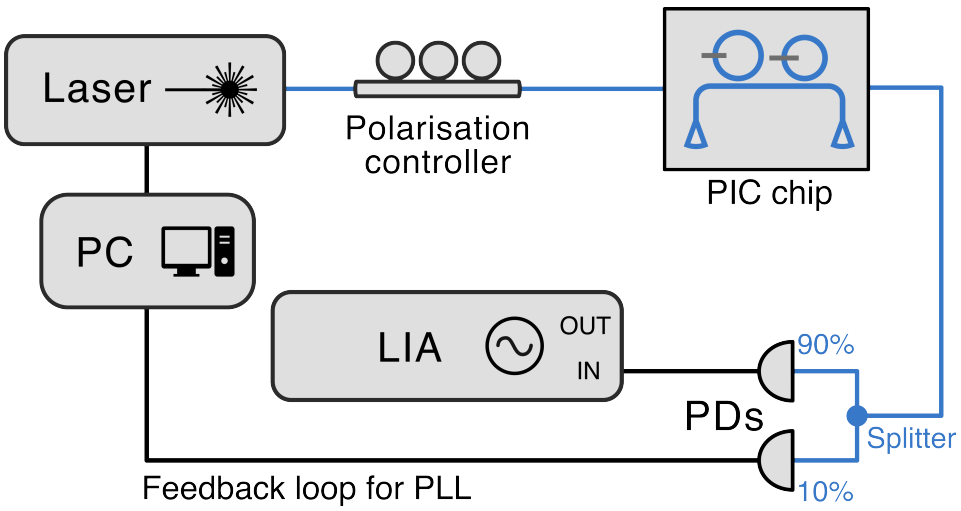


Figure 4.6: Schematics showing the experimental set-up that is used to measure thermal noise spectrum of the device under ambient pressure with the PLL.

180 and 140 µm, respectively. The distances between the supports around them are 5.8 and 5.2 µm, and the NWs placed on them are labelled NW 1 and NW 2, respectively. To measure the thermal noise spectrum of Ring 1 and NW 1, optical input with a wavelength near one of Ring 1's resonances is sent to the device, and the output is collected by the fast PD and analysed by the LIA. Similarly, the thermal noise spectrum of Ring 2 and NW 2 can be measured with the optical input at a wavelength near one of Ring 2's resonances.

The thermal noise responses of these two MRRs are measured under ambient pressure and are shown in Figure 4.7 (a). There are two major peaks corresponding to the response from Ring 1 with NW 1 and Ring 2 with NW 2. NW 1 shows a lower resonant frequency at around 15 MHz, with a smaller shoulder peak at a slightly lower frequency, while NW 2 shows a resonant frequency around 30 MHz. The two graphs share a similar baseline, which is the noise floor of the fast PD and is relevant to the optical power. After normalisation, fitting, and subtraction of the baseline, the graphs become Figure 4.7 (b). With the baseline removed, the two resonant peaks are fitted using the Lorentzian equation. Their central resonant frequencies are 15.36 and 28.71 MHz, and their quality factors are 43 and 68, respectively.

Since NW 1 has a longer suspended length than NW 2, the fundamental resonant frequency of NW 2 should be approximately 1.2 times higher than that

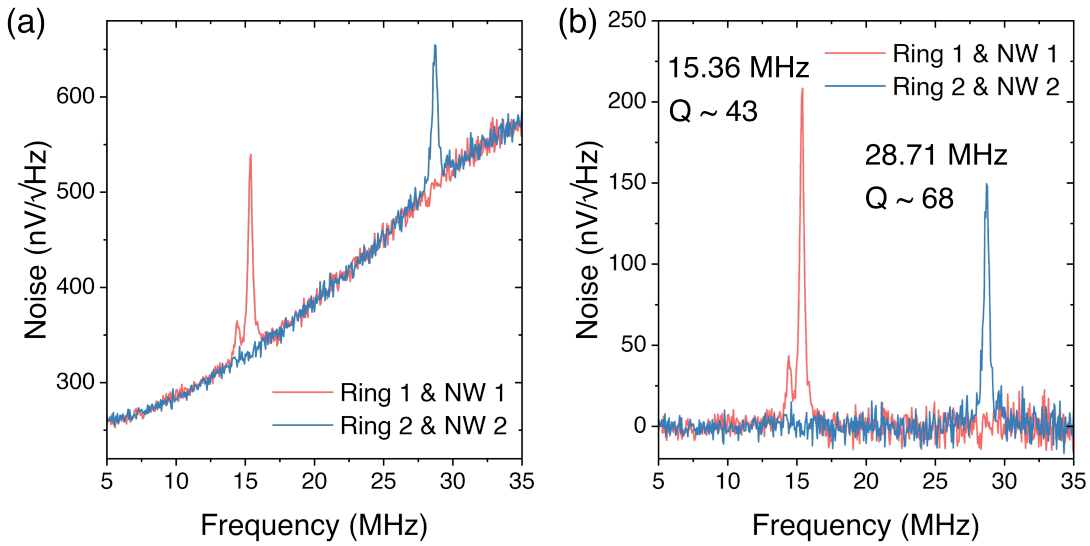


Figure 4.7: Thermal noise spectra under ambient pressure. (a) Thermal noise spectrum of a 2-ring device measured under ambient pressure. (b) Thermal noise from (a) with baseline subtracted, centre frequency and quality factors from Lorentzian fitting.

of NW 1, according to Equation 3.3. However, the resonant frequency of NW 2 is approximately 1.9 times that of NW 1. This is due to the fact that NW 2 also has a larger diameter than NW 1, which further increases the resonant frequency. On the left slope of the peak of NW 1, there is another peak with a much smaller amplitude and a slightly lower centre frequency. This is likely correlated with mode splitting due to asymmetry. A NW may be modelled as a cylindrical vibrating beam whose fundamental flexural resonance is, in principle, degenerate across all directions of vibration. However, when small imperfections are present in the cross section, this degeneracy is lifted, and the single resonance frequency splits into two closely spaced frequencies associated with orthogonal principal planes of motion [123]. The weaker mode may have a smaller displacement or couple less efficiently to the optical field, leading to a smaller amplitude peak at almost the same frequency.

Although the two peaks show good SNR, the quality factors are very low as a result of the damping effects of air molecules under ambient pressure. The damping effects would be significantly reduced if the chip is inserted into a vacuum chamber, and thus the quality factor would be much higher. Frequency response measurements

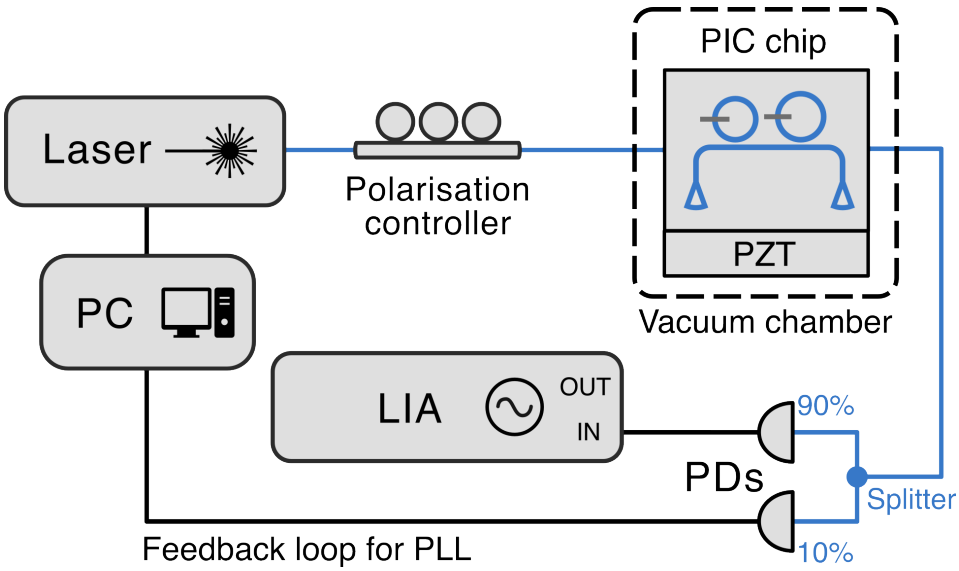


Figure 4.8: Schematics showing the experimental set-up that is used to measure thermal noise spectrum of the device under vacuum with the PLL.

of the thermal noise under ambient pressure are primarily conducted to confirm the quality of the transferred NWs. It ensures that the NWs can resonate with a detectable amplitude and that the coupling gap between the NW and the MRR is suitable for mechanical resonance readout. Since the subsequent insertion into the vacuum chamber requires glueing the fibre array and the printed circuit board (PCB), which is non-reversible and time-consuming, ensuring the detectable frequency response under ambient pressure is necessary for high throughput and efficiency.

Thermal Noise Measurement Under Vacuum

After obtaining valid resonance readouts under ambient thermal noise, the fibre array would be glued to the chip, and the chip would be glued to the PZT (PA4FKW, Thorlabs) and the PCB. Finally, the whole assembly would be carefully inserted into the vacuum chamber. The set-up used is shown in Figure 4.8, and it is almost the same as the set-up used for ambient measurements, except that the PIC chip is inside a vacuum chamber. After the polarisation controller, the optical input is sent to a fibre feedthrough (SQS Fibre Optics) through a 15-m-long fibre to connect fibres outside and inside the vacuum chamber. The optical output from the PIC chip also needs to go through another feedthrough and then to the PD.

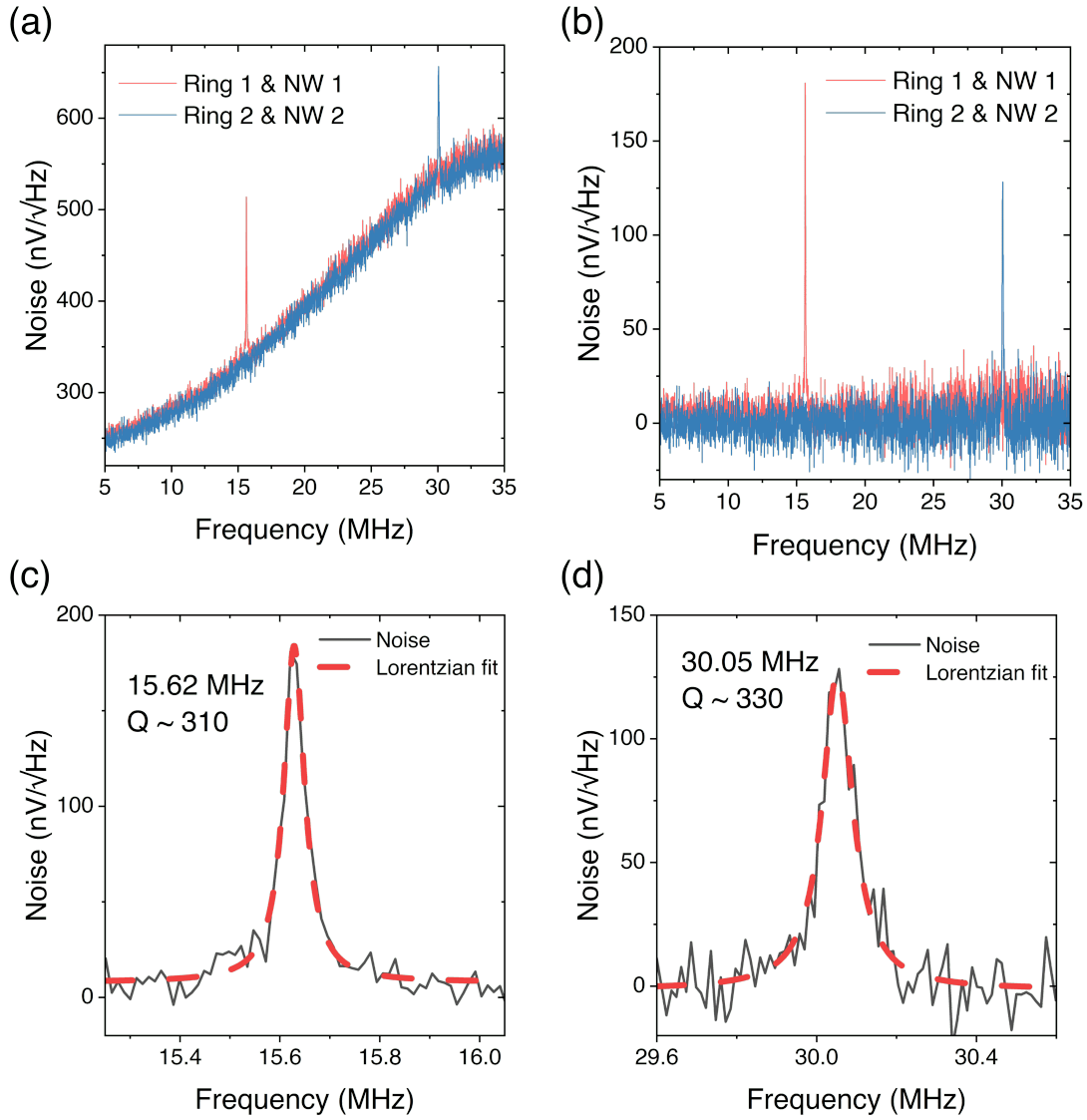


Figure 4.9: Thermal noise spectra under vacuum. (a) Thermal noise spectra of a 2-ring device measured under vacuum. (b) Thermal noise from (a) with baseline subtracted. The thermal noise spectra and Lorentzian fittings of resonances from (c) Ring 1 and NW 1 and (d) Ring 2 and NW 2.

Compared to ambient pressure, the quality factor is expected to be much higher when the device is under vacuum due to much smaller damping effect from much fewer air molecules. However, the optical transmission is also lower due to the extra losses introduced by the long optical fibres from the laser to the vacuum chamber and back, and the optical feedthroughs. As a result, the readout amplitude is likely to be similar, although the quality factors would be higher.

The thermal noise responses under vacuum from the same device used for ambient thermal noise response measurements are shown in Figure 4.9 (a). Two peaks correspond to two NWs with different suspended lengths coupled to two rings with different radii. The peak positions are similar, but the linewidths of the peaks are much smaller, suggesting a large increase in the quality factors. With the baseline subtracted, the responses, as shown in Figure 4.9 (b), are fitted with Lorentzian distributions to estimate the quality factors. The zoomed-in graphs of the resonance peaks of NW 1 and NW 2, with the baseline subtracted and Lorentzian fittings, are shown in Figure 4.9 (c) and (d). Compared with the measurements under ambient pressure, the quality factors increase from 43 to 310 for NW 1 and from 68 to 330 for NW 2. This increase is expected, as operating the NWs under vacuum significantly reduces viscous damping from the surrounding gas, thereby narrowing the mechanical resonance linewidth.

The resonant frequencies also increase slightly, from 15.36 to 15.62 MHz for NW 1 and from 28.71 to 30.05 MHz for NW 2. The thermal noise-driven resonance measured here is not a free-decay oscillation but can be seen as a forced oscillation that is continuously driven by stochastic thermal forces. Therefore, the fitted quality factor describes the resonance linewidth, whereas the resonance frequency is mainly governed by the effective stiffness and effective mass of the NW. The increase in resonant frequency should not be attributed to the increase in the quality factor, but is more likely due to the reduction in effective mass under vacuum. In ambient conditions, a thin water layer can adsorb onto the NW surface and add mass to the resonator. When the device is placed under vacuum, partial removal of this water layer reduces the effective mass. Since the resonance frequency scales as $f_0 \propto \sqrt{k_{\text{eff}}/m_{\text{eff}}}$, a reduction in effective mass leads to an increase in the measured resonance frequency [81].

The increase in the quality factor and the resonant frequency serves as evidence that the frequency responses originate from the suspended NW, rather than from other components in the system. It is further verified with thermal noise measurements of multiple devices without suspended NW, as shown in Figure

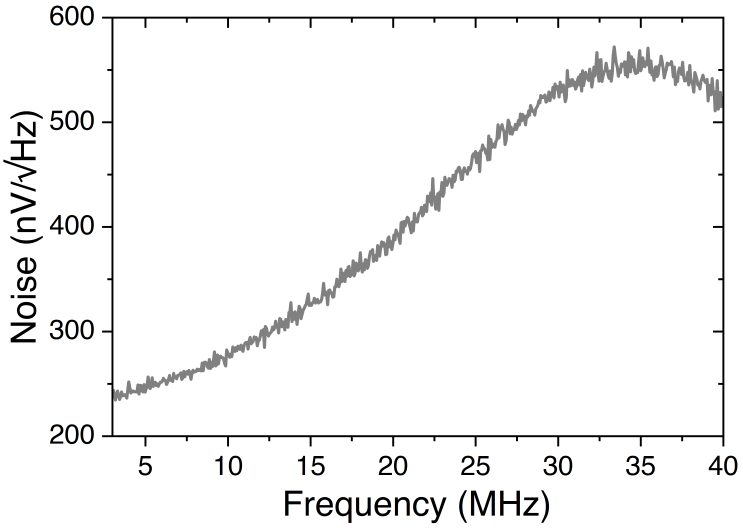


Figure 4.10: Thermal noise spectra of a device with MRR but without suspended NW. There is no resonance peak, but only the baseline from the noise floor of the PD.

4.10. The spectrum is very similar to the baseline of the thermal noise responses with NWs, but since there is no NW in this device, there is no resonant peak in this frequency range.

4.3.3 Wavelength Dependence of Response

During the measurements, it was noticed that the amplitude of the response captured by the LIA changes with wavelength within the same optical resonance dip, which is expected from the FDTD and numerical simulations, as discussed in Chapter 3. To measure how the amplitude of the LIA response changes with the wavelength of the optical input, the wavelength is first set to a specific value, and a frequency sweep within a small frequency range around the mechanical resonant frequency is performed in the LIA to measure the amplitude of the response at this wavelength. The measurement is repeated for different wavelengths of the optical input. It is also performed with thermal noise-driven and piezoelectric stack-driven systems (the same driving power is used for every measurement), and these two conditions yield similar results. The amplitude of the response is plotted against the wavelength, as shown in Figure 4.11, and the MRR spectrum is also plotted in the background for reference.

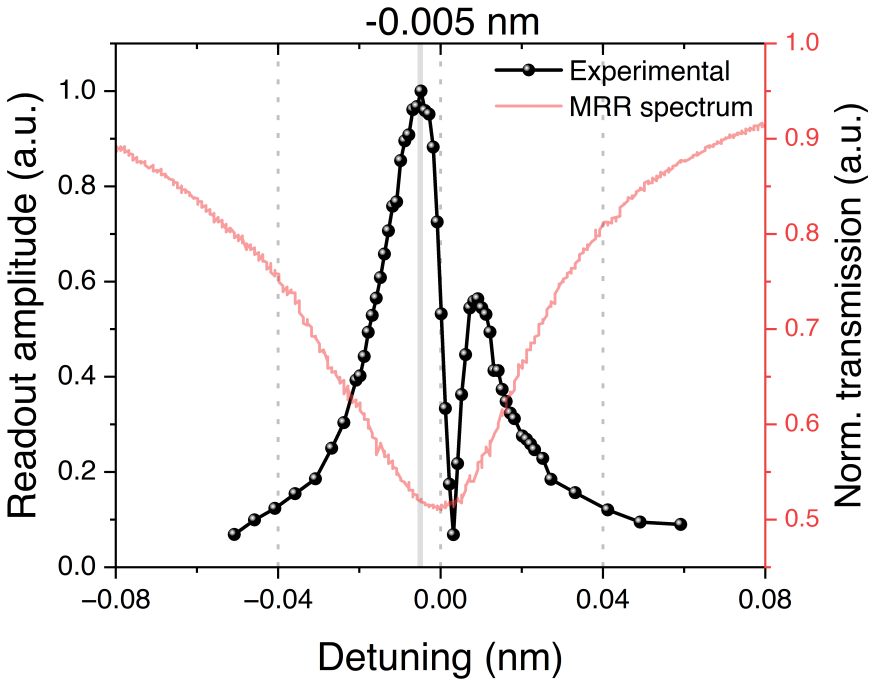


Figure 4.11: Wavelength (detuning) dependence of the response amplitude and the MRR spectrum.

The graph shows two asymmetrical maxima with a dip between them, and the left maximum is taller. Therefore, the detuning (wavelength) of the left maximum, which is slightly negative, is defined as the position of highest sensitivity. At the highest sensitivity position, the optical output of the device is most sensitive to the mechanical vibration of the NW, and thus the readout amplitude is highest. As discussed previously, the response measured by LIA is the AC component of the PD output, which is the amplitude of the alternating component of the optical output. The amplitude depends on the difference in transmission between the two extreme positions of the NW's vibration, i.e., when the NW is at peak and trough positions. The maximum readout amplitude at -0.005 nm detuning indicates that the transmission difference between the two positions of the NW at this wavelength is the largest. This result is similar to the FDTD-simulated result shown in Figure 3.4 (b) and the Lorentzian-based numerically simulated result shown in Figure 3.5 (f), where there are two maxima, and the left maximum is higher. However, although the FDTD-simulated result shows a similar pattern, the height difference

between the maxima is smaller than that of the experimental result in Figure 4.11, and therefore exhibits a smaller asymmetry. The numerically simulated result, on the other hand, is very similar to the pattern observed in the experimental results, where the left maximum is much higher than the right maxima.

The reason why the result from the FDTD simulation does not reproduce the same asymmetry as the experiment or the Lorentzian numerical model is that the two approaches represent different limits of the system response. In the FDTD simulation, the spectra are obtained for two static NW positions, and their difference represents a finite displacement response. Because the NW displacement amplitude is set to be very large (75 nm), the subtraction corresponds to a nonlinear mixing of red-shift and broadening effects. These nonlinear contributions tend to partially cancel and produce a more symmetric line shape. The FDTD difference is closer to a large-signal transmission difference, not the first-order dynamic response.

By contrast, the numerical Lorentzian model directly encodes a resonance that is both red-shifted and broadened, and then examines the difference relative to the unperturbed state. This mimics the small-signal modulation regime: a cavity perturbed simultaneously in frequency and linewidth. In this case, the difference spectrum is very close to the derivative-like signal extracted in a lock-in measurement, which naturally gives rise to two asymmetric lobes, with one side being larger. This explains why the Lorentzian-based numerical simulation matches the experiment much more closely.

Although there is no direct evidence to prove that the wavelength dependence of the readout amplitude is due to the red-shift and peak broadening when the NW is at the trough position compared to when it is at the peak position, the agreement of the experimental results with both FDTD simulations and Lorentzian-based numerical simulations suggests a possible explanation.

A similar wavelength-dependent sensitivity of the readout amplitude is observed in multiple devices. To ensure that the readout amplitude is always at the left maximum, a PLL is employed to maintain the optical input at the wavelength corresponding to the maximum readout amplitude.

Phase-Locked Loop for Micro-Ring Resonator

During the measurements of the frequency responses of the device, the laser should ideally always be at the wavelength with the highest sensitivity, which is on the left slope of the MRR spectrum with a very small negative detuning. However, since the MRR has a very high Q, the MRR spectrum is very sensitive to any changes in n_{eff} that could be caused by a slight variation in the waveguide temperature. Changes in n_{eff} induce shifts in the resonant wavelength of the MRR through Equation 3.1 which can easily move the probe wavelength away from the highest sensitivity position if there is no feedback loop controlling the probe wavelength.

During experiments under vacuum, it was found that the transmission naturally drifts when the optical power of the input is high and the wavelength is fixed at the highest sensitivity position, as shown in Figure 4.12. At first, the transmission level is around 4.5×10^{-4} mW, which is the transmission level when the wavelength is at the highest sensitivity position in a specific device. As discussed previously and shown in Figure 4.11, the highest sensitivity position has a slightly negative detuning, indicating that its wavelength is slightly lower than the centre resonant wavelength. The transmission level increases slowly over 80 seconds, as shown in Figure 4.12. Since the wavelength is set to a small negative detuning, the increase in transmission indicates a red-shift of the optical resonance and, thus, an increase in the effective index of the ring.

This behaviour is consistent with the thermo-optic effect. In an MRR, the resonant wavelength is determined by the resonance condition given in Equation 3.1. When the temperature increases, the refractive index of Si_3N_4 increases due to its positive thermo-optic coefficient [124]. This increases the effective index of the guided mode and consequently shifts the MRR resonance to a longer wavelength. The thermo-optic coefficient is defined as $\frac{\mathrm{d}n}{\mathrm{d}T}$, and the corresponding resonance shift can be estimated as:

$$\frac{\Delta\lambda}{\lambda_0} \approx \frac{1}{n_{\text{eff}}} \frac{\mathrm{d}n_{\text{eff}}}{\mathrm{d}T} \Delta T, \tag{4.2}$$

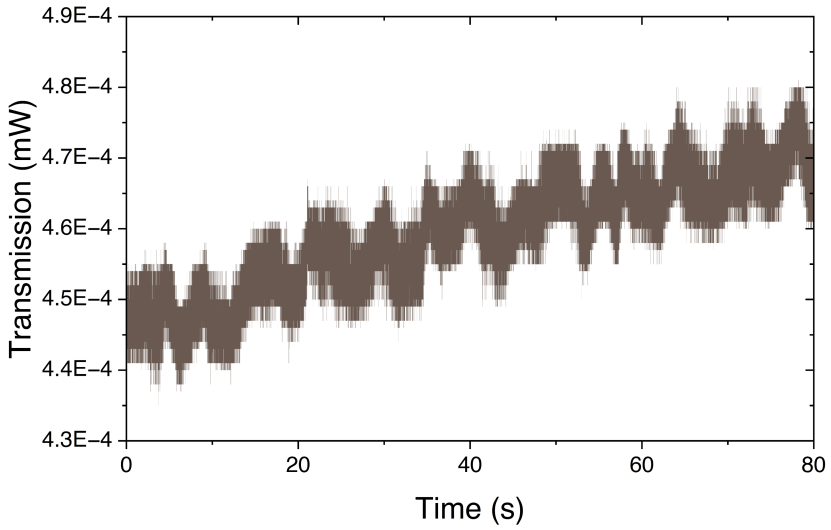


Figure 4.12: Drift of transmission when the wavelength of the optical input is set to the highest sensitivity position, which has a small negative detuning and is very close to the resonant wavelength, under vacuum environment.

From Figure 4.12, the transmission level increased from $(4.48 \pm 0.07) \times 10^{-4}$ mW to $(4.71 \pm 0.09) \times 10^{-4}$ mW over 80 seconds, giving a transmission change of around 0.23×10^{-4} mW. In an MRR similar to the one shown in Figure 4.11, this transmission change indicates a wavelength red-shift of approximately 0.005 nm. Using $\lambda_0 \approx 1510$ nm, $n_{\text{eff}} \approx 2.0$, and $\mathrm{d}n/\mathrm{d}T \approx 2.45 \times 10^{-5}$ K^{-1} for Si_3N_4, the temperature change can be estimated as [124]:

$$\Delta T \approx n_{\text{eff}} \frac{\Delta\lambda}{\lambda_0} \div \frac{\mathrm{d}n_{\text{eff}}}{\mathrm{d}T} \approx 2.0 \times \frac{0.005}{1510} \div (2.45 \times 10^{-5}) \approx 0.27 \text{ K} \tag{4.3}$$

This corresponds to an effective thermal tuning coefficient of approximately 18.5 pm/K. This estimate is only approximate since the measured thermo-optic response depends on the modal overlap with Si_3N_4, SiO_2, air, the InP NW, and any residual materials near the optical mode. It indicates that the measured resonance drift is compatible with a small but measurable temperature increase in the MRR.

The slow red-shift is likely caused by the optical absorption of structural defects, as well as organic residues or particles introduced during the pick-and-place process. These imperfections can form localised absorption sites even when the bulk Si_3N_4 waveguide has intrinsically low optical loss [125, 126]. Under the highest optical

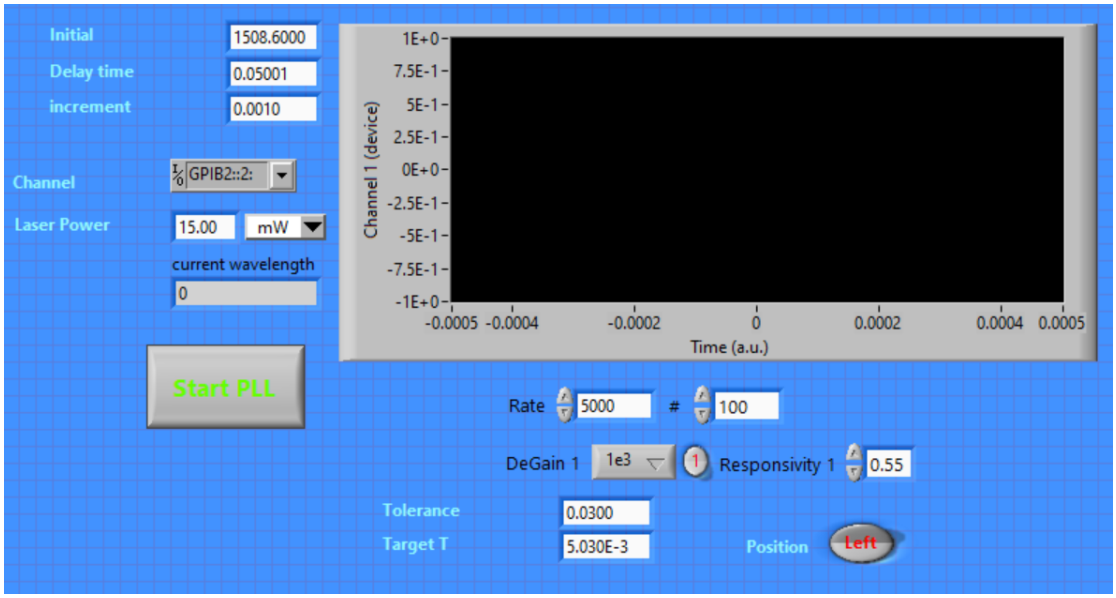


Figure 4.13: The user interface for the PLL LabVIEW VI. The loop maintains a fixed transmission (hence detuning) by adjusting the laser wavelength, locking to the left-slope maximum sensitivity point.

input power used here, 15 mW, and under vacuum conditions, such localised heating becomes more evident because heat removal through the surrounding gas is suppressed.

Under vacuum, convective cooling is eliminated, and thermal conduction becomes the dominant heat removal pathway. However, this pathway is limited by the relatively low thermal conductivity of the Si_3N_4 film (≈ 2.7 W m^{-1} K^{-1}) and the underlying silicon oxide layer (≈ 1.4 W m^{-1} K^{-1}) [127, 128]. Consequently, the thermal time constant of the system is increased, resulting in a gradual build-up of temperature within the MRR. This produces the observed slow red-shift of the optical resonance as heat diffuses through the nitride–oxide–silicon stack and into the surrounding chip assembly.

Therefore, a PLL is designed and used in most measurements that is responsible for locking the probe wavelength always at the highest sensitivity position. The PLL is based on National Instruments LabVIEW, which is a PC software that is responsible for receiving data from the DAQ board and giving commands to multiple pieces of equipment via GPIB cables. The user interface of the PLL VI (LabVIEW code file) is shown in Figure 4.13. To implement the PLL, the set-up is

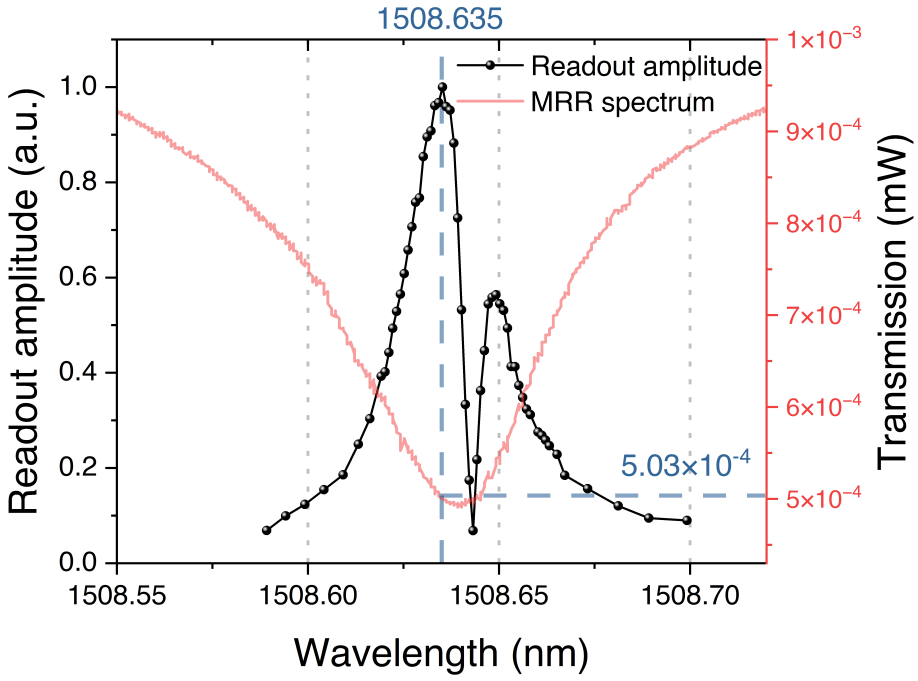


Figure 4.14: Wavelength dependence of the response amplitude and the MRR spectrum in absolute transmission.

configured so that the PD output of the 10% split light is sent to the DAQ board. A normal wavelength sweep is run to collect the entire spectrum of the device, and a high transmission resonance dip is chosen for the input wavelength window. The graph in Figure 4.11 is re-plotted in Figure 4.14 with actual transmission and wavelength instead of normalised transmission and detuning to better illustrate the PLL. From the experimental result, it is realised that the -0.005 nm detuning or 1508.635 nm gives the largest readout amplitude, and from the MRR spectrum, the transmission at this wavelength is 5.03×10^{-4} mW. The overall transmission level is relatively low due to the loss from the long optical fibres and vacuum feedthroughs, and only 10% of the optical output is received and used for the PLL.

To run the VI, parameters need to be set properly first. The correct GPIB channel is chosen, and a laser power is input, usually at 15 mW (maximum power of the Santec laser). Then a starting wavelength is chosen, and here 1508.600 nm is selected and input into the 'initial' box in the VI. Any wavelength on the left slope of the resonant dip can be chosen, as the VI will gradually adjust the wavelength to

the highest sensitivity position. The 'Target T' box is for the targeted transmission level, and the transmission of the MRR when the optical input is at the highest sensitivity position, 5.03×10^{-3} mW, should be input here. The 'tolerance' box is to set the proportion tolerance for the targeted transmission level, and 0.03 is set as the tolerance here. Since the transmission is unlikely to always be exactly 5.03×10^{-3} mW, a tolerance is necessary, and the VI will only shift the wavelength if the transmission falls outside of $5.03 \times 10^{-3} \times (1 \pm 3\%)$ mW. 'DeGain' is the gain setting of the PD, which is now 1000, and it should match the actual gain of the PD. 'Responsivity' is the responsivity coefficient of the PD, which is 0.55 for the specific PD. 'Rate' is the data collection rate of the PD and is usually set as shown (5000). 'Position' indicates which slope the wavelength is on in the resonance dip, and since the highest sensitivity is on the left slope, it is usually set as 'left'.

The main operation behind the VI is an if loop. When all the settings are input, the 'Start PLL' button is clicked, and the laser is set to the initial wavelength (1508.600 nm), power (15 mW), and is switched on. The reading from the PD would be collected, multiplied by the gain and the responsivity, and plotted in the main window against time. Now, the 'if loop' is executed, if the transmission calculated from the PD reading is larger than the tolerance range, the wavelength is likely to be high up the slope, and the detuning is too negative. Thus, the wavelength would be increased to approach the resonant dip and decrease the magnitude of detuning. In contrast, if the transmission is smaller than the tolerance range, the wavelength is too close to the resonance dip, and the detuning is not negative enough, and thus the wavelength would be decreased to increase the magnitude of detuning. Otherwise, if the transmission is within tolerance, the wavelength would not be changed. If 'Position' is set to 'right', the direction of wavelength shifts would be reversed. The 'if loop' effectively maintains the detuning when the resonant wavelength shifts by tracking the transmission level and changing the wavelength until the transmission level matches the input 'Target T' within 'Tolerance'. 'Increment' specifies the step of wavelength change, and 'Delay time' specifies the time gap between each check of whether the transmission level is within tolerance.

For example, if the initial wavelength is 1508.600 nm, as shown in Figure 4.13, the transmission should be around 7.3×10^{-3} mW, which is larger than the target transmission with a tolerance of $5.03 \times 10^{-3} \times (1 \pm 3\%)$ mW. Therefore, in the first loop, the wavelength would be increased to 1508.601 nm, which is the initial wavelength plus one increment of 0.001 nm. The transmission would still be higher than the target, so the wavelength would be increased to 1508.602 nm after an interval of 0.05 s. The wavelength would be increased until the transmission is within tolerance, then the transmission would still be checked every 0.05 s. If the resonance shifts and moves the transmission level outside the tolerance, the programme would adjust the wavelength again back to the correct detuning.

To eliminate the effect of the resonance shift due to the thermo-optic effect and to maintain the highest sensitivity, the PLL is always active for the measurements made for thermal noise, driven responses, and the subsequent filter demonstration.

4.3.4 Driven Response

Although the resonances of the NWs can be readout using frequency responses from thermal noise driven resonances, it is difficult to encode light with any information. Since the driving force from thermal noise is difficult to control, inputting information as thermal fluctuations is challenging and unrealistic. Additionally, and the driving force from thermal fluctuations is relatively small, resulting in a very low readout amplitude. Therefore, indirect piezoelectric actuation through PZT is adopted here to provide a larger and more controllable actuation method, where information to encode can be input as an electrical voltage to the PZT. Before the information is input to the PZT to demonstrate the filtering and encoding capabilities, the frequency response of the NW under simple sinusoidal PZT actuation is measured.

The set-up for driven response measurements is shown in Figure 4.15. Compared to the set-up used for noise measurements, the output of the LIA is sent to a 45 dB high power amplifier (HPA) (Mini-Circuits) to drive the PZT and the vibration of the NWs. The output of the LIA is a continuous sinusoidal wave with a set frequency of up to 50 MHz and an amplitude of up to 10 V. However, operating the LIA at high

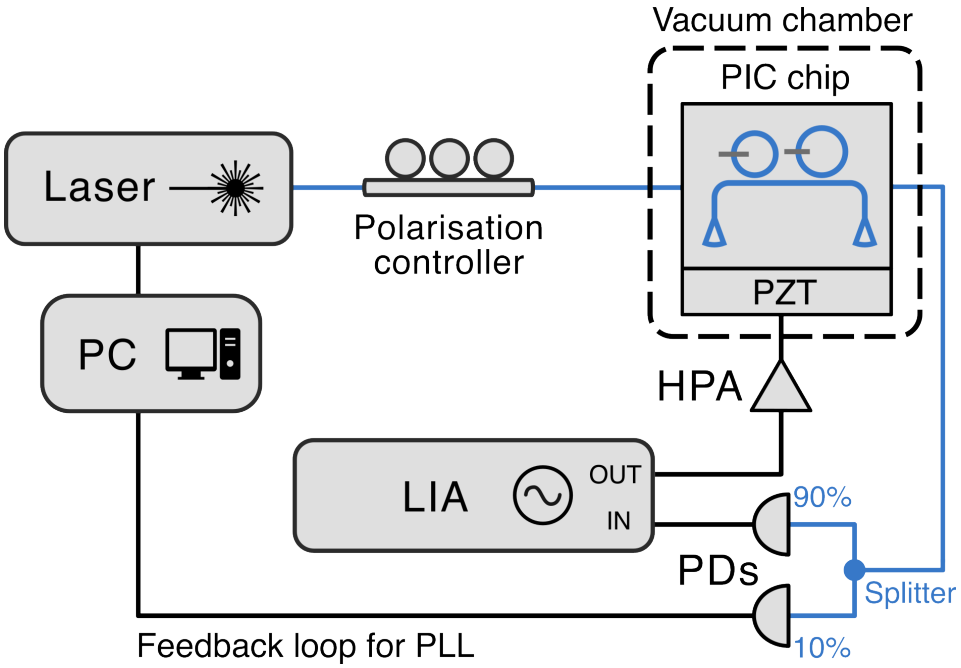


Figure 4.15: Schematics showing the experimental set-up that is used to measure PZT-driven frequency response of the device under vacuum with the PLL.

output voltage levels compromises signal integrity due to increased output impedance at high frequencies, current limitations when driving capacitive PZT loads, and thermal noise that degrades the SNR [129]. Additionally, the impedance mismatch between the LIA's frequency-dependent output impedance and the capacitive PZT load creates signal reflections and reduces power transfer efficiency, particularly at high frequencies where parasitic effects become significant [130]. Using the HPA allows the LIA to operate in its optimal low-distortion range while providing the necessary high-current drive capability specifically designed for capacitive loads, ensuring stable low-noise operation across the full frequency range [131].

The driven responses of the two MRRs with two NWs, using the frequency response sweep function of the LIA, are shown in Figure 4.16 (a). The output amplitude of the LIA is set to 5 mV, and it will be amplified to 0.889 V by the 45 dB HPA and sent to the PZT as the driving voltage. The noise observed between 5 and 13 MHz originates primarily from the coupling of the piezoelectric actuator into multiple mechanical and electrical paths within the bonded assembly. First, although the assembly of the PZT chip, epoxy for bonding the fibre array and

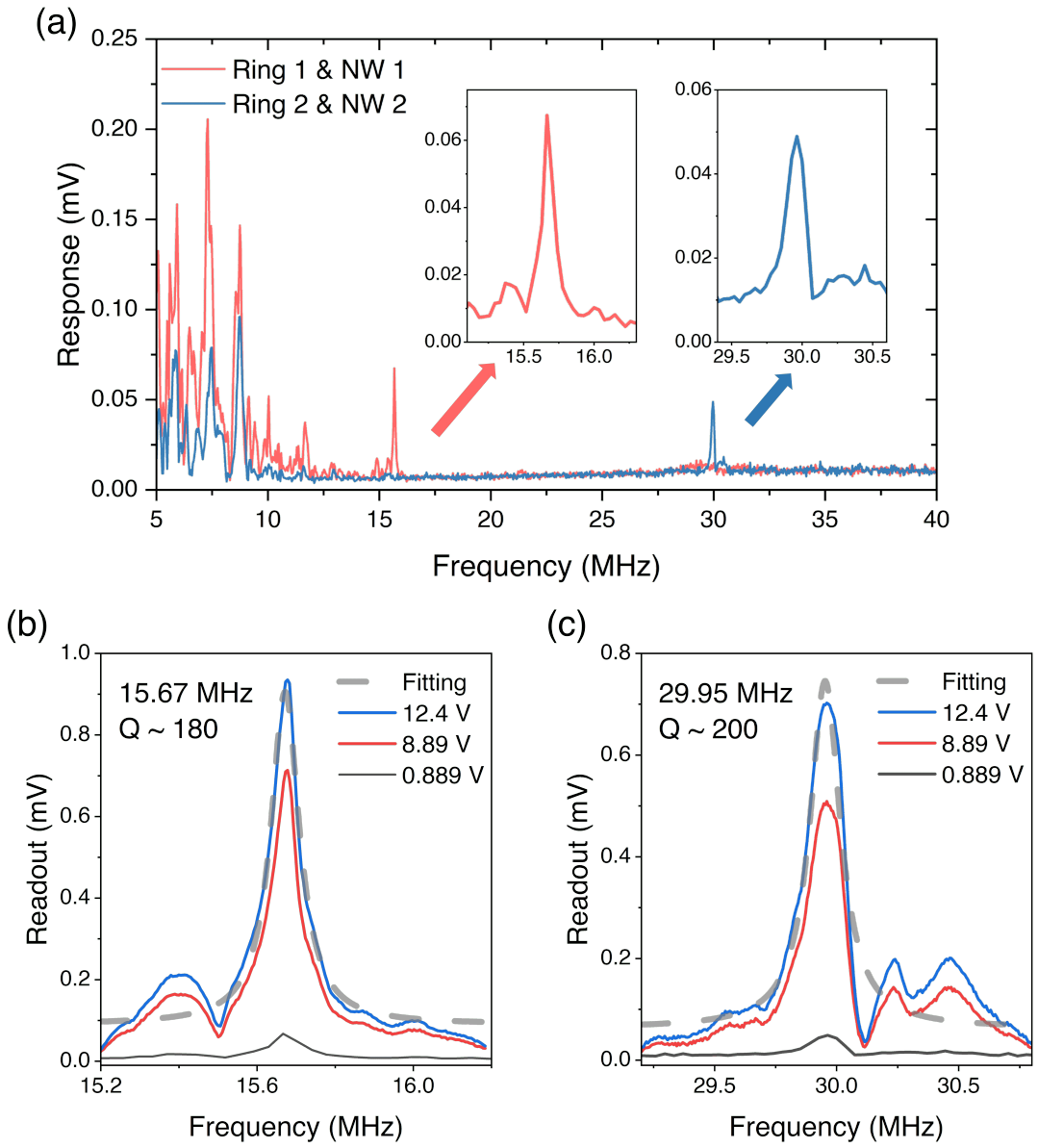


Figure 4.16: Driven responses of the device. (a) Driven responses of the two MRRs with two NWs over a large range with a driving voltage of 0.889 V. The peaks from 5 to 13 MHz are noise from the vibration of the assembly and spurious modes of the PZT chip. The peaks around 15.6 and 30.0 MHz are the driven responses of the NWs. Driven responses of: (b) Ring 1 & NW 1; (c) Ring 2 & NW 2, with larger driving amplitudes, higher resolution, and Lorentzian fitting.

the PZT to the photonic chip, the photonic chip, the fibre array, and the PCB is macroscopically bulky compared to the NW, its constituent layers support flexural and plate modes whose characteristic dimensions lie in the sub-mm to mm range, corresponding to natural frequencies in the low-MHz domain [81, 132]. These modes are readily excited under sinusoidal driving. Since the NW motion is transduced with the PIC, vibrations of the assembly modulate the fibre-grating coupler alignment and distance, and induce strain in the waveguides, which modulates the effective refractive index, thereby fluctuating the through port output of the MRR [133, 134]. Such mechanically induced optical intensity variations are indistinguishable from genuine NW-induced modulation at the PD, and hence appear in the LIA output as broadband noise. In addition, higher-order PZT resonances and lateral modes, even though the fundamental is sub-MHz (around 390 kHz), extend into the MHz range and further contribute to the noise [135, 136].

From Figure 4.16 (a), the shapes of the noise spectra from 5 to 13 MHz are similar, but the amplitudes are different, with Ring 1 and NW 1 showing larger noise amplitudes. Although the two MRR-NW systems experience the same assembly-driven background vibrations, the noise amplitudes detected in each channel differ because of variations in their optomechanical transduction pathways. First, the broadband features observed between 5-13 MHz primarily originate from the common-mode motion of the bonded assembly (PZT-adhesive-chip-fibre-PCB) rather than from the NW eigenmodes. Each MRR transduces this motion with a different gain $G = \mathrm{d}T/\mathrm{d}x$ owing to distinct coupling conditions and resonance slopes, and hence different background amplitudes cross the two channels [137, 138]. Second, the displacement of the NW would be enhanced when the assembly or other components are resonating, giving frequency responses even when they are not at their resonant frequency. Additionally, the NWs have different suspended lengths and effective masses, which modify their mechanical susceptibility to substrate motion and hence the degree to which assembly vibrations are transferred into the optical mode [81].

In addition to noise, two peaks could be found around 15.6 MHz and 30.0 MHz, which correspond to Ring 1 & NW 1 and Ring 2 & NW 2, as shown in the insets of Figure 4.16 (a). These frequencies are very close to the frequency found when measuring the thermal noise spectra, which confirms that they are the readouts of the driven resonances of the NWs. To better characterise the resonances, the driving voltage was increased, and frequency sweeps were performed with higher resolution. The LIA output amplitude was set to 50 and 70 mV, which are amplified to 8.89 and 12.4 V, respectively, and the driven frequency responses of the two resonances are shown in Figure 4.16 (b) and (c). The resonances with the largest driving voltage are also fitted with the Lorentzian equation to find the centre frequencies and quality factors. The centre frequencies 15.67 and 29.95 MHz are very close to the frequencies found in thermal noise measurements, 15.62 and 30.05 MHz, but the quality factors 180 and 200 are smaller than 310 and 330. Furthermore, the resonance peaks of thermal noise yield near-ideal Lorentzian line shapes, while the peaks of the driven response are asymmetrical and distorted from the ideal Lorentzian line shape.

This is because Brownian motion provides a broadband, stochastic drive that couples uniformly to the mechanical mode without introducing external distortions. Under such conditions, the resonator is excited within its linear regime, and the observed spectrum reflects the intrinsic mechanical susceptibility, preserving both the symmetry and the quality factor of the mode [81, 139]. By contrast, piezoelectric actuation introduces several non-idealities through its indirect coupling via the substrate. Energy is transferred from the actuator to the NW through bonding interfaces and the supporting chip, which creates additional dissipation channels and frequency-dependent coupling efficiencies [135]. Spurious substrate and adhesive modes are often excited in parallel, leading to asymmetric line shapes and background fluctuations that distort the fundamental Lorentzian profile. Moreover, finite mechanical impedance mismatches between the PZT, adhesive, and substrate produce phase shifts and amplitude modulations that broaden the apparent linewidth and reduce the effective peak amplitude. As a result, the effective quality factor measured under PZT drive is lower than the intrinsic value

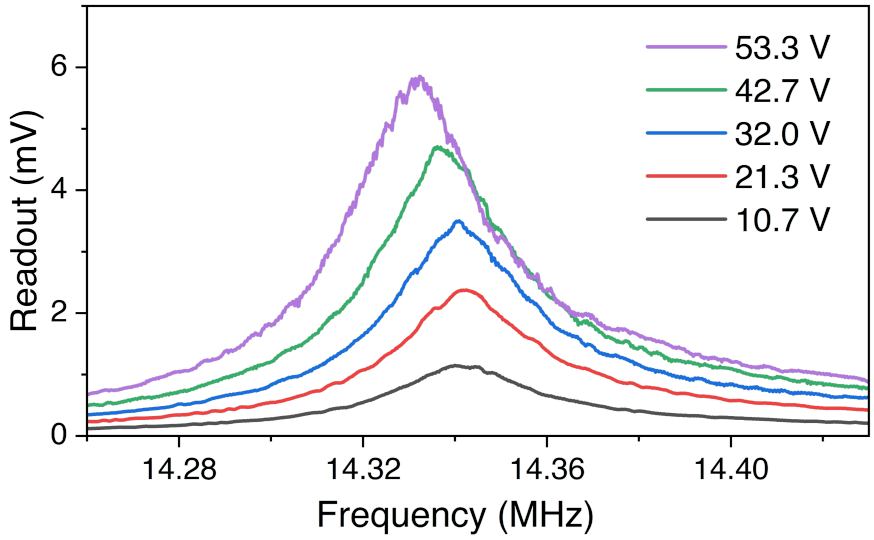


Figure 4.17: Driven responses of a device with driving voltage up to 53.3 V. The readout amplitude stays linear with the driving voltage until the assembly breaks when the driving voltage increases beyond 53.3 V.

because additional loss pathways and mode mixing increase the total damping rate experienced by the NW [80].

Higher Driving Voltage and Duffing Nonlinearity

Duffing nonlinearity describes the deviation of a mechanical resonators response from the symmetric Lorentzian line shape when it is driven into the large amplitude regime [140]. In the framework of Euler-Bernoulli beam theory, the restoring force of a slender beam is primarily governed by its flexural rigidity, and the relationship between displacement and restoring force remains linear only for small deflections. As the oscillation amplitude increases, geometric nonlinearities emerge due to mid-plane stretching, introducing an additional cubic term into the effective spring constant. This modification causes a shift in the resonance frequency with amplitude, which is typically hardening for tensile-dominated systems and softening for compressive ones. In nanomechanical systems, the observation of Duffing behaviour is of particular interest, as it not only validates the nonlinear elastic response predicted by beam theory but is also widely regarded as an indicator of high-quality devices with precise control over their dynamic range [141, 142].

To investigate the Duffing nonlinearity in the device, the InP NW is driven with high voltages, and the frequency responses under high driving voltages are shown in Figure 4.17. Since the driving frequency (5-30 MHz) is well above the recommended frequency range of the PZT chip, driving the PZT at high voltages may cause the generation of excessive heat that could melt the adhesives and lead to irreversible damage. Therefore, the measurements were performed on another device to prevent damaging the main device, so the resonance line shape and the resonant frequency in Figure 4.17 are different from the previous results. The LIA output amplitude is set from 60 to 300 mV, and the amplified voltage ranges from 10.7 to 53.3 V. The response amplitude changes linearly with the driving voltage across the range, and the line shape does not show any Duffing-like features. The device stopped giving a readout when the voltage was above 53.3 V. After removing the assembly from the vacuum chamber, the adhesives bonding the fibre array, the photonic chip, and the PZT chip were found to be melted, breaking the assembly. The PZT chip was also found to be delaminated, with the adhesives melted. As a result, 53.3 V was the highest driving voltage that could be applied to the chip, but the NW displacement did not reach the Duffing threshold under this driving voltage.

The absence of the Duffing response can be attributed to several factors. First, the pick-and-place transfer process and clamping likely introduce large axial tension in the NW, which increases the effective linear stiffness and suppresses the relative contribution of geometric nonlinearity, thereby pushing the Duffing threshold amplitude beyond the accessible range. Second, the energy transfer from the piezoelectric actuator to the NW is indirect and mediated by the substrate. As a result, the effective modal forcing is smaller than what the driving voltage suggests, keeping the displacement below the Duffing threshold. Finally, the relatively small quality factor of the device limits the maximum achievable amplitude by dissipating energy into the substrate and bonding layers, further ensuring that the NW remains in the linear regime even under strong driving. Together, these factors explain why the resonance retains its Lorentzian profile across all driving voltages explored in this study.

In Figure 4.17, the centre frequency of the resonance shifts downward as the driving voltage increases. The observed decrease in resonant frequency may be attributed to a heating-induced softening effect. At high driving voltages and frequencies, the PZT chip dissipates electrical energy as heat due to dielectric losses and internal friction [135, 136]. This local heating can be transferred through the substrate and bonding layers to the NW, leading to an increase in its temperature. As the elastic modulus of InP decreases with temperature, the effective stiffness of the NW is reduced, resulting in a downshift of the resonance frequency [81].

The magnitude of this temperature rise can be estimated from the measured frequency shift. According to Equation 3.3, the resonance frequency scales approximately as:

$$f_0 \propto \sqrt{E}, \tag{4.4}$$

where E is the Young's modulus of the NW. Therefore, if the geometry and density of the NW are assumed to remain unchanged, the Young's modulus at the lower resonance frequency can be estimated as:

$$E_1 = E_0 \left(\frac{f_1}{f_0}\right)^2. \tag{4.5}$$

Taking the Young's modulus of InP at room temperature to be $E_0 = 65$ GPa, and using the measured resonance frequencies $f_0 = 14.343$ MHz and $f_1 = 14.331$ MHz, this gives [103]:

$$E_1 = 65 \text{ GPa} \left(\frac{14.331}{14.343}\right)^2 \approx 64.891 \text{ GPa}. \tag{4.6}$$

The corresponding change in Young's modulus is therefore -0.109 GPa.

To convert this modulus change into an estimated temperature rise, the temperature-dependent elastic properties of InP reported by Branicio *et al.* are used as a guide [143]. Their molecular-dynamics calculations show that the Young's modulus of InP decreases with temperature with a coefficient $\frac{\mathrm{d}E}{\mathrm{d}T}$ of -0.040 GPa/K. Therefore, the temperature rise of the NW can be estimated as

$$\Delta T = \frac{\Delta E}{\mathrm{d}E/\mathrm{d}T} = \frac{-0.109 \text{ GPa}}{-0.040 \text{ GPa/K}} \approx 2.7 \text{ K}. \tag{4.7}$$

This estimate should be interpreted cautiously. It assumes that the frequency shift is caused only by the temperature-dependent softening of the InP Young's modulus, using a coefficient inferred from bulk-like simulations, and neglects possible changes in residual stress, clamping conditions, substrate expansion, and the piezoelectric actuation pathway. Since the device assembly failed at the highest driving voltage, the actual temperature rise in parts of the assembly may be higher than this estimate.

4.4 Filtering and Encoding Capabilities

After characterising the driven responses of the device, its performance under sinusoidal drive was determined. The next step would be to send signals composed of different frequencies to the device and characterise the multi-channel filtering and multi-wavelength encoding capabilities.

The experimental set-up used to demonstrate the filtering capability is shown in Figure 4.18 (a). Similar to the set-ups used previously, the PIC chip and the PZT chip are inside the vacuum chamber, and the optical output is split for LIA analysis and the PLL. However, the signal sent to the HPA is no longer the sine wave from the LIA output. Instead, two different audio signals, Audio 1 and Audio 2, are prepared and sent from the arbitrary wavefront generator (AWG) and mixed with sine waves at frequencies f_1 and f_2 (15.67 and 29.95 MHz, the resonant frequencies of NW 1 and NW 2 found from driven response measurements) using two frequency mixers (ZLW-6+, Mini-Circuits). Effectively, the two audio signals are amplitude modulated (AM) with f_1 and f_2. In the experiment, the two sine waves from the local oscillators (LOs) are outputs of the LIA, but they do not necessarily have to be from the LIA, since the phase does not matter.

To obtain a higher readout amplitude for better SNR than the measured driven response of around 1 mV, the input amplitude should be increased. In the driven response measurement, an input of 12.4 V gave rise to a readout amplitude of around 1 mV. If a higher amplitude readout of 3 mV is desired for a larger SNR, the input should be increased to 37.2 V, and the amplitude of the AM signal before the 45 dB

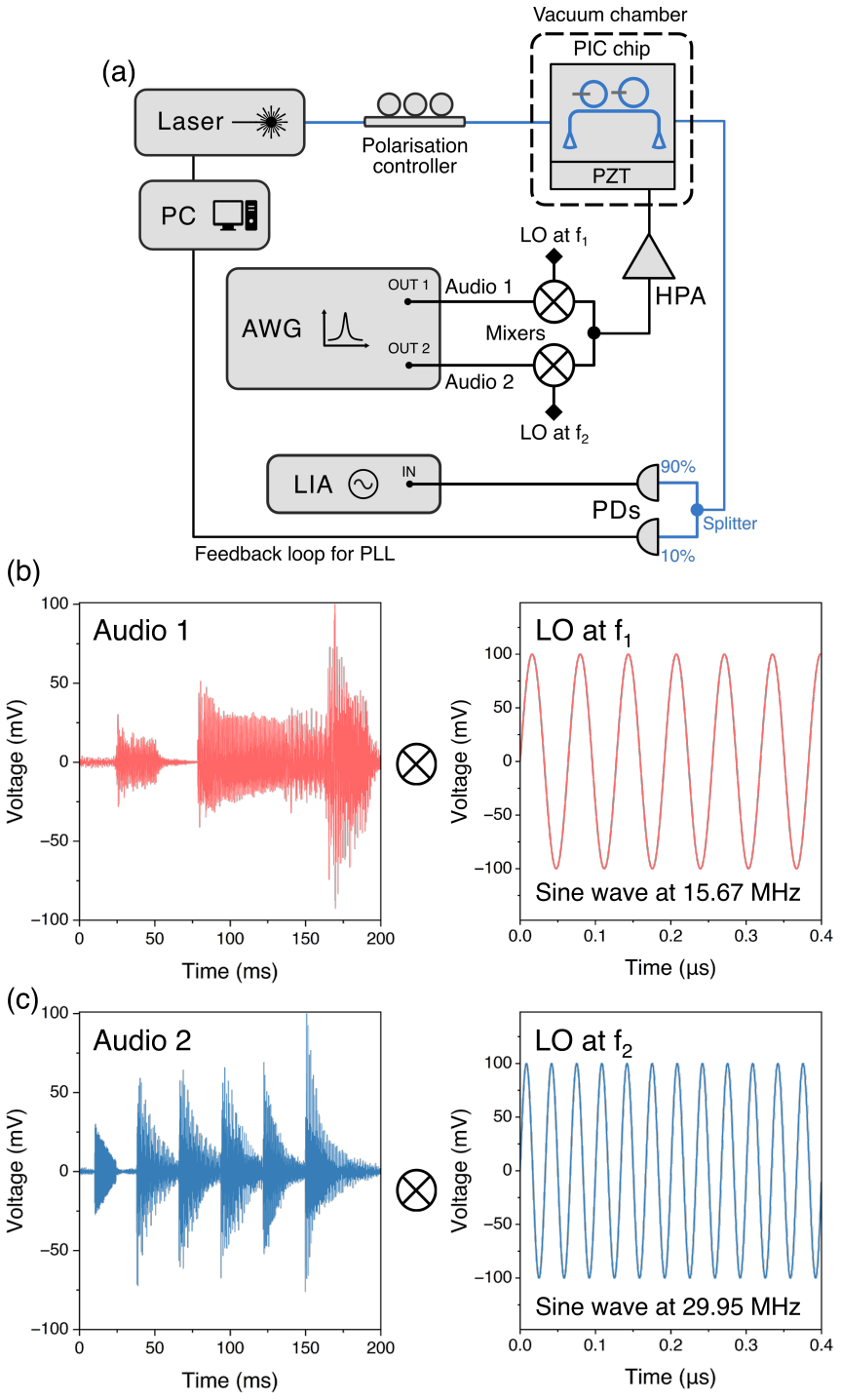


Figure 4.18: Filtering and encoding capability experiment. (a) Schematics showing the experimental set-up that is used to show the filtering and encoding capabilities of the device. AWG: arbitrary wavefront generator; LO: local oscillator. (b) Prepared Audio 1 signal with an amplitude of 100 mV (output from the AWG) that would be mixed with the sine wave at f_1, 15.67 MHz, with an amplitude of 100 mV (output from the LIA) by one of the frequency mixers. (c) Prepared Audio 2 signal with an amplitude of 100 mV that would be mixed with the sine wave at f_2, 29.95 MHz, with an amplitude of 100 mV by the other frequency mixer.

voltage amplification by the HPA should be $37.2 \div 10^{45/20} = 0.209$ V. Therefore, the amplitudes of the audio signals and sine waves should be around 100 mV for a 100% modulation depth and an AM signal with an amplitude of around 200 mV. The two audio signals and the corresponding sine waves at f_1 and f_2 are shown in Figure 4.18 (b) and (c). The two audio signals last for 200 ms, and both are composed of 6000 data points. After mixing, the two AM signals are added electrically using a BNC T connector and sent to the HPA as the electrical input to the PZT. This input drives the PZT to vibrate at both f_1 and f_2. Ideally, NW 1 would only react to vibration at f_1 and encode light in Ring 1 with Audio 1; similarly, NW 2 would only react to vibration at f_2 and encode light in Ring 2 with Audio 2.

The optical part of the set-up is identical to the set-up used in the previous measurements. Previously, the LIA was set to sweeper mode, where the local oscillator (LO) frequency was swept over a range to characterise frequency responses. Instead, the LIA is set to plotter mode to plot the in-phase (X) and quadrature (Y) components of the demodulated input signal in the time domain so that the original time domain audio signals can be retrieved and reconstructed. However, the bandwidth of the LPF needs to be carefully chosen so that the audio signal is fully preserved within the passband while unwanted high-frequency components and carrier residuals are effectively suppressed, ensuring accurate recovery of the envelope without introducing distortion or excessive noise. The effective bandwidth of the audio signal is determined by the sampling rate of the original recording. Since the envelope signals were digitised at approximately 6000 **Sa** $\div$ 200 **ms** = 30 **kSa/s**, the Nyquist theorem dictates that the highest frequency component that can be represented without aliasing is half of this value, around 15.0 kHz [144]. Consequently, the spectral content of the audio is inherently confined to the range of 0-15.0 kHz, and any system used for modulation or demodulation must accommodate this bandwidth to ensure the accurate recovery of the original information. The LPF should be wide enough to pass this entire 0-15.0 kHz range without significant distortion while still suppressing higher frequency noise components; thus, 20 kHz would be a good choice.

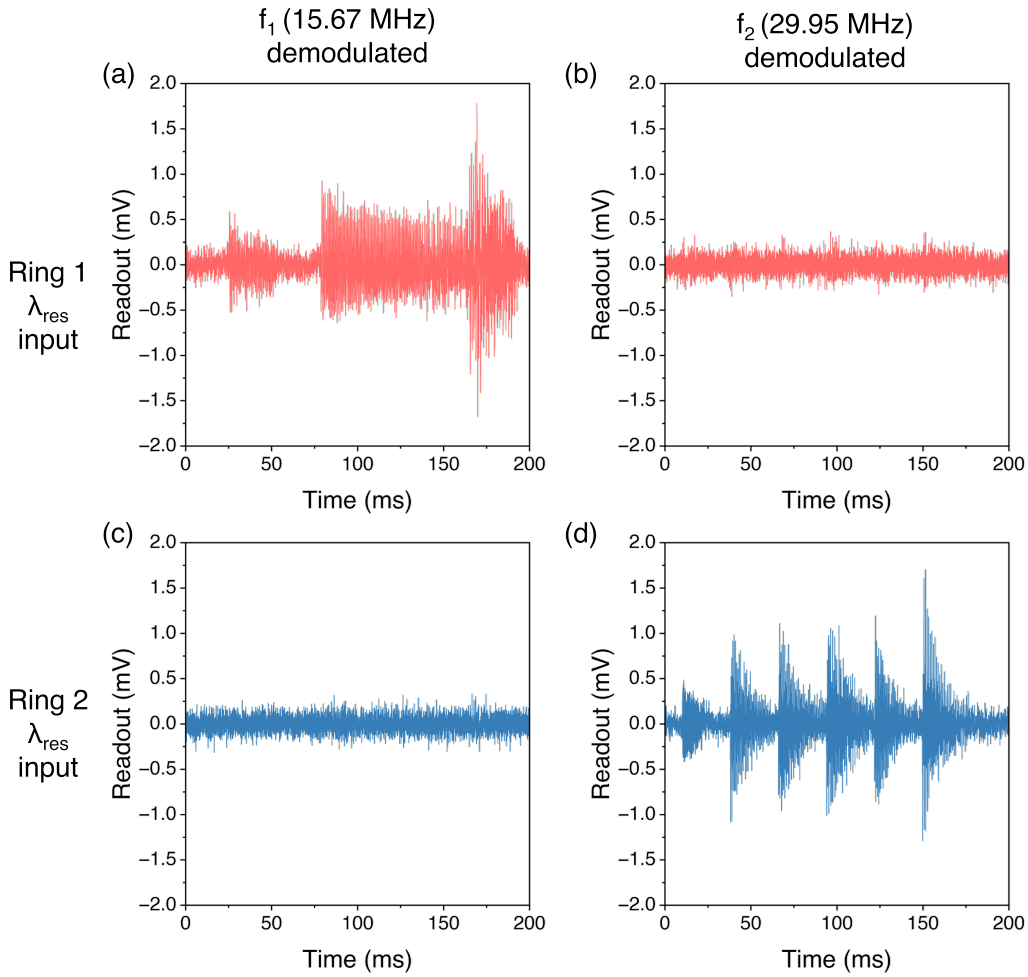


Figure 4.19: Time-domain demodulated outputs. (a,b) Optical input at Ring 1's resonant wavelength: demod at f_1 recovers Audio 1; demod at f_2 shows slight leakage. (c,d) Optical input at Ring 2's resonant wavelength: demod at f_1 shows only noise; demod at f_2 recovers Audio 2.

The data transfer rate should also be carefully chosen as the choice of data transfer rate must ensure that the demodulated audio signal is sampled with sufficient temporal resolution. However, a data rate set too high could overwhelm the system's ability to handle the data stream and cause packet loss. Since the audio envelope extends up to approximately 15.0 kHz, the Nyquist criterion requires a minimum transfer rate of twice this value. However, in practice, a significantly higher rate is advisable to avoid distortion and aliasing and to represent transient variations accurately. A transfer rate in the range of 200-250 kSa/s, therefore, provides a safe margin above the minimum requirement, ensuring that the full

audio spectrum is captured reliably while maintaining compatibility with the HF2LI LIA streaming capabilities.

Firstly, the optical input is set to one of Ring 1's λ_{res} to send light into Ring 1 and encode the light by the vibration of NW 1 at f_1. The demodulator frequency of the LIA is set first to f_1 and then to f_2 to demodulate any signals at f_1 and f_2 from the optical output. Secondly, the optical input is set to one of Ring 2's resonant wavelengths, and the same procedure is repeated. The demodulated signals from different input wavelengths and demodulation frequencies are shown in Figure 4.19. (a) and (b) display the demodulated outputs when the optical input is set to one of Ring 1's resonant wavelengths. When it is demodulated at f_1, Audio 1 can be retrieved, while it is demodulated at f_2, there is mostly the noise floor. There could be some leakage of Audio 2 in (b), indicated by spikes corresponding to the peaks in Audio 2. This is due to the slightly higher amplitude of Ring 1 & NW 1's driven response than the noise floor around f_2, as shown in Figure 4.16 (a). However, the amount of leakage is relatively low and could be avoided by a more efficient actuation method, such as local piezoelectric actuation. (c) and (d) show the demodulated outputs when the optical input is set to one of Ring 2's resonant wavelengths and only show Audio 2 when it is demodulated at f_2. When it is demodulated at f_1, there is only the noise floor. The retrieved audio signals retain the general shapes of the original signals with a loss of some details, and the amplitudes of the demodulated signals are approximately 2 mV, as expected. The successfully retrieved audio signals using different wavelengths demonstrate the 2-channel RF filtering and 2-wavelength optical encoding capability of the device.

The original and filtered signals are plotted in parallel in Figure 4.20 (a) and (c), and parts of them are zoomed in and plotted in (b) and (d) for a detailed comparison. The high amplitude fractions are well retrieved with good overlap with the original signal, but the low amplitude fractions are flooded with the noise floor of the device. The noise floor of the device comes mainly from the same source as in driven responses, i.e., coupling among the PZT drive, mechanical, and electrical paths.

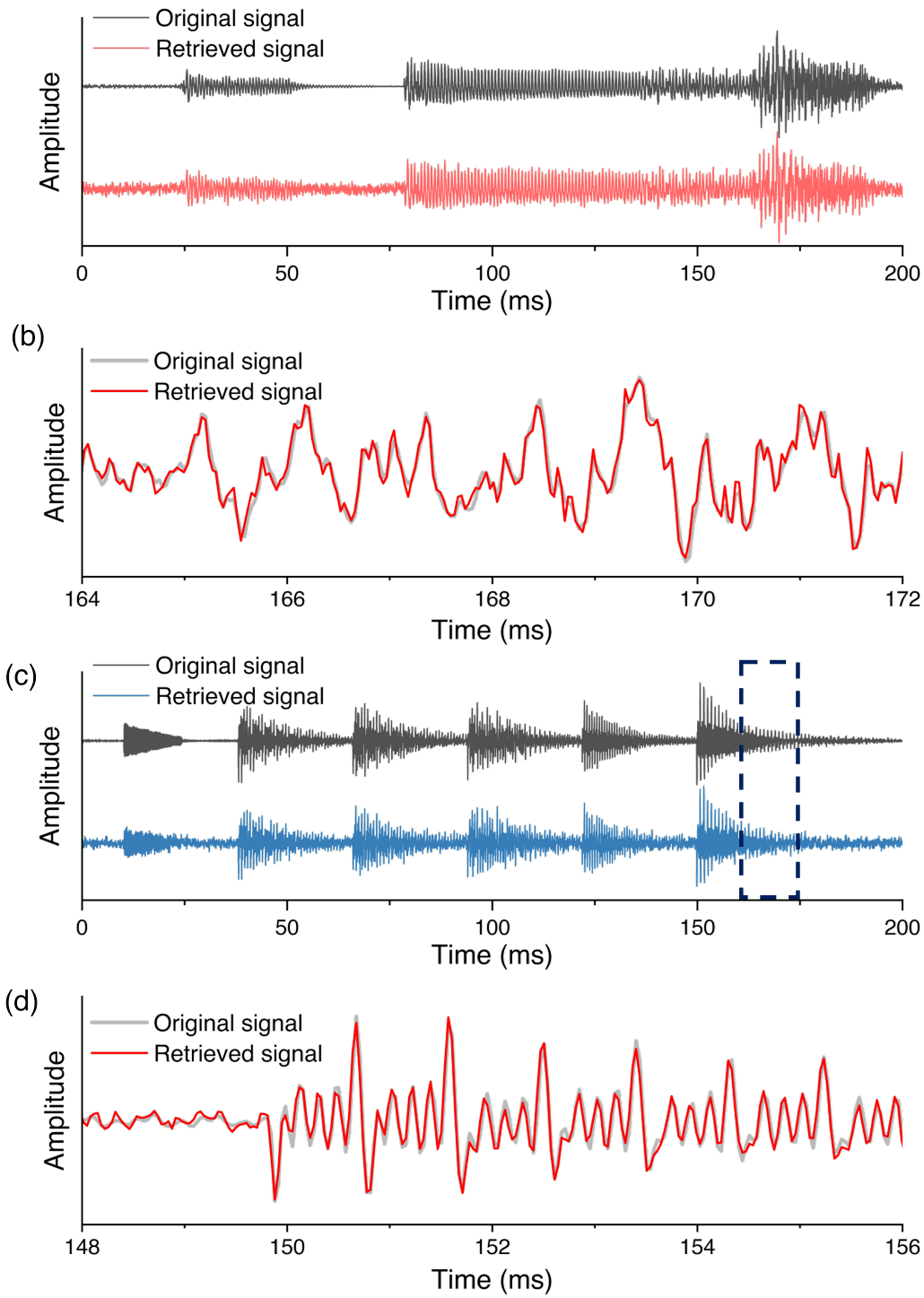


Figure 4.20: Original audio envelopes (black) and retrieved signals (red) for both channels: (a,c) full 200 ms; (b,d) zoom-ins. High-amplitude features are recovered; low-level details are limited by the background noise floor.

The optical encoding capability is further investigated by sending an AM triangular wave of f_1 (carrier frequency) into the device and comparing the demodulated signal at f_1 with the input triangular wave. The triangular wave was selected because it contains multiple harmonics that allow the encoding capability of the device to be clearly demonstrated, while most of its power remains concentrated in the fundamental and first few harmonics. This ensures that the waveform can be transmitted through the system with minimal distortion, even under limited bandwidth. In addition, the linear ramp portions of the triangular wave make it easier to observe small amplitude or phase distortions, providing a more reliable basis for estimating the SNR. Thus, it offers a suitable balance between spectral richness and robustness for the intended measurements.

First, the effect of driving voltage on the SNR of the demodulated output is investigated. An AM triangular wave with a 15.67 MHz carrier frequency and a 4.2 kHz envelope frequency is sent to the PZT chip as the driving signal. The amplitude of the driving signal is set to very small and gradually increased, while the optical power (15 mW), the bandwidth of the LPF (30 kHz), and the data transfer rate (320 kSa/s) remain unchanged. The amplitude of the demodulated triangular wave increases linearly with the driving voltage, as shown in Figure 4.21 (a). The demodulated signals at different driving voltages are normalised and shown in Figure 4.21 (c). When the driving voltage is very small, ranging from 0.356 to 1.07 V, the amplitude of the signal of interest is very low, leading to a very small SNR (ranging from 5 to 12). As the driving voltage increases, the readout amplitude increases, thereby increasing the SNR, as shown in Figure 4.21 (b). However, the SNR does not increase indefinitely. It reaches a maximum of 30.4 dB when the driving amplitude is 7.12 V. The input signal and some demodulated outputs are plotted together for comparison in Figure 4.22 (a). The SNR decreases at voltages higher than 7.12 V because the input triangular wave theoretically contains an infinite number of harmonics, extending far beyond the measurement bandwidth. With the LPF set to 30 kHz, only harmonics up to the 7th order ($\simeq$ 29.4 kHz) are preserved, while all higher-order harmonics are removed. At low driving voltages, the SNR is

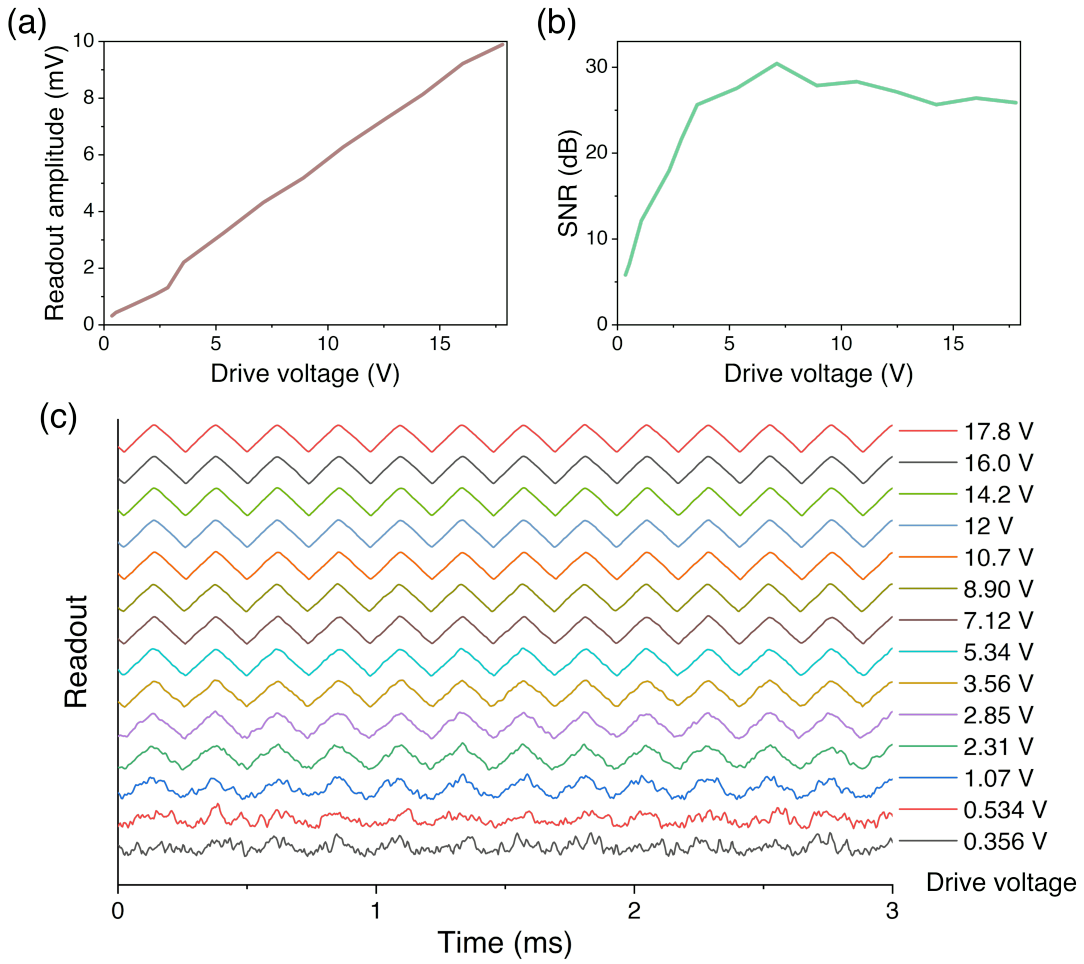


Figure 4.21: AM triangular-wave test at f_1 with 4.2 kHz envelope. (a) Output amplitude plotted against driving voltage, showing linear scaling. (b) SNR plotted against driving voltage, showing that SNR rises then saturates at ∼30 dB. (c) Normalised recovered envelopes at different driving voltages.

limited by the background noise floor, so increasing the drive leads to a proportional improvement. However, at higher driving voltages, the SNR no longer depends on the noise level but instead approaches the theoretical limit imposed by the LPF bandwidth, since further increases in amplitude cannot recover harmonics outside the 30 kHz passband. From Figure 4.22 (a), the distortion of the triangular wave can be observed around the peak of the wave, where it is not as sharp as the original signal. This explains the observed saturation of the SNR at approximately 30 dB.

Next, the effect of the LPF bandwidth on the demodulated readout is investigated while keeping the driving voltage (3.56 V) and data transfer rate (230 kSa/s)

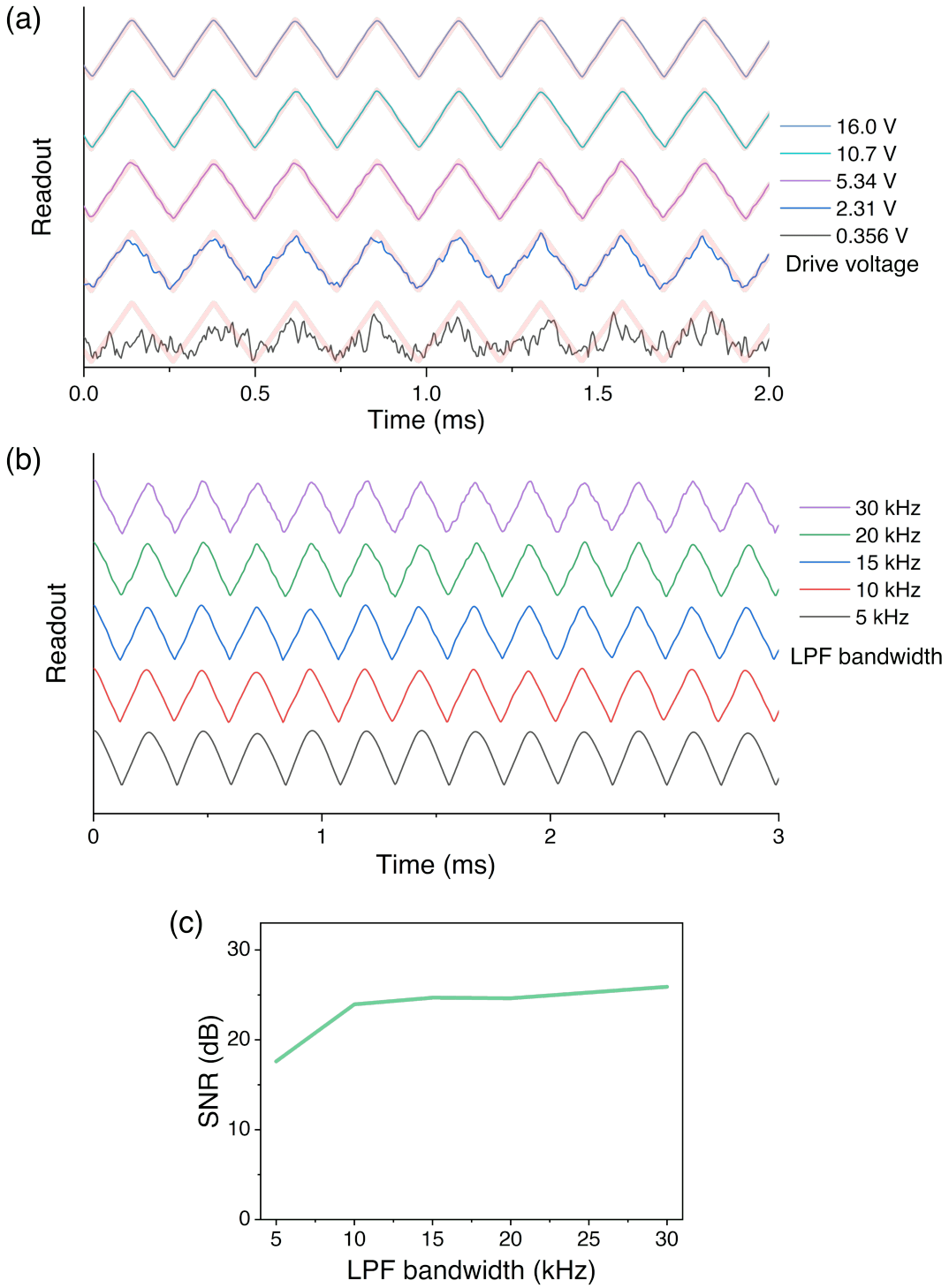


Figure 4.22: (a) Recovered outputs at several drive levels with the input triangular wave in the background. (b) Bandwidth study at fixed drive, increasing LPF bandwidth sharpens waveform but raises noise level. (c) SNR plotted against LPF bandwidth, showing improvement that plateaus as noise increases.

unchanged. Figure 4.22 (b) shows the readout signals obtained at bandwidths of 5, 10, 15, 20, and 30 kHz. At low bandwidths, such as 5 kHz, the triangular waveform suffers from severe distortion, with the peaks appearing rounded due to the removal of higher harmonics, even though the noise floor is significantly suppressed. As the bandwidth increases, the triangular shape becomes progressively sharper and closer to the input signal, indicating reduced distortion, but at the cost of an elevated noise level. Therefore, the choice of bandwidth represents a trade-off between preserving waveform fidelity and minimising noise. Overall, the SNR still increases with the LPF bandwidth, as shown in Figure 4.22 (c), though it soon plateaus as the noise level increases. The optimised bandwidth depends on the components of the envelope signal. If the envelope does not contain many high-frequency components, a smaller bandwidth yields a larger SNR since the distortion would not be severe, and most noise would be eliminated. However, if the envelope does contain a large portion of high-frequency components, a larger bandwidth should be used to prevent excessive distortion of the signal, even if the noise level could be higher.

In summary, the measurements confirm that the noise level remains essentially constant as the driving voltage increases, while the signal amplitude grows linearly until reaching the bandwidth-limited SNR ceiling. This behaviour indicates that the device performs robust optical encoding, accurately transferring the input modulation onto the optical carrier without introducing additional noise. Such stability demonstrates the suitability of the system for high-quality signal processing applications.

4.5 Conclusion

This chapter demonstrates a Si_3N_4 photonic device that couples mechanical and optical resonances to achieve simultaneous RF multi-channel filtering and multi-wavelength optical encoding on a single PIC experimentally. Each channel comprises a Si_3N_4 MRR addressed at a distinct optical resonance and a suspended InP NW positioned within the rings evanescent field. When driven at its mechanical

resonance, the NW perturbs the effective index of the cavity, $n_{\text{eff}} + \mathrm{i}k_{\text{eff}}$, thereby imprinting an RF-rate intensity modulation on the through-port optical signal.

In the previous chapter, the operating mechanism is analysed first through simulations. COMSOL eigenfrequency analysis provides the fundamental mode shape and frequency of the doubly-clamped NW. FDTD simulations reveal a red-shift and broadening of the optical resonance between the NWs peak and trough positions, consistent with increased overlap-induced absorption and scattering. A Lorentzian model accounts for the experimentally observed asymmetric detuning dependence of optomechanical transduction and clarifies the preferred working point on the resonance slope.

A design rationale and fabrication route for a two-channel optoelectronic filter bank are discussed. The material choices (InP for high index but low loss, Si_3N_4 for low-loss cavity operation, and Au supports for robust clamping), together with large ring radii and differentiated support spacings, were selected to maximise optomechanical transduction while preserving channel separability. A two-step EBL process with full Si_3N_4 etch and Cr/Au PVD, followed by PDMS-assisted NW transfer, yields reproducible suspensions confirmed by microscopy and SEM.

The MRR spectra of the fabricated devices are measured, showing high quality factors. After the NW transfer, optical resonances red-shift and broaden with a reduced extinction ratio, indicating an increase in both n_{eff} and k_{eff} due to the high-index scatterer. Thermal noise measurements resolve the NW resonances under ambient conditions and, under vacuum, show a substantial increase in the quality factor (from $\sim$50 to $\sim$300), along with a slight frequency up-shift due to reduced fluid loading. Because optimum sensitivity occurs on a steep resonance slope and thermal drift is worse under vacuum, a PLL is employed to stabilise the detuning during all measurements.

Under piezoelectric drive via a bulk PZT stack, both channels present clear mechanical resonances with centre frequencies in close agreement with those extracted from thermal noise data. The driven quality factors are lower than the intrinsic values owing to substrate-mediated coupling and background assembly

modes; nevertheless, the responses remain linear over the accessible range, and no Duffing nonlinearity is observed before the failure of the assembly. Finally, a two-channel demonstration is performed in which two distinct baseband audio envelopes are amplitude-modulated onto separate RF carriers, summed, amplified, and applied to the PZT. Optical outputs at λ_1 and λ_2 with demodulation at f_1 and f_2 selectively recover the intended envelopes with low inter-channel leakage. A controlled study with triangular envelopes quantifies the SNR as a function of driving voltage and low-pass bandwidth, with performance limited by readout bandwidth and assembly-induced common-mode noise.

Limitations. The present implementation is limited by: (i) excess optical loss and Q degradation introduced by the NW and any transfer residues; (ii) mechanical and electrical cross-coupling from the off-chip PZT/adhesive/fibre/PCB assembly into the PIC, which gives rise to the background noise between 5-13 MHz; and (iii) thermo-optic drift under vacuum that necessitates active detuning stabilisation. These constraints restrict the achievable SNR and obscure fine waveform features; yet they also reveal clear opportunities for improvement in material processing, packaging integration, and thermal management in future device iterations.

5

RF Filter Bank Based on a Nanomechanical Resonator Array

Contents

5.1 Introduction 110
5.2 Analytical Model 113
5.3 Design and Fabrication 119
5.3.1 Dimensions of the Beams 120
5.3.2 Design Iterations 121
5.3.3 Fabrication Methods 124
5.3.4 Etching of Silicon Nitride 126
5.3.5 Buffered Oxide Etch 129
5.3.6 Failed Fabrications 132
5.4 Actuation and Readout 135
5.4.1 Measurement Results 135
5.5 Reasons of Failure 140
5.5.1 Tensile Stress in the Silicon Nitride Film 140
5.5.2 Inadequate Transduction Efficiency 141
5.6 Conclusion 143

5.1 Introduction

As introduced in Chapter 1, nanomechanical resonators are widely employed as hardware RF filters owing to their high quality factors and relative ease of fabrication. Following the thermoelastic actuation and piezoresistive detection

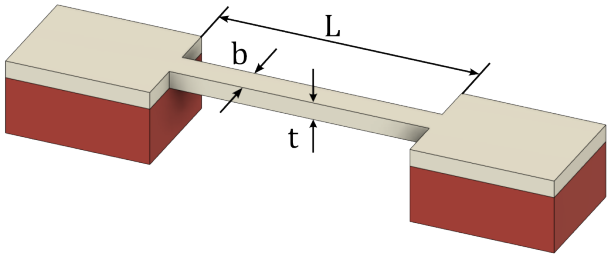


Figure 5.1: A doubly clamped beam resonator with length L, width b and thickness t.

schemes developed by Bargatin *et al.*, a nanomechanical resonator operating at its fundamental frequency, f_0, can be fabricated and employed as an electrical RF filter [54]. The mixed signal containing the signal of interest at f_0 can be sent to the actuation electrode as input. Only the signal of interest can be recovered at the detection electrode, acting as a bandpass filter. The fundamental mode frequency of the doubly clamped beam with dimensions as shown in Figure 5.1 can be calculated through substitution ($\beta_1 = 4.730$, $A = bt$, $I = \frac{wt^3}{12}$) into Equation 3.2 in Chapter 3:

$$\omega_0 = 2\pi(1.05)\sqrt{\frac{E}{\rho}}\frac{t}{L^2} \tag{5.1}$$

This form makes explicit the quadratic dependence on beam length and linear dependence on thickness for stress-free beams, which is central to the tuning strategy of this work. For example, there is a resonator with l_1 resonating at f_1, and if there is another resonator with $l_2 = 0.9l_1$ (all remaining dimensions are the same), the fundamental frequency of the second resonator should be at $f_2 = f_1 \times (1 \div 0.9^2) = 1.23f_1$. This scaling law forms the basis of the concept of the filter bank: by fabricating beams with systematically varied lengths, a set of resonant frequencies can be engineered to cover a desired RF spectrum. If a resonator can be demonstrated to have a filtering ability in its fundamental frequency, multiple resonators with different dimensions can be fabricated to construct a filter bank with the desired RF spectrum.

Suppose that there are four resonators with centre frequencies f_1, f_2, f_3, and f_4 in the filter bank as shown in Figure 5.2. When operating, an electrical signal containing

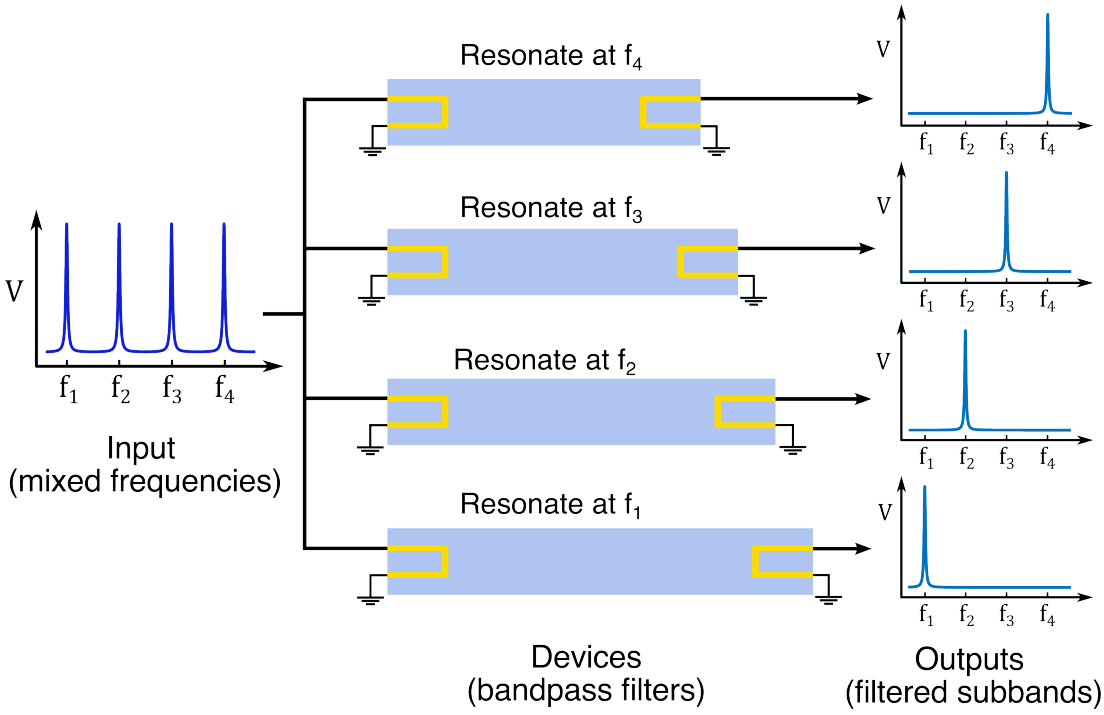


Figure 5.2: Schematics showing the working principle of the electromechanical filter bank system with 4 suspended beams with different length resulting in 4 bandpass filters with different frequencies. All beams are actuated via thermoelastic method, and readout via piezoresistive method.

different signals with mixed frequencies f_1, f_2, f_3, f_4 is sent to the actuation electrodes. The devices (silicon nitride (Si_3N_4) nanobeams) act as bandpass filters that allow only the transmission of signals at their resonant frequency. At each detection electrode, the signal of interest at the corresponding frequency can be recovered as the output.

This filter bank system has numerous advantages, including high tunability (in the design and fabrication stage), a compact footprint, ease of integration, compatibility with CMOS technology, high performance (high quality factor), no memory costs, very low energy consumption, and high speed operation.

While SAW and BAW filters dominate current commercial RF filtering applications due to their high performance and scalability, they face limitations in terms of CMOS compatibility and monolithic integration [5]. In contrast, nanomechanical resonators, particularly those based on Si_3N_4, offer higher quality factors, reduced power consumption, and the potential for dense on-chip integration

with photonic integrated circuits (PICs) [8, 39, 41]. Unlike piezoelectric-based acoustic filters, which require specific materials and layered structures, Si_3N_4 resonators can be fabricated using standard CMOS-compatible processes, offering enhanced versatility. Moreover, while many MEMS-based filters still rely on complex packaging or hybrid integration, the approach adopted in this work seeks to advance a scalable, monolithically integrable electromechanical filter bank with potential for cointegration into photonic platforms, thereby addressing the growing demand for compact, low-loss, multiband RF filtering in next-generation communication systems.

5.2 Analytical Model

An analytical model is detailed here starting from the thermoelastic actuation of the resonator, providing a guideline and rough estimate of the readout amplitude.

Thermoelastic actuation relies on periodic Joule heating in the electrode, and the mismatch of thermal expansion causes a flexural stress on the resonator that drives its vibration [54]. The Joule heating power from a sinusoidal voltage at $\omega/2$ can be calculated using Equation 1.3; hence, the time-dependent temperature modulation $\Delta T(t)$ is:

$$\Delta T(t) = \Delta T_0 \cos(\omega t) \tag{5.2}$$

where ΔT_0 is the peak temperature rise, which depends on both the input power and the thermal properties.

Thermal Analysis. Firstly, convection and radiation are ignored as the device is driven at MHz in vacuum. Subsequently, since Joule heating (the driving force) is periodic at MHz, only a segment of the beam within the thermal penetration depth participates in each cycle, and the heat flux is phase shifted relative to temperature. The thermal properties in this case can be analysed by the thermal admittance Y_{th}, which captures the frequency-dependent amplitude and phase, whereas a DC thermal conductance G_{th} does not [145]. In contrast, a static thermal conductance

presumes steady heat flow to a distant isothermal sink and therefore underestimates the local oscillatory temperature rise under harmonic forcing [146, 147]. Therefore, the peak temperature rise ΔT_0 can be given as [148]:

$$\Delta T_0 \;=\; \frac{P_{\text{avg}}}{|Y_{\text{th}}(\omega)|} \;=\; \frac{V_{\text{rms}}^2/R_{\text{actuation}}}{|Y_{\text{th}}(\omega)|}. \tag{5.3}$$

where Y_{th} here is the magnitude of the complex thermal admittance of the nanobeam with the gold actuation electrode, and V_{rms} is the root mean square (RMS) voltage across the actuation electrode. To estimate Y_{th}, the routes of heat flow must be considered. Heat flows (i) across the Au/Si_3N_4 interface over the area of the gold electrode A_{gold} and (ii) along the Si_3N_4 beam (in both directions) over the thermal penetration depth $\delta_{\text{th}} = \sqrt{2\alpha/\omega}$ where $\alpha = k_{\text{SiN}}/(\rho c)$, k_{SiN} is the thermal conductivity of Si_3N_4, and ρc is the volumetric heat capacity of Si_3N_4 [147, 149]. This approximation of the penetration depth δ_{th} is only valid when the thermal fluctuation frequency ω is large, making the penetration depth much smaller than the length of the beam, which is applicable in this case [146]. The magnitudes of the thermal admittances across the Au/Si_3N_4 interface and along the Si_3N_4 beam can be given as [145, 146, 150]:

$$|Y_{\text{int}}(\omega)| = hA_{\text{gold}} \quad \text{and} \quad |Y_{\parallel}(\omega)| = 2 \cdot A_{\text{SiN}}\sqrt{k_{\text{SiN}}\rho c\,\omega} \tag{5.4}$$

where h is the thermal conductance between Au and Si_3N_4, A_{SiN} is the cross-sectional area of the beam. The amplitude of the combined thermal admittance $|Y_{\text{th}}(\omega)|$ is given by:

$$|Y_{\text{th}}(\omega)| = \left(\frac{1}{|Y_{\text{int}}(\omega)|} + \frac{1}{|Y_{\parallel}(\omega)|}\right)^{-1} = \left(\frac{1}{hA_{\text{gold}}} + \frac{1}{2A_{\text{SiN}}\sqrt{2k_{\text{SiN}}\rho c\,\omega}}\right)^{-1} \tag{5.5}$$

With an estimated $|Y_{\text{th}}(\omega)|$, ΔT can also be estimated.

Driving force analysis. Under the same temperature modulation, two materials (Au and Si_3N_4) expand differently due to their different coefficients of thermal expansion (CTEs). The difference in expansions can be calculated as [151]:

$$\varepsilon_{\text{diff}}(t) = (\alpha_{\text{Au}} - \alpha_{\text{SiN}})\,\Delta T(t) \tag{5.6}$$

where α_{Au} and α_{SiN} are CTEs of gold and Si_3N_4, respectively. This difference causes a thermal strain mismatch at the interface, which creates internal thermal stress in the gold electrode:

$$\sigma_{\text{Au}}(t) = E_{\text{Au}}\,(\alpha_{\text{Au}} - \alpha_{\text{SiN}})\,\Delta T(t) \tag{5.7}$$

where E_{Au} is the Young's modulus of gold. The total force applied at the anchor of the resonator due to this thermal stress is:

$$F_{\text{therm}} = \psi \cdot \sigma_{\text{Au}}(t) \cdot A_{\text{Au}} = \psi E_{\text{Au}} A_{\text{Au}} (\alpha_{\text{Au}} - \alpha_{\text{SiN}}) \Delta T(t) \tag{5.8}$$

where A_{Au} is the contact area between the gold electrode and the resonator, and ψ is an empirical scaling factor that corrects the idealised thermal expansion model to the actual actual driving efficiency, which is typically much smaller than 1 [8, 54, 81]. F_{therm} can also be substituted with ΔT_0:

$$F_{\text{therm}} = F_0 \cos(\omega t) \quad \text{where} \quad F_0 = \psi E_{\text{Au}} A_{\text{Au}} (\alpha_{\text{Au}} - \alpha_{\text{SiN}}) \Delta T_0 \tag{5.9}$$

This would be the driving force of the nanomechanical resonator from the thermoelastic actuation method.

Displacement analysis. The doubly-clamped beam can be modelled as a damped harmonic oscillator subject to a harmonic driving force at frequency ω. Its motion in time-domain can be described by the equation [81]:

$$m\ddot{x}(t) + m\gamma\dot{x}(t) + kx(t) = F(t) \tag{5.10}$$

where m is the effective mass of the oscillator ($m = 0.735 \cdot m_{\text{actual}}$ for the fundamental mode of a uniform doubly clamped beam), γ is the damping coefficient, k is the spring constant, $x(t)$ is the displacement, and $F(t)$ is the arbitrary driving force for the oscillator. This is a standard second-order linear differential equation that describes how the displacement $x(t)$ evolves over time under the influence of both restoring and damping forces. Since the frequency response of the displacement of the oscillator is the subject of interest, the Fourier transform of Equation 5.10 is taken as [152]:

$$X(\omega) = \frac{F(\omega)}{k - m\omega^2 + im\gamma\omega} \quad \text{where} \quad k = \omega_0^2 m, \quad so \quad X(\omega) = \frac{F(\omega)/m}{\omega_0^2 - \omega^2 + i\gamma\omega} \tag{5.11}$$

where ω_0 is the resonant frequency of the fundamental mode. The driving force F_{therm} can be substituted with the driving force from thermoelastic actuation, which is calculated using Equation 5.9. The amplitude of the driving force is F_0, thus the displacement amplitude is:

$$|X(\omega)| = \frac{F_0/m}{\sqrt{(\omega_0^2 - \omega^2)^2 + (\gamma\omega)^2}} \tag{5.12}$$

At its resonant frequency ω_0, the displacement amplitude becomes:

$$|X|_{\omega=\omega_0} = \frac{QF_0}{k} \quad \text{where} \quad Q = \frac{\omega_0}{\gamma} \tag{5.13}$$

Strain and readout amplitude analysis. In order to estimate the strain experienced by the piezoresistive readout electrode at the clamp, it is convenient to first calculate the radius of curvature of the beam deflection rather than the surface strain directly. Within Euler-Bernoulli beam theory, the surface strain is linearly related to the local curvature by:

$$\varepsilon(x) = z \cdot \kappa(x) \quad \text{where} \quad \kappa(x) = \frac{1}{R(x)} = \frac{d^2w}{dx^2}, \tag{5.14}$$

where z is the distance from the neutral axis to the surface, κ is the curvature, R is the radius of curvature, and w is the transverse displacement field [153]. Hence, once

the curvature is known from the displacement profile, the strain at the electrode surface follows directly by a simple proportionality. The transverse displacement field w can be estimated using a simplified cosine approximation of the fundamental mode of the doubly clamped beam, and it is given as [152, 154]:

$$w(x) \approx |X|\left[1 - \cos\left(\frac{2\pi}{L}x\right)\right] \tag{5.15}$$

Since the readout electrode is located at the clamping site of the beam, i.e., $x = 0$, the curvature at the electrode is approximated as:

$$w''(0) \approx \left(\frac{2\pi}{L}\right)^2 |X| \tag{5.16}$$

Hence, the surface strain in the gold readout electrode, located a distance z_g from the neutral axis, at the fundamental mode is [153]:

$$\varepsilon(x) \approx z_g w''(x) \tag{5.17}$$

Since the piezoresistive readout electrode has a finite footprint L_g, the measured strain is the axial average over the electrode length. For $L_g/L \ll 1$, this introduces a correction factor η between surface strain when the electrode covers the whole beam and when the electrode only covers a small length [155, 156]:

$$\varepsilon_g = \eta\varepsilon \approx \eta z_g\left(\frac{2\pi}{L}\right)^2 |X| \quad \text{where} \quad \eta \approx 1 - \frac{1}{6}\left(\frac{2\pi L_g}{L}\right)^2 \tag{5.18}$$

The piezoresistive readout electrode works like a strain gauge, where the strain causes a change in resistance. The ratio between the change in resistance ΔR and the nominal resistance R_0 is [155]

$$\frac{\Delta R}{R_0} = \mathrm{GF} \cdot \varepsilon_g \tag{5.19}$$

where GF is the gauge factor of the material, which is around 2 for gold and most metallic gauges [155]. In the experiment, the readout electrode would be biased with a DC voltage V_b and readout by a lock-in amplifier (LIA). Inside the LIA, the input would be connected in series to an internal resistor with a resistance of

R_s, and the voltage ΔV across R_s would be measured and lock-in amplified. By analysing the frequency and amplitude of ΔV, the change in resistance, and hence the displacement of the resonator can be estimated. Linearising for $|\Delta R| \ll R_0 + R_s$, which is valid for most cases, the AC voltage amplitude at the LIA is:

$$\Delta V = \frac{V_b R_s R_0}{(R_0 + R_s)^2} \mathrm{GF} \varepsilon_g \tag{5.20}$$

Numerical Estimates. With these analytical results, the readout amplitude of an exemplar device with specific dimensions can be predicted using certain estimations and assumptions. For the exemplar device, the beam geometry is $L = 12$ µm, $w = 1$ µm, $t = 100$ nm, the actuation electrode geometry is $A_{\mathrm{gold}} = 0.2$ µm^2, $t_{\mathrm{Au}} = 80$ nm, and the readout electrode geometry is $L_g = 1$ µm, $t_{\mathrm{Au}} = 80$ nm. The electrical resistances of the actuation and readout electrodes are estimated from their dimensions, and they are approximately $R_{\mathrm{actuation}} = 4\ \Omega$ and $R_0 = 6\ \Omega$. Other material properties are used including $E_{SiN} = 260$ GPA [157], $E_{Au} = 69$ GPA [158], $h = 1 \times 10^8$ W m^{-2} K^{-1} (typical value for metal-dielectric interfaces)[146], $k_{\mathrm{SiN}} = 2.7$ W m^{-1} K^{-1} [127], $\rho = 3100$ kg m^{-3} [159], $c = 700$ J kg^{-1} K^{-1} [160], $\alpha_{Au} = 14.2 \times 10^{-6}$ K^{-1} [161], $\alpha_{\mathrm{SiN}} = 2.8 \times 10^{-6}$ K^{-1} [162]. Assumed parameters including $Q = 1 \times 10^6$, $\psi = 10^{-5}$ [54].

The fundamental mode resonance frequency of this exemplar beam would be $\omega_0 \approx 4.196 \times 10^7$ rad/s ($f_0 = 6.68$ MHz). The combined thermal admittance $|Y_{\mathrm{th}}|$ at this frequency is approximately 3.63×10^{-6} W K^{-1}, thus $\Delta T_0 \approx 6.89 \times 10^4\, V_{\mathrm{rms}}^2$ K. Therefore, $F_0 \approx 1.08 \times 10^{-7}\, V_{\mathrm{rms}}^2$ N. With $k \approx 4.81$ N m^{-1}, $|X| \approx 2.25 \times 10^{-2}\, V_{\mathrm{rms}}^2$ m, and $\varepsilon_g \approx 5.30 \times 10^2\, V_{\mathrm{rms}}^2$. The readout voltage is then $\Delta V \approx 1.01 \times 10^2\, V_b\, V_{\mathrm{rms}}^2$ V. Note that V_b is the total DC voltage applied across the readout circuit, including the readout electrode, on-chip routings, electrical contacts, and wire bonds, but V_{rms} is the RMS of the AC voltage across the actuation electrode specifically. Practically, the voltage applied across the actuation circuit V_{applied} is much larger than V_{rms} due to the parasitic resistance from other parts of the circuit, which is much larger than the resistance of the actuation electrode. As an estimate, $V_{\mathrm{rms}} = V_{\mathrm{applied}}/100$.

Therefore, in terms of the AC actuation voltage and the DC readout voltage, the analytical AC readout of the device ΔV is approximately $1.36 \times 10^{-2}\, V_b\, V_{\text{applied}}^2$ V.

Discussion. The analytical results highlight the strong non-linear scaling of the thermoelastic response with the driving voltage, revealing that even small changes in actuation power can significantly alter the mechanical displacement and electrical readout. Although the simplified thermal model produces values that are far greater than practical values and represents upper bounds rather than exact predictions, it provides important physical insight into the relative influence of different parameters. For instance, the dependence of ΔT_0 on the thermal admittance emphasises the crucial role of heat dissipation pathways, suggesting that engineering the anchor geometry or adding thermal shunts could be an effective route to tune the actuation efficiency. Similarly, the proportionality of the displacement amplitude to the quality factor Q indicates the importance of minimising damping through vacuum operation and material choice. From the numerical estimations, the strain and readout voltage values are clearly overestimated. For more accurate estimates, a careful calibration of ψ, the efficiency factor, which encapsulates geometric mode-shape overlap and interfacial coupling losses, is crucial.

In experimental practice, this analytical model acts as a guide for interpreting the order of magnitude of signals, identifying dominant loss mechanisms, and optimising design parameters such as beam geometry, electrode footprint, and clamping conditions. While quantitative agreement with measurements will require more sophisticated finite-element thermal modelling, the present framework establishes the expected scaling laws and highlights which parameters most critically govern device performance.

5.3 Design and Fabrication

Si_3N_4 was chosen as the nanobeam material due to its high quality factor when used to construct nanomechanical resonators, which has been reported to reach 10^6

[163]. Arı et al. have shown that the thermoelastic actuation and piezoresistive detection schemes also work on Si_3N_4 nanobeams with high sensitivity [164].

Fabrication starts from a 1-mm thick silicon chip with 3 µm thermally grown silicon oxide and 330 nm low pressure chemical vapour deposition (LPCVD) grown Si_3N_4. This constraint significantly influenced the subsequent design, as described in the following sections.

5.3.1 Dimensions of the Beams

To ensure that the resonant frequencies of the fabricated resonators lie within the operational range of the LIA (DC-50 MHz), calculations and simulations are performed to determine the limits of the dimensions (length, width, and thickness) of the resonators.

Since the thickness of the Si_3N_4 layer of the wafer is 330 nm, the maximum thickness of the resonators is also 330 nm. The thickness should not be less than 100 nm to maintain adequate bending stiffness. According to Equation 3.2, the eigenfrequency of the resonator does not depend on width but on thickness and length. Figure 5.3 (a) shows a plot of the length of the beam against the thickness of the beam, with two curves. The Young's modulus and density of Si_3N_4 used in the calculations involving Equation 5.1 are 250 GPa and 3100 kg/m^3, respectively, from the COMSOL MEMS Materials Database. The black curve represents the case when the beam has a resonant frequency of 50 MHz, while the red curve represents the case when the beam has a resonant frequency of 5 MHz. 5 MHz is chosen as the lower frequency limit to avoid environmental and electronic noise, which is usually around and below 1 MHz. Additionally, the lower frequency requires longer beams, which is not ideal for a compact device footprint [165]. Any combination of length and thickness falling between the two curves should yield a resonant frequency between 5 and 50 MHz.

Simulation was also performed to verify the results. A beam with a width of 600 nm, a thickness of 200 nm, and a length of 12 µm is chosen as an example

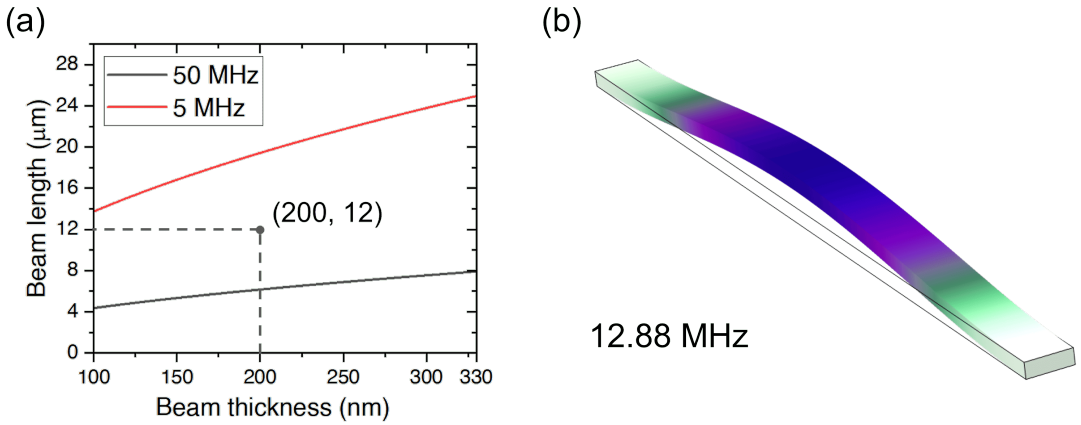


Figure 5.3: Simulated eigenfrequency mapping and mode shape. (a) Beam length that would result in upper and lower frequency limits for different thicknesses calculated using Equation 3.2. Any combinations within the two curves result in frequency between 5 and 50 MHz. An example was chosen to have 200 nm thickness and 12 µm length. (b) Simulated (by COMSOL Multiphysics) mode shape of fundamental z-plane mode of the 200 nm thick, 12 µm long and 600 nm wide beam. Simulated eigenfrequency is 12.88 MHz which lies in the target range.

within the range. The simulated mode shape is shown in Figure 5.3 (b), and the simulated eigenfrequency is 12.88 MHz which lies well in the 5-50 MHz range.

5.3.2 Design Iterations

The design of the filter bank device has undergone 2 major iterations with successive improvements.

First iteration. The main components of the device include the etched area that defines the beams, the actuation and readout electrodes, the electrical connections between the electrodes and the contact pads, and the contact pads. The complete design of the first iteration is shown in Figure 5.4. In this design, there are a total of 49 (7×7) devices on the chip, and in each row, the width of the nanobeam increases from 0.3 to 0.9 µm. Devices in different rows are identical. Within each device, there is an array of NWs with different lengths, actuation and readout electrodes, electrical routings, and source and ground contact pads for wire bonding.

This design of the first iteration has several problems:

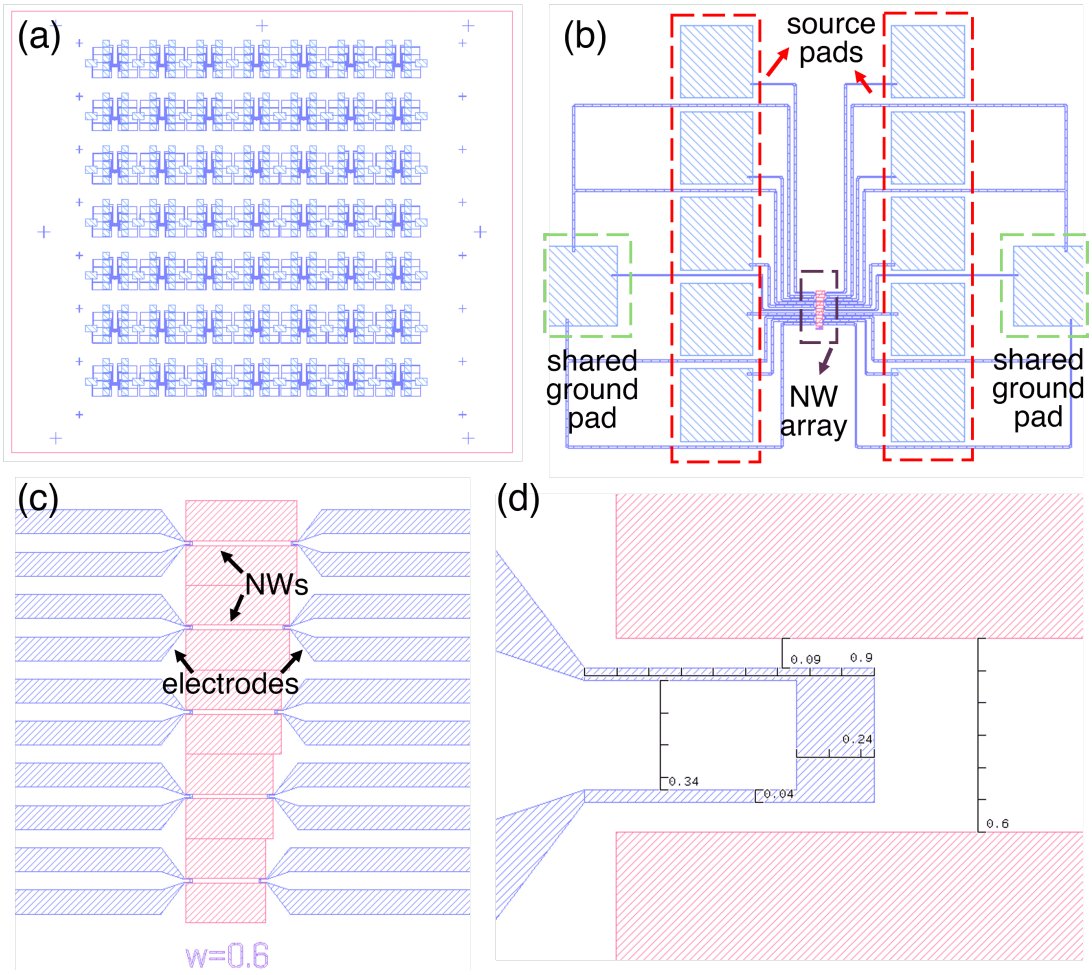


Figure 5.4: Design of the first iteration. (a) Overall chip layout including in total 49 devices. (b) Design of a single device showing the NW array, source pads and the shared ground pads. (c) Details of the NW array and electrodes. (d) Dimensions of the electrode and the nanobeam.

- As shown in Figure 5.4 (b), ground contact pads are not only shared by multiple electrodes in the same device but also by neighbouring devices. This risks damage to multiple devices if pulses of high amplitude or long duration are accidentally sent to the electrode.

- As shown in Figure 5.4 (c), the electrodes on the beams and the electrical routings between the electrodes and the contact pads are fabricated in the same layer, i.e., they would be written in the same lithography step. Since writing the electrodes requires the highest available resolution of the EBL tool, the smallest aperture and current will be used to write this layer, despite

the fact that the routings have much larger dimensions and do not require high resolution. As a result, the total writing time for this step would be unnecessarily long.

- As shown in Figure 5.4 (d), the dimensions of the electrodes are too small (40 and 90 nm) and are close to the resolution limit of the EBL tool. Therefore, the real dimensions of the electrodes may deviate from the designed dimensions, and in the worst case, the electrode loop may not be properly written.

- As shown in Figure 5.4 (d), the gap between the electrode and the edge of the beam is very small (90 nm). Without local markers in the design, the alignment between the two lithography steps would be very difficult, leading to the electrode not being properly placed on the beam.

Second iteration. Due to these problems, the fabrication of this design failed several times and was very difficult. To address the problems, a redesign was necessary, and the design of the second iteration is shown in Figure 5.5. In Figure 5.5 (a), the total number of devices on a chip has decreased to 6 for shorter writing times. In Figure 5.5 (b), the source and ground contact pads are larger for easier wire bonding, and the ground pads are no longer shared between devices to avoid damaging multiple devices at once. In Figure 5.5 (c), the actuation and readout electrodes are in a different layer from the electrical routings so that the electrodes can be written with a smaller current for higher resolution and the routings, which do not require high resolution, can be written with a larger current for faster speed. Local markers are added for much more accurate alignments. In Figure 5.5 (d), the dimensions of the electrodes have been increased, and the gap between the electrode and the edge of the beam also increases for higher tolerance.

Fabrication using the second design has become much easier and more reproducible.

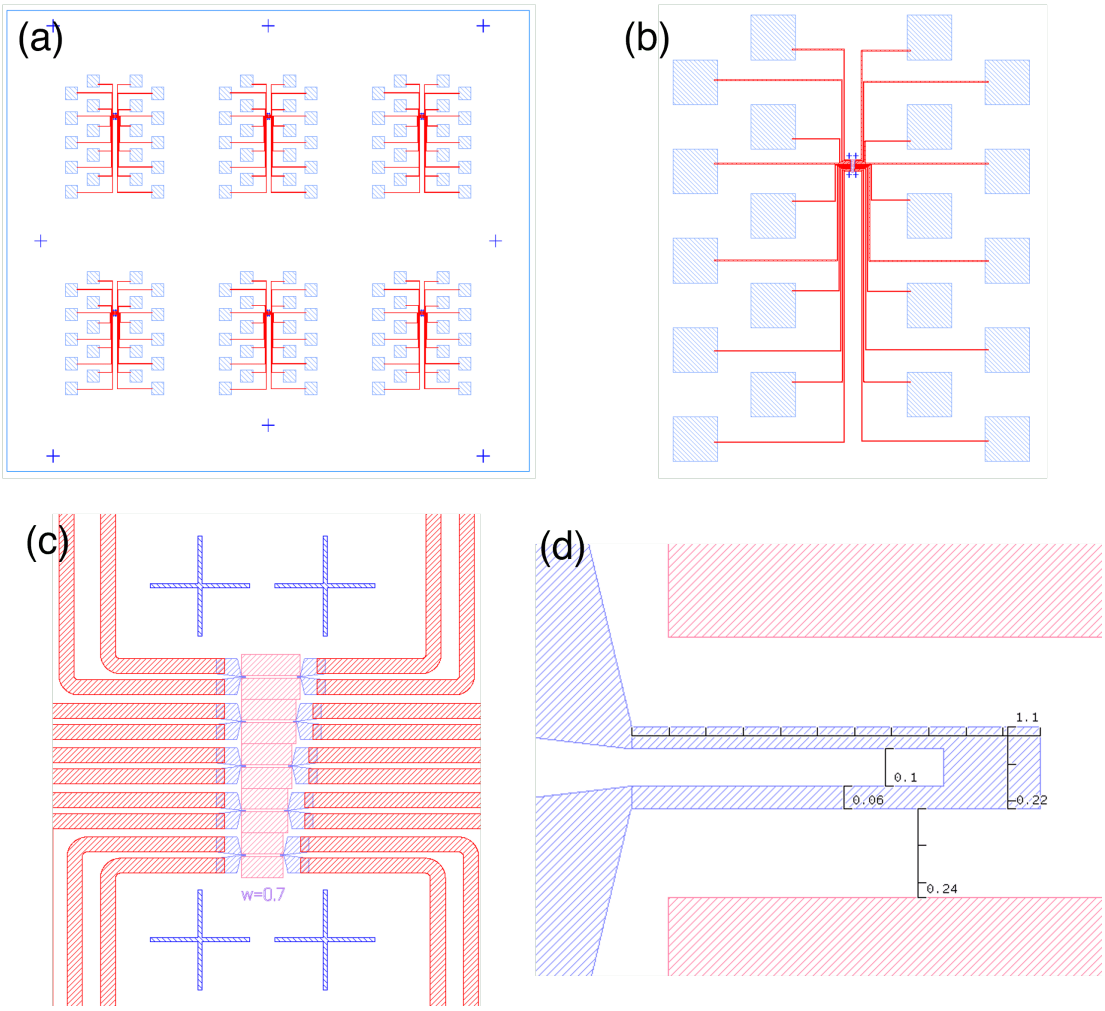


Figure 5.5: Design of the second iteration addressing the problems of the first iteration. (a) Overall chip layout including in total 6 devices. (b) Design of a single device showing the NW array, electrical routings and contact pads. (c) Details of the NW array, electrodes and electrical routings to contact pads. (d) Dimensions of the electrode and the nanobeam.

5.3.3 Fabrication Methods

The fabrication sequence is summarised schematically in Figure 5.6. The fabrication starts with a 1×1 cm chip diced from the silicon wafer with 330 nm of Si_3N_4 on 3 µm of silicon oxide. The first step is to clean the chip (sonicating in isopropanol (IPA) and acetone for 5 minutes each) and to perform dry etching of the Si_3N_4 layer via RIE. The length and width of the nanobeam can be defined by lithography, while the thickness is determined by the thickness of the Si_3N_4 layer, which is originally 330 nm. Compared to the thickness of the beam used in the literature, 80 nm, 330 nm is too thick and may cause a significant reduction in the vibration

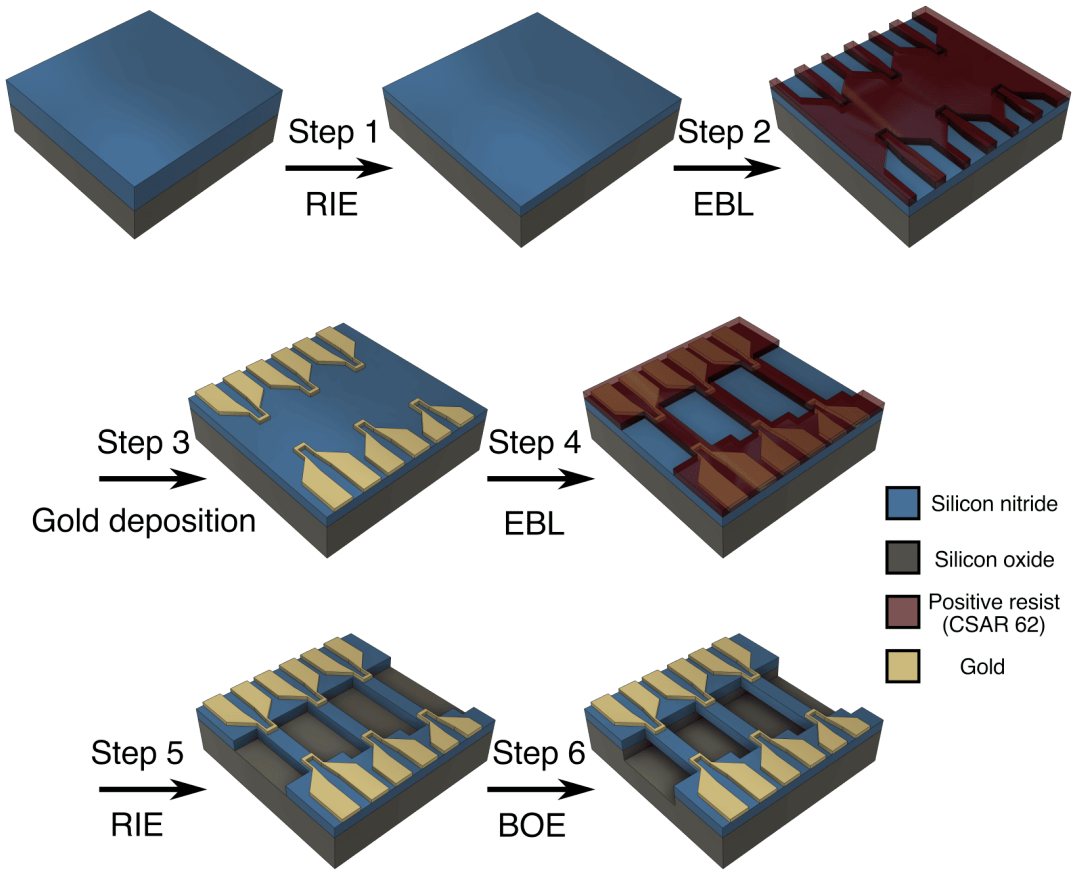


Figure 5.6: Nanofabrication process flow of the nanobeam array (not to scale).

amplitude [54]. Hence, the Si_3N_4 layer is dry etched to a suitable thickness using RIE as the first step, which is described in detail in Section 5.3.4.

In the second step, a mask is patterned with actuation and detection electrodes using a positive electron beam resist (CSAR 62) exposed in EBL. After development, the patterns appear in the mask made of the resist. The third step is to deposit gold via thermal evaporation deposition and lift off the remaining resist. In the fourth step, another mask for the nanobeam array was patterned using the same resist and EBL. The fifth step is to etch away the Si_3N_4 area that is not protected by the mask from the fourth step so that the silicon oxide around the nanobeams is exposed.

Then, the nanobeams are released by the buffered oxide etching (BOE) process, in which the chip is immersed in buffered hydrofluoric acid to etch away the exposed silicon oxide and undercut the Si_3N_4 beams. This process is discussed in detail in

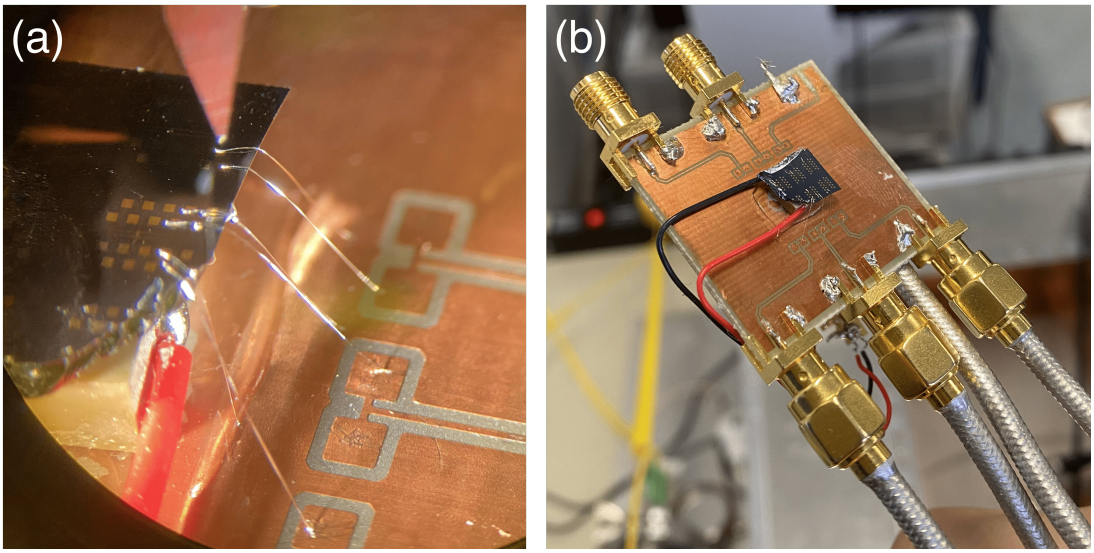


Figure 5.7: (a) Optical microscope image showing the wires connecting the on-chip electrodes and the electrical contacts on the PCB. (b) Image showing the whole PCB with the device chip glued on it, and with SMA cables connected. The chip was broken accidentally during dicing, but the filter bank device was undamaged. Note that there is a piezoelectric chip underneath the device chip, and it is for the alternative piezoelectric actuation method which would be explained in Section 5.4.1.

Section 5.3.5. After successful and sufficiently long etching, the Si_3N_4 nanobeams are released and free-standing, allowing them to vibrate when driven.

After the nanofabrication processes, the Si_3N_4 beams are ready for actuation and measurements. The chip is glued to a pre-designed printed circuit board (PCB). The electrodes on the chip are electrically bonded to electrical contacts on the PCB by a wire bonder using aluminium wires as shown in Figure 5.7 (a). The PCB is designed to connect the electrical contacts to SMA connectors, as shown in Figure 5.7 (b), so that signals can be transmitted to the PCB and then to the electrodes on the chip via SMA cables. The fabrication procedures are then finished, and the whole device is inserted into the vacuum chamber for actuation and readout experiments under vacuum.

5.3.4 Etching of Silicon Nitride

As mentioned above, the original thickness of the LPCVD-grown Si_3N_4 is 330 nm, and it is too thick to be driven using the thermoelastic actuation method. The larger thickness leads to a greater beam mass, which reduces the system's

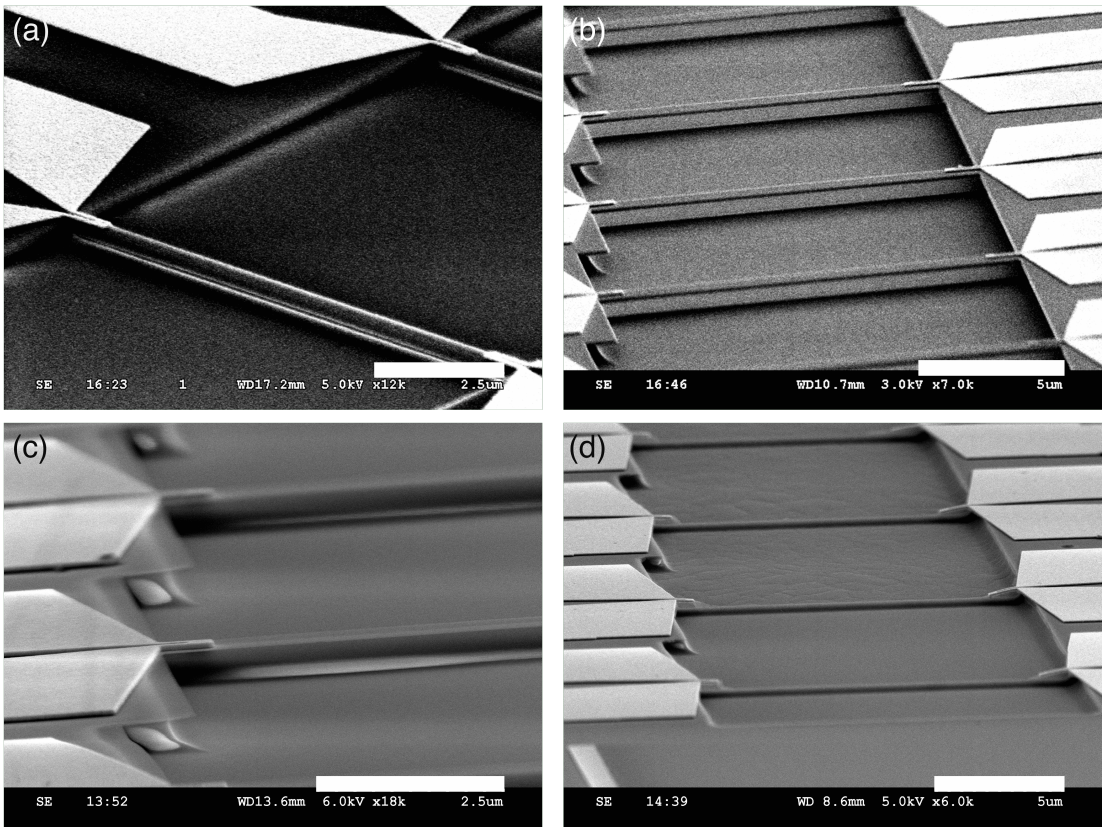


Figure 5.8: Nanobeams fabricated with different thicknesses of Si_3N_4. (a) Original thickness (330 nm). Scale bar: 2.5 µm. (b) 165 nm. Scale bar: 5 µm. (c) 100 nm. Distortions and abnormal bright spots due to local charging effect. Scale bar: 2.5 µm. (d) 80 nm, the beams collapsed. Scale bar: 5 µm.

acceleration and displacement amplitude under a given driving force [166]. As a result, to obtain higher readout signals, a smaller thickness is preferred, and the Si_3N_4 was thinned by RIE to reduce thickness before other fabrication processes. However, the thickness cannot decrease infinitely. The bending stiffness decreases with decreasing thickness, and there is a minimum requirement for bending stiffness to support the free-standing beam with a high aspect ratio. Therefore, there must be a minimum thickness to ensure that the bending stiffness is not too small. Furthermore, although thinner beams improve motional impedance, they are also more susceptible to anchor loss, where vibrational energy is radiated into the supports and substrate, particularly at higher mode frequencies or lower beam stiffness [102]. As the minimum bending stiffness is difficult to quantify, the minimum thickness is determined through experiments.

The nanobeam fabricated using the original unetched Si_3N_4 layer (330 nm) is shown in Figure 5.8 (a). It is very thick and difficult to operate, hence it did not give any meaningful readout signals. Figure 5.8 (b) shows the fabricated nanobeam array, where the thickness of the nitride is etched to 165 nm. The thickness of Si_3N_4 is halved and is visibly thinner under SEM. The nanobeams appear to be straight and suspended, indicating that the thickness is still large enough to provide the necessary bending stiffness to support the beams. Although it did not provide the expected readout signals, it indicated that the original thickness is more than enough for the bending stiffness and that it is possible to decrease the thickness of the nanobeams further. The Si_3N_4 was then etched further down to 100 nm, and the suspended nanobeam with a thickness of 100 nm is shown in Figure 5.8 (c). From the SEM image, the Si_3N_4 layer becomes semi-transparent. This is because electrons are able to penetrate through the thin enough Si_3N_4 layer, reach the silicon oxide substrate, and generate signals from the oxide layer [167]. There are also distortions and abnormal bright spots in the SEM image caused by the local charging effect from the insulating nitride and oxide under the SEM. Although the thickness is very small, the beams are still straight and taut, indicating that they have adequate bending stiffness to support the beam. However, the resonance of the nanobeam was still not observed in the measurements of the 100-nm thick nanobeams; thus, a fourth attempt was made to further reduce the thickness.

In the fourth attempt, the thickness of Si_3N_4 was reduced to 80 nm, and the nanobeams fabricated with the 80 nm thick Si_3N_4 are shown in Figure 5.8 (d). The nanobeams collapsed, the gold electrodes bent downwards, and the Si_3N_4 layer was barely visible. It indicates that the thickness is too small and that the bending stiffness of the beam is no longer enough to support the suspended structure. The overly small bending stiffness leads to the collapse of the nanobeams during the drying of the liquid due to capillary pressure. Hence, it is learnt that 80 nm is too thin for the suspended nanobeam structure, 100 nm is chosen to be the smallest width, and all devices in the measurement section have a thickness of 100 nm.

5.3.5 Buffered Oxide Etch

In this work, the buffered solution used in BOE is a 5:1 buffered hydrofluoric acid. It refers to 5 parts by weight of 40 $wt\%$ ammonium fluoride (NH_4F, the buffer) to 1 part by weight of 49 $wt\%$ hydrofluoric acid (HF, the etchant). In total, the solution contains around 33 $wt\%$ ammonium fluoride and 8.3 $wt\%$ hydrofluoric acid [168]. The rate of this commercial buffered etchant has been reported to be around 100 nm/min at room temperature [168]. However, since the nanobeams need to be free-standing, they must be released from the silicon oxide substrate, and the BOE must etch away all the oxide underneath the nanobeam that is attached to it, i.e., undercut. The time needed is difficult to estimate due to diffusion-limited transport, geometric constraints, and surface depletion effects, and thus is better determined through experiments [168, 169].

Firstly, beams of different widths and lengths for the testing device were designed. After lithography and development, the mask is shown in Figure 5.9 (a). In this design, the widths of the beams are 0.4, 0.5, 0.6 and 1 µm, and the length was swept from 4 to 24 µm. Subsequently, the chip was dry etched using RIE and the recipe specified in the appendix to fully remove the exposed nitride, leaving beams made of Si_3N_4 on top of silicon oxide. This device was etched with BOE for 3 minutes, then dipped in deionised (DI) water, acetone, and IPA each for 15 seconds. The chip is dried using nitrogen gas and tissue paper. The SEM images of the beams are shown in Figure 5.9 (b) and (c). Figure 5.9 (b) clearly shows a gap between the 4 µm long beam and the oxide underneath, indicating that the beam has been successfully released and is now suspended. Figure 5.9 (c) also shows the successful release of the 0.6 µm wide, 24 µm long beam. For such a large aspect ratio between length and width (24:0.6=40), the beam is subject to collapse due to capillary forces during the drying process after BOE [80]. The fact that this beam did not collapse suggests that the nitride film has adequate bending stiffness to construct beams, even with a large aspect ratio of around 40. However, in both SEM images, there are large pieces of residue around the etched areas, and they could not be washed away with acetone or IPA. Their crystalline morphology suggests that they could

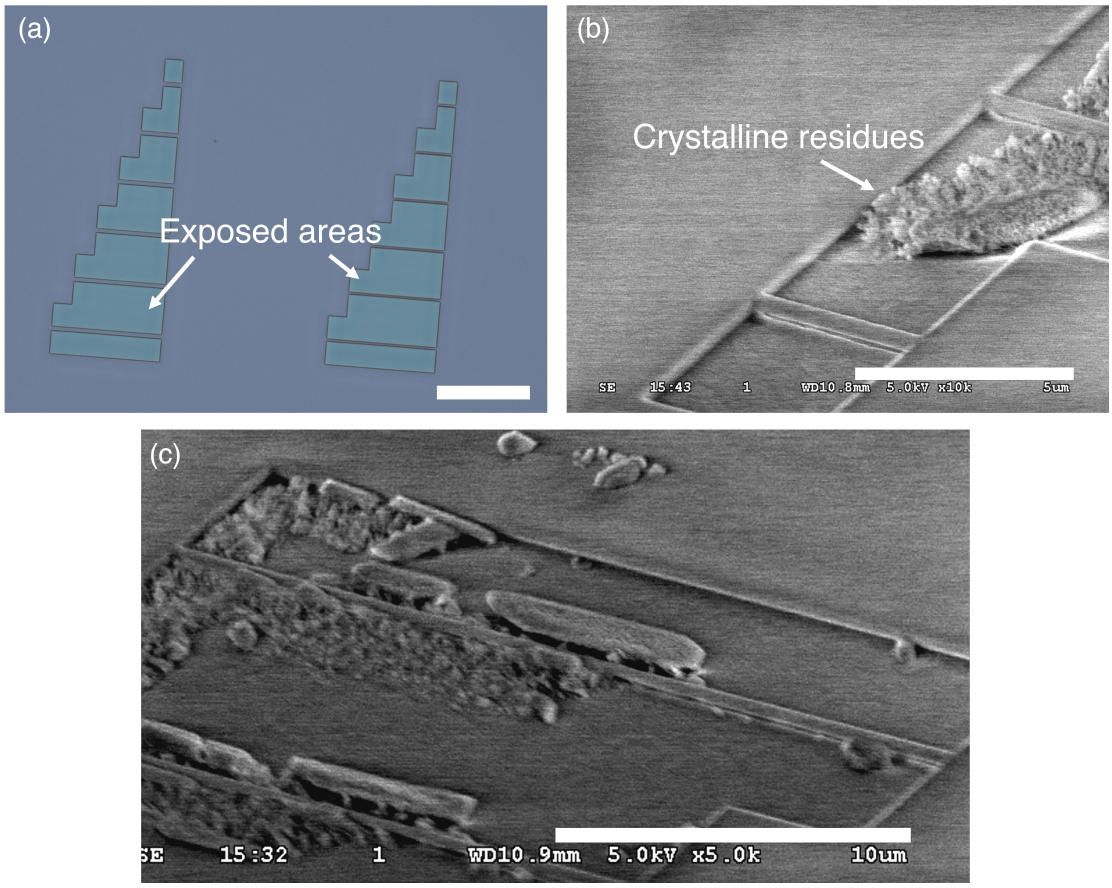


Figure 5.9: (a) Developed mask of the lithographically defined beams of different widths and lengths. The Si_3N_4 in the exposed areas would first be etched via RIE to expose oxide, and the oxide would then be etched via BOE. Scale bar: 20 µm. (b) and (c) SEM image showing BOE etched beams with 3 minutes of etching. (b) A beam with 0.6 µm width and 4 µm length showing a suspension (gap between the beam and the substrate). Scale bar: 5 µm. (c) A beam with 0.6 µm width and 24 µm length also showing suspension, but also the large amount of residues around the etched areas. Scale bar: 10 µm.

be ammonium salt crystals, specifically ammonium fluoride (NH_4F) or ammonium fluorosilicate ($(NH_4)_2SiF_6$) [79]. Ammonium fluoride is the buffering agent and can precipitate during drying, while ammonium fluorosilicate is the byproduct of the reaction between HF and SiO_2. They both appear as crystals under SEM and are insoluble in acetone or IPA but are soluble in water or dilute acids [79]. The reason these salt crystals were not removed or rinsed away in the first DI water rinse after HF could be that the water contained a large amount of dissolved ammonium salt, and the remaining water still leads to salt crystal deposition.

Hence, another DI water rinsing step was added after the IPA and acetone

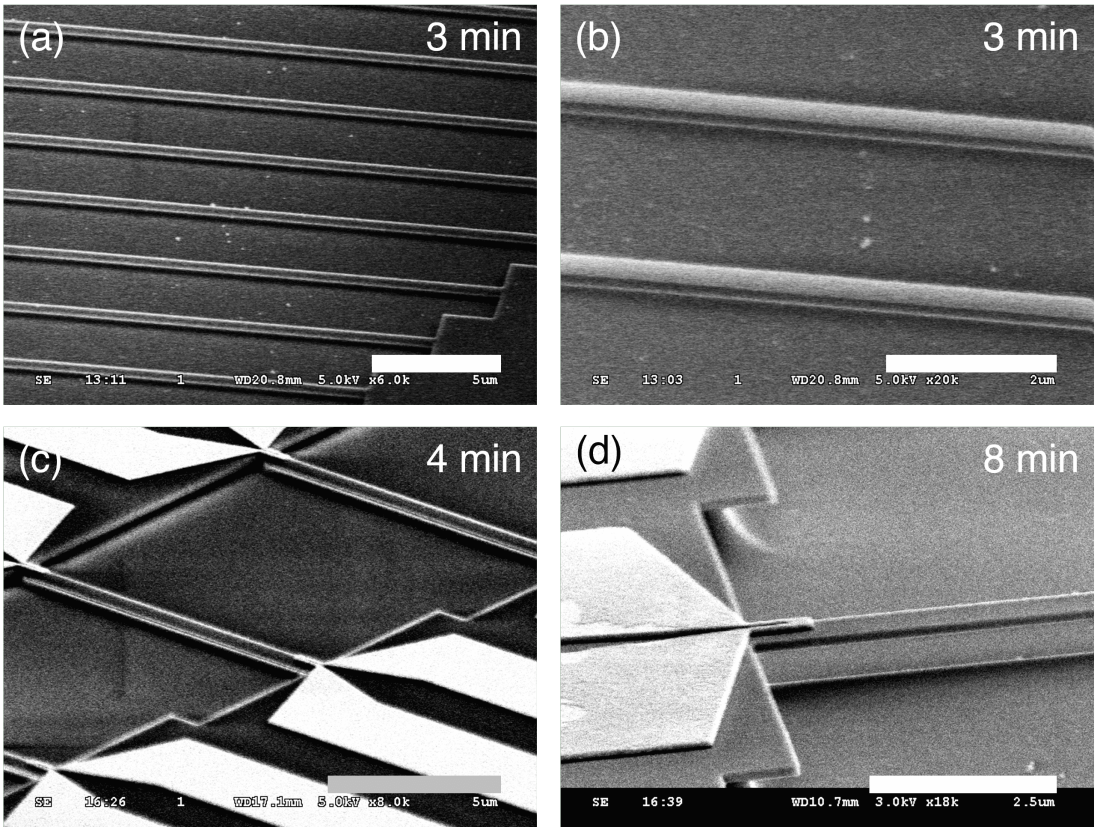


Figure 5.10: (a) SEM image of the sample after the second BOE run (3 minutes of BOE) where lengths of the beams are increased, and another DI water rinsing step was added. The crystalline residues are not present. Scale bar: 5 µm. (b) Close up image of the sample after the second BOE run. Scale bar: 2 µm. (c) SEM image of a sample with gold electrodes after 4 minutes of BOE. The suspension is visible, but very small. Scale bar: 5 µm. (d) SEM image of a sample with gold electrodes after 8 minutes of BOE. The suspension is large, showing complete release of the Si_3N_4 beam. Note that the thickness of nitride is also thinner, since the first RIE step is added for this sample. Scale bar: 2.5 µm.

rinsing steps to help remove ammonium salt residues. In the second run, the etching time was kept the same, but the lengths of the beams were increased to test the limit of the aspect ratio. As shown in Figure 5.10 (a) and (b), crystalline residues are not present, suggesting that the additional DI water rinsing step has successfully removed them. However, the suspension of the beams is not as obvious as in the previous run, and this could be due to the variation in the concentration of the etchant, which leads to different etching rates. As a result, the etching time for the following runs should be increased to ensure the obvious suspension of the beams.

Since the etching rate of Si_3N_4 is much smaller than that of silicon oxide (ratio

of 1:20 to 1:50) [170]. As long as the thickness of the nitride film is not too small, the etching time can be safely increased to ensure the complete release of the beams. The etching time is increased to 4 min for the next sample, and the SEM image of the sample after BOE is shown in Figure 5.10 (c). The suspension is slightly larger, as indicated by the more obvious gap and shadow under the nanobeams. Unlike the bare nanobeams in Figure 5.10 (a) and (b), the electrodes are patterned at both ends of this sample. Because the actuation and readout electrodes are made of gold, which has a negligible etching rate under BOE, the electrodes are patterned before BOE in this sample to investigate whether BOE would affect the quality of the gold electrodes and the chromium adhesion layer. In the SEM image, the gold electrodes remain intact without peeling off from the substrate, and the surface of the electrodes does not seem to be damaged by the BOE process. Furthermore, if BOE was performed before metal deposition, spin coating, development, and removal of the organic electron-beam resist would be carried out after the release of the beams. These processes could possibly exert further capillary pressure on the suspended beams and cause collapses, or leave organic residues under the suspended beams that damp the mechanical vibrations of the beams [81]. To increase the suspension gap between the nanobeam and the silicon oxide substrate, the etching time is further increased to 8 min, and the etched nanobeam is shown in Figure 5.10 (d). The suspension of this sample is much more obvious and visible, with a large gap between the nanobeam and the substrate. The electrodes and the Si_3N_4 film survive the 8-minute BOE, thus 8 min is determined to be the optimum BOE time for the following devices.

5.3.6 Failed Fabrications

Many fabrication rounds failed for various reasons. In the first design, the dimensions of the actuation and readout electrodes approach the resolution of the EBL system, and any defocus of the electron beam could cause imperfections in the electrodes. As shown in Figure 5.11 (a), during lithography, the electrode loop was not properly written by the EBL process due to defocus, thus the actual electrode does not have

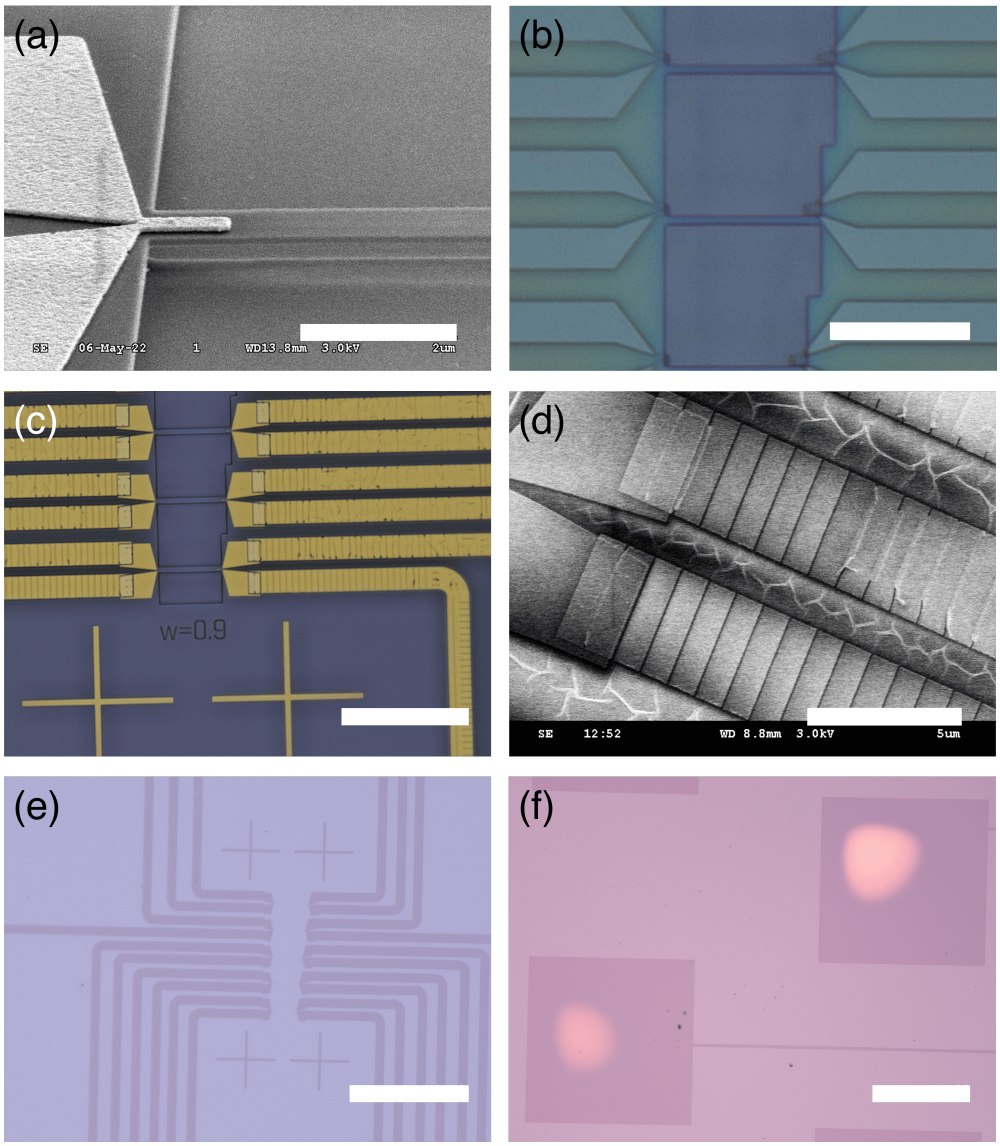


Figure 5.11: Images of failed fabrications. (a) SEM image of a device with improperly patterned electrode with an unopened loop. Scale bar: 2 µm. (b) Image of a device where the mask for electrodes and routings misaligned with the nanobeams. Scale bar: 10 µm. (c) Image of a device where the deposited gold layer is patterned with vertical and horizontal lines. Scale bar: 20 µm. (d) SEM image of the same sample in (c), showing the gaps between the segments of gold. Scale bar: 5 µm. (e) Image of a device where the deposited gold layer disappeared after the lift-off process. Scale bar: 50 µm. (f) Image of a device where a small portion of the deposited gold layer remains. Scale bar: 100 µm.

the loop pattern and could not be used for actuation or readout. These problems are addressed in the design of the second iteration, where the dimensions of the electrodes are increased, and the focus was adjusted more carefully during the EBL process.

In the first design, there were no local markers to increase the accuracy of the alignment for the second EBL process, which led to failed fabrication, as shown in Figure 5.11 (b), where the electrodes are misaligned with the nanobeams. This problem was addressed in the second design, where local markers were introduced to avoid misalignment.

In one of the later fabrication rounds, the gold routings that connect the electrodes and contact pads were found to be periodically segmented, as shown in Figure 5.11 (c). Under SEM, as shown in Figure 5.11 (d), there are gaps between neighbouring segments, indicating that the segments are likely to be electrically isolated from each other; thus, the device could not be used. The reason for these periodic segments could be that the JEOL EBL system fractures large polygons, like the routing pattern, into field-aligned rectangles and exposes them field-by-field. Any mis-calibration of the deflection scale, inadequate field-overlap, or delays at sub-field edges in the setting produce dose discontinuities. Since the resist in the areas does not receive an adequate dose, it remains after development and appears as periodic seams across all lines, which later lead to gaps after lift-off [171]. The routings in this device were written using the smallest aperture and current mode (100 pA, AP4) of the EBL system. The small current has the highest resolution, but it takes the longest writing time, and long writes exacerbate thermal drift and intrafield deflection distortion, increasing both mean and random stitch errors. The long writing time and deflection distortion over the writing duration finally caused some parts of the resist to be underexposed, leading to the formation of stitching errors and periodic seams [171]. In later fabrications, routings were written with a larger aperture and current mode (3 nA, AP3) to decrease the writing time, and an additional calibration step was added before the exposure to minimise deflection.

In another round of fabrication, after gold deposition and subsequent lift-off, the gold layer was found to have disappeared, as shown in Figure 5.11 (e). The patterns

for electrodes, local markers, and routings remained, but the dull colour suggests that the gold layer has been removed, leaving chromium (most likely oxidised) behind. A small portion of the gold layer remained in larger areas, such as the contact pads, as shown in Figure 5.11 (f). The boundaries of the remaining gold are blurred, suggesting that the removal of gold may have started from the edges of the pattern and gradually progressed to the central areas. The reasons could be related to the remover used during the lift-off process after the deposition of gold and chromium. For this sample, 80 nm of gold was deposited with a 5 nm chromium adhesion layer. Subsequently, REM 700, a mildly alkaline DMSO-based remover with pH $\approx$ 8, was used as the remover, and the chip was left in the remover at 50 °C for more than 20 hours. This alkaline environment provided by REM 700, elevated temperature, and prolonged soaking time together facilitated the corrosion and dissolution of chromium and its oxide [172, 173]. Mechanical delamination at already-fragile Au/Cr edges easily occurs in this environment. However, these conditions are not harsh enough to strip the entire layer of chromium or oxides, which is why it remains intact [172]. To address this problem, Remover 1165 was used instead of REM 700, and the soaking time was reduced to 3 hours. Remover 1165 is a NMP-based neutral remover, which is less likely to attach chromium, and the reduced soaking time decreases the chances of chromium corrosion.

5.4 Actuation and Readout

After the fabrication procedures, the filter bank device is ready for measurement. As mentioned previously, thermoelastic actuation and piezoresistive readout methods will be used. The displacement of the beam caused by the thermoelastic actuation method was analysed. The set-ups used to characterise the device and the measurement results are demonstrated in this section.

5.4.1 Measurement Results

A setup similar to Figure 1.7 (b) is used with some modifications. Since the eigenfrequencies of the beams are expected to lie within the working range of the

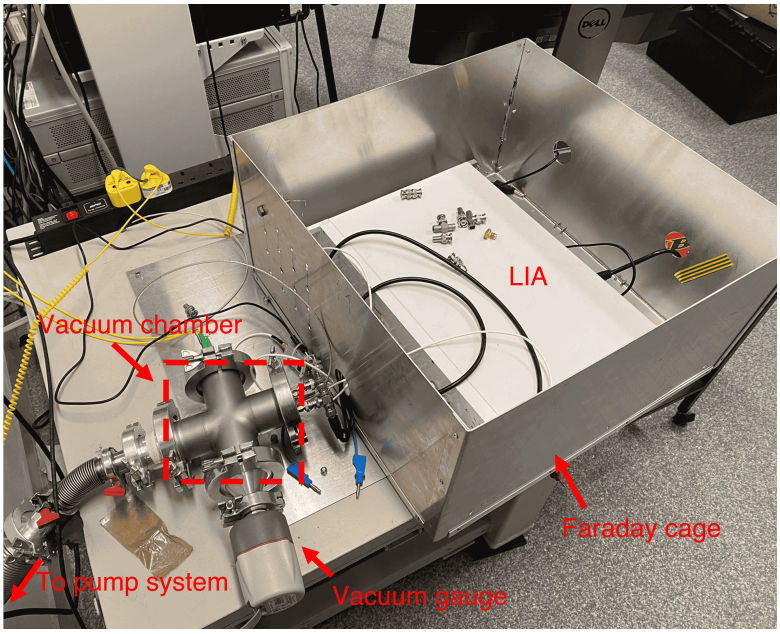


Figure 5.12: An image of the setup used to characterise the filter bank device.

LIA, down-mixing is not necessary. An image of the setup is shown in Figure 5.12. The device is placed inside the vacuum chamber, which is modified from an aluminium cross vacuum fitting, to reduce the damping effect of air molecules. The electrical contacts from the device are connected to a feedthrough flange with 7 SMA connectors. An LIA shielded by a Faraday cage is used to drive and readout the device.

The scheme used to detect the response of a single beam is shown in Figure 5.13 (a). Suppose that the resonant frequency of interest of the beam is f, then the AC driving voltage sent to the thermoelastic actuation electrode should have a frequency of $f/2$. To read out the frequency response, a DC voltage is applied to the readout electrode; hence, the variation of the resistance of the readout electrode loop would lead to a small AC component in the current. The DC-blocking capacitor, removes the DC component in the current for more robust AC measurements. The AC component is measured by the LIA referenced at the second harmonic, as described in Chapter 2. In the experiment, the LO frequency of the LIA is set to $f/2$, and the demodulator is set to the second harmonic of the LO, which is at f, so that the input to the LIA which is at f can be read properly.

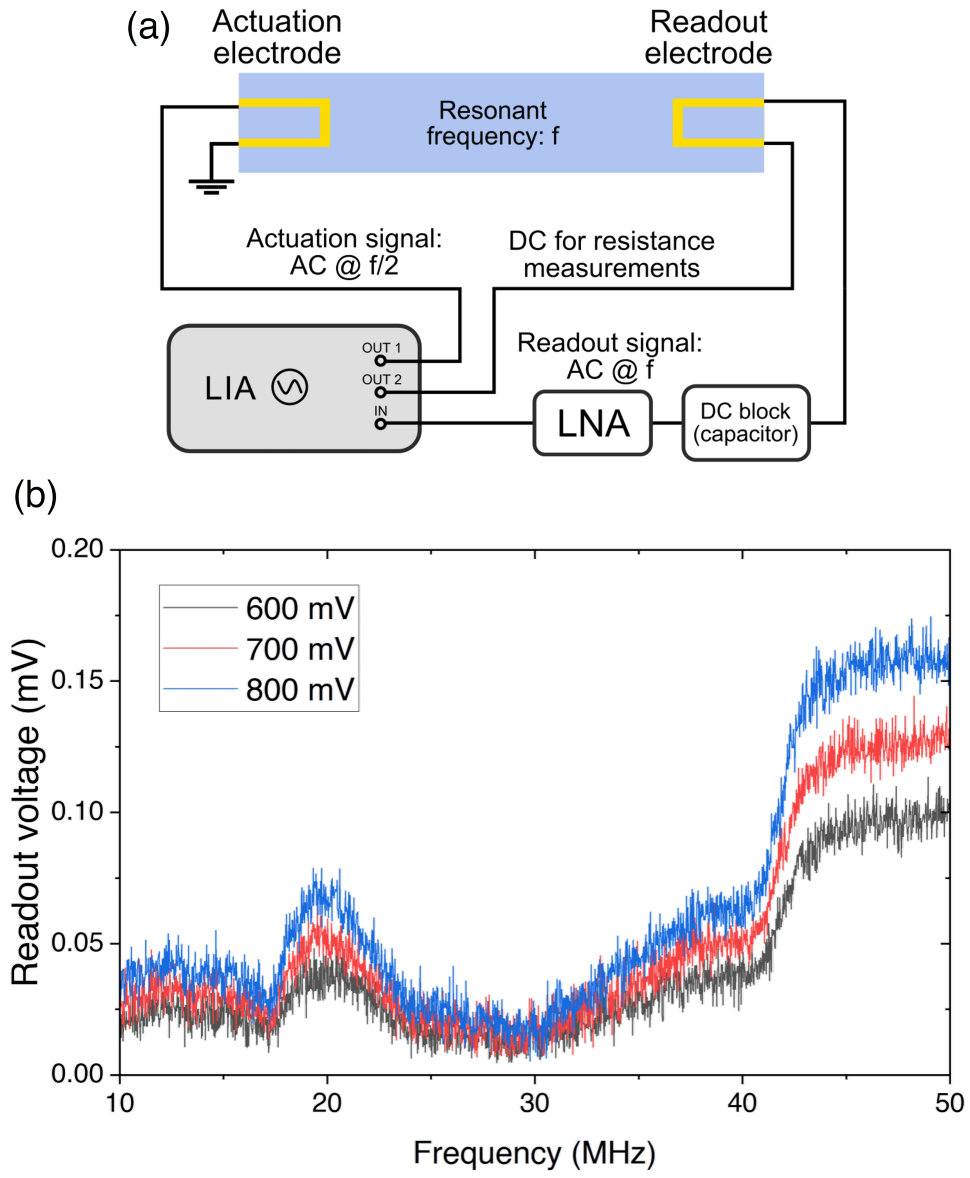


Figure 5.13: (a) The schematics used for thermoelastic actuation and piezoresistive readout the device. LIA: lock-in amplifier; LNA: low-noise amplifier. (b) Readout signal of a single beam using the setup. The DC voltage on readout electrode is 100 mV. The expected resonant frequency of the measured beam is 12.88 MHz.

The measured readouts are shown in Figure 5.13 (b) where the actuation voltage (for thermoelastic actuation) increases from 600 to 800 mV and the readout voltage is 150 mV. The device measured here is a beam with the same dimensions as in Figure 5.3, hence the expected resonant frequency is 12.88 MHz. However, there is no peak with high quality factor in the graph that could be related to the Si_3N_4 nanomechanical resonator. The background noise level in this actuation and readout scheme is low (sub mV) because the output (signal for actuation) of the LIA is not at the same frequency as the demodulator frequency. Otherwise, the output signal can easily couple to the input of the LIA through the common ground shared by the electrical connections, resulting in a very high noise level and making the measurements very difficult.

The measurement through thermoelastic actuation and piezoresistive readout methods was not successful, suggesting that either the actuation or the readout method was ineffective. To troubleshoot, one of the methods should be bypassed to verify whether the other method is effective. In this case, the piezoresistive method is difficult to bypass since adding other readout methods requires more delicate designs and efforts. The most feasible alternative method would be to replace the thermoelastic actuation method with an indirect piezoelectric actuation method by glueing a piezoelectric stack underneath the device chip. To use piezoelectric actuation, the setup is modified with schematics as shown in Figure 5.14 (a). The local oscillator (LO) frequency of the LIA is set to f, the same as the demodulator frequency, and the sine wave output is amplified by the high power amplifier (HPA) (45 dB voltage amplification, Mini-Circuits) and then sent to a PZT piezoelectric stack (PA4FKW, Thorlabs) glued to the bottom of the chip as the actuation signal. The readout part remains the same as before. The measurement results are shown in Figure 5.14, and no high Q peak is observed. The noise level here is much higher than that of the thermoelastic actuation method because the output at f is coupled to the input of the LIA and is picked up by the LIA. Due to the very high noise level, even if there is a peak due to mechanical resonance, the peak would have been buried under the noise.

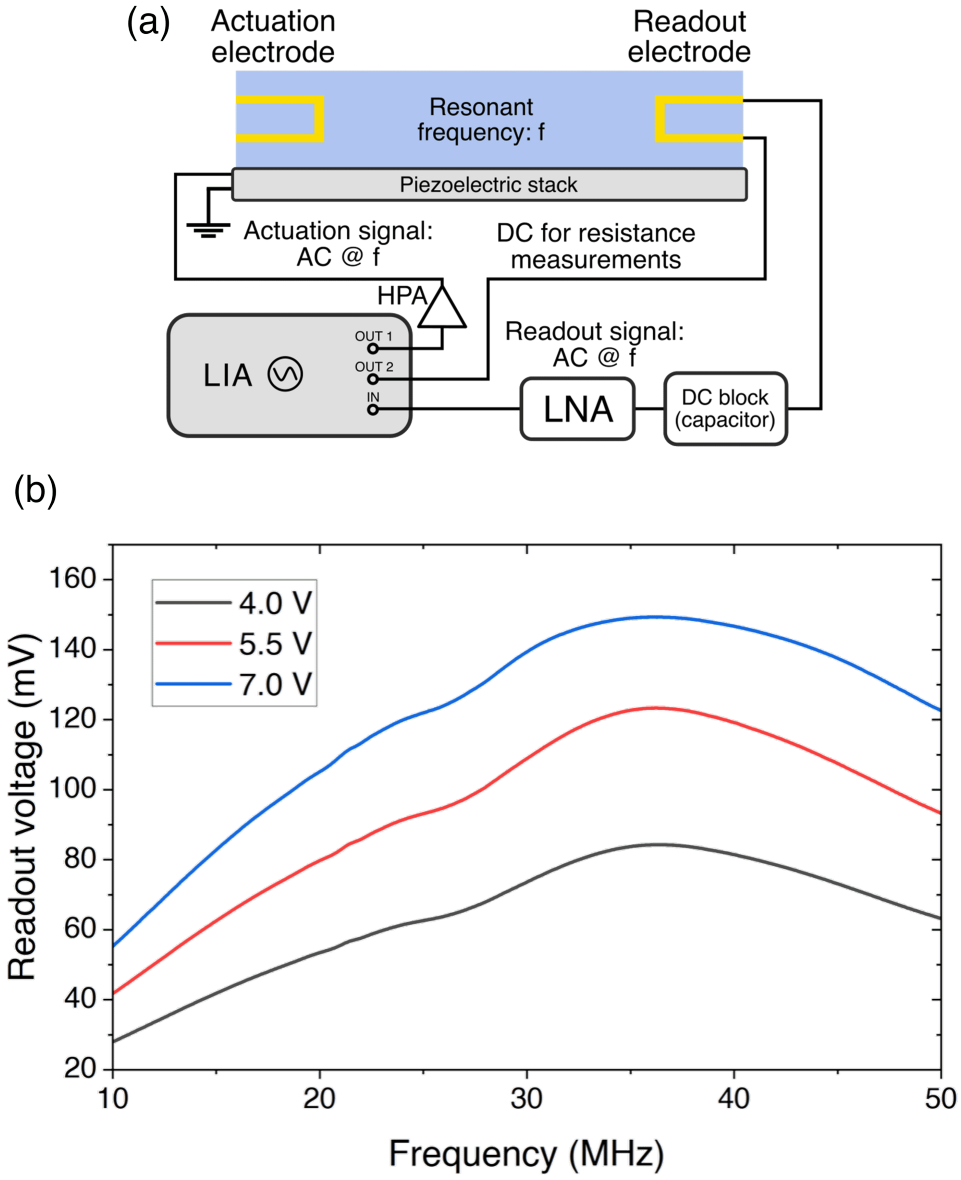


Figure 5.14: (a) The schematics used for indirect piezoelectric actuation and piezoresistive readout the device. HPA: high-power amplifier. (b) Readout signal of a single beam with indirect piezoelectric actuation and piezoresistive readout methods. The expected resonant frequency of the measured beam is 12.88 MHz.

5.5 Reasons of Failure

Although the fabrication was successful after some iterations and the actuation and readout methods have been proven to be effective for a similar device, this study was not successful. The resonance of a single resonator was not readout successfully, and there was no point in continuing the measurements for multiple resonators. Several possible reasons why the measurements failed are discussed.

5.5.1 Tensile Stress in the Silicon Nitride Film

A probable reason could be that there is residual tensile stress in the LPCVD-grown Si_3N_4 film, and the tensile stress effectively increases the mechanical resonant frequency by adding tension to the resonator. The high tensile stress exists due to the high-temperature and low-pressure chemical reactions involved in its synthesis [174]. The precise stress level depends on the deposition temperature, the gas flow, and the stoichiometry of the film. However, the stress within the film is very hard to quantify, and the exact increase in the resonant frequency is also difficult to determine. Tensile stress in the LPCVD-grown Si_3N_4 film has been reported to be above 1 GPa [174–176]. The effect of tensile stress on the eigenfrequency can be calculated [81]:

$$f = f_0 \cdot \sqrt{1 + \frac{\sigma A L^2}{\beta_n^2 E I}} \tag{5.21}$$

where f_0 is the resonant frequency of the unstressed beam, σ is the tensile stress in the beam, A is the cross-sectional area, L is the beam length, ρ is the mass density of beam material (3100 kg/m^3 for Si_3N_4, COMSOL library), β_n is the dimensionless mode-dependent constant (for the first flexural mode of a doubly clamped beam, $\beta_1 = 4.730$), E is the Young's modulus (250 GPa for Si_3N_4, COMSOL library), and I is the second moment of area (for out-of-plane bending of a rectangular beam, $I = wt^3/12$) [81].

With this equation, the eigenfrequency of the stressed free-standing Si_3N_4 beam can be estimated. A tensile stress of 1 GPa is assumed, and the example shown in Figure 5.3 with a thickness of 200 nm, a length of 12 µm and a width of 600 nm

is used. The eigenfrequency of the unstressed beam is 12.88 MHz. With a tensile stress of 1 GPa, the eigenfrequency of the beam is estimated to be 38.04 MHz, which is approximately 3 times the original frequency. Though it is still within the working range of LIA and should be readout, it has largely deviated from the expected frequency. If another beam is designed to have a resonant frequency of 40 MHz, the resonant frequency under stress can easily fall outside the working range. The tensile stress used here is also an estimate from other sources, while the actual tensile stress inside the Si_3N_4 film can be higher, which would cause a larger increase in the resonant frequency.

Moreover, stress gradients across the film thickness, caused by thermal gradients or non-uniform deposition, can induce curvature or warping of the beam, further altering the effective stiffness and reducing the signal-to-noise ratio in the readout [80]. High tensile stress also tends to suppress non-linearities, limiting the dynamic range and reducing the amplitude of vibration under small driving forces [177].

5.5.2 Inadequate Transduction Efficiency

Another plausible explanation for the failure to detect the mechanical resonance lies in the insufficient efficiency of the actuation and readout schemes, which are critical for converting electrical signals into mechanical motion and subsequently transducing the mechanical response back into the electrical domain.

Problems in Thermoelastic Actuation

Thermoelastic actuation relies on efficient heat transfer from the Joule-heated metal layer into the resonant structure to induce thermal expansion and mechanical oscillation. However, in nanoscale dimensions, the interfacial thermal resistance (ITR, also known as thermal boundary resistance or Kapitza resistance) at the metal-dielectric interface becomes significant [178]. Studies have shown that ITR can impede thermal energy flow across metal-dielectric boundaries such as Au/Si_3N_4, resulting in reduced or delayed thermal actuation [179]. The quality of the metal-substrate interface depends on surface cleanliness, roughness, and the use of adhesion

layers, such as chromium. In this study, chromium was indeed employed as an adhesion layer between the gold actuator and the Si_3N_4 beam to promote interfacial bonding and enhance thermal energy transfer. Although this approach aligns with established best practices, it is noteworthy that the thickness of the gold electrode in this design (80 nm) is much greater than that typically reported in the literature, which commonly employs values around 30 nm [54].

This increased thickness can have several unintended effects. Firstly, a thicker gold film increases the thermal mass of the actuator, reducing the rate at which it heats and cools under AC excitation. As thermoelastic actuation relies on rapid temperature modulation to drive mechanical motion, an elevated thermal time constant may weaken the amplitude of mechanical oscillation, particularly at higher frequencies [180]. Secondly, the mismatch in the thermal expansion coefficients between gold and Si_3N_4 can generate greater interfacial stresses in thicker films, increasing the risk of delamination or stress relaxation over time [181]. Although thicker films can reduce electrical resistance and improve mechanical robustness, the trade-off in thermal and dynamic response may outweigh these benefits in the context of high-frequency NEMS resonators, leading to failed actuation.

Problems in Piezoresistive Readout

The effectiveness of the piezoresistive readout method critically depends on the intrinsic piezoresistive properties of the material (i.e., its gauge factor). The Gauge factor is defined as the ratio of the relative change in electrical resistance to the mechanical strain applied to the strain sensor, in this study, the gold electrode. However, gold thin films typically have a low gauge factor of around 2 to 4, which is much lower than that of semiconductors such as silicon, whose gauge factors can exceed 100 [182]. Although metallic strain gauges are robust and widely commercialised, metals generally have small gauge factors, and metallic strain gauges are not as sensitive as semiconductor strain sensors for nanoscale applications.

Furthermore, there is only one loop in the readout electrode design, which limits the sensitivity and effectiveness of the piezoresistive readout. Having more loops

in the electrode can maximise the length of conductor subjected to strain, thereby increasing the total resistance change for a given amount of strain [183].

5.6 Conclusion

This chapter presents the design, fabrication, and characterisation of a Si_3N_4 nanomechanical resonator array intended for use as an RF filter bank. The concept exploits the dimensional scaling of mechanical resonance frequencies to create multiple bandpass filters on a single chip, offering potential advantages in terms of CMOS compatibility, power consumption, and monolithic integration compared to existing SAW and BAW technologies.

The fabrication process was successfully developed through two design iterations, addressing critical challenges, including electrode patterning at nanoscale dimensions, precise alignment between lithography steps, and the optimisation of BOE for reliable beam release. Key achievements include the demonstration of suspended Si_3N_4 beams with aspect ratios exceeding 40:1 and the development of a reproducible process flow that combines electron beam lithography, reactive ion etching, and wet chemical etching.

However, despite successful fabrication, the electrical characterisation failed to demonstrate clear mechanical resonances using either thermoelastic actuation with piezoresistive readout or piezoelectric actuation. The absence of detectable resonance peaks suggests fundamental challenges in the transduction mechanisms rather than simple fabrication defects. Analysis indicates two primary failure modes: (1) residual tensile stress in the LPCVD Si_3N_4 film, potentially shifting resonance frequencies by a factor of 3 or more beyond the expected values, and (2) insufficient transduction efficiency due to high interfacial thermal resistance and low piezoresistive gauge factor in the gold electrodes.

These findings highlight critical considerations for future NEMS filter development. First, stress engineering through annealing or alternative deposition methods appears essential for predictable frequency control. Second, the transduction scheme requires optimisation, potentially through thinner metal electrodes, alternative

electrode materials with higher gauge factors, or entirely different transduction mechanisms such as capacitive or optical detection. Third, comprehensive mechanical characterisation, including laser Doppler vibrometry, could help decouple fabrication issues from transduction limitations.

While this work did not achieve a functional filter bank, it provides valuable insights into the challenges of integrating multiple transduction mechanisms in high-aspect-ratio NEMS devices. The fabrication procedures developed here, particularly the controlled thickness reduction of Si_3N_4 and the optimised BOE process, represent useful contributions to the broader NEMS community. Future work should prioritise in-situ stress measurement, systematic exploration of the frequency space accounting for stress effects, and investigation of alternative transduction schemes better suited to stressed Si_3N_4 resonators.

6
Conclusion and Outlook

Contents

6.1 Summary of Research 145
6.2 Principal Findings 146
6.2.1 Optoelectronic Filter Bank 146
6.2.2 Electrical Nanomechanical Filter Bank 147
6.3 Implications and Integration 148
6.4 Future Work 149
6.4.1 Optoelectronic RF Filter Bank 149
6.4.2 Electrical RF Filter Bank 150
6.5 Concluding Remarks 152

6.1 Summary of Research

This thesis has advanced two complementary approaches to compact, scalable radio-frequency (RF) filtering for next-generation hybrid electronic-photonic systems. Both routes aim to address the persistent challenge at the RF-photonics interface, where electrical signals must be filtered, channelised, and coupled efficiently into photonic or optoelectronic domains [11–13].

The first route, developed across Chapters 3 and 4, proposed and demonstrated an *optoelectronic multi-channel RF filter bank with a multi-wavelength optical encoder* on a Si_3N_4 photonic integrated circuit (PIC). Each channel combines a high-Q

micro-ring resonator (MRR) with a suspended indium phosphide (InP) nanowire (NW) positioned within the evanescent field. Mechanical motion of the NW perturbs both the real and imaginary parts of the MRRs effective index, thereby modulating the optical resonance and mapping RF passbands $\{f_i\}$ to optical wavelengths $\{\lambda_i\}$. This architecture demonstrated multi-wavelength optical encoding of RF signals on a PIC, addressing the limited scalability of conventional electro-optic and acousto-optic RF filters [105, 106].

The second route, detailed in Chapter 5, explored an *electrical nanomechanical filter bank* implemented in Si_3N_4. Building on Euler-Bernoulli beam theory and the thermoelastic-piezoresistive transduction scheme established by Bargatin *et al.* [54], an array of lithographically defined doubly-clamped nanobeams was designed to provide multiple RF bandpass responses through systematic variation of beam length and thickness. The devices were fabricated using a fully CMOS-compatible process comprising reactive-ion etching (RIE), two-step electron-beam lithography, metallisation, and buffered oxide etching (BOE) release. The resulting Si_3N_4 beams showed clearly visible suspension and achieved aspect ratios exceeding 40:1, confirming process reliability and reproducibility.

Together, these two routes offer complementary strategies for scalable RF filtering and channelisation: one focuses on electronic-photonic interfacing, the other on electrical compactness and integration fidelity.

6.2 Principal Findings

6.2.1 Optoelectronic Filter Bank

The eigenfrequency solver of COMSOL confirmed the mode shape of the NW resonance. FDTD and numerical Lorentzian analyses confirmed that NW displacement within a near-field gap (within 50 nm) induces measurable changes in both n_{eff} and k_{eff}, producing the characteristic asymmetric difference spectra observed between the peak and trough positions of the mechanical vibration. Fabricated two-channel prototypes validated these predictions experimentally, with thermally driven resonances identified near 15.5 MHz and 30.0 MHz, and wavelength-selective optical

recovery of modulated RF signals at distinct optical carriers. Two-channel RF filtering with multi-wavelength optical encoding is demonstrated by recovering mixed AM audio and triangular envelopes. These results represent a first demonstration of multi-channel RF filtering combined with multi-wavelength encoding using suspended InP NWs on a Si_3N_4 PIC.

However, several limitations were also established. Evanescent coupling inevitably introduces excess scattering loss, degrading ring Q and extinction ratio; residual thermal drift under vacuum complicates detuning stability; and bulk PZT actuation excites unwanted substrate modes. Nevertheless, the demonstration verifies that mechanically mediated RF filtering can be achieved directly within a low-loss photonic cavity and extended to multiple wavelength channels, thus bridging a critical gap in integration of microwave photonics and RF network [11].

6.2.2 Electrical Nanomechanical Filter Bank

Chapter 5 realised a fully electrical route towards multi-channel RF filtering. The numerical model estimates the expected readout amplitude from the actuation and detection efficiencies, though the result relies on several simplifying assumptions. A comprehensive fabrication workflow was developed through two design iterations. The second iteration introduced local alignment markers, separated high-resolution electrode writing from low-resolution routing, enlarged pad geometries for wire-bonding, and removed shared ground pads. These improvements significantly increased reproducibility. Systematic optimisation of RIE thinning and BOE release identified a practical lower limit of 100 nm for Si_3N_4 thickness: thinner films (80 nm) collapsed due to capillary forces, while thicker films (>165 nm) yielded insufficient displacement amplitude.

Although the fabrication was successful, the electromechanical characterisation did not yield resolvable resonance peaks under either thermoelastic or indirect piezoelectric actuation. Critical analysis points to three interacting factors:

1. **Residual tensile stress** in LPCVD Si_3N_4 films (>1 GPa) could increase eigenfrequencies by up to threefold, likely shifting resonances beyond the measured band [174, 175].

2. **Low transduction efficiency**, limited by interfacial thermal resistance at the Au/Si_3N_4 boundary and the low gauge factor of gold thin-film readouts (GF $\approx$ 2-4) [182].

3. **High actuator thermal mass**, as 80 nm Au electrodes exhibit longer thermal time constants, reducing actuation efficiency at MHz frequencies [180].

Despite the absence of a clear mechanical response, this work yielded several enduring outcomes: (i) a verified lithographic design space for Si_3N_4 NEMS beams in the 5-50 MHz regime; (ii) a validated process for controlled nitride thinning and residue-free BOE release; and (iii) an analytical thermal-mechanical model linking actuation power to displacement and readout voltage via the concept of complex thermal admittance [145, 146]. These results establish a solid foundation for subsequent optimisation and re-implementation.

6.3 Implications and Integration

Viewed together, the two routes form a continuum between electrical compactness and photonic functionality. The Si_3N_4 nanobeam array exemplifies a high-Q, CMOS-compatible electrical filter bank suitable for dense on-chip integration. The Si_3N_4-InP optoelectronic filter bank extends these mechanical filtering principles into the photonic domain, providing direct wavelength-division multiplexing of filtered RF signals. A heterogeneous platform combining the two could, for example, use a purely electrical filter array for coarse pre-selection, followed by optomechanical channelisation for optical encoding [11, 13].

6.4 Future Work

6.4.1 Optoelectronic RF Filter Bank

Future work on the optoelectronic multi-channel filter bank should focus on improving local actuation and advancing NW definition techniques to enhance device stability, scalability, and transduction fidelity. Two particularly promising directions are outlined below.

Localised and mode-selective actuation. In the current architecture, the NW is indirectly driven via substrate-coupled piezoelectric stacks, which often leads to unwanted coupling to global chip modes and introduces parasitic resonances. A more effective approach would employ localised actuation, implemented using thin-film piezoelectric materials such as aluminium nitride (AlN) integrated directly on the PIC [184, 185]. AlN thin films, when patterned adjacent to the NW supports, can generate strong, spatially confined strain fields in response to an applied RF signal, enabling controlled excitation of the fundamental out-of-plane mode while suppressing spurious vibrations and largely reducing energy consumption [186, 187]. Integrating local piezoelectric actuation would significantly enhance the signal-to-noise ratio of mechanical modulation, improve overall frequency selectivity and reduce drive amplitude, while remaining compatible with standard CMOS and photonic integration processes.

3D NW fabrication via two-photon polymerisation. Another major limitation of the current platform lies in the manual pick-and-place process used to transfer the InP NWs onto the PIC. This approach, while viable for proof-of-concept demonstrations, is inherently limited in throughput and reproducibility, and constrains the achievable placement precision to the micron scale. To overcome these constraints, future work should explore the use of three-dimensional nanoprinting based on two-photon polymerisation, also known as direct laser writing on polymer resists, using systems such as the Nanoscribe Quantum X. This technique enables sub-micrometre resolution and allows direct definition of overhanging polymeric NWs on

the PIC surface with precisely controlled geometries, including diameter, curvature, and suspension height [188, 189]. There is a wide choice of polymer photoresins with distinct mechanical and optical properties, resulting in variations in both resonant frequency and optical coupling [190]. By optimising the NW dimensions accordingly, precise channel definition and targeted frequency-wavelength mapping can be achieved. Such a process would eliminate manual alignment errors, greatly increase device yield, achieve accurate control of dimensions and frequencies, and facilitate large-scale fabrication of multi-channel arrays with uniform coupling gaps and consistent mechanical responses.

Together, these developments represent key steps towards a fully monolithic and scalable optoelectronic filter bank. By confining actuation to the NW level and replacing manual assembly with lithographically defined 3D fabrication, future iterations of the device could achieve robust, low-noise, and reproducible RF-to-optical transduction across densely multiplexed channels, paving the way for practical integration into next-generation microwave photonic systems.

6.4.2 Electrical RF Filter Bank

Future development of the lithographically defined Si_3N_4 nanomechanical filter bank should focus on three key directions: stress engineering and frequency predictability, enhanced transduction efficiency, and potential hybrid photonic-mechanical integration.

Stress engineering and frequency predictability. Residual tensile stress in LPCVD-grown Si_3N_4 films, often exceeding 1 GPa, has been identified as one of the factors affecting the mechanical resonance frequency and stability of nanobeams [174, 176]. While such stress can increase the quality factor Q by suppressing internal friction, it simultaneously shifts resonance frequencies away from the designed values, reducing predictability and complicating multi-channel filter design. Future efforts should concentrate on systematic stress characterisation and control. This can be achieved through pre- and post-deposition annealing, tuning of stoichiometry

during LPCVD, or using plasma-enhanced deposition at lower temperatures to moderate intrinsic film tension [191–193]. The stress intensity across the film could be characterised using wafer curvature measurements based on the Stoney equation to obtain the global average stress, complemented by micro-cantilever deflection analysis to resolve local variations arising from non-uniform film tension [194–196]. Implementing these techniques will be essential to fabricate predictable and tightly spaced resonance spectra required for scalable RF filter arrays.

Optimisation of transduction efficiency. The performance of the Si_3N_4 resonator array is ultimately limited by the weak coupling efficiency of the thermoelastic actuation and piezoresistive readout scheme. Larger gains can be achieved by introducing alternative transduction mechanisms that provide stronger electromechanical coupling and lower noise floors. One promising direction is the integration of thin-film piezoelectric materials, such as aluminium nitride (AlN) or scandium-doped AlN (AlScN), to enable direct piezoelectric actuation [197]. These materials exhibit strong electromechanical coefficients and are fully compatible with standard CMOS and Si_3N_4 process flows. For the piezoresistive readout, the gold electrode could be replaced with materials exhibiting higher gauge factors, such as silicon and germanium, to enhance piezoresistive sensitivity and overall signal strength [198, 199]. The readout signal can also be enhanced by increasing the effective length of the electrode by adopting serpentine or extended gauge geometries. These methods increase the effective resistive path through the high-strain region and thereby amplify the piezoresistive signal [200]. Developing a more efficient actuation-readout scheme will therefore be key to unlocking the full dynamic range and sensitivity of the nanomechanical filter array.

Hybrid photonic-mechanical co-integration. A longer-term goal for the Si_3N_4 filter bank is its seamless integration with PIC, forming a hybrid optoelectromechanical platform capable of direct RF-to-optical transduction. Such co-integration could take advantage of the well-established Si_3N_4 photonics platform, enabling the mechanical and optical resonators to be fabricated together on the same substrate.

This would not only simplify packaging but also enable new functionalities, such as all-optical readout of mechanical vibrations at different frequencies or wavelength-division multiplexing of filtered RF channels. The convergence of these technologies could yield chip-scale RF photonic processors with low power consumption, broad bandwidth, and reconfigurable channel selectivity. Achieving this integration will require co-optimisation of fabrication steps, particularly ensuring that mechanical release and photonic patterning processes are mutually compatible.

In summary, advancing the Si_3N_4 nanomechanical filter bank towards practical implementation will require improvements in the control of film stress and efficient transduction. If successful, it could serve as a new RF front end for compact, low-power, and frequency-agile communication systems, providing a CMOS-compatible and scalable alternative to conventional MEMS and acoustic-wave filters. It could also be integrated with PIC to harness the advantages of low-loss optical signal processing and wavelength-division multiplexing for multi-band RF applications.

6.5 Concluding Remarks

This thesis demonstrates that mechanically mediated RF filtering can be realised within both electrical and optoelectronic domains. While the InP-on-Si_3N_4 device achieved the first proof of multi-channel RF filtering and multi-wavelength optical encoding, the Si_3N_4 nanomechanical array provided a parallel electrical route highlighting fabrication and transduction challenges in scaling mechanical RF filters. With continued optimisation in stress control, transduction, and integration, these architectures provide a credible pathway towards compact, low-loss, and scalable RF filter banks capable of seamless operation at the RF-photonics boundary.

References

[1] George L. Matthaei, E. M. T. Jones, and Leo Young. *Microwave Filters, Impedance-Matching Networks, and Coupling Structures*. Artech House, 1985.

[2] J Jason Yao. "RF MEMS from a Device Perspective". In: *Journal of Micromechanics and Microengineering* 10.4 (Oct. 2000). DOI: 10.1088/0960-1317/10/4/201.

[3] Henri Hodara and Edvin Skaljo. "From 1G to 5G". In: *Fiber and Integrated Optics* 40.2-3 (May 2021), pp. 85–183. DOI: 10.1080/01468030.2021.1919358.

[4] Kai Yang et al. "Advanced RF Filters for Wireless Communications". In: *Chip* 2.4 (Dec. 2023), p. 100058. DOI: 10.1016/j.chip.2023.100058.

[5] Clemens C. Ruppel. "Acoustic Wave Filter Technology-a review". In: *IEEE Transactions on Ultrasonics, Ferroelectrics, and Frequency Control* 64.9 (Sept. 2017), pp. 1390–1400. DOI: 10.1109/tuffc.2017.2690905.

[6] David Morgan. *Surface acoustic wave filters with applications to electronic communications and Signal Processing*. Elsevier Science, 2010.

[7] Ken-ya Hashimoto. *RF bulk acoustic wave filters for communications*. Artech House, 2009.

[8] Scott S. Verbridge et al. "Macroscopic tuning of nanomechanics: substrate bending for reversible control of frequency and quality factor of nanostring resonators". In: *Nano Letters* 7.6 (May 2007), pp. 1728–1735. DOI: 10.1021/nl070716t.

[9] Reza Abdolvand et al. "Micromachined Resonators: A Review". In: *Micromachines* 7.9 (Sept. 2016), p. 160. DOI: 10.3390/mi7090160.

[10] Johannes Rieger et al. "Frequency and Q factor control of nanomechanical resonators". In: *Applied Physics Letters* 101.10 (Sept. 2012). DOI: 10.1063/1.4751351.

[11] José Capmany and Dalma Novak. "Microwave photonics combines two worlds". In: *Nature Photonics* 1.6 (June 2007), pp. 319–330. DOI: 10.1038/nphoton.2007.89.

[12] G. P. Agrawal. *Fiber-optic communication systems*. John Wiley & Sons, Inc, 2022.

[13] David Marpaung, Jianping Yao, and José Capmany. "Integrated Microwave Photonics". In: *Nature Photonics* 13.2 (Jan. 2019), pp. 80–90. DOI: 10.1038/s41566-018-0310-5.

[14] Submarin Telecoms Forum. URL: https://subtelforum.com/submarine-cable-map/.

[15] Amanda H.A. Watson. "Undersea cables: The Official Perspectives expressed in the Pacific region". In: *Marine Policy* 178 (Aug. 2025), p. 106735. DOI: 10.1016/j.marpol.2025.106735.

[16] Nikolaos Farmakidis, Bowei Dong, and Harish Bhaskaran. "Integrated photonic neuromorphic computing: Opportunities and challenges". In: *Nature Reviews Electrical Engineering* 1.6 (June 2024), pp. 358–373. DOI: 10.1038/s44287-024-00050-9.

[17] DustPhotonics Siro. *History of silicon photonics*. Nov. 2024. URL: https://www.dustphotonics.com/an-overview-of-the-evolution-of-silicon-photonics/.

[18] Tianran Liu et al. "Integrated Nano-optomechanical displacement sensor with ultrawide optical bandwidth". In: *Nature Communications* 11.1 (May 2020). DOI: 10.1038/s41467-020-16269-7.

[19] Kejie Fang et al. "Optical transduction and routing of microwave phonons in cavity-optomechanical circuits". In: *Nature Photonics* 10.7 (June 2016), pp. 489–496. DOI: 10.1038/nphoton.2016.107.

[20] I-Tung Chen et al. "Intermodal microwave-to-optical transduction using silicon-on-sapphire optomechanical ring resonator". In: *Science Advances* 11.37 (Sept. 2025). DOI: 10.1126/sciadv.adx6485.

[21] Rajiv Baby. *What are Radio Frequency Bands and Its Uses?* May 2024. URL: https://www.rfpage.com/what-are-radio-frequency-bands-and-its-uses/.

[22] W. W. Hansen. "A Type of Electrical Resonator". In: *Journal of Applied Physics* 9.10 (Oct. 1938), pp. 654–663. DOI: 10.1063/1.1710371.

[23] Erich Christian. *LC-Filters: Design, testing, and manufacturing*. Wiley, 1983.

[24] Urvashi Sengal and Giri Krishnamurthy. *Understanding Lumped Element Filters - Mini-Circuits Blog*. Mar. 2023. URL: https://blog.minicircuits.com/understanding-lumped-element-filters/.

[25] Arthur Bernard Williams and Fred J. Taylor. *Electronic Filter Design Handbook*. McGraw-Hill, 2006.

[26] Adel S. Sedra et al. *Microelectronic Circuits*. Oxford University Press, 2021.

[27] Wesley A. Gee and Phillip E. Allen. "CMOS Integrated LC RF Bandpass Filter with Transformer-Coupled Q-Enhancement and Optimized Linearity". In: *2007 IEEE International Symposium on Circuits and Systems (ISCAS)* (May 2007), pp. 1445–1448. DOI: 10.1109/iscas.2007.378574.

[28] Sam Benzacar. *Understanding Filter Types and Their Characteristics*. URL: https://anatechelectronics.com/media/wysiwyg/AnaMPD-510.pdf.

[29] Amelie Hagelauer et al. "From microwave acoustic filters to millimeter-wave operation and new applications". In: *IEEE Journal of Microwaves* 3.1 (Jan. 2023), pp. 484–508. DOI: 10.1109/jmw.2022.3226415.

[30] Lord Rayleigh. "On waves propagated along the plane surface of an elastic solid". In: *Proceedings of the London Mathematical Society* s1-17.1 (Nov. 1885), pp. 4–11. DOI: 10.1112/plms/s1-17.1.4.

[31] Chunxiao Jiao et al. "Finite element analysis model of electronic skin based on Surface Acoustic Wave Sensor". In: *Nanomaterials* 13.3 (Jan. 2023), p. 465. DOI: 10.3390/nano13030465.

[32] R. M. White and F. W. Voltmer. "Direct Piezoelectric Coupling to Surface Elastic Waves". In: *Applied Physics Letters* 7.12 (Dec. 1965), pp. 314–316. DOI: 10.1063/1.1754276.

[33] Junyao Shen et al. "High-performance surface acoustic wave devices using linbo3/sio2/sic multilayered substrates". In: *IEEE Transactions on Microwave Theory and Techniques* 69.8 (Aug. 2021), pp. 3693–3705. DOI: 10.1109/tmtt.2021.3077261.

[34] Songbin Gong et al. "Microwave acoustic devices: Recent advances and outlook". In: *IEEE Journal of Microwaves* 1.2 (Apr. 2021), pp. 601–609. DOI: 10.1109/jmw.2021.3064825.

[35] Hui Wang et al. "Temperature Performance Study of SAW sensors based on AlN and AlScN". In: *Micromachines* 14.5 (May 2023), p. 1065. DOI: 10.3390/mi14051065.

[36] Pu Chen, Guangxi Li, and Zhiyuan Zhu. "Development and application of SAW Filter". In: *Micromachines* 13.5 (Apr. 2022), p. 656. DOI: 10.3390/mi13050656.

[37] R. Aigner et al. "Bulk-acoustic-wave filters: Performance Optimization and Volume Manufacturing". In: *IEEE MTT-S International Microwave Symposium Digest, 2003* 3 (2003), pp. 2001–2004. DOI: 10.1109/mwsym.2003.1210552.

[38] Supratik Datta. *Intro to piezoelectric Baw Resonator modeling*. Sept. 2013. URL: https://www.comsol.com/blogs/piezoelectric-baw-resonator-modeling.

[39] Bo Xu et al. "Nanomechanical resonators: Toward atomic scale". In: *ACS Nano* 16.10 (Sept. 2022), pp. 15545–15585. DOI: 10.1021/acsnano.2c01673.

[40] MEMS. *What are the advantages and challenges of using MEMS resonators in RF filters?* Mar. 2023. URL: https://www.linkedin.com/advice/0/what-advantages-challenges-using-mems-resonators-rf-filters.

[41] Lei Wei et al. "The recent progress of MEMS/NEMS resonators". In: *Micromachines* 12.6 (June 2021), p. 724. DOI: 10.3390/mi12060724.

[42] Anastasiia Ciers et al. "Nanomechanical crystalline AlN resonators with high quality factors for quantum optoelectromechanics". In: *Advanced Materials* 36.44 (Sept. 2024). DOI: 10.1002/adma.202403155.

[43] F.D. Bannon, J.R. Clark, and C.T.-C. Nguyen. "High-Q HF microelectromechanical filters". In: *IEEE Journal of Solid-State Circuits* 35.4 (Apr. 2000), pp. 512–526. DOI: 10.1109/4.839911.

[44] Warner J. Venstra, Hidde J. Westra, and Herre S. van der Zant. "Mechanical stiffening, bistability, and bit operations in a microcantilever". In: *Applied Physics Letters* 97.19 (Nov. 2010). DOI: 10.1063/1.3511343.

[45] Gianluca Piazza, Philip J. Stephanou, and Albert P. Pisano. "Piezoelectric aluminum nitride vibrating contour-mode MEMS resonators". In: *Journal of Microelectromechanical Systems* 15.6 (Dec. 2006), pp. 1406–1418. DOI: 10.1109/jmems.2006.886012.

[46] Cheng Li et al. "An optical interferometry based MEMS accelerometer applicable to seismic-grade measurement". In: *IEEE Transactions on Instrumentation and Measurement* 71 (2022), pp. 1–10. DOI: 10.1109/tim.2022.3191649.

[47] Patrick A. Truitt et al. “Efficient and sensitive capacitive readout of nanomechanical resonator arrays”. In: *Nano Letters* 7.1 (Dec. 2006), pp. 120–126. DOI: 10.1021/nl062278g.

[48] S. Trolier-McKinstry and P. Muralt. “Thin film piezoelectrics for MEMS”. In: *Electronic Materials: Science and Technology* (2005), pp. 199–215. DOI: 10.1007/0-387-23319-9_10.

[49] B. M. Zwickl et al. “High quality mechanical and optical properties of commercial silicon nitride membranes”. In: *Applied Physics Letters* 92.10 (Mar. 2008). DOI: 10.1063/1.2884191.

[50] Tian-Bing Xu et al. “An ultra-high-power density piezoelectric cryogenic actuator”. In: *AIAA SCITECH 2024 Forum* (Jan. 2024). DOI: 10.2514/6.2024-0263.

[51] A. N. Oliveira et al. “Cryogenic Mount For Mirror and piezoelectric actuator for an optical cavity”. In: *Review of Scientific Instruments* 88.6 (June 2017). DOI: 10.1063/1.4989404.

[52] Shupeng Wang et al. “A survey of piezoelectric actuators with long working stroke in recent years: Classifications, principles, connections and distinctions”. In: *Mechanical Systems and Signal Processing* 123 (May 2019), pp. 591–605. DOI: 10.1016/j.ymssp.2019.01.033.

[53] Minghui Zhao et al. “Optical interferometric MEMS accelerometers”. In: *Laser & Photonics Reviews* 18.2 (Dec. 2023). DOI: 10.1002/lpor.202300713.

[54] I. Bargatin, I. Kozinsky, and M. L. Roukes. “Efficient electrothermal actuation of multiple modes of high-frequency nanoelectromechanical resonators”. In: *Applied Physics Letters* 90.9 (Feb. 2007). DOI: 10.1063/1.2709620.

[55] Mo Li, H. X. Tang, and M. L. Roukes. “Ultra-sensitive nems-based cantilevers for sensing, scanned probe and very high-frequency applications”. In: *Nature Nanotechnology* 2.2 (Jan. 2007), pp. 114–120. DOI: 10.1038/nnano.2006.208.

[56] Shiyue Hua et al. “An integrated large-scale photonic accelerator with ultralow latency”. In: *Nature* 640.8058 (Apr. 2025), pp. 361–367. DOI: 10.1038/s41586-025-08786-6.

[57] Zhihao Xu et al. “Large-scale photonic chiplet Taichi empowers 160-tops/W Artificial General Intelligence”. In: *Science* 384.6692 (Apr. 2024), pp. 202–209. DOI: 10.1126/science.adl1203.

[58] Lili Guo. *Introducing Taichi - a large-scale photonic chiplet empowers 160-tops/W Artificial General Intelligence*. URL: https://www.tsinghua.edu.cn/en/info/1399/12830.htm.

[59] Saman Jahani et al. “Controlling evanescent waves using silicon photonic all-dielectric metamaterials for dense integration”. In: *Nature Communications* 9.1 (May 2018). DOI: 10.1038/s41467-018-04276-8.

[60] Keji Huang, Shuangyang Yang, and Limin Tong. “Modeling of evanescent coupling between two parallel optical nanowires”. In: *Applied Optics* 46.9 (Mar. 2007), p. 1429. DOI: 10.1364/ao.46.001429.

[61] Carlos Ríos et al. “In-memory computing on a photonic platform”. In: *Science Advances* 5.2 (Feb. 2019). DOI: 10.1126/sciadv.aau5759.

[62] J. Feldmann et al. “Parallel convolutional processing using an integrated photonic tensor core”. In: *Nature* 589.7840 (Jan. 2021), pp. 52–58. DOI: 10.1038/s41586-020-03070-1.

[63] Wen Zhou et al. “In-memory photonic dot-product engine with electrically programmable weight banks”. In: *Nature Communications* 14.1 (May 2023). DOI: 10.1038/s41467-023-38473-x.

[64] Xuan Li et al. “Fast and reliable storage using a 5 bit, nonvolatile photonic memory cell”. In: *Optica* 6.1 (Dec. 2018), p. 1. DOI: 10.1364/optica.6.000001.

[65] Ji Xia et al. “Opto-mechanical photonic Crystal Cavities for sensing application”. In: *Applied Sciences* 10.20 (Oct. 2020), p. 7080. DOI: 10.3390/app10207080.

[66] Markus Aspelmeyer, Tobias J. Kippenberg, and Florian Marquardt. “Cavity Optomechanics”. In: *Reviews of Modern Physics* 86.4 (Dec. 2014), pp. 1391–1452. DOI: 10.1103/revmodphys.86.1391.

[67] G. Anetsberger et al. “Near-field cavity optomechanics with nanomechanical oscillators”. In: *Nature Physics* 5.12 (Oct. 2009), pp. 909–914. DOI: 10.1038/nphys1425.

[68] Jianping Yao. “Microwave Photonic Systems”. In: *Journal of Lightwave Technology* 40.20 (Oct. 2022), pp. 6595–6607. DOI: 10.1109/jlt.2022.3201776.

[69] Preetpaul Singh Devgan. *Applications of modern RF Photonics*. Artechhouse, 2018.

[70] Shi Jia et al. “Integrated dual-laser photonic chip for high-purity carrier generation enabling Ultrafast Terahertz Wireless Communications”. In: *Nature Communications* 13.1 (Mar. 2022). DOI: 10.1038/s41467-022-29049-2.

[71] Yi Zhou et al. “Microwave photonic filters and applications”. In: *Photonics* 10.10 (Sept. 2023), p. 1110. DOI: 10.3390/photonics10101110.

[72] Hanke Feng et al. “Integrated lithium niobate microwave photonic processing engine”. In: *Nature* 627.8002 (Feb. 2024), pp. 80–87. DOI: 10.1038/s41586-024-07078-9.

[73] Weipeng Zhang et al. “A system-on-chip microwave photonic processor solves dynamic RF interference in real time with picosecond latency”. In: *Light: Science & Applications* 13.1 (Jan. 2024). DOI: 10.1038/s41377-023-01362-5.

[74] Francesco Morichetti. “High-performance analog signal processing with photonic integrated circuits”. In: *Light: Science & Applications* 14.1 (Mar. 2025). DOI: 10.1038/s41377-025-01806-0.

[75] Aashish A. Clerk and Florian Marquardt. “Basic theory of Cavity Optomechanics”. In: *Cavity Optomechanics* (2014), pp. 5–23. DOI: 10.1007/978-3-642-55312-7_2.

[76] Gaurav Bahl et al. “Brillouin cavity optomechanics with microfluidic devices”. In: *Nature Communications* 4.1 (June 2013). DOI: 10.1038/ncomms2994.

[77] Wikipedia. *Reactive-Ion Etching*. May 2025. URL: https://en.wikipedia.org/wiki/Reactive-ion_etching.

[78] T. E. Standaert et al. "Role of fluorocarbon film formation in the etching of silicon, silicon dioxide, silicon nitride, and amorphous hydrogenated silicon carbide". In: *Journal of Vacuum Science & Technology A: Vacuum, Surfaces, and Films* 22.1 (Nov. 2003), pp. 53–60. DOI: 10.1116/1.1626642.

[79] Stephen A. Campbell. *The Science and Engineering of Microelectronic Fabrication*. Oxford University Press, 1996.

[80] Stephen D. Senturia. *Microsystem design*. Springer US, 2001.

[81] Andrew N. Cleland. *Foundations of nanomechanics: From solid-state theory to device applications*. Springer Berlin, 2003.

[82] Paul G. Slade. *Electrical contacts: Principles and applications*. CRC Press, 2017.

[83] D. M. Mattox. *Handbook of physical vapor deposition (PVD) processing (2nd ed.)* William Andrew Publishing, 2010.

[84] Milton Ohring. *Materials science of thin films: Deposition and structure*. ELSEVIER ACADEMIC PRESS, 2025.

[85] Isaku Kanno, Hidetoshi Kotera, and Kiyotaka Wasa. *Handbook of Sputter Deposition Technology: Fundamentals and applications for functional thin films, nanomaterials, and MEMS*. Elsevier, 2012.

[86] J T Gudmundsson. "Physics and technology of magnetron sputtering discharges". In: *Plasma Sources Science and Technology* 29.11 (Nov. 2020), p. 113001. DOI: 10.1088/1361-6595/abb7bd.

[87] B. Janarthanan et al. "Basic deposition methods of thin films". In: *Journal of Molecular Structure* 1241 (Oct. 2021), p. 130606. DOI: 10.1016/j.molstruc.2021.130606.

[88] Carlos Ramos et al. "Surface temperature of a 2 in. ti target during DC magnetron sputtering". In: *Journal of Vacuum Science & Technology A* 42.3 (Mar. 2024). DOI: 10.1116/6.0003481.

[89] Leonid R. Shaginyan, Mikhail I. Mironov, and Anatoly I. Kuzmichev. "in situ calorimetric temperature measurements of Cu, Cr, ti targets during DC magnetron sputtering". In: *Journal of Vacuum Science & Technology A* 43.1 (Dec. 2024). DOI: 10.1116/6.0003994.

[90] Terry M. Tritt. *Thermal conductivity: Theory, properties, and applications*. Springer International Publishing, 2005.

[91] Vac Coat. *Why should have a back-plated sputtering target?* June 2025. URL: https://vaccoat.com/blog/why-should-a-sputtering-target-be-back-plated/.

[92] Michael Elliott Schoff. "Sputter target erosion and its effects on long duration DC magnetron sputter coating". PhD thesis. University of California, San Diego, 2009.

[93] N Brenning et al. "The role of ohmic heating in DC magnetron sputtering". In: *Plasma Sources Science and Technology* 25.6 (Nov. 2016), p. 065024. DOI: 10.1088/0963-0252/25/6/065024.

[94] Kiumars Aryana et al. "Optical and thermal properties of $Ge_2Sb_2Te_5$, Sb_2Se_3, and Sb_2S_3 for reconfigurable photonic devices [invited]". In: *Optical Materials Express* 13.11 (Oct. 2023), p. 3277. DOI: 10.1364/ome.503178.

[95] Kurt J. Lesker company. *Ramp Procedure for Ceramic Target Conditioning*. URL: https://www.lesker.com/newweb/deposition_materials/rampprocedure_ceramictarget_materials.cfm?pgid=0.

[96] Angstrom Engineering. *Sputter deposition reference sheet*. Oct. 2024. URL: https://angstromengineering.com/resources/sputter-deposition-reference-sheet/.

[97] Utku Emre Ali et al. "A Universal Pick-and-Place Assembly for Nanowires". In: *Small* 18.38 (Aug. 2022). DOI: 10.1002/smll.202201968.

[98] Zurich Instruments. *White Paper: Principles of Lock-in Detection and the State of the Art*. Apr. 2023. URL: https://www.zhinst.com/europe/en/resources/principles-of-lock-in-detection.

[99] Ansys Lumerical. *Finite difference time domain (FDTD) solver introduction - ansys optics*. URL: https://optics.ansys.com/hc/en-us/articles/360034914633-Finite-Difference-Time-Domain-FDTD-solver-introduction.

[100] COMSOL. *The COMSOL software product suite*. URL: https://www.comsol.com/products.

[101] COMSOL. *Multiphysics Cyclopedia: Eigenfrequency Analysis*. URL: https://www.comsol.com/multiphysics/eigenfrequency-analysis.

[102] K. L. Ekinci, Y. T. Yang, and M. L. Roukes. "Ultimate limits to inertial mass sensing based upon Nanoelectromechanical Systems". In: *Journal of Applied Physics* 95.5 (Mar. 2004), pp. 2682–2689. DOI: 10.1063/1.1642738.

[103] Mikhail Dunaevskiy et al. "Youngs modulus of wurtzite and zinc blende InP nanowires". In: *Nano Letters* 17.6 (May 2017), pp. 3441–3446. DOI: 10.1021/acs.nanolett.7b00312.

[104] COMSOL. *Structural Mechanics Module Users Guide*. 2022. URL: https://doc.comsol.com/6.1/doc/com.comsol.help.sme/StructuralMechanicsModuleUsersGuide.pdf.

[105] Laurent Vivien and Lorenzo Pavesi. *Handbook of silicon photonics*. CRC Press, 2020.

[106] Bahaa E. A. Saleh and Malvin Carl Teich. *Fundamentals of photonics. part 2 photonics*. Wiley, 2019.

[107] G. D. Pettit and W. J. Turner. "Refractive index of INP". In: *Journal of Applied Physics* 36.6 (June 1965), pp. 2081–2081. DOI: 10.1063/1.1714410.

[108] M.K. Smit et al. *Handbook for Generic Photonic IC Design*. Photonic Integration group, Eindhoven University of Technology, 2024.

[109] Eric Sage et al. "Single-particle mass spectrometry with arrays of frequency-addressed nanomechanical resonators". In: *Nature Communications* 9.1 (Aug. 2018). DOI: 10.1038/s41467-018-05783-4.

[110] Brian Stern et al. "Compact narrow-linewidth integrated laser based on low-loss silicon nitride ring resonator". In: *Conference on Lasers and Electro-Optics* (2018). DOI: 10.1364/cleo_si.2018.sth1a.4.

[111] Abdul Rahim et al. "Expanding the silicon photonics portfolio with silicon nitride photonic integrated circuits". In: *Journal of Lightwave Technology* 35.4 (Feb. 2017), pp. 639–649. DOI: 10.1109/jlt.2016.2617624.

[112] Michael J. Strain et al. "Tunable Q-factor silicon microring resonators for ultra-low power parametric processes". In: *Optics Letters* 40.7 (Mar. 2015), p. 1274. DOI: 10.1364/ol.40.001274.

[113] Jinan Nijem et al. "High-Q and high finesse silicon microring resonator". In: *Optics Express* 32.5 (Feb. 2024), p. 7896. DOI: 10.1364/oe.514080.

[114] Aleksandr Biberman et al. "Ultralow-loss silicon ring resonators". In: *The 9th International Conference on Group IV Photonics (GFP)* (Aug. 2012), pp. 39–41. DOI: 10.1109/group4.2012.6324079.

[115] Shuai Cui et al. "Ultra-high-quality factor Micro-Ring resonator based on silicon nitride". In: *2023 Conference on Lasers and Electro-Optics Europe & European Quantum Electronics Conference (CLEO/Europe-EQEC)* (June 2023), pp. 1–1. DOI: 10.1109/cleo/europe-eqec57999.2023.10232531.

[116] Kevin Luke et al. "Overcoming si*n* film stress limitations for high quality factor ring resonators". In: *Optics Express* 21.19 (Sept. 2013), p. 22829. DOI: 10.1364/oe.21.022829.

[117] Matthew W. Puckett et al. "422 million intrinsic quality factor planar integrated all-waveguide resonator with sub-mhz linewidth". In: *Nature Communications* 12.1 (Feb. 2021). DOI: 10.1038/s41467-021-21205-4.

[118] Valerio Vitali et al. "Highly efficient dual-level grating couplers for silicon nitride photonics". In: *Scientific Reports* 12.1 (Sept. 2022). DOI: 10.1038/s41598-022-19352-9.

[119] S. Hadi Badri and M.M. Gilarlue. "Coupling SI3N4 waveguide to SOI waveguide using transformation optics". In: *Optics Communications* 460 (Apr. 2020), p. 125089. DOI: 10.1016/j.optcom.2019.125089.

[120] Joseph Goldstein et al. *Scanning electron microscopy and X-ray microanalysis*. Springer, 2018.

[121] Peter R. Saulson. "Thermal noise in mechanical experiments". In: *Physical Review D* 42.8 (Oct. 1990), pp. 2437–2445. DOI: 10.1103/physrevd.42.2437.

[122] R Kubo. "The fluctuation-dissipation theorem". In: *Reports on Progress in Physics* 29.1 (Jan. 1966), pp. 255–284. DOI: 10.1088/0034-4885/29/1/306.

[123] John P. Mathew, Anand Bhushan, and Mandar M. Deshmukh. "Tension mediated nonlinear coupling between orthogonal mechanical modes of nanowire resonators". In: *Solid State Communications* 282 (Oct. 2018), pp. 17–20. DOI: 10.1016/j.ssc.2018.07.009.

[124] Amir Arbabi and Lynford L. Goddard. "Measurements of the refractive indices and thermo-optic coefficients of Si_3N_4 and SiO_x using microring resonances". In: *Optics Letters* 38.19 (Sept. 2013), p. 3878. DOI: 10.1364/ol.38.003878.

[125] Saeed Khan et al. "Silicon-on-nitride optical waveguides for mid- and near-infrared integrated photonics". In: *CLEO: 2013* (2013). DOI: 10.1364/cleo_si.2013.cth4f.4.

[126] Dawn T. Tan and Xavier X. Chia. "Ultra-low loss silicon nitride becomes even cooler". In: *Light: Science & Applications* 13.1 (Sept. 2024). DOI: 10.1038/s41377-024-01576-1.

[127] M T Alam et al. "Influence of strain on thermal conductivity of silicon nitride thin films". In: *Journal of Micromechanics and Microengineering* 22.4 (Mar. 2012), p. 045001. DOI: 10.1088/0960-1317/22/4/045001.

[128] MIT. *6.777J/2.751J Material Properties Database: Thermal silicon oxide*. URL: https://www.mit.edu/~6.777/matprops/sio2.htm.

[129] Gustavo Ciardi. *Understanding the specifications of lock-in amplifiers*. Feb. 2023. URL: https://www.zhinst.com/ch/en/blogs/understanding-specifications-lock-in-amplifiers.

[130] N. C. Pisenti et al. "An ultra-low noise, high-voltage piezo-driver". In: *Review of Scientific Instruments* 87.12 (Dec. 2016). DOI: 10.1063/1.4969059.

[131] Jeff Court. *How to drive piezoelectric actuators*. URL: https://blog.piezo.com/how-to-drive-piezoelectric-actuators.

[132] Karl F. Graff. *Wave motion in elastic solids*. Dover Publications, 2012.

[133] Maurício M Lima and Paulo V Santos. "Modulation of photonic structures by surface acoustic waves". In: *Reports on Progress in Physics* 68.7 (June 2005), pp. 1639–1701. DOI: 10.1088/0034-4885/68/7/r02.

[134] I.C. Chang. "I. Acoustooptic devices and applications". In: *IEEE Transactions on Sonics and Ultrasonics* 23.1 (Jan. 1976), pp. 2–21. DOI: 10.1109/t-su.1976.30835.

[135] D. Royer and E. Dieulesaint. *Elastic waves in solids*. Springer, 2000.

[136] Bernard Jaffe. *Piezoelectric Ceramics*. Elsevier Science, 2014.

[137] A. Yariv. "Universal relations for coupling of optical powerbetweenmicroresonators and dielectric waveguides". In: *Electronics Letters* 36.4 (Feb. 2000), pp. 321–322. DOI: 10.1049/el:20000340.

[138] Kerry Vahala. *Optical microcavities*. World Scientific, 2007.

[139] K. L. Ekinci and M. L. Roukes. "Nanoelectromechanical Systems". In: *Review of Scientific Instruments* 76.6 (May 2005). DOI: 10.1063/1.1927327.

[140] DEAN T. NAYFEH ALI H.. MOOK. *Nonlinear oscillations*. WILEY-VCH, 2024.

[141] C. Samanta et al. "Nonlinear nanomechanical resonators approaching the quantum ground state". In: *Nature Physics* 19.9 (June 2023), pp. 1340–1344. DOI: 10.1038/s41567-023-02065-9.

[142] I. Kozinsky et al. "Basins of attraction of a nonlinear nanomechanical resonator". In: *Physical Review Letters* 99.20 (Nov. 2007). DOI: 10.1103/physrevlett.99.207201.

[143] Paulo Sergio Branicio et al. "Interaction potential for indium phosphide: A molecular dynamics and first-principles study of the elastic constants, Generalized Stacking Fault and surface energies". In: *Journal of Physics: Condensed Matter* 21.9 (Jan. 2009), p. 095002. DOI: 10.1088/0953-8984/21/9/095002.

[144] C.E. Shannon. "Communication in the presence of noise". In: *Proceedings of the IEEE* 72.9 (1984), pp. 1192–1201. DOI: 10.1109/proc.1984.12998.

[145] David W. Hahn and M. Necati Özk. *Heat conduction*. Wiley, 2012.

[146] David G. Cahill et al. "Nanoscale Thermal Transport". In: *Journal of Applied Physics* 93.2 (Jan. 2003), pp. 793–818. DOI: 10.1063/1.1524305.

[147] E. T. Swartz and R. O. Pohl. "Thermal boundary resistance". In: *Reviews of Modern Physics* 61.3 (July 1989), pp. 605–668. DOI: 10.1103/revmodphys.61.605.

[148] Barbara Larwa et al. "Parameters of the Carslaw-jaeger equation describing the temperature distribution in the ground". In: *Czasopismo Techniczne* 9 (2018). DOI: 10.4467/2353737xct.18.132.8971.

[149] Eric Pop. "Energy dissipation and transport in nanoscale devices". In: *Nano Research* 3.3 (Mar. 2010), pp. 147–169. DOI: 10.1007/s12274-010-1019-z.

[150] Horatio S. Carslaw and J. C. Jaeger. *Conduction of heat in solids by H. S. Carslaw and J. C. Jaeger*. Clarendon Press, 1959.

[151] James M. Gere and Barry J. Goodno. *Mechanics of Materials*. Cengage Learning, 2013.

[152] Robert D. Blevins. *Formulas for natural frequency and mode shape*. Krieger Pub. Co, 2001.

[153] S. Timoshenko and J. M. Gere. *Mechanics of Materials*. 5th. PWS Publishing, 1997.

[154] Singiresu S. Rao. *Vibration of continuous systems*. John Wiley & Sons, Inc, 2019.

[155] R. L. Hannah and S. E. Reed. *Strain gage users handbook*. Chapman & Hall; Society for Experimental Mechanics, 1994.

[156] James W. Dally and William F. Riley. *Experimental stress analysis*. College House Enterprises, 2005.

[157] W.-H. Chuang et al. "Mechanical property characterization of LPCVD silicon nitride thin films at cryogenic temperatures". In: *Journal of Microelectromechanical Systems* 13.5 (Oct. 2004), pp. 870–879. DOI: 10.1109/jmems.2004.836815.

[158] A. Bogozi et al. "Elastic modulus study of gold thin film for use as an actuated membrane in a superconducting RF mem switch". In: *IEEE Transactions on Appiled Superconductivity* 15.2 (June 2005), pp. 980–983. DOI: 10.1109/tasc.2005.850157.

[159] Hugh O. Pierson. *Handbook of Refractory Carbides and nitrides: Properties, characteristics, processing and applications*. Noyes publication, 1996.

[160] Hugh O. Pierson. *Handbook of Chemical Vapor Deposition: Principles, technology and applications*. Elsevier Science, 2014.

[161] F. C. Nix and D. MacNair. "The thermal expansion of Pure Metals: Copper, gold, aluminum, nickel, and iron". In: *Physical Review* 60.8 (Oct. 1941), pp. 597–605. DOI: 10.1103/physrev.60.597.

[162] S. M. Sze and Kwok Kwok Ng. *Physics of semiconductor devices*. Wiley-Interscience, 2007.

[163] Roghayeh Nikbakht et al. "High quality factor silicon nitride nanomechanical resonators fabricated by maskless femtosecond laser micromachining". In: *Journal of Vacuum Science and Technology B* 41.2 (Mar. 2023). DOI: 10.1116/5.0124150.

[164] Atakan B. Ar et al. "Intermodal coupling as a probe for detecting nanomechanical modes". In: *Physical Review Applied* 9.3 (Mar. 2018). DOI: 10.1103/physrevapplied.9.034024.

[165] Mo Li. "Very high frequency nanoelectromechanical resonators and their chemical sensing applications". PhD thesis. California Institute of Technology, 2007.

[166] Allan G. Piersol, Thomas L. Paez, and Cyril M. Harris. *Harris shock and Vibration Handbook*. McGraw-Hill, 2010.

[167] L. Reimer et al. *Scanning electron microscopy: Physics of image formation and microanalysis*. Springer Berlin / Heidelberg, 2013.

[168] K.R. Williams and R.S. Muller. "Etch rates for micromachining processing". In: *Journal of Microelectromechanical Systems* 5.4 (1996), pp. 256–269. DOI: 10.1109/84.546406.

[169] David J. Monk, David S. Soane, and Roger T. Howe. "A review of the chemical reaction mechanism and kinetics for hydrofluoric acid etching of silicon dioxide for surface micromachining applications". In: *Thin Solid Films* 232.1 (Sept. 1993), pp. 1–12. DOI: 10.1016/0040-6090(93)90752-b.

[170] Marc J. Madou. *Fundamentals of microfabrication and nanotechnology*. CRC Press, 2012.

[171] Ripon Kumar Dey and Bo Cui. "Stitching error reduction in electron beam lithography with in-situ feedback using self-developing resist". In: *Journal of Vacuum Science & Technology B, Nanotechnology and Microelectronics: Materials, Processing, Measurement, and Phenomena* 31.6 (Nov. 2013). DOI: 10.1116/1.4831769.

[172] S. E. Ziemniak, M. E. Jones, and K. E. Combs. "Solubility and phase behavior of cr(iii) oxides in alkaline media at elevated temperatures". In: *Journal of Solution Chemistry* 27.1 (Jan. 1998), pp. 33–66. DOI: 10.1023/a:1022688528380.

[173] Barbara Zydorczak et al. "Dissolution of cr2O3(s) and the behavior of chromium in concentrated NaOH Solutions". In: *Industrial & Engineering Chemistry Research* 51.51 (Dec. 2012), pp. 16537–16543. DOI: 10.1021/ie302096e.

[174] H.W. van Zeijl. "LPCVD silicon nitride-on-silicon spacer technology". In: *Conference: Proceedings - Electrochemical Society* PV 2005-08 (Jan. 2005). DOI: https://ris.utwente.nl/ws/portalfiles/portal/108989455/lpcvd.pdf.

[175] Rogue Valley Microdevices. *Silicon Nitride*. Sept. 2022. URL: https://roguevalleymicrodevices.com/thin-films/nitride/.

[176] Simen Martinussen et al. "Thick waveguides of low-stress stoichiometric silicon nitride on Sapphire (sinos)". In: *Optics Express* 32.21 (Sept. 2024), p. 36835. DOI: 10.1364/oe.536578.

[177] Scott S. Verbridge et al. “High quality factor resonance at room temperature with nanostrings under high tensile stress”. In: *Journal of Applied Physics* 99.12 (June 2006). DOI: 10.1063/1.2204829.

[178] Taehee Jeong et al. “Thermal boundary resistance for gold and CoFe alloy on silicon nitride films”. In: *Journal of Applied Physics* 111.8 (Apr. 2012). DOI: 10.1063/1.3703571.

[179] T. S. Biswas et al. “High-Q gold and silicon nitride bilayer nanostrings”. In: *Applied Physics Letters* 101.9 (Aug. 2012), p. 093105. DOI: 10.1063/1.4748977.

[180] V.T. Srikar and S.D. Senturia. “Thermoelastic damping in fine-grained polysilicon flexural beam resonators”. In: *Journal of Microelectromechanical Systems* 11.5 (Oct. 2002), pp. 499–504. DOI: 10.1109/jmems.2002.802902.

[181] S. Papaleo, W. H. Zisser, and H. Ceric. “Factors that influence delamination at the bottom of open tsvs”. In: *2015 International Conference on Simulation of Semiconductor Processes and Devices (SISPAD)* (Sept. 2015), pp. 421–424. DOI: 10.1109/sispad.2015.7292350.

[182] Joshua Kim et al. “Highly stretchable wrinkled gold thin film wires”. In: *Applied Physics Letters* 108.6 (Feb. 2016). DOI: 10.1063/1.4941439.

[183] Xiang Liu et al. “Future development directions of high-temperature strain gauges: A comprehensive review of structure and performance characteristics”. In: *Nanoscale Advances* (2025). DOI: 10.1039/d5na00039d.

[184] S. Sandeep et al. “Piezoelectric aluminum nitride thin films for CMOS compatible MEMS: Sputter deposition and doping”. In: *Critical Reviews in Solid State and Materials Sciences* 50.2 (Oct. 2024), pp. 161–188. DOI: 10.1080/10408436.2024.2406247.

[185] Almur A. Rabih et al. “Aluminum nitride out-of-plane piezoelectric MEMS actuators”. In: *Micromachines* 14.3 (Mar. 2023), p. 700. DOI: 10.3390/mi14030700.

[186] Cheng Tu, Joshua E.-Y. Lee, and Xiao-Sheng Zhang. “Dissipation analysis methods and Q-enhancement strategies in piezoelectric MEMS laterally vibrating resonators: A Review”. In: *Sensors* 20.17 (Sept. 2020), p. 4978. DOI: 10.3390/s20174978.

[187] Gayathri Pillai and Sheng-Shian Li. “Piezoelectric MEMS resonators: A Review”. In: *IEEE Sensors Journal* 21.11 (June 2021), pp. 12589–12605. DOI: 10.1109/jsen.2020.3039052.

[188] Simone Pagliano et al. “Micro 3D printing of a functional MEMS accelerometer”. In: *Microsystems & Nanoengineering* 8.1 (Sept. 2022). DOI: 10.1038/s41378-022-00440-9.

[189] David E. Marschner et al. “A methodology for two-photon polymerization micro 3D printing of objects with long overhanging structures”. In: *Additive Manufacturing* 66 (Mar. 2023), p. 103474. DOI: 10.1016/j.addma.2023.103474.

[190] Nanoscribe. *Nanoscribe photoresins specifically designed for two-photon polymerization*. URL: https://www.nanoscribe.com/en/products/ip-photoresins/.

[191] Wanli Jiang et al. “Effect of hyperthermal annealing on LPCVD silicon nitride”. In: *Materials Science in Semiconductor Processing* 43 (Mar. 2016), pp. 222–229. DOI: 10.1016/j.mssp.2015.12.020.

[192] Antony Premkumar Peter et al. “Effect of rapid thermal annealing on the mechanical stress and physico-chemical properties in plasma enhanced atomic layer deposited silicon nitride thin films”. In: *Journal of Vacuum Science & Technology B* 40.5 (Aug. 2022). DOI: 10.1116/6.0001922.

[193] Dong-ling Li et al. “Stress control of silicon nitride films deposited by plasma enhanced chemical vapor deposition”. In: *Optoelectronics Letters* 12.4 (July 2016), pp. 285–289. DOI: 10.1007/s11801-016-6058-6.

[194] R.W. Hoffman. “Stresses in thin films: The relevance of grain boundaries and impurities”. In: *Thin Solid Films* 34.2 (May 1976), pp. 185–190. DOI: 10.1016/0040-6090(76)90453-3.

[195] L. B. Freund and S. Suresh. *Thin film materials: Stress, defect formation, and Surface Evolution*. Cambridge University Press, 2009.

[196] Hyun-Jong Kim et al. “High-throughput analysis of thin-film stresses using arrays of micromachined cantilever beams”. In: *Review of Scientific Instruments* 79.4 (Apr. 2008). DOI: 10.1063/1.2912826.

[197] Yohan Jung, Dongseok Lee, and Jongbaeg Kim. “Recent progress in aluminum nitride for piezoelectric MEMS mirror applications: Enhancements with scandium doping”. In: *Microsystems & Nanoengineering* 11.1 (Sept. 2025). DOI: 10.1038/s41378-025-01053-8.

[198] R. Voss et al. “Silicon angular rate sensor for automotive applications with piezoelectric drive and piezoresistive read-out”. In: *Proceedings of International Solid State Sensors and Actuators Conference (Transducers 97)* 2 (1997), pp. 879–882. DOI: 10.1109/sensor.1997.635242.

[199] Charles S. Smith. “Piezoresistance effect in germanium and Silicon”. In: *Physical Review* 94.1 (Apr. 1954), pp. 42–49. DOI: 10.1103/physrev.94.42.

[200] Joseph C. Doll and Beth Pruitt. *Piezoresistor design and applications*. Springer, 2013.